High Reynolds-number flows over bluff bodies

Von der Fakultät Maschinenbau der

Gottfried Wilhelm Leibniz Universität Hannover

zur Erlangung der *venia legendi* für das Fachgebiet

Strömungsmechanik

genehmigte Habilitationsschrift

von

Dr.-Ing. Nils Paul van Hinsberg

aus 's-Hertogenbosch, die Niederlande

Göttingen, 2024

In memoriam
URS, DORIE, BIENE

Preface

This monograph was written and published following my professional activities as a research associate and leader of the research group *Aeroelastic Wind-Tunnel Experiments* at the Institute of Aeroelasticity of the German Aerospace Center (DLR e.V.) in Göttingen, Germany. It covers the majority of the experiments on the time-resolved fluid dynamics of two-dimensional cylindrical and prismatic bluff bodies in a cross-flow, which were carried out by my students and myself in the unique High-Pressure wind tunnel facility Göttingen (HDG) in the period from January 2013 to December 2021. The content of the work at hand should be regarded by you, the reader, as a very detailed reference book and could be used, for example, as a source for validating your CFD codes.

For the comprehensive support, I would like to express my sincere gratitude to the leader of the department *Aeroelastic Experiments*, Dr. rer. nat. Holger Mai, who not only gave me the opportunity to lead the research group, but also granted me the crucial scientific freedom to carry out the experimental research on which this monograph is based. My deep appreciation goes to Prof. Dr.-Ing. Jörg Seume, who gave me the opportunity to set up my own lecture series in *Flow-Induced Vibrations* from scratch, in that way enabling me to carry out my habilitation at the Institute of Turbomachinery and Fluid Dynamics of the Gottfried Wilhelm Leibniz University Hannover, Germany. I am grateful for the support by Dipl.-Ing. Jan Gößling in the annual planning and preparation of the lecture series, as well as for the co-supervision during the subsequent examination of the students. My special thanks goes to my predecessor Dr. rer. nat. Günter Schewe for the many years of scientific and personal support during my time at Institute of Aeroelasticity and for awakening my fascination for bluff body flows at high to very high Reynolds numbers. While the majority of the experiments were financed from the DLR's internal pot for fundamental research, financial support from Chevron Corporation and Technip USA, Inc. in the framework of a third-party project is gratefully acknowledged. I am grateful to all of my former group members. I would especially like to mention Dipl.-Ing. Johannes Nuhn for his professional support in setting up the experiment and the intensive discussions about the applied measurement techniques. Above all, I will remember his many personal and vivid anecdotes about the adventures and subsequent high vet bills of his two cats. For the design and manufacture of my experimental setups and wind tunnel models, I would like to express my sincere thank to (in alphabetical order) Nikolai Burbach, M. Eng. Helena Fink, Dipl.-Ing. Thorsten Gleisberg, Joachim Grimme, M. Eng. Nikola Mengel, Dipl.-Ing. Marc Tegeler, Bianca Eilerts, and all other persons at Systemhaus Technik. In the course of this, Deharde GmbH should also be mentioned, because they carried out the manufacture of several of the many wind tunnel models. Special thanks also go to my Bachelor and Master students Annika Frede, Francesco Gava, Robin Höltzcke, Jan-Markus Lückhof, and Julius Sieg. It is thanks to their commitment and dedication that my ideas could so often be quickly put into experimental practice. Among them, I would especially like to thank Annika for carrying out the delicate wind tunnel measurements described in Chapter 4.2 as part of her Master thesis

Göttingen, September 2024   Dr.-Ing. Nils Paul van Hinsberg

Abstract

Circular cylinders or prisms with square cross-sections in a uniform, steady cross-flow are inherently coupled with large regions of massive, large-scale flow separation, a broad base region containing highly unsteady, recirculating flow and low pressures, and eddy shedding in the near wake. This not only produces a high total drag on the bluff body, but leads also to the well-known *Kármán vortex street* in its wake. The eddy shedding occurs over a wide range of Reynolds numbers and causes pressure fluctuations on those bluff bodies both parallel and transverse to the oncoming flow. In case they are mounted elastically, these prisms or cylinders can thereupon experience various types of flow-induced vibrations with significant additional increases in the mean drag and the lift fluctuations, with *galloping* being the most dangerous fluid-elastic instability owing to the increase in the amplitude of the limit cycle oscillation with increasing flow velocity.

Modern, high-fidelity Computational Fluid Dynamics (CFD) and reduced-order models already play nowadays a central role in optimising appropriate countermeasures, either passive or active, in the design process to avoid or suppress flow-induced structural excitations. A robust and accurate prediction modelling of the effect of vibration control methods on the (highly) unsteady and complex flow over square-section prisms and circular cylinders, based on sophisticated nonlinear dynamic models, requires even to this day precise statistical validation data that can only be obtained by experiments beforehand. Tests on full-scale structures are costly, not seldom have to be conducted under difficult conditions and time pressure, and are mostly accompanied with a priori unknown and highly dynamic flow conditions, such as impacting waves, atmospheric turbulence, wind gusts, or strong spatial variations in wind shear. Small-scale parametric studies in a laboratory environment, on the other hand, have the advantage of a virtually "unlimited" measurement time and can be performed at well-defined and reproducible boundary conditions.

The present monograph deals with the detailed analysis of the impact of various governing and influencing model and flow parameters on the flow over 2D prismatic bluff bodies with square cross-sections, arranged either as isolated or as a pair in a tandem configuration in a cross-flow. Eleven experimental measurement campaigns were conducted in the High-Pressure wind tunnel facility Göttingen in a low subsonic flow at Reynolds numbers in the range of 1.0×10^5 to 1.0×10^7. Besides the Reynolds number, the wide range of studied parameters also includes the incidence angle, the lateral edge roundness, the surface roughness, and, in the case of two prisms placed in-line, additionally the spacing between them. Isolated, in pairs, and in combinations of three or more parameters, their influence on the mean and fluctuating aerodynamic forces on the prisms as well as on the eddy shedding frequency is evaluated. Additional mean surface pressure distributions provide information on the locations of boundary layer separation and free shear layer reattachment. In this way, it is assessed to what extent these parameters enable potential valuable countermeasures that can successfully be applied in a passive way to reduce undesired flow-induced excitations.

Zusammenfassung

Kreisförmige Zylinder und Prismen mit quadratischen Querschnitt in einer gleichmäßigen, stationären Querströmung sind von Natur aus mit großen Bereichen massiver, großflächiger Strömungsablösung, einem breiten Totwassergebiet mit stark instationärer, rezirkulierender Strömung und niedrigen Drücken, sowie mit Wirbelablösung in der Nachlaufströmung gekoppelt. Dies führt nicht nur zu einem hohen Gesamtwiderstand des stumpfen Körpers, sondern auch zu der bekannten *Kármán Wirbelstraße* in seinem Nachlauf. Die Wirbelablösung tritt über einen großen Bereich von Reynolds-Zahlen auf und verursacht Druckfluktuationen auf diese stumpfen Körper sowohl parallel als auch quer zur Anströmung. Wenn sie elastisch gelagert sind, können diese Prismen und Zylinder daraufhin verschiedene Arten strömungsinduzierter Schwingungen mit signifikanter zusätzlicher Erhöhung des mittleren Widerstandes als auch der Fluktuationen im Auftrieb erfahren, wobei *Galloping* die gefährlichste fluidelastische Instabilität aufgrund der Zunahme der Amplitude der Grenzzyklusschwingung mit zunehmender Strömungsgeschwindigkeit ist.

Moderne numerische Strömungssimulationen (CFD) und "*reduced-order models*" spielen heutzutage bereits im Entwurfsprozess eine zentrale Rolle bei der Optimierung geeigneter passiver oder aktiver Gegenmaßnahmen, um strömungsinduzierte Strukturanregungen zu vermeiden oder zu unterdrücken. Eine robuste und genaue Vorhersagemodellierung der Wirkung von Schwingungsregelungsmethoden auf die (stark) instationäre und komplexe Strömung über Prismen mit quadratischen Querschnitt und Kreiszylindern, welche auf anspruchsvollen nichtlinearen dynamischen Modellen basiert, erfordert auch heute noch präzise statistische Validierungsdaten, die nur durch Experimente im Vorfeld gewonnen werden können. Versuche an Strukturen im Originalmaßstab sind kostspielig, müssen nicht selten unter schwierigen Bedingungen und unter Zeitdruck durchgeführt werden und gehen meist mit a priori unbekannten instationären Strömungsbedingungen einher, wie z. B. aufprallenden Wellen, atmosphärischen Turbulenzen, Windböen oder starken räumlichen Variationen der Windscherung. Parametrische Studien in kleinem Maßstab in einer Laborumgebung haben dagegen nicht nur den Vorteil, dass die Messzeit nahezu "unbegrenzt" ist, sondern auch, dass sie unter genau definierten und gut reproduzierbaren Randbedingungen durchgeführt werden können.

Die vorliegende Monographie befasst sich mit der detaillierten Analyse der Auswirkung verschiedener maßgeblicher und beeinflussender Modell- und Strömungsparameter auf die Strömung über 2D prismatische stumpfe Körper mit quadratischem Querschnitt, die entweder isoliert oder als Paar in einer Tandemkonfiguration innerhalb einer Querströmung angeordnet sind. Elf experimentelle Messkampagnen wurden im Hochdruck-Windkanal Göttingen in einer Unterschallströmung bei Reynolds-Zahlen im Bereich von 1.0×10^5 bis 1.0×10^7 durchgeführt. Zu den untersuchten Parametern gehören neben der Reynolds-Zahl auch der Anstellwinkel, die seitliche Kantenabrundung, die Oberflächenrauhigkeit und bei zwei hinter einander angeordneten Prismen zusätzlich der Abstand zwischen ihnen. Isoliert, paarweise und in Kombinationen von drei oder mehr Parametern wird ihr Einfluss auf die mittleren und fluktuierenden aerodynamischen Kräfte auf die Prismen sowie auf die Wirbelablösefrequenz bewertet. Zusät-

zliche gemittelte Druckverteilungen auf der Oberfläche geben Aufschluss über die Positionen der Grenzschichtablösung und des Wiederanlegens der freien Scherschichten. Auf diese Weise wird abgeschätzt, inwieweit diese Parameter potentiell wertvolle Gegenmaßnahmen ermöglichen, die passiv zur Reduzierung unerwünschter, strömungsinduzierter Anregungen erfolgreich eingesetzt werden können.

Contents

List of Figures

LIST OF FIGURES

List of Tables

Nomenclature

Symbol	Description	Unit
Alphabets		
A	Amplitude	m
C_D	Global drag coefficient	$-$
C_d	Sectional drag coefficient	$-$
C_L	Global lift coefficient	$-$
C_l	Sectional lift coefficient	$-$
C_M	Global torsional moment coefficient	$-$
C_m	Sectional pitch moment coefficient	
C_p	Pressure coefficient	$-$
C_y	Lateral force coefficient	$-$
D	Diameter	m
	Face length of prism	m
	Global drag force	$kg \cdot m/s^2$
d	Sectional drag coefficient	$kg \cdot m/s^2$
	Width	m
f	Frequency	$1/s$
F_y	Lateral force	$kg \cdot m/s^2$
H	Test section height	m
h	Height	m
k_s	Equivalent sand-grain roughness	m
L	Length	m
	Global lift force	$kg \cdot m/s^2$
l	Sectional lift coefficient	$kg \cdot m/s^2$
L_f	Length of near-wake / eddy formation length	m
L_t	Location of laminar-turbulent transition in free shear layer	m
n	Normal	$-$
p	Pressure	$kg/(m \cdot s^2)$
q	Dynamic pressure	$kg/(m \cdot s^2)$
r	Radius	m
S	Gap size	m
s	Circumferential location on surface	m
T	Time	s
t	Time	s

U	Total velocity	m/s
u	Horizontal velocity component	m/s
v	Vertical velocity component	m/s
W	Width of near-wake	m
X	Downstream direction	$-$
Z	Cross-flow direction	$-$

Greek symbols

α	Incidence angle	$^\circ$
Δ	Difference	$-$
δ	Boundary layer thickness	m
μ	Dynamic viscosity	$kg/(m \cdot s)$
φ	Circumferential angle	$^\circ$
ρ	Density	kg/m^3

Superscripts

$(\ )'$	fluctuating part

Subscripts

$(\ )_0$	at rest, total
$(\ )_{1,2}$	first and second, upstream and downstream
$(\ )_\infty$	based on free stream
$(\ )_b$	base
$(\ )_{cr}$	critical
$(\ )_{cyl}$	circular cylinder
$(\ )_f$	front face
$(\ )_{gal}$	galloping
$(\ )_i$	integer
$(\ )_L$	based on global lift
$(\ )_{lam}$	laminar
$(\ )_{max}$	maximum
$(\ )_{min}$	minimum
$(\ )_n$	natural
$(\ )_{pot}$	potential
$(\ )_{proj}$	projected
$(\ )_r$	reduced
$(\ )_{ref}$	reference
$(\ )_{rms}$	Root Mean Square
$(\ )_s$	separation, shedding, structure, surface coordinate
$(\ )_{scan}$	scanning
$(\ )_{single}$	isolated
$(\ )_{test\_sec}$	test section
$(\ )_{turb}$	turbulent
$(\ )_w$	wake

Dimensionless numbers

M	Mach number
Re	Reynolds number
St	Strouhal number

Abbreviations

$2D$	Two-dimensional
AI	Artificial intelligence
AR	Aspect ratio
CPU	Central processing unit
DLR	German Aerospace Center (in German: *Deutsches Zentrum für Luft- und Raumfahrt*)
DNS	Direct Numerical Simulation
DNW	German-Dutch Wind Tunnels (in German: *Deutsch-Niederländische Windkanäle*)
DoF	Degree of freedom
$ex.kt$	Excess kurtosis
HDG	High-Pressure wind tunnel facility Göttingen
HWA	Hot-Wire Anemometry
LCO	Limit cycle oscillation
LDV	Laser Doppler Velocimetry
LES	Large Eddy Simulation
LSB	Laminar separation bubble
PIV	Particle Image Velocimetry
POD	Proper Orthogonal Decomposition
PSD	Power spectral density
$RANS$	Reynolds Averaged Navier-Stokes Simulation
sk	Skewness
TI	Turbulence intensity
TrW	Transition-in-the-wake state of flow
VIV	Vortex-induced vibrations

Chapter 1

Introduction

1.1 Overview

Flows around bluff bodies, and in particular those having circular, square, or rectangular cross-sectional shapes, occur in many different fields related to aerospace, civil, and mechanical engineering, as well as in marine sciences and on- and offshore wind engineering. Stand-alone or arranged in small or large groups, these cylindrical and prismatic structures can be found, among others, as struts of landing gears and wings of aeroplanes, as constructions like high-rise buildings, cooling towers, chimney stacks, and radio and television towers, as towers of on- and offshore wind turbines, foundation elements of fixed or floating offshore renewables and oil and gas rigs, as bridge pylons and decks, as trains and road trains, ships and their wind-assisted propulsion devices, and as heat-exchanger tubes and solar panels (Figure 1.1). They exist not only as rigid structures, but can just as well be found as flexible elements like cables of suspension bridges, overhead transmission bundles, mooring lines of floating offshore constructions, deep sea risers, submarine power and data cables, submerged pipelines, etc. Investigations of circular cylinder flows have also gained an increasing importance in sports like speed skating (Oggiano *et al.* [171], Timmer and Veldhuis [246]), cycling (Malizia and Blocken [144]), and downhill skiing or snowboarding (Oggiano and Sætran [170]), in order to optimise the flow over parts of the athlete's body and sport equipment such that a minimum amount of total drag is achieved. Even in nature, flows over cylindrical elements are frequently encountered, leading to various phenomena such as the motion of leafless tree branches and Ammophila (marram or beach grass) every time the wind picks up or the waving of long tentacle plate corals by the water current, e.g. Hearn [96], Samson *et al.* [205], Samson and Miller [206].

Flows over cylindrical or prismatic structures are in most common cases unavoidable. They could even be (highly) undesirable, since in the worst case they may lead to a possible partial structural damage or a complete failure of the structure resulting from the occurrence of vortex- or motion-induced vibrations. In particular situations, though, these induced vibrations are actually intentional and even enhanced in their amplitude, e.g. the enhanced cooling of microchips by heat sinks with internal micro cylindrical pins (Yan *et al.* [284]) or the harvesting of clean energy through ocean current-induced oscillations of an elastically suspended floating circular cylinder (Barrero-Gil *et al.* [21], Zhang *et al.* [298]).

(a) Landing gear of Bombardier Dash8-Q402

(b) Skyscraper in Manhattan, New York City, USA

(c) RWE Power plant in Niederaussem, Germany

(d) Kaknästornet in Stockholm, Sweden
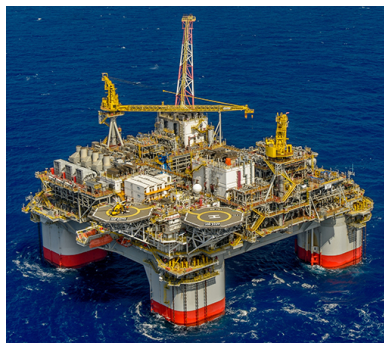
(e) Semi-submersible floating production unit of Chevron

(f) MHI Vestas assembly facility of wind turbines at the Port of Esbjerg, Denmark

(g) Viaduc de Millau, France

(h) Tarik Ibn Ziyad Oil Tanker in dry dock in Lisbon, Portugal

(i) Flettner rotor on Enercon's E-Ship 1

(j) U Tube bundle Heat Exchanger

Figure 1.1: Examples of structures having a bluff cross-sectional shape, e.g. circular, square, or rectangular. *(a)-(d)*, and *(g)*: Photo from Pixabay; *(e)*: Photo from Chevron Corporation; *(f)*: Photo by courtesy of Vestas Wind Systems A/S; *(h)*: Photo by Ibrahimuo (2015) from Wikimedia Commons; *(i)*: Photo by A. Jamieson (2010) from Wikimedia Commons; *(j)*: Photo from Cixi Fly Pipe Equipment Co.,Ltd.

1.2 Flow-induced vibrations of circular cylinders and rectangular prisms in cross-flow

Flows over two-dimensional, i.e. "infinite" circular cylinders or prisms with square or rectangular cross-sections are characterised by boundary layer separation from their surfaces, interactions between the resultant free shear layers, and the regular formation and shedding of vortices in the wake. When mounted elastically to allow rotational or linear motions, those rigid bluff bodies can undergo fluid-structure interactions in a uniform, oscillating, or unsteady flow. The development of an uneven pressure distribution between the upper and lower surface(s) of a bluff body, induced either by the (periodic) shedding of vortices in its wake or by the motion of the structure, results in alternating out of plane pressure forces which can have such considerable magnitudes, that – dependent on its cross-sectional shape – the structure can experience different types of flow-induced vibrations (Naudascher and Rockwell [155], Blevins [32], Païdoussis *et al.* [179], Kaneko *et al.* [120]).

1.2.1 Vortex-induced and turbulence-induced vibrations of circular cylinders

Long, slender circular cylinders, placed in a steady cross-flow, are for example in particular prone to *vortex-induced vibrations* (VIV), an instability-induced excitation according to the classification of flow-induced oscillation phenomena by Naudascher and Rockwell [155]. Depending on the amount of degrees of freedom of the flexible-mounted cylinder, these vibrations are possible either in-line, transverse to the flow, or in both main directions. The vibrations parallel to the flow are caused by the overall fluctuating drag force and their dominant frequency equals twice the Kármán eddy shedding frequency. In contrast, the cross-flow vibrations are induced by the fluctuating lift force and have a dominant frequency that is equivalent to the Kármán eddy shedding frequency. Since the magnitude of the fluctuating drag is generally much smaller than that of the fluctuating lift force, the latter vibration mode is much more dominant. In the case the frequency with which the eddies are shed from the circular cylinder approaches or equals the transverse or longitudinal natural frequency of the structure, *resonance*, also called *wake capture* takes place. In that case the eddy shedding frequency "locks" into the structural natural frequency of the system f_n (Feng [77]). Hence, a synchronisation of both frequencies occurs. Figure 1.2(a) shows the typical behaviour of both the eddy shedding frequency and the frequency of the transverse vibration of the cylinder with the reduced velocity in the vicinity and within the "lock-in" regime. The reduced velocity is thereby defined as

$$U_r = \frac{U_\infty}{f_n L_{ref}} \tag{1.1}$$

where L_{ref} equals the diameter D. Such a "lock-in" can occur in cross-flow and in flow direction, meaning that the lift and drag force oscillate with the cylinder motion and twice its value, respectively. In this "lock-in" regime, both the drag and lift force, as well as the vibration amplitudes show a considerable increase in magnitude, as is examplary shown in Figure 1.2(b) for the ampliutude in cross-flow direcion. The reason for this is twofold. On the one hand, the larger cylinder oscillation in transverse direction increases the correlation of the eddy shedding process in spanwise direction (Figure 1.3), as it organises the three-dimensional wake along the span of the cylinder which thus becomes more two-dimensional (Toebes [247], Novak and Tanaka [167]). On the other hand, the strengths of the shed vortices become larger as well, since the time scale of the process of eddy formation is similar to the reciprocal of the cylinder's
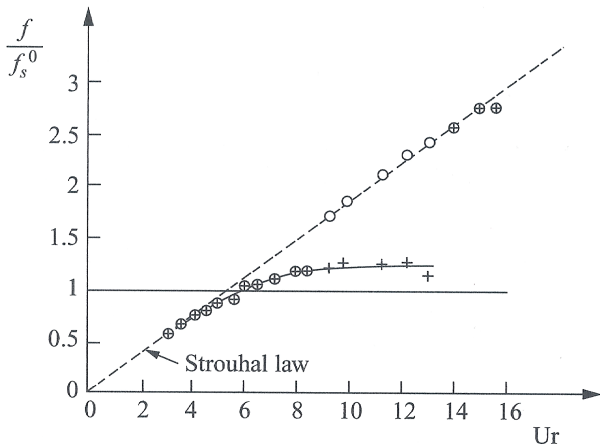
(a) Dimensionless vibration and eddy shedding frequencies
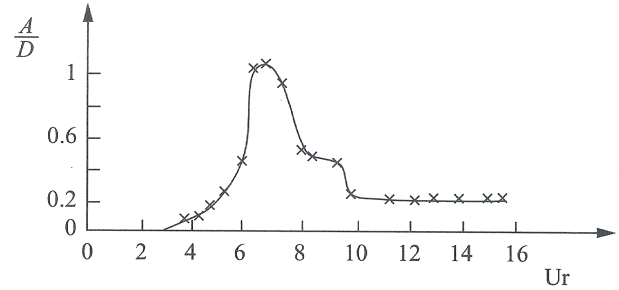
(b) Dimensionless vibration amplitude A/D

Figure 1.2: Evolution of the eddy shedding ($\circ$) and vibration ($+$) frequencies *(a)* and the non-dimensional vibration amplitude *(b)* of an elastically supported circular cylinder with reduced flow velocity (Mutlu Sumer and Fredsøe [149]).

vibration frequency (Bishop and Hassan [29], Davies [56]). Sarpkaya [207] furthermore stated that the vertical projected area of the cylinder in cross-flow, being subjected to a transverse vibration at or near the shedding frequency, is over a full oscillation cycle larger than the projected area of a stationary cylinder. This also results in an amplification of the mean drag force with vibration amplitude, as observed by Tanida *et al.* [243] and Torum and Anand [248] at different Reynolds numbers and presented in Figure 1.4 as ratio of the mean drag coefficients with and without vibration amplitude. A similar observation, but regarding the fluctuating drag force, was made already fourteen years previous in an experimental study by Bishop and Hassan [29]. Last, but not least, a synchronisation leads to a change in the eddy shedding modes, hence, the sequence, phase, and pattern (Figure 1.5) of the shed vortices in the wake
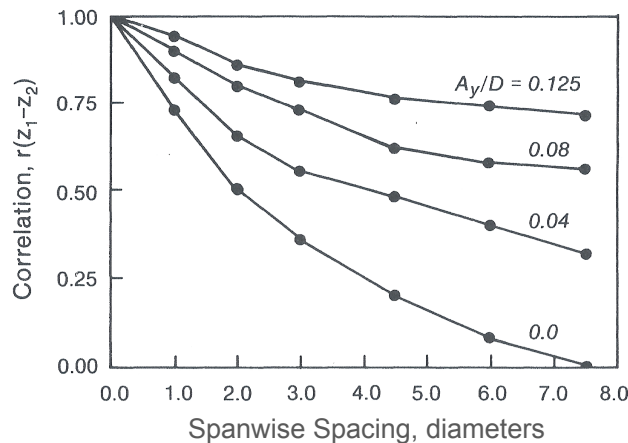
Figure 1.3: Correlation of eddy shedding process along the span of a rigid circular cylinder at "lock-in" (Toebes [247]).
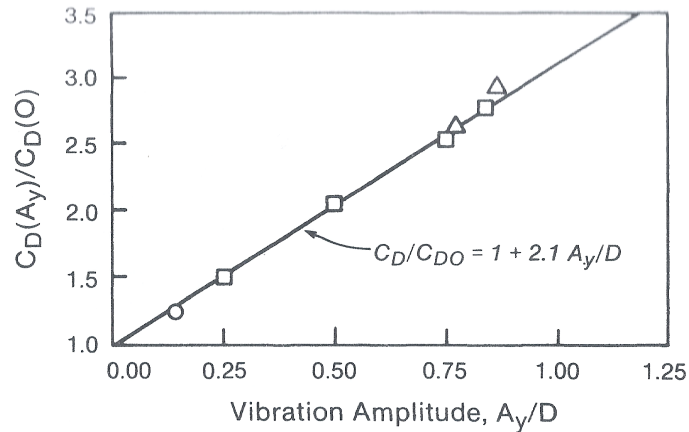
Figure 1.4: Growth of the mean drag force acting on a rigid circular cylinder with transverse vibration amplitude at resonance with the frequency of eddy shedding (Blevins [32]). ○: $Re_D = 4\,000$ (Tanida *et al.* [243]); □: $Re_D = 8\,000$ (Sarpkaya [207]); △: $Re_D = 15\,000$ (Torum and Anand [248]).

(e.g. Zdravkovich [291], Öngören and Rockwell [169], Williamson and Roshko [273]). It can furthermore be observed, that the larger the amplitude of the vibration as a result of a smaller structural damping, the broader the frequency range in which resonance does occur (Figure 1.6). Other variables that influence the cylinder vibrations are the mass ratio being equal to the ratio of the sum of the structural and "added" mass to the mass of the fluid it displaces, the Reynolds number, and the surface roughness of the cylinder (Mutlu Sumer and Fredsøe [149]).

Interestingly, circular cylinders in a turbulent cross-flow can even be caused to vibrate when the structural eigenfrequency is well separated from the (dominant) shedding frequency. Provided that the turbulence level of the oncoming flow is high enough, a turbulence-induced vibration, i.e. buffeting can be "imposed" on the cylinder through its excitation by wind-band
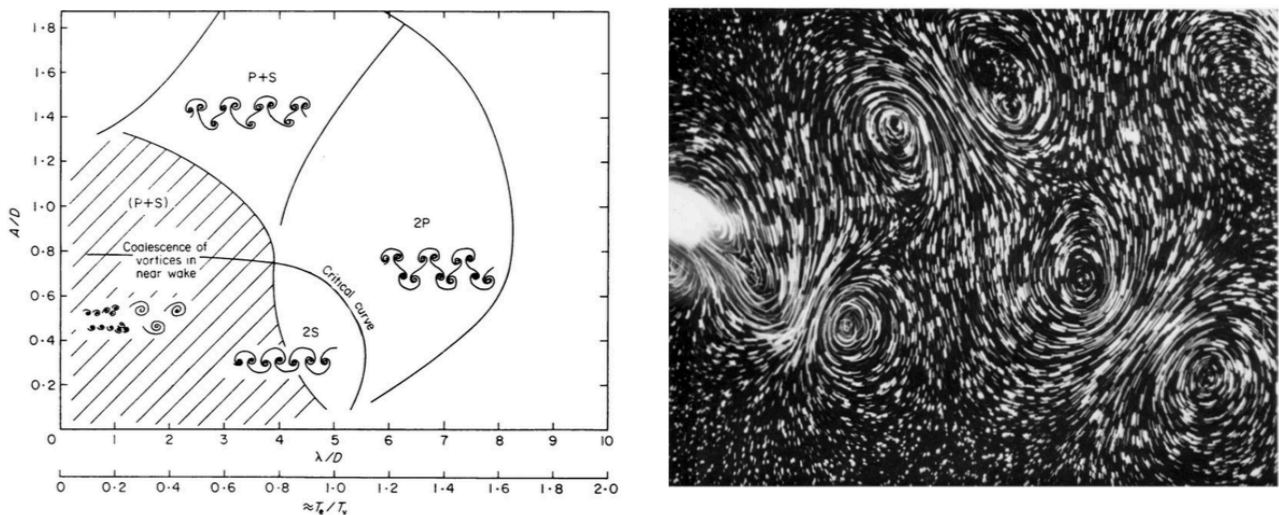
Figure 1.5: Effect of a variation in the vibration amplitude and frequency on the vortex pattern in the wake of a rigid cylinder under forced harmonic transverse motion (Williamson and Govardhan [274]).

5

components of the turbulence spectrum that lie the closest to the eigenfrequency of the structure (e.g. So *et al.* [227]). Naudascher and Rockwell [155] assigned this latter excitation to the *extraneously induced excitations* in their classification of flow-induced oscillation phenomena, since they are "*caused by fluctuations in flow velocities ... that are independent of any flow instability originating from the structure considered and independent of structural movements except for added-mass and fluid-damping effects.*"
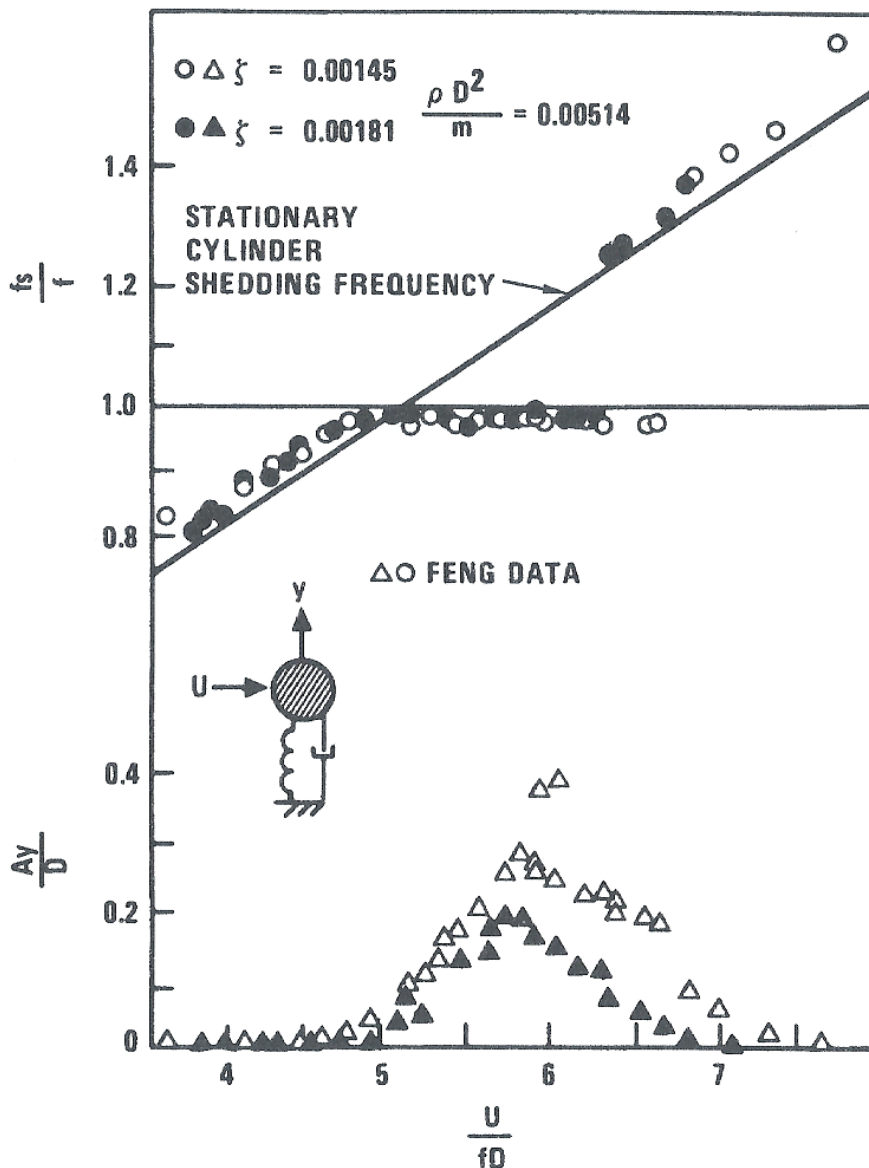
Figure 1.6: Dependency of the eddy shedding frequency and vibration amplitude in cross-flow direction on the structural damping of a rigid cylinder that is both spring-supported and damped (Feng [77]).

1.2.2 Rectangular prisms in cross-flow: vortex- and turbulence-induced vibrations and galloping

Similar to circular cylinders, prisms with rectangular or square cross-sections in cross-flow can undergo both turbulence-induced and vortex-induced vibrations. In both cases, the physical mechanism is similar to the case of a circular cylinder in cross-flow. *Resonance* or "lock-in", both transverse to as well as in flow direction, of the eddy-shedding frequency to the structural natural frequency may also occur for prisms with a rectangular or square cross-section when the former approaches the latter frequency. As a result, the structural vibration frequency and oscillation frequency of the lift and/or drag force that act on the structure equal the structural natural frequency (or twice its value in the case of a transverse vibration) as well. Regarding turbulence-induced vibrations, it is noteworthy to mention that the magnitudes of the vibration amplitudes are for prisms with rectangular or square cross-sections generally larger than found for circular cylinders (Naudascher and Rockwell [155]). The main influencing parameters for both vibration types are the flow characteristics, i.e. Reynolds number and turbulence intensity of the oncoming flow, the cross-sectional shape (angle of incidence, aspect ratio, and corner modification), the surface texture of the prism, and – in the case of vortex-induced vibrations – the characteristics of the prism itself, like structural mass, eigenfrequency, and damping in the flow, cross-flow, and rotational directions.

In contrast to circular cylinders, the variation of the fluid force experienced by stationary bluff bodies having a non-circular cross-section is a direct result of the body's orientation to the oncoming flow, i.e. its angle of incidence. When the prismatic bluff body vibrates in transverse direction to the flow or performs an periodic angular rotation along its longitudinal central axis that lies perpendicular to the oncoming flow, its angle of incidence changes periodically as well and the fluid force on the body oscillates. In the least favourable case in which the structure is fluid-dynamically unstable, the oscillating fluid force that acts on the structure amplifies the vibration. The resultant amplitudes can reach very large magnitudes and may therefore even cause structural failure.

This third category of possible excitations of flexibly mounted primsatic bluff bodies that are subjected to a cross-flow is called "*galloping*", a motion-induced excitation that arises from the motion of the vibrating body itself and is thus self-excited (Blevins [32], Amandolese and Hémon [18], Païdoussis *et al.* [179]). Flexible structures with circular cross-sections, like cables of suspension bridges or isolated overhead transmission lines, are generally unsusceptible to this vibration. However, under certain circumstances also they can become prone to *galloping*. Ice and rain leads to a deviation of their cross-sectional shapes from circular and thus a change in the aerodynamic and aeroelastic loads (Hikami and Shiraishi [99], Flamand [79], Demartino *et al.* [59], Demartino and Ricciardelli [60]). This may result in ice-accreted or rain-wind induced vibrations. The same counts for deep sea risers and submarine power and data cables as a result of marine fouling (Wolfram [276], Wright *et al.* [277], Yang *et al.* [285], Spraul *et al.* [237]). Even dry *galloping* of stay cables with a pure circular cross-section has been reported, being the result of both non-zero incidence and yaw angles with respect to the oncoming wind (Virlogeux [265], Nikitas and Macdonald [157]). Besides the non-circular cross-section, a second prerequisite for *galloping* to occur is that the structure needs to have at least one degree of freedom, i.e. either in rotational or transverse direction. This means that *galloping* is not necessarily limited to either an angular or a translational motion, since structures can also be free to rotate and translate simultaneously. When the elastic axis of the structural cross-section does not coincide with the axis that goes through the centre of mass, translation and torsion of the structure are inertially coupled. The result is a two-degree-of-freedom *galloping*, whereby in

most cases torsional *galloping* is combined with transverse *galloping* (e.g. Slater [225], Blevins and Iwan [33], Modi and Slater [148]).

At its initial rest position, the body experiences small oscillations in translational and torsional direction around its static equilibrium position, induced by the fluctuating lift and drag forces and pitch moment, respectively. Provided that in this rest position the free shear layers do not reattach to any of the faces of the prismatic bluff body up to its trailing edge, the resultant of the lift and drag force or the torsional moment can act in the same direction of the vibration or angular velocity. This leads to a dynamically instable situation, since the periodic motion itself induces a negative dynamic damping as per oscillation cycle more energy is taken out of the fluid and transferred to the vibrating structure than vice versa. Hence, the fluctuating fluid force or torsional moment that acts on the structure tends to increase the body's motion. The vibration amplitude thus steadily increases over each vibration cycle until a limit cylce oscillation (LCO) has been reached which can possess very large amplitudes. It is therefore not surprising that *galloping* ends not seldom in a failure of vibrating parts or a total collapse of the structure (Gupta *et al.* [90], Valentín *et al.* [251]).

Compared to vortex-induced vibrations, the frequency with which the structure vibrates is in the case of *galloping* much lower than the structural eigenfrequency, as is shown later on in this section. Both for VIV and *galloping* to appear, a lower threshold of the reduced velocity has to be exceeded; however, in the case of *galloping* this critical flow velocity has a much higher value than for the self-excited vibration by the Kármán eddy shedding. Once exceeded, the maximum possible vibration amplitude at a certain reduced velocity is limited for both flow-induced vibrations (Blevins [32], Païdoussis *et al.* [179]). But, whereas the range of reduced velocities in which VIV can occur is bounded by an upper limit as well (Figure 1.6), the *galloping* amplitude increases with increasing reduced velocities (Figure 1.7). At a fixed reduced velocity above the onset velocity, the maximum possible vibration amplitude is self-limited, though, which results in the appearance of the LCO. In the case of plunge, i.e. transverse *galloping*, the *galloping* body does not only experience a steady increase in its transverse vibration amplitude during each oscillation cycle, but also in its transverse velocity. Hence, the maximum instantaneous angle between the velocity vectors of the steady, i.e. constant free stream and of the fluid relative to the moving body increases per oscillation cycle. At a certain point, the value of the transverse velocity is that high that a reattachment of one of both free shear layers to the surface of the body does occur. For prisms with sharp-edged square cross-sections in cross flow, for example, free-shear-layer-reattachment takes place at an angle of incidence of about 13° (Lee [130], Rockwell [193], Obasaju [168], Igarashi [108], Knisely [126], Van Oudheusden *et al.* [260], Huang *et al.* [106], Huang and Lin [105], Yen and Yang [286]). At that instantaneous angle of incidence, the maximum resultant aerodynamic force in transverse direction is reached. A further increase in incidence angle leads to an upstream movement of the reattachment point along the surface and induces in that way a smaller resultant aerodynamic force that acts in the vibration direction on the body. In the case all boundary conditions remain constant once the maximum possible amplitude has been reached, the prism will continue to perform a limit cycle oscillation with a constant frequency and amplitude. In a similar manner, the maximum occurring angular amplitude is self-limited for torsional *galloping* at each reduced velocity above the threshold value. The lower threshold in reduced velocity for onset of *galloping*, the growth rate of the vibration amplitude, and the value of the maximum amplitude for a certain reduced velocity, as well as the steepness of the amplitude incline with increasing reduced velocity all depend on the same physical parameters as previously mentioned for turbulence-induced and vortex-induced vibrations. Among those, the most prevailing and thus mostly studied ones with respect to prisms with square or rectan-
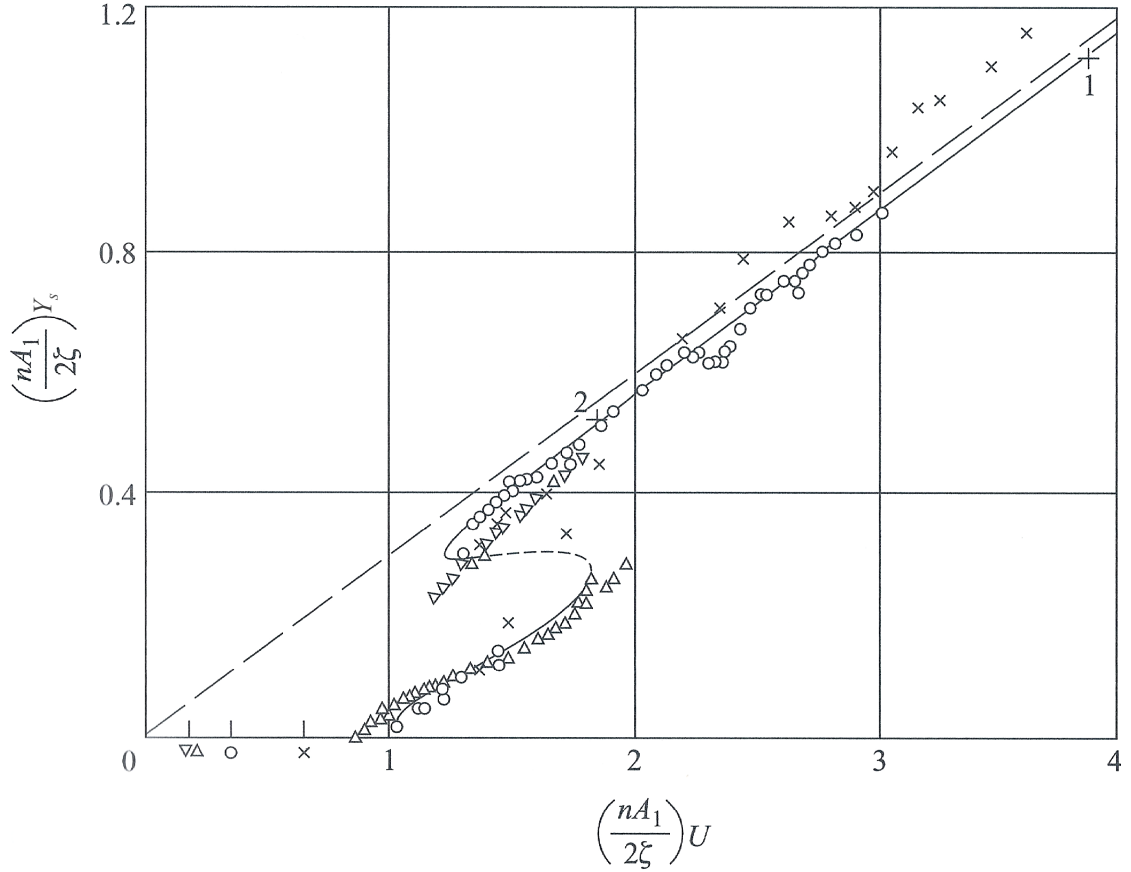
Figure 1.7: Dimensionless transverse *galloping* amplitude versus reduced flow velocity for a sharp-edged square prism (Parkinson and Smith [183]). $---$: experimental unstable limit cylce; $-$: theoretical stable limit cylice. Experimental data [183]: $\times$: $\zeta = 0.00107$; $\circ$: $\zeta = 0.00196$; $\triangle$: $\zeta = 0.00364$; $\triangledown$: $\zeta = 0.00372$; +1: $\zeta = 0.0012$; +2: $\zeta = 0.0032$. Reynolds number range: $Re_D = 4{\cdot}10^3 – 2{\cdot}10^4$.

gular cross-sections are the aspect ratio – including the shape of the afterbody, the latter being the remaining part of the bluff body downstream of the points of boundary layer separation – and the turbulence intensity of the oncoming flow (Novak [161], Novak and Davenport [162], Laneville and Parkinson [128], Novak [163], Novak [164], Novak [165], Novak and Tanaka [166], Parkinson [181]).

When focussing in particular on prisms with shard-edged rectangular cross-sections, a proneness to *galloping* exists for a sufficiently small ratio of the width d to height h (i.e. the ratio of the lengths of the faces in flow direction and cross-flow direction) of the prism's cross-section. For aspect ratios of $0.75 \leqslant d/h \leqslant 3.0$–$3.2$ the prisms are categorised as *soft oscillators*, which means they will oscillate from rest in a laminar and steady oncoming flow once the reduced onset velocity for 1D plunge *galloping* has been exceeded (Brooks [36], Smith [226], Parkinson [181], Bearman *et al.* [26], Parkinson [182]). As presented in Figure 1.8, within this range, a steady decrease of the maximum ratio of reduced *galloping* amplitude to reduced velocity occurs for larger values of d/h, induced by the previously described self-limitation of the maximum amplitude. For tall prisms with $d/h < 0.75$, the afterbody of the prism is too short for it to be susceptible to *galloping* from its rest position. Nonetheless, under certain condition *galloping*
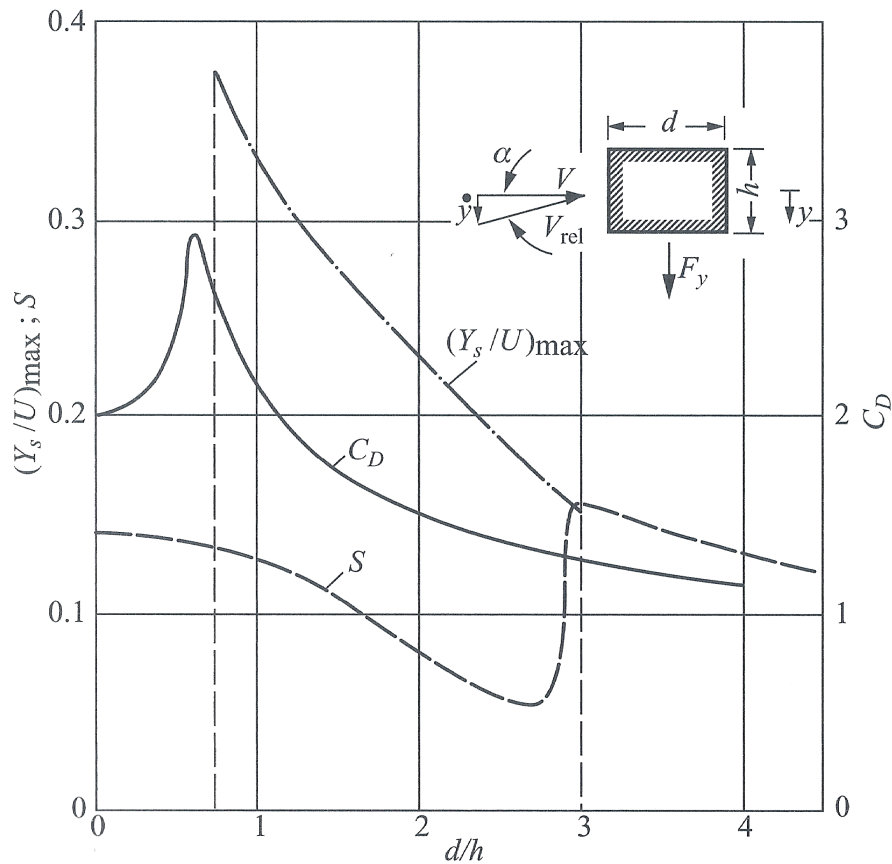
Figure 1.8: Influence of aspect ratio d/h of sharp-edged rectangular prism on maximum transverse *galloping* amplitude $(Y_s/U)_{max}$, dimensionless eddy shedding frequency S, and mean drag coefficient C_D (Parkinson [181]).

is also possible for these short prisms. This occurs when a sufficiently large initial impulse in the form of a perturbation in transverse direction is supplied to the prism, for example by a sudden strong wind gust, above the threshold amplitude and, at that same instant, the reduced velocity of the oncoming flow lies above the onset of *galloping*. These kind of prisms are therefore categorised as *hard oscillators*. On the contrary, sharp-edged prisms with a long afterbody above $d/h = 3.0$–3.2 are stable with regard to *galloping*, since the free shear layers that have separated from both windward edges of the prisms are able to reattach to the trailing edges of the afterbody's side surfaces and therefore "*provide a pressure loading on the afterbody that opposes small transverse disturbances*" (Païdoussis *et al.* [179]). Interestingly, the impingement of leading edge vortices – hence, distinct vortices resultant from the roll-up of the free shear layers above both side surfaces – onto the side faces upstream of the trailing edge of prisms with long afterbodies up to approximately $d/h = 10$ can give rise to *impinging leading-edge vortex excitations* instead (Deniz and Staubli [62]). A change in turbulence intensity ($T.I.$) of the oncoming flow strongly influences the plunge *galloping* behaviour of sharp-edged rectangular prisms in several ways. An increase in its value leads not only to a narrower range of d/h values within which *soft galloping* can occur, but also shifts both its boundaries towards lower values, as seen in Figure 1.9. In addition, the decline of the maximum ratio of reduced *galloping* amplitude to reduced velocity with increasing d/h becomes larger, since the values of this maximum ratio at the lower and upper bounding d/h-value increase, respectively, decrease. As a result of both phenomena, short prisms that were *hard oscillators* in a laminar and steady
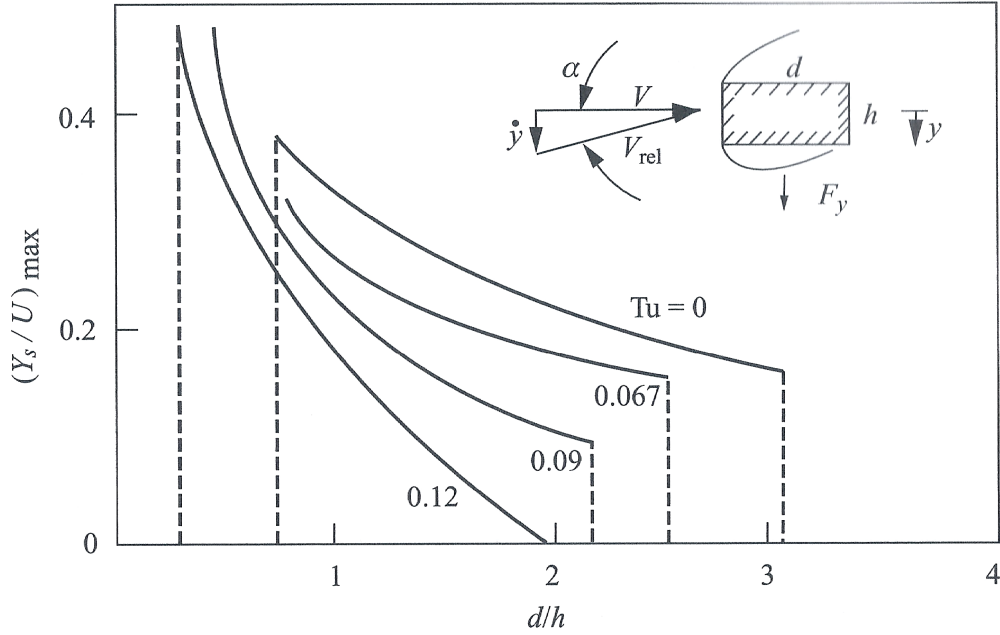
Figure 1.9: The effect of the turbulence intensity of the free stream Tu on the transverse *galloping* amplitude $(Y_s/U)_{max}$ and the limits (i.e. vertical dashed lines) of the soft- and hard-galloping ranges for various aspect ratio d/h of a sharp-edged rectangular prism (Parkinson [182]).

oncoming flow, now suddenly become susceptible to *galloping* at their rest position and can gallop with increased amplitudes at much lower onset velocity, as shown in Figure 1.10 for a sharp-edged rectangular prism with $d/h = 1/2$, while *soft oscillators* with longer afterbodies are now stabilised against *galloping* (Novak [164], Parkinson [182]). The reason can be found in the earlier reattachment of the free shear layers on the side faces of the prisms for larger turbulence intensities. The increased entrainment of the fluid into the separated flow region leads to thicker free shear layers. Their inner boundaries therefore approach the side faces faster and can as such interfere with and reattach to them already at shorter afterbody lengths.

Based on a quasi-steady fluid dynamic approach, Glauert [88] and Den Hartog [61] proposed independently from one another a criterion that has to be fulfilled for a bluff body to be potentially susceptible to plunge, i.e. transverse galloping:

$$\left.\frac{\partial C_y}{\partial \alpha}\right|_{\alpha_0} = -\left.\frac{\partial C_L}{\partial \alpha}\right|_{\alpha_0} - C_D(\alpha_0) > 0 \tag{1.2}$$

where $dC_y/d\alpha|_{\alpha_0}$ and $dC_L/d\alpha|_{\alpha_0}$ are the change of the force coefficient in transverse direction (C_y, positive downwards) and of the lift coefficient, respectively, with angle of incidence α at the angle of incidence at rest α_0, and C_D the drag coefficient. Hence, in case the slope of the $C_L(\alpha)$-curve is negative and steeper than the value of the drag coefficient at α_0, the transverse fluid force F_y induces an amplification of the bluff body's plunge motion. However, the additional condition that the negative of the magnitude of the fluid dynamic damping is larger than the structural damping has to be met as well for the motion to be self-excited from rest. For the quasi-steady theory to be applicable to transverse *galloping*, Blevins [31] stated that the frequency of the limit cycle oscillation must be smaller than half the eddy
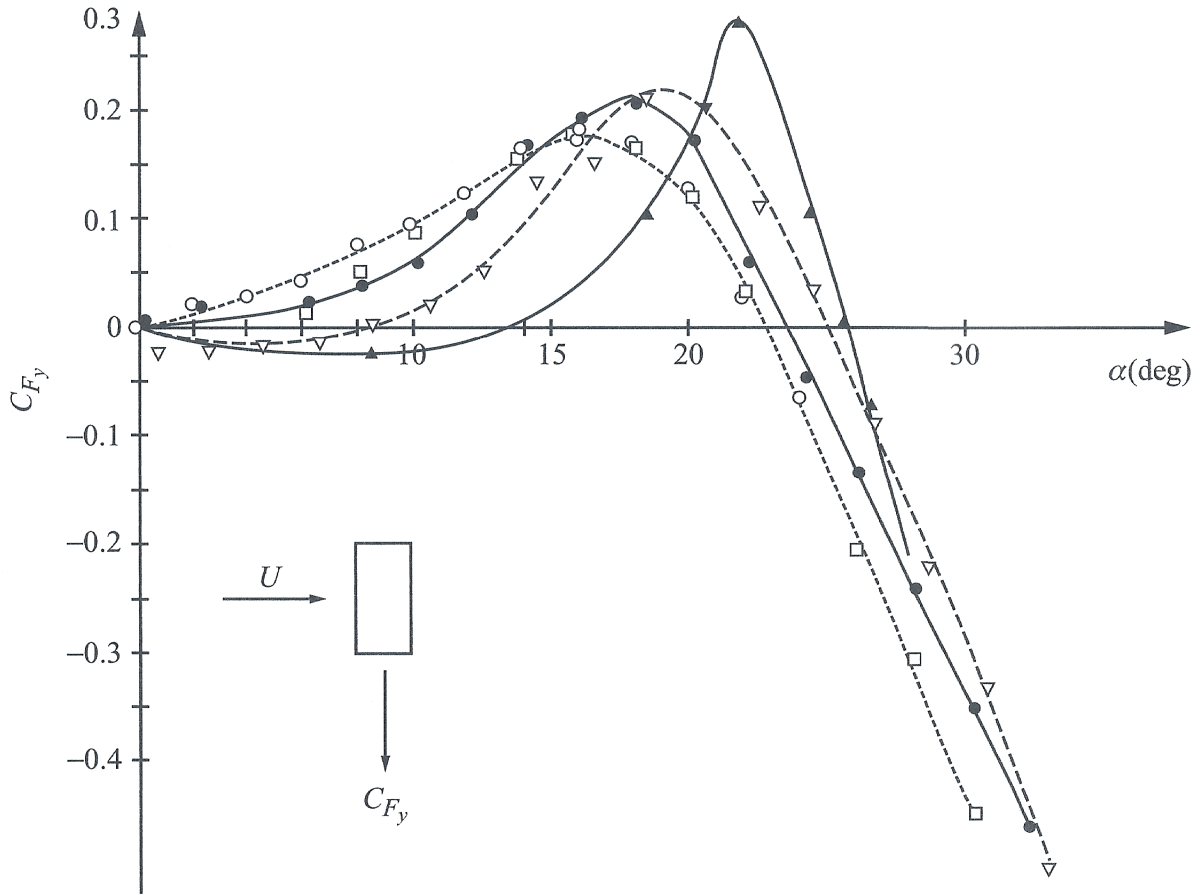
Figure 1.10: Characteristics of the coefficient of the transverse force C_y with angle of incidence α of a sharp-edged rectangular prism with $d/h = 1/2$ for various free-stream turbulence intensities Tu. Experimental data (Laneville and Parkinson [128]): ▲: $Tu = 0.07\%$; ▽: $Tu = 6.7\%$; •: $Tu = 9.0\%$; ○, ▢: $Tu = 12\%$.

shedding frequency. Translated to a reduced *galloping* frequency $V/(f_{gal}h)$ in which V equals the free-stream velocity and f_{gal} the *galloping* oscillation frequency, its value should be larger than 10. This criterion is in accordance with the conclusion drawn by Fung [85] two decades previous. Later on, this condition has been sharpened by Bearman *et al.* [26], who stated that the ratio of oscillation to *galloping* frequency should be at least lower than $1/3$, i.e. $V/(f_{gal}h)$ > 30. Otherwise, disturbances that have been introduced into the flow by the motion of the bluff body at a certain phase of the oscillation, i.e. at a specific incidence angle of the body to the oncoming flow, have not been carried far enough downstream with the flow in the near wake behind the body and are therefore still able to directly influence the flow around the bluff body at exactly the same vibration phase one oscillation period later (Fung [85]). With respect to torsional or rotational *galloping*, also known as called 1-DoF flutter, a similar criterion has been derived (e.g. Slater [225], Nakamura and Mizota [151]). Based once again on a linear quasi-steady analysis, a susceptibility to this instability may be present for a bluff body, when

$$\left.\frac{\partial C_M}{\partial \alpha}\right|_{\alpha_0} < 0 \tag{1.3}$$

where C_M equals the coefficient of the torsional moment M. Additionally, the total damping has to become negative. Analogue to transverse *galloping*, this is the case when the fluid

dynamic damping exceeds the structural damping. Is equation (1.3) not satisfied, divergence, a steady instability, may occur instead (e.g. Richardson *et al.* [191]). At this stage, it has to be remarked that equation (1.3) can only be used to obtain a preliminary verification of the possible proneness of a bluff body to rotational *galloping* in quite a fast way with relatively low effort. For a more precise and reliable confirmation, the unsteady fluid dynamic theory has to be used, since it takes into account the unsteady effects that appear as a result of a phase lag between the motion of the bluff body and the surrounding viscous flow (Nakamura and Mizota [152], Nakamura [150]). The latter follows from the time delay in adjustment of the flow around and thus the surface pressures on the body to the change of the body's position in the flow field during the oscillation, as described in detail by Païdoussis *et al.* [179].

1.3 Control methods of flows around 2D circular cylinders and rectangular prisms

From the aforementioned outline of the various flow-induced vibrations that may occur, it can be derived that there exists an urgent vital need for the efficient flow control and in particular the influence of the eddy shedding process in the wake of cylindrical and prismatic structures in the broad regime of engineering applications. Theoretically, vortex-induced vibrations can be completely suppressed and thus avoided; in practice, the measures that have to be taken for a complete avoidance of this excitation are often too expensive and thus noneconomic. In case of turbulence-induced excitations, a total elimination is even impossible, independent of the countermeasures taken. On the other hand, as much effort as possible should be invested in the overall avoidance of *galloping*, since the maximum amplitude of the limit cycle oscillation of the structure increases linearly with increasing reduced velocity above the onset velocity.

Two main categories of control methods of flows around bluff bodies can be distinguished: passive, and active control methods, of which the latter one can be further subdivided into active open-loop and closed-loop (Choi *et al.* [51]). Whereas for active open-loop control methods the motion of the flow is monitored by an actuator based on pre-defined commands, additional sensors, positioned in the flow field, are used in the case an active closed-loop that monitor and feed back the effect of the actuator on the flow around a bluff body in real-time. In the review articles by Zdravkovich [290], Choi *et al.* [51], Chen *et al.* [48], and Ran *et al.* [187] a very detailed overview is given regarding the various passive, respectively active flow controls methods applied to circular cylinders to manipulate the flow around them such that the oscillating transverse fluid dynamic force on the body and thus the alternating eddy shedding are effectively decreased or even almost fully suppressed. In the following, a brief summary on those controls methods is presented, together with active and passive countermeasures to prevent transverse *galloping* of prismatic structures with rectangular cross-sections.

1.3.1 Passive vibration control methods

Independent of the cross-sectional shape of two-dimensional cylindrical or prismatic bluff bodies, the majority of commonly used suppression methods of flow-induced vibrations are passive. Because they do not depend on or require actuators and control loops and therefore have no need for a continuous input of external power, they are more straightforward, the required financial and technical investment is relatively minor, and their implementation is easy and fast. There exist three methods of controlling flow-induced vibrations in a passive way:

(a) Increase of stiffness by external X-bracing

(b) Fairing of landing gear of Piper PA28 Warrior II
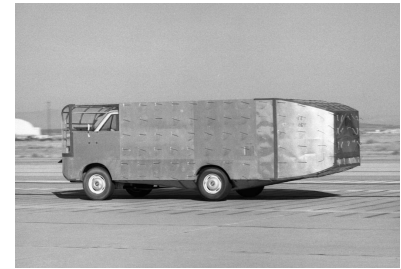
(c) Boat-tailing of rear of truck
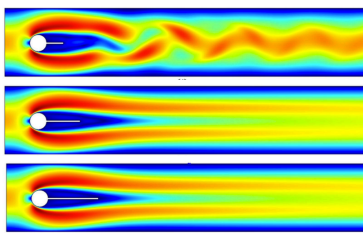
(d) Splitter plate behind a circular cylinder in cross-flow

(e) Guiding plates at rear of truck

(f) Spoiler on top of truck
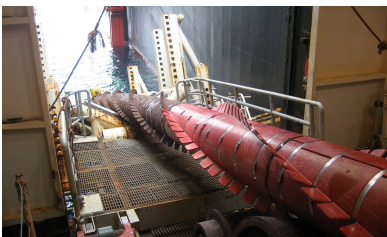
(g) Helical strakes on ocean risers

(h) Fins on marine riser

(i) Edge roundness on foundation of King's Quay semi-submersible
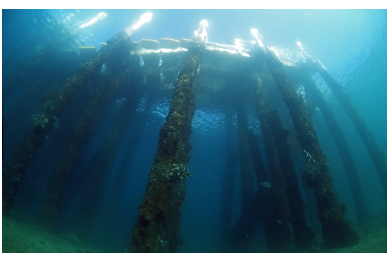
(j) Damping through marine fouling
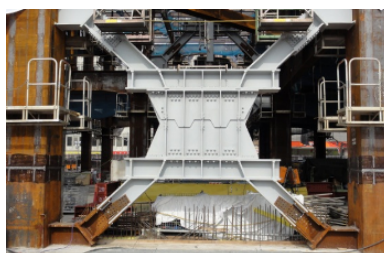
(k) Passive vibration damper inside JP Tower Nagoya, Japan
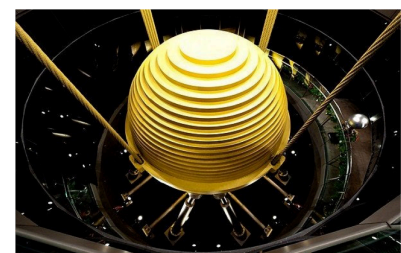
(l) Tuned mass damper inside Skyscraper Taipei 101, Taiwan

Figure 1.11: Examples of passive vibration control methods of structures with bluff cross-sections. *(a)*: Photo from Pixabay; *(c)*: Photo from NASA *(d)*: Ain *et al.* [10]; *(e)*: Photo from ZF Friedrichshafen AG; *(f)*: Photo from Pixabay; *(g)* and *(h)*: Photos from Lankhorst Engineered Products B.V.; *(i)*: Photo from Murphy Oil Corporation; *(j)*: Photo by John Turnbull from Flickr (CC BY-NC-SA 2.0); *(k)*: Inoue *et al.* [111]; *(l)*: Yucel *et al.* [288].

(a.) decrease of the reduced velocity through modification of the structure to alter the structural dynamics of the system.

The purpose of the applied countermeasures is to keep the reduced velocity by all means at a value below the critical value for onset of vibrations at all possible flow conditions that the complete structure or the critical structural components may experience. According to equation (1.1), this is achieved by increasing either the natural frequency of the system f_n, or the reference length L_{ref} (i.e. the diameter D in case of a circular cylinder and the height h for prisms with rectangular cross-sections), or a combination of both. Higher structural natural frequencies are realised by a stiffening of the structure, e.g. by bracing(Figure 1.11(a)). A drawback of this method is that a stiffening may be accompanied with a possible increase of the structural mass as well, because of their mutual influence, and can therefore usually not be adjusted separately from each other. The mass increase may shift the natural frequency of the structure to lower values, which would result in an increase of the reduced velocity towards the critical value for the onset of vibrations instead of its decrease. In case the previously mentioned control mechanisms cannot be implemented, a synchronisation of the resonance frequencies of the structure with the eddy shedding frequency has to be prevented as good as possible to keep the structural vibration amplitude small. Hence, the structure should be designed such that its natural frequencies clearly lie outside the range of expected or experienced excitation frequencies by eddy shedding.

(b.) control of the eddy shedding process.

Of the three categories of passive control methods, the current one is the most economical and effective control method. It aims at a weakening or elimination of the aerodynamic or hydrodynamic excitation forces by altering, hence, controlling the flow around the structure and thus the eddy shedding behaviour in its near wake. As formulated by Naudascher and Rockwell [155] "*it requires thorough knowledge of the basic flow-structure interactions and it involves, typically, a modification of the geometry of the structural flow boundaries or the use of appropriate fittings*". In terms of the control mechanisms, Ran *et al.* [187] distinguish between three main categories.

(1.) Those methods that belong to the first category all aim at a hindrance of the communication between the distinct eddies that are alternatingly formed on the upper and lower surface of the body. The recirculation region in which the fully decoupled free shear layers roll up into eddies can in that way be extended further downstream, thereby inducing a smaller negative static pressure in the base region and thus a lower mean drag force on the bluff body. Additionally, since a symmetric pattern of the shed vortices appears in the wake, a reduction or partial elimination of the fluctuating components of the transverse aerodynamic or hydrodynamic force that is responsible for the excitation of the structure in this direction can be achieved. To the common passive control methods in this category count those that modify the geometry of the downstream section of the body and those that alter the flow structure in the base by additional external elements. Examples of the former are a fairing (Figures 1.11(b)), tapering, or stepwise boat-tailing (Figures 1.11(c)) of the bluff body's rear section, i.e. a surface prolongation further downstream and a reduction of the effective surface on which the low base pressure acts, and a chamfering or bevelling of the rear end which induces a vortex bursting in the base region.

Splitter plates – solid, porous, hinged, pivoted, flexible, or with a wavy trailing edge – either touching the base surface of the body at the rear stagnation point or positioned at a certain distance downstream of it (Figure 1.11(d)), guide plates (Figure 1.11(e)), streamlined fairings, sawtooth fins, and bleed fluid injection into the wake by self-issued jets from the interior of the body through slits in its surface or communication channels between the windward and leeward stagnation points count to the latter group of common passive control methods.

(2.) A (partial) disruption of the boundary layer on the surface of the cylinder or prism and a reduction or even complete prevention of the spanwise correlation of the eddy shedding process around the bluff body characterises the mechanism of the control methods that belong to the second category. Depending on the surface coverage ratio of the control method, a mixture of weak and strong vortices is formed, of which the latter quickly burst into many smaller and thus weaker ones, upon which their energy can quickly dissipate in the wake. Spoilers (Figure 1.11(f)), vortex generators, helical strakes (Figure 1.11(g)) and wires, curved separation lines on the surface, ribbons, spanwise grooves, rectangular fins, (staggered) straight fins (Figure 1.11(h)) or straight separation wires that extend along (part of) the span of the cylinder or prism are just a few of the many possible control methods that are nowadays applied worldwide.

(3.) The last category comprises those control methods that induce a delayed separation of the boundary layer from the surface. They shift the location at which the laminar-turbulent transition takes place in upstream direction, hence a pronounced increase in the momentum exchange in the boundary layer with the outer flow can occur, resulting in a boundary layer that can withstand the adverse pressure gradient over a longer distance along the surface of the body before its separation. Devices that are widely used in case of circular cylinder flows are perforated shrouds with circular or square holes, arrays of axial rods encircling the cylindrical structure, as well as fine mesh gauzes. For prisms with rectangular cross-sections stable aerodynamic or hydrodynamic contours are obtained by rounding or chamfering their spanwise edges (Figure 1.11(i)). The continuous curvature of the surface allows a smooth downstream shift of the boundary-layer separation locations along the two forward-directed edges of the prism, as well as along both downstream-directed edges for the secondary separation points in case of a reattachment of the free shear layers on one or both side surfaces. In contrast to its sharp-edged counterpart, a delayed separation from the prism's surface is thus achieved. An increased surface texture through a (partial) coverage with dimples, grooves, or roughness elements, the latter being either intentional or natural (i.e. soft and hard marine fouling, Figure 1.11(j)), can also be used as a means of flow control.

(c.) increase of the reduced damping.

The critical velocity for the onset of both transverse and torsional *galloping* instability are proportional to the product of the transverse or rotational structural damping and the structural mass or polar mass moment of inertia of the structure. The resultant *galloping* amplitudes are, then again, inverse proportional to those parameters. A similar relation exists between the resonant vibration amplitude and the structural mass and damping coefficients in the case of vortex-induced excitation of the structure. Hence, an increase of

the reduced damping by an increase of either the structural damping, the structural mass, or a combination of both are effective methods of controlling flow-induced vibrations. As was previously mentioned, one should take care that a higher structural mass may have a negative impact on the reduced velocity of the vibrating system through a decrease of the natural frequency of the structure. A higher structural damping factor can be achieved in several ways, depending, among others, on the accessibility of the structural parts which vibration needs to be damped, and whether the system is already in operation. Dissipative dampers are based on the energy extraction from the vibrating structure or structural parts and are usually positioned at those locations at which a relative motion between vibrating parts occurs (Figure 1.11(k)). Materials with a high internal energy dissipation, like viscoelastic materials, rubber, wood, etc., are very common as a damping method, but also fluid damping through radiation to a surrounding fluid, viscous dissipation, or fluid sloshing through high-resistance passages, and structural damping due to impact, scraping, or friction are well-proven and reliable damping approaches. An alternative to dissipative dampers are tuned mass dampers (Figure 1.11(l)). These dynamic vibration absorbers consist of an additional mass that is attached to the structure by one or more helical or torsional spring systems. They are commonly placed at positions at which the maximum vibration amplitude of the structure is to be expected. In case of excitation by a structural vibration, they will vibrate at the natural frequency of the structure, but with a phase shift with respect to the structure itself and extract in that way energy from the vibrating system.

1.3.2 Active vibration control methods

Compared to passive flow control methods, active ones are controllable, adjustable, and manoeuvrable. This means, that when positioned properly in the flow field, their implementation can not only manipulate the dynamic and complex fluid dynamic processes such as boundary layer transition and separation, free shear layer reattachment, eddy shedding, etc., but also establish an optimal and effective reduction and, in some applications, even a complete suppression of flow-induced vibrations. A disadvantage of active control technologies is the need for significantly complex and expansive actuators to execute the required flow control in real-time, and, in case of closed-loop methods, extra cost functions and an optimisation strategy for the feedback control. In closed-loop control methods, the feedback signals from both the flow field around the structure and the (vibrating) structure namely have a central function in the efficient and optimised performance of those flow control systems.

Fuid jets (Figure 1.12) or steady fluid suction and/or blowing (Figure 1.13) are active control methods that, similar to the passive counterpart of bleed fluid injection into the wake by self-issued jets, induce an attenuation of the eddy shedding process and thus of the (mainly transverse) excitation of the structure by a modification of the shear layers and an alteration of the pattern of the shed vortices appearing in the wake from asymmetric to symmetric, i.e. a stabilisation of the wake flow. Suction induces furthermore a delay of the boundary-layer separation, thereby narrowing the near wake behind the bluff body and reducing the drag force, whereas blowing leads to the exact opposite. Parameters that influence the effectiveness of this control method are, among others, the frequency, duty cycle, phase shift, waveform (e.g. sinusoidal, square, triangular, or sawtooth), and flux momentum of the pulsating jet(s), the location and cross-section of the cavities on the surface, the azimuthal angle, as well as the amount and velocity of steady suction and/or blowing. Apart from those, application of an electromagnetic
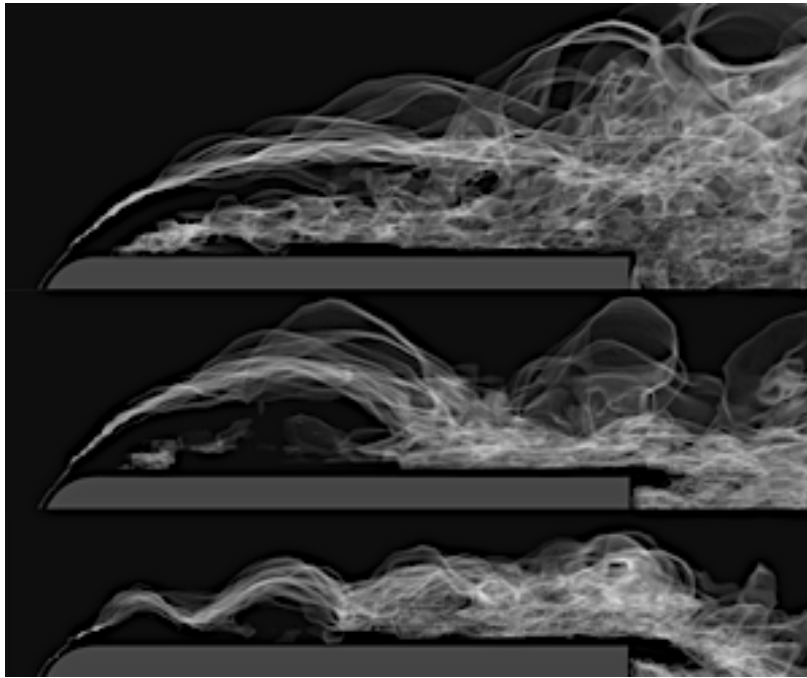
Figure 1.12: Visualisation of the effectiveness of a fluid actuation at the leading edge of a square-section prism with an leading edge curvature of $r/D = 0.05$ – where r is the dimensional edge radius – on the size of the detached flow area above the side surface and the reattachment location of the free shear layer (Minelli *et al.* [146]).

force, heating of the body, and acoustic excitation can also be used to attenuate the fluid-induced vibrations of a bluff body in an active way. While by heating of the structure the resultant buoyancy force, induced by a change of the density of the surrounding gas or liquid, is the key driver to an effective means for suppression of the structural flow-induced vibration, acoustic excitation benefits from an enhancement and drastic reduction of, respectively, the lift and drag force, the latter due to an elongation of the near wake. The large-scale eddies that are shed from the structure are modified into smaller ones, the frequency with which they are shed is shifted, and the velocity fluctuations in the wake behind the bluff body are significantly suppressed. An optimal control effect by acoustic excitation can be attained by adjusting the same influencing parameters as mentioned previously for the control methods based on fluid jets or steady fluid suction and/or blowing. Electromagnetic forcing or plasma actuators generate a Lorentz force to active control the flow, as this force induces a modification of the wake from an asymmetric to a symmetric one and in that way an elimination of the eddy shedding and (transverse) excitation of the structure (Figure 1.14). Although this control method is easy in use and robust, it requires an extensive and continuous energy input. In case of circular cylinders, oscillating or non-oscillating angular motions of the primary structure or of additional rods are proven practical active flow control instruments as well. The angular rotation affects the boundary layer on the cylinder as it generates a deceleration of the flow on one side of the cylinder and an acceleration on the other such that the flow separation locations are shifted to a position further upstream or downstream. In that way, an additional lift force on the cylinder is generated and the characteristics of the near wake are altered.
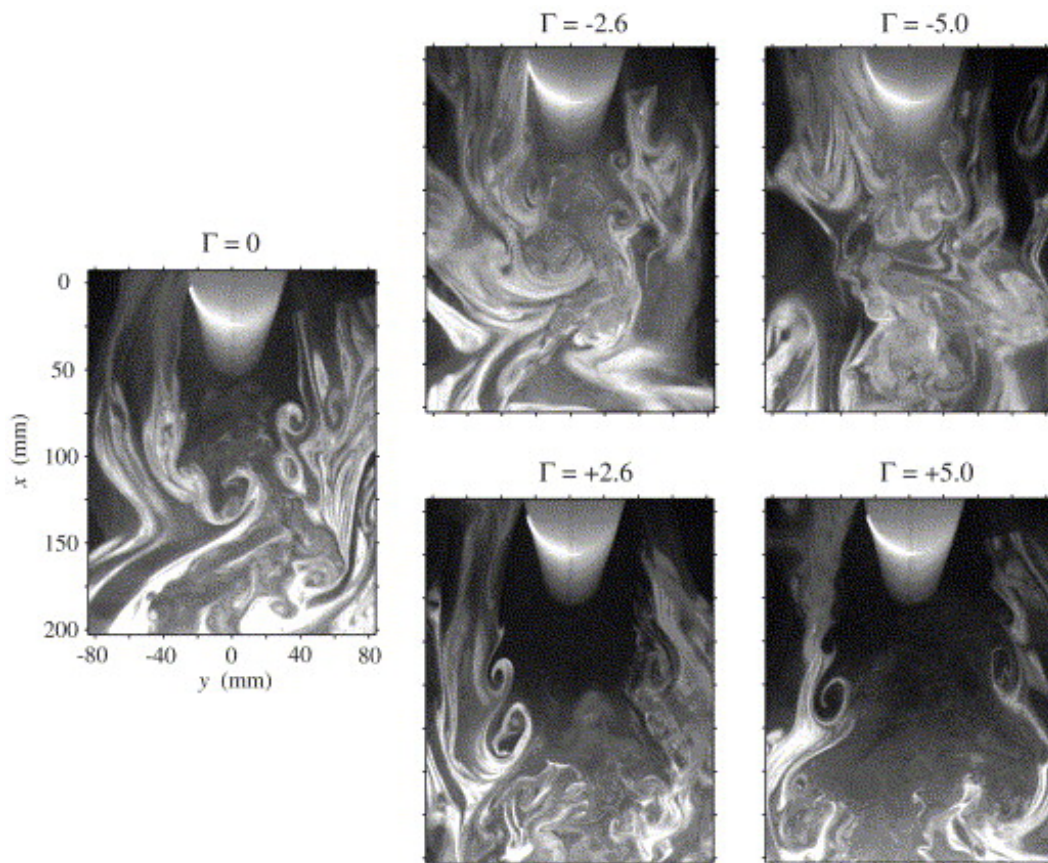
Figure 1.13: Smoke visualisation images of the modification of the instantaneous flow field in the base region and near wake of a porous circular cylinder at subcritical Reynolds numbers through continuous blowing or suction (Fransson *et al.* [83]). *(left)*: natural case; *(upper centre and upper right)*: continuous suction; *(lower centre and lower right)*: continuous blowing. Γ: dimensionless suction (negative value) and blowing (positive value) rate.
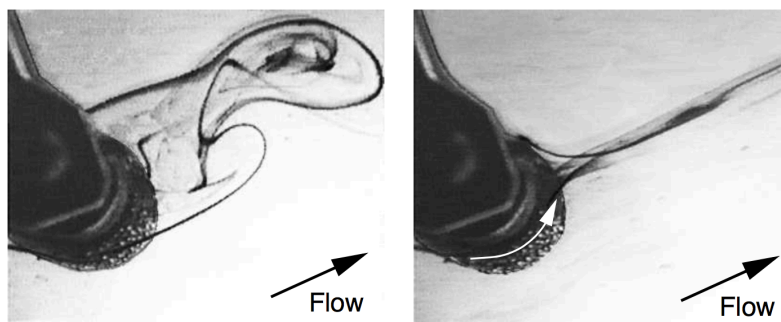
Figure 1.14: Suppression of the unsteady separation and thus the appearance of the Kármán vortex street by application of a downstream-directed Lorentz force (Weier *et al.* [268]). *(left)*: baseline; *(right)*: active electromagnetic force.

1.4 Objectives, contribution, and content of this monograph

The significant complexity of flow-induced vibrations of two-dimensional circular cylinders and prisms with rectangular cross-sections makes it difficult to extract the desired information from both the highly unsteady flow field and the excited structure that is required for the optimisation of the cost functions and the continuous adjustment of the active control strategy of closed-loop control methods by the sensors' feedback signals. Moreover, when multiple bodies are involved, that are placed that close together such that they have a common flow field, the fluid-dynamic interference between them alters the fluctuating surface pressures and shear stresses acting on their surfaces and the resultant time-mean and fluctuating aero- or hydrodynamic forces and moments. In addition, the flow structures both around the separate bodies and in their separate or common near and far wake(s) are also modified, which has an impact on their excitation and vibration behaviour. Hence, in particular in case of such a mutual interference many monitor probes are required that are not only able to measure the various fluidic and structural parameters (e.g. pressure, force, position, velocity, acceleration, bending, torsion, etc.), but gather those data also at such a high speed that a real-time analysis of the incoming signals and a transmission of the feedback signals back into the active control system is guaranteed. On top of that, it is very time-consuming and above all costly to explore the isolated effect of a variation in the value of each of the previously mentioned influencing parameters on the instability-induced or motion-induced excitation of the complete structure or the critical structural components and their resultant vibrations, as well as on the formulation of the feedback signals of the control system(s) at all possible flow conditions, since all influencing key parameters are linked together in some complex way. A change in the oncoming flow velocity, for example, influences not only the properties of the boundary layer and the flow topology in the base region and near wake, but may shift the value of the reduced frequency towards the critical value for onset of flow-induced vibrations, or in case of *galloping* to values at which the critical vibration amplitude for a possible collapse of the structure is exceeded. Recent technologies that are based on Artificial Intelligence (AI) can provide a remedy for this problem, since they have the capacity to deal with highly complex and multi-dimensional fluid-dynamic problems in an efficient way and provide possible optimisation solutions for both open-loop and closed-loop control strategies. Nonetheless, before such methods like (deep) reinforcement learning can be adopted their algorithms require an enormous amount of fluid-dynamic data, obtained by high-fidelity computational studies or experimental investigations, for their internal learning and optimisation purposes. A fruitful application of those numerical codes or reduced-order models requires precise statistical validation data as well, that are once again provided by experiments beforehand. Since those experimental studies mainly focus on the (un)steady fluid dynamics of bluff bodies and their susceptibility and response to flow-induced excitations at relatively low Reynolds numbers and laminar flow conditions, the derived control strategies are mostly limited to those flow states as well.

These limitations have provided the motivation for this monograph, which aims at the physical description of the various fluid-dynamic processes taking place around rigid two-dimensional square-section prisms with (in)finite edge roundness in cross-flow in both a single, i.e. isolated, and as tandem or in-line constellation in a Reynolds-number range of high up to very high. In an attempt to provide the reader not only with a unified overview and a profound understanding of flows over two-dimensional square-section prismatic bluff bodies, but also with a large detailed database of validation data for future developments of mathematical models to be

implemented in numerical codes, the following aspects of those bluff body flows are addressed:

(1.) angle of incidence of isolated square-section prisms,

(2.) edge roundness value of isolated square-section prisms,

(3.) surface roughness value of isolated square-section prisms with and without applied edge roundness,

(4.) longitudinal spacing between two tandem square-section prisms at incidence.

Flow phenomena taking place around two-dimensional rigid circular cylinders and their susceptibility to vortex- and instability-induced vibrations have been treated by a variety of engineering disciplines, thereby focussing on particular physical aspects that are of specific interest in each scientific field. Even after many decades, numerical, experimental, and/or analytical research is still being performed intensively on, among others, the behaviour of the surface boundary layer, the fluid dynamic forces acting on the cylinder, the parameterisation of the unsteady flow in its base region and near wake (e.g. the formation, growth rate, shedding frequency, and strength of the distinct vortices, the mean and fluctuating three-dimensional velocity field, the pattern of the shed vortices, etc.), and the response in terms of amplitude and frequency to a flow-induced excitation in the case of "lock-in" with the structural natural frequency of the cylinder. Depending on the value of the Reynolds number, being the most crucial governing flow parameter for flows over smooth circular cylinders, and the associated changes in the condition and behaviour of the surface boundary layer, various characteristic Reynolds-number flow regimes have been classified. On the other hand, 2D sharp-edged square-section prisms are known for their fixed boundary layer separation points, the large drag force acting on them, and, as mentioned previously in section 1.2.2, their proneness to the motion-induced *galloping* excitation. In contrast to circular cylinders, their fluid dynamics is largely Reynolds-number independent, but therefore dominated by the angle of incidence with respect to the free-stream velocity vector owing to a reattachment of the free shear layer on the side surface exposed to the wind and subsequent re-separation at its trailing edge above the critical angle of incidence. Hence, depending on the angle of incidence the flow around such a prism can be assigned a certain flow regime. An extensive review of the various fluid-mechanical phenomena associated with flows over these two kinds of bluff bodies and the experienced fluid-dynamic loading, as well as their changes caused by the application of two passive vibration control methods, namely surface roughness and edge roundness – the latter only for square-section prisms –, each in response to a variation of various influencing flow and structural parameters, is presented in Chapter 2.

The separation of the boundary layer from the surface of a sharp-edged square-section prism, positioned at $0°$ angle of incidence, at both its upstream-directed lateral edges governs the structure of the flow around the prism and in its recirculation region directly downstream of the base surface. These in turn dominate the pressure and shear forces on the faces of the prism and thus the mean and fluctuating loads in both flow and cross-flow direction. At the critical incidence angle $\alpha_{cr} \approx 13°$, the reattachment and subsequent re-separation of one of both free shear layers modifies the overall structure of the flow field around the prism from a symmetric to a highly asymmetric one, resulting in abrupt and sharp changes in not only the fluid-dynamic forces and moments, but also in the frequency and strength of the shed eddies. By introducing a rounding of the edges, the fixed separation locations of the laminar or turbulent boundary layer from the surface are released, as they are enabled to meander along the continuously curved edge surface. This leads to a return of the Reynolds-number dependency

of the flow field and fluid dynamics for this kind of square-section prisms in cross-flow. The extent to which the edges of these two-dimensional prisms are rounded plays in this case an important role, as it can be used to optimise both the prism's fluid-dynamic and fluid-structural excitation properties, based on the selection of the positive flow characteristics of each of both generic cross-sections, i.e. circular and square with sharp corners, as is shown in Chapter 3.

A roughening of the surface of a bluff body can on the one hand be intentional, for example to artificially simulate high-Reynolds-number flow phenomena at physically low Reynolds numbers in water or wind tunnel studies or as a passive vibration control method, or on the other hand caused naturally as a result of mainly possible external influencing factors, like rust, impact of bugs, precipitation, ice and snow accumulation, erosion, surface paint, or soft and hard marine growth. No matter the cause, its main result is an alteration of the properties of the surface boundary layer (e.g. the locations of both the laminar-turbulent transition and the separation) and of the free shear layers, such as a possible reattachment to the surface and the resultant size of the laminar separation bubble(s) over the surface. Computational modelling of such flows is even today still very challenging owing to many factors, including the requirement to encompass laminar, transitional, and turbulent flow and the necessity of a very fine numerical grid in the vicinity of the surface for resolving even the smallest unsteady flow features that appear due to the presence of the roughness. The effect of a change in the mean surface roughness height, by a variation of the mean diameter of uniformly distributed grainy roughness elements, on the fluid dynamics of both 2D circular cylinders and square-section prisms have therefore been explored experimentally over a wide range of Reynolds numbers and, in the case of the prisms, furthermore in dependence of the incidence angle and edge roundness. The outcomes are presented in Chapter 4.

Pairs of rounded square-section prisms possess a common flow field when placed in-line at close distance. The upstream one of the two experiences an undisturbed oncoming free stream, whereas the downstream one faces a clearly altered inflow, its exact appearance being a function of, among other factors, the gap size between both prisms, the incidence angle, and the Reynolds number. The latter two parameters lead to a distinct modification of both the flow topology around the downstream prism and the induced fluid dynamic loads. However, as a result of their proximity, these fluid dynamic changes can be fed back to the upstream prism as well; hence, a mutual interference between the two bluff bodies occurs that leads to changes in the topology of the flow around the upstream body and thus in the fluid-dynamic forces and moments as well. This may give rise to the manifestation of additional flow-induced vibrations, such as wake *galloping* or resonance between both structures. Chapter 5 focuses on the configuration of the two in-line square-section prisms and the changes in their fluid dynamic characteristics depending on the surface roughness value, angle of incidence, longitudinal spacing, and Reynolds number.

Chapter 2

Theoretical background on the fluid dynamics of isolated, two-dimensional cylindrical and square-section prismatic bluff bodies in a uniform, laminar cross-flow

2.1 Flow over circular cylinders with and without surface roughness

Of all possible bluff bodies, no other one has attracted so much interest and has been studied so intensively as the circular cylinder, both as a three-dimensional body, i.e. with a free ending as found in the vast majority of common applications, and as its "strong" simplification as an "infinite" body, i.e. two-dimensional. Their unsteady flow phenomena have been subject of a numerous amount of experimental, numerical, and theoretical investigations, of which a detailed overview can for example be found in the works of Niemann and Hölscher [156], Williamson [272], Zdravkovich [294], and Mutlu Sumer and Fredsøe [149], owing to which the underlying valuable physics of the time- and phase-dependent aero- or hydrodynamics of these bluff bodies can nowadays be described and modelled in quite a detailed extent (e.g. Catalano *et al.* [46], Ong *et al.* [177], and Cheng *et al.* [49]).

Because of its continuously curved surface and axisymmetric cross section, both the behaviour of the flow over a single two-dimensional smooth circular cylinder and the resultant loading it experiences are governed by the Reynolds number when the cylinder is placed in a laminar, i.e. disturbance-free, or low-turbulence oncoming flow field. In this monograph, the Reynolds number $Re_{L,ref}$ is defined as

$$Re_{L,ref} = \frac{\rho U_\infty L_{ref}}{\mu} \qquad (2.1)$$

where ρ equals the density of the fluid, U_∞ the free stream velocity of the oncoming flow, L_{ref} the diameter D of the circular cylinder, and μ the dynamic viscosity of the fluid. As will be shown hereafter, an increase in Reynolds number introduces tremendous changes in the flow field. However, as stressed by Zdravkovich [294], in real applications a wide variety of so-called *influencing parameters* can disturb the flow as well, thereby affecting the non-dimensional

quantities like force and pressure coefficients and Strouhal number, hence, the normalised eddy shedding frequency, to a certain extent. By exceeding a certain threshold, each one of these *influencing parameters* can alter in its own way the Reynolds number at which the laminar-turbulent transition takes place and has, in that case, thus become a governing parameter as well. Zdravkovich categorised the "*most frequently encountered influencing parameters*" into various groups:

(a.) irregular disturbances, among which the free stream turbulence intensity $T.I.$ and the surface roughness are the two most commonly encountered ones. The latter one is characterised by both the texture (i.e. the shape and/or distribution of the roughness elements over the surface) and the ratio of the mean size of the roughness k to the reference length L_{ref}, here the diameter D of the cylinder. Often, this ratio is expressed by the ratio k_s/D where k_s represents the dimensional equivalent sand-grain surface roughness;

(b.) steady disturbances. These include, among other things, the geometric wind or water tunnel blockage ratio D/H, where H is the dimensional height of the test section of the respective tunnel at the location of the circular cylinder, the aspect ratio L/D of the cylinder with longitudinal length L, and the proximity of the cylinder to the test section wall (hence, the gap size S) in case of a positioning of the cylinder out of the centre of the test section, expressed by S/D;

(c.) periodic disturbances, such as the regular cylinder vibrations, both in-line and transverse to the flow. In the case of resonance within the "lock-in" regime, the structural vibration frequency and amplitude can not only become governing parameters, but also even the most pronounced ones.

Regarding the flow around an isolated two-dimensional circular cylinder, the focus lies in this monograph on the effect of the Reynolds number as the governing parameter in combination with the surface roughness as the selected influencing parameter on the mean and fluctuating fluid dynamic loading and on the eddy shedding frequency.

2.1.1 Classification of the characteristic flow regimes based on smooth circular cylinders

By variation of the Reynolds number from $Re_D \sim 0$ up to its theoretically maximum value of $Re_D \to \infty$, the flow over a circular cylinder passes through several distinct states: from a fully laminar state at very low Re_D values, over the three transition states with a laminar-to-turbulent transition in the wake, in the free shear layers, or in the boundary layer on the surface of the cylinder, up to the fully turbulent state at very high Reynolds numbers. In the following, only a brief summary on these various states or flow regimes is presented, based on the works by Roshko [197] and Schewe [209]. The main emphasis in the current overview is on the two upper flow transition states. A very extensive treatment of each of the characteristic flow regimes for circular cylinders is provided by Zdravkovich [294].

In case of a laminar oncoming flow, the thin boundary layer on the surface of the circular cylinder is laminar at the forward stagnation point and increases in thickness as it develops along the cylinder's circumference towards its shoulders and beyond them. While for Reynolds numbers up to about 5, i.e. *Stokes flow* or *creeping flow* as shown in the Figure 2.1, the laminar flow remains attached to the surface of the bluff body up to the downstream stagnation point (Kim and Karrila [124]), a separation of the boundary layer from the smooth cylinder's surface
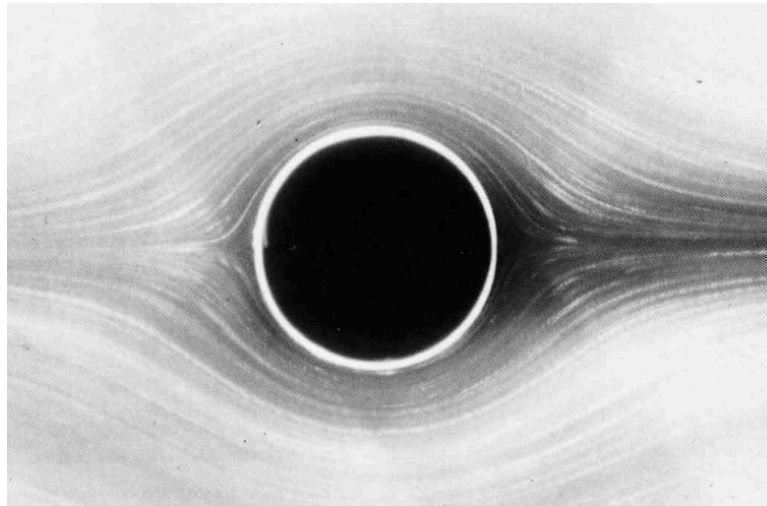
Figure 2.1: Streamline visualisation of the creeping flow around a circular cylinder in a laminar cross-flow for $Re_D = 0.16$ (Photo by S. Taneda in Van Dyke [252].

characterises the flow field around this bluff body at higher Reynolds numbers. Regarding the exact location of flow separation, as well as the nature of the boundary layer at that point and of the resultant free shear layers, the value of the Reynolds number plays a dominant role, as is presented hereafter. The exact point of flow separation on the circular cylinder is defined by the local velocity gradient normal to the cylinder's surface, at the surface, which equals zero at this point, thereby inducing a zero wall shear stress. Owing to the no-slip condition at the wall of the cylinder, a gradual velocity gradient normal to the cylinder's surface from zero at the wall to the free stream velocity in the outer flow is present in the boundary layer. Inside the boundary layer, the flow experiences a strong viscous flow resistance that leads to a relatively low flow momentum. The boundary layer is therefore sensitive to an external pressure gradient. At the stagnation point the kinetic energy of the fluid particles is converted into pressure and the local flow velocity of the fluid is thus zero. While wandering from this point in downstream direction along the continuously curved surface of the cylinder towards its shoulders, the surface boundary layer experiences a negative, hence favourable, pressure gradient as a result of the steady flow acceleration, as shown in Figure 2.2. Simultaneously, the velocity of near-wall fluid elements decreases as a result of the tangential shearing of those fluid particles along the surface of the cylinder. This also reduces the velocity gradient near the wall. By passing the shoulders of the cylinder, the decreasing local projected area of the cylinder induces an increase in the effective cross section of the flow. The adverse (positive) pressure gradient that is present in this region induces a deceleration of the flow over the first section of the downstream-directed face of the cylinder. The kinetic energy of the near-wall fluid particles is no longer sufficient to overcome both the friction force and the static pressure rise. Their velocity gradually reduces until the point is reached at which the velocity and the velocity gradient are both equal to zero. At this location, the viscous shear force at the wall must thus also equal zero. From this point on, an additional pressure increase causes the flow direction of the near-wall particles to reverse, hence they are forced back against the actual oncoming flow direction, and the wall shear stress changes direction as well. This results in the occurrence of a local backflow area, the attached boundary layer can no longer progress along the surface, and the laminar flow is forced to detach itself from the surface of the cylinder, as illustrated in Figure 2.3(a).

Once the laminar flow has separated from the cylinder's surface, the behaviour of the flow
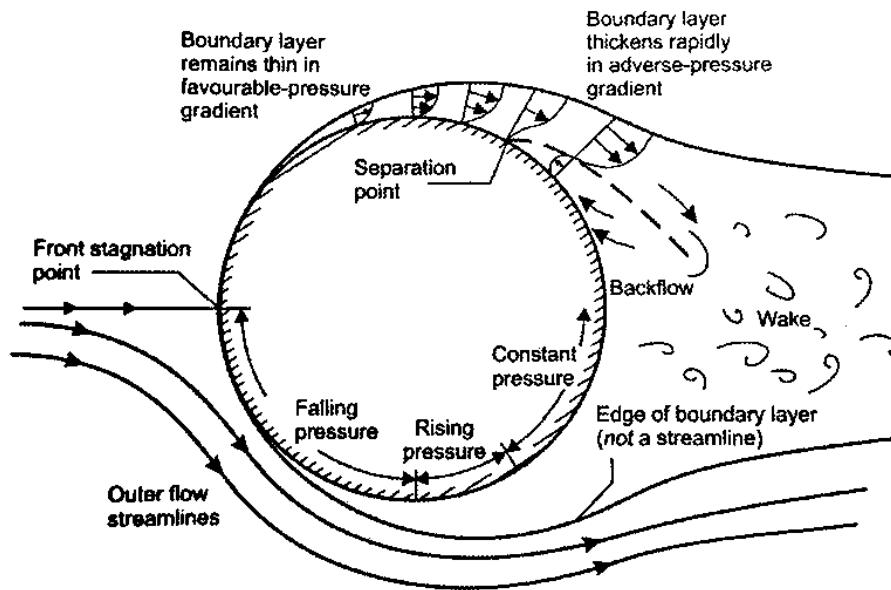
Figure 2.2: Velocity distribution on the cross-sectional surface of a circular cylinder in cross-flow (Groh [89]). The boundary layer is assumed to be laminar at least up to its separation from the cylinder surface.
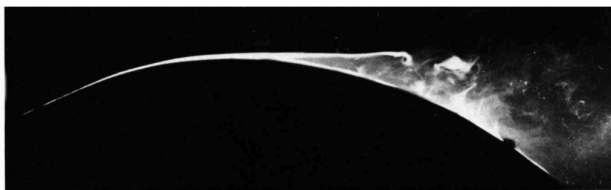
(a) Laminar boundary layer separation

(b) Turbulent boundary layer separation

Figure 2.3: Comparison of the separation of a laminar (top) and turbulent (bottom) boundary layer from a convex surface (Photos from Head [95] in Van Dyke [252]).

directly behind the cylinder, i.e. its base region, in the near wake, and in the far wake remain mainly Reynolds-number dependent. For $5 < Re_D < 40$, the steady two free shear layers converge to meet at a certain distance behind the cylinder (its exact location shifting downstream in the near wake with increasing Reynolds number, Van Dyke [252]), thereby forming a closed near-wake region in which two fixed, nearly symmetric recirculating eddies are captured, as presented in Figure 2.4.

A further increase in Reynolds number induces an instability in the recirculation region behind the circular cylinder, which leads to a loss in symmetry between both recirculating flows and the appearance of a sinusoidal oscillation of the shear layers, at first with a small amplitude and in the far wake (Figure 2.5(a)). For higher Reynolds numbers up to $Re_D \sim 200$ the initial location at which the oscillation starts wanders upstream towards the base of the cylinder. Simultaneously, the amplitude of the oscillating flow increases, the free shear layers start to roll up into eddies along the trail, thereby increasing their size whilst being carried downstream (Figures 2.5(b) and 2.5(c)). At the end of this third flow regime the eddies are shed alternately at either side of the cylinder, thereby forming a laminar Kármán vortex shedding street in the
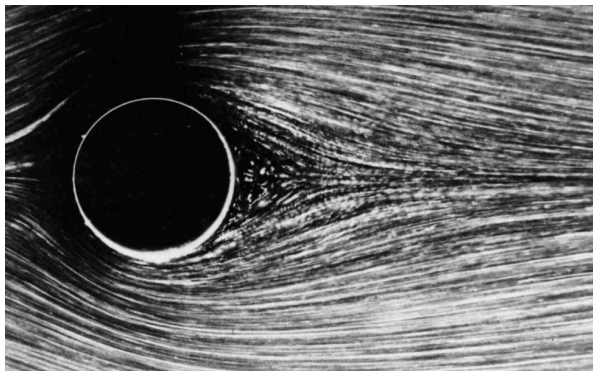
(a) Reynolds number: 9.6
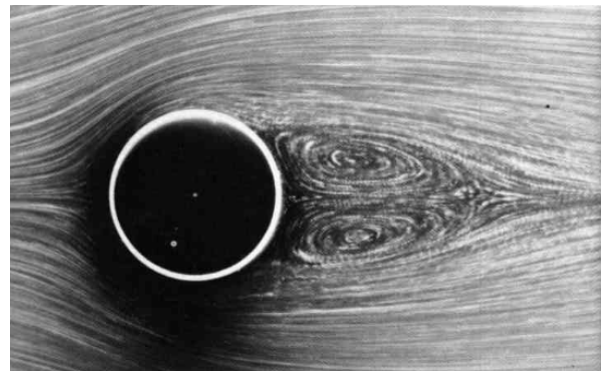
(b) Reynolds number: 26
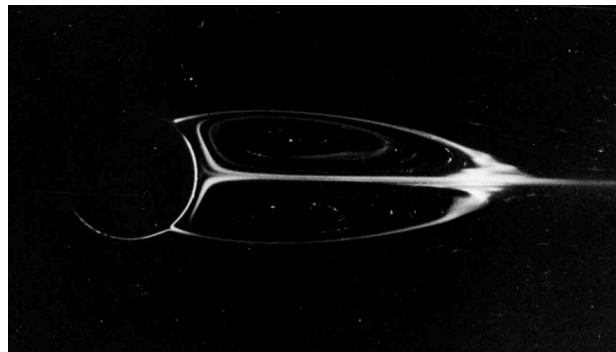
(c) Reynolds number: 41

Figure 2.4: Streamline visualisation of the separated flow around a circular cylinder in a laminar cross-flow with two recirculating eddies fixed in its steady near wake for $Re_D = 9.6$ (top), 26 (centre), and 41 (bottom) (Photos by S. Taneda in Van Dyke [252]).

(a) Reynolds number: 55
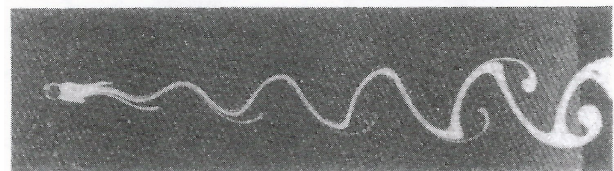
(b) Reynolds number: 65

(c) Reynolds number: 102
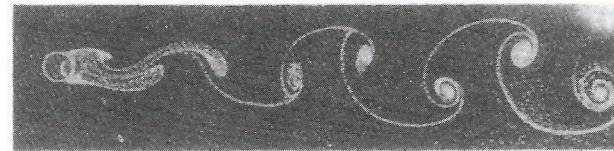
(d) Reynolds number: 161

Figure 2.5: Formation of the laminar eddy shedding in the wake of smooth circular cylinder with increasing Reynolds number (Homann [101]).

wake behind the cylinder (Figure 2.5(d)).

At Reynolds numbers around $Re_D = 200$, a transition from laminar to turbulent occurs

27

far downstream in the laminar periodic wake region, due to the random initiation and growth of irregularities. While increasing the Reynolds number even further, this transition location moves upstream along the laminar wake towards the base of the cylinder (Figure 2.6), until at $Re_D \sim 300$ – the upper boundary of the current flow state – the laminar-turbulent transition has spread that far upstream that its location can actually be found on the eddies during their formation. Hence, at the moment of shedding from the cylinder, each eddy is already turbulent.
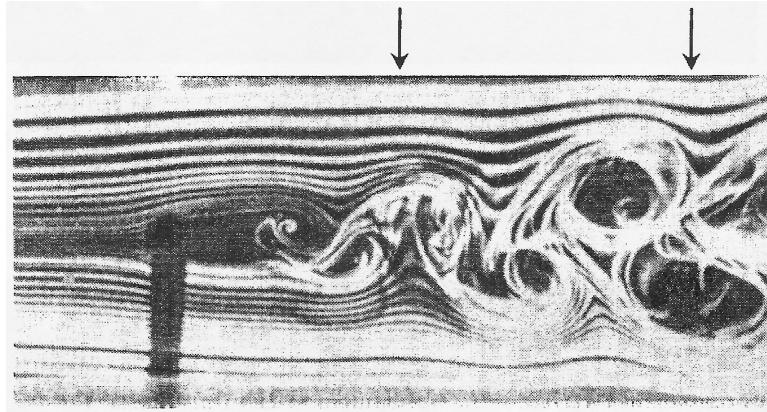
Figure 2.6: Transitional vortex street behind a smooth circular cylinder at $Re_D = 270$ within the TrW flow state (Photo by Beluche in Coutanceau and Defaye [53]). The arrows mark the positions at which the transverse flow between eddies becomes turbulent.

Zdravkovich [294] has named this first characteristic transition state the *Transition-in-the-wake state of flow* (*TrW*). In contrast to the categorisation by Mutlu Sumer and Fredsøe [149], he prolongs this flow state up to $Re_D = 350$ to 400 and divided it further into an lower and upper transition regime, depending on whether the laminar eddies are regular or irregular whilst being formed. While in the laminar flow states with Reynolds numbers up to $Re_D = 200$, the process of eddy shedding is highly two-dimensional, i.e. constant along the span of the cylinder, it becomes increasingly three-dimensional in the current flow state (Gerrard [87], Williamson [271]) with multiple cells (each with a different longitudinal length) appearing in spanwise direction. Although the characteristics of the eddy shedding within each cell are constant, variations in shedding frequency and phase between neighbouring cells do occur. As cells may also break up, disappear, and reappear, the number of cells and their lengths along the span of the cylinder vary continuously in time.

The boundary between the first and the second transition state of the flow over a smooth circular cylinder is located around $Re_D = 300$ (Mutlu Sumer and Fredsøe [149]) or 350 to 400 (Zdravkovich [294]) and characterised by a turbulent wake. The term adopted for this flow state in this monograph is the *subcritical* flow regime, in agreement with Wieselsberger [270]. This flow state continues up to a Reynolds number of 2×10^5 to 3×10^5. After separation of the still laminar boundary layer from the cylinder surface, the transition to turbulence takes place in the initially laminar free shear layers in the near wake. This means, that at the instant both free shear layers alternately roll up into eddies, they are already turbulent. With growing Reynolds number, the transition location progressively wanders along the free shear layers in upstream direction in the direction of the boundary layer separation points on the surface of the cylinder. This persuaded Zdravkovich [294] to split the overall *subcritical* flow regime into three sub-regimes for different phases of transition, i.e. from *lower subcritical* for Reynolds numbers

(a) Lower subcritical; Reynolds number: 2×10^3
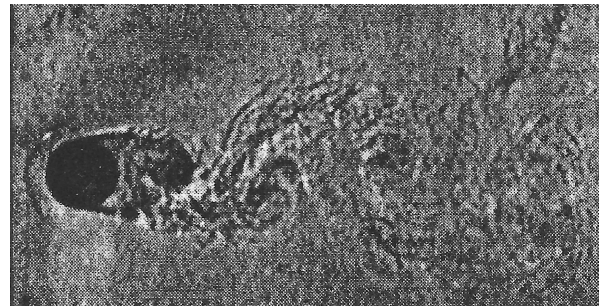
(b) Upper subcritical; Reynolds number: 1.1×10^5
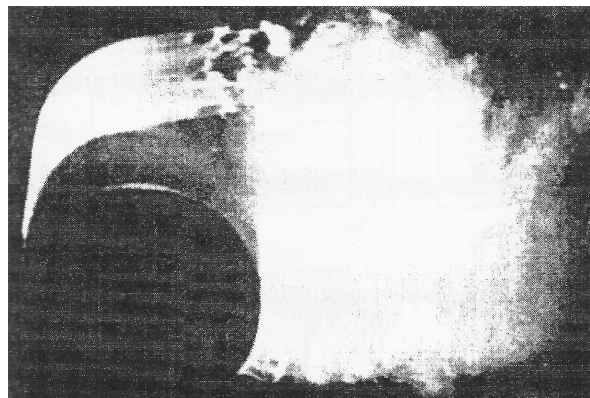
(c) Upper subcritical; Reynolds number: 1.5×10^5

Figure 2.7: Transition in the free shear layers behind a smooth circular cylinder in cross-flow. *(a)*: $Re_D = 2 \times 10^3$ within the *lower subcritical* regime (Gerrard [87]); *(b)*: $Re_D = 1.1 \times 10^5$ within the *upper subcritical* regime (Photo by Dymont in Van Dyke [252]); *(c)*: $Re_D = 1.5 \times 10^5$ within the *upper subcritical* regime (Werlé [269]).

up to $Re_D = 1 \times 10^3$ to 2×10^3 in which "*the transition waves appear first as undulations of the free shear layers*" and "*stabilize the near wake*" (Figure 2.7(a)), over *intermediate subcritical* where "*the transition eddies are formed as a chain along free shear layers....before becoming turbulent and then roll up in alternate eddies*", up to *upper subcritical* in which "*the transition to turbulence is reduced to a spot of a sudden burst in free shear layers close to the cylinder*" and "*is accompanied by a very short near wake*" at 2×10^4–$4 \times 10^4 < Re_D < 1 \times 10^5$–$2 \times 10^5$ (Figures 2.7(b) and 2.7(c)). The nature of the flow in this last sub-regime is defined as quasi-invariable, as a result of the stabilizing effect produced on the transition location in the free shear layers in this range of Reynolds numbers. The latter may result from an acceleration of the flow alongside the near wake, induced by a combination of a short eddy formation region, a consequential wide near wake, and a resultant relocation of the free shear layers into the flow that surrounds the cylinder (Zdravkovich [294]).

In the ensuing Reynolds-number flow regime, designated as the *critical* flow regime, the transition location can be found close to the surface of the cylinder in the first portion of the free shear. In this flow regime, the aforementioned stabilising effect of the transition region gradually weakens with increasing Reynolds number and the transition to turbulence in the free shear layers resumes its progressive advancement towards the points of boundary layer separation on the cylinder. This flow state is the last one, in which the boundary layer is

still laminar at separation. Upon separation, the fast growth of the instabilities in the free shear layers and the subsequent transition to turbulence allows a reattachment of the separated and now turbulent free shear layers onto the cylinder surface, as portrayed in Figure 2.8. Below the free shear layer, a *laminar separation bubble* (LSB) with a enclosed recirculation
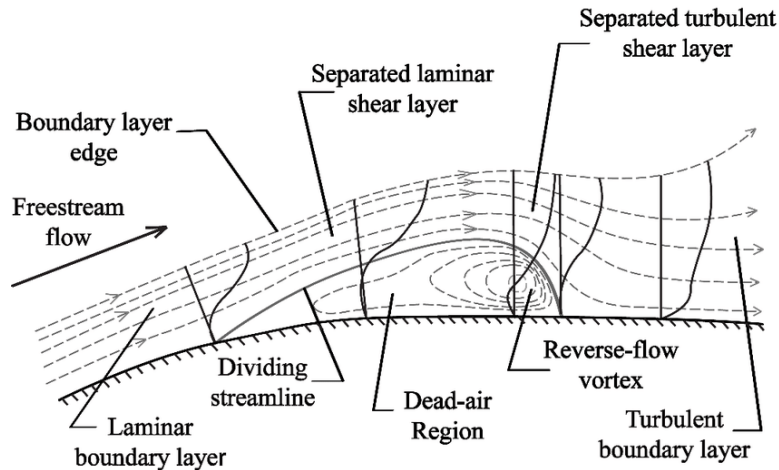
Figure 2.8: Schematic of the transition to turbulence over a laminar separation bubble above the surface of a smooth circular cylinder (Horton [103]).

is formed on the surface (e.g. Bearman [24], Schewe [209, 210], Lehmkuhl *et al.* [131]), and the "secondary" separation of the reattached turbulent boundary layer is delayed to a point a substantial distance downstream of the cylinder shoulders (Figure 2.3(b)). For a narrow band of Reynolds numbers around $Re_D = 3\times10^5$–3.8×10^5, the appearance of such a laminar separation bubble is limited to either one of the two sides of the smooth circular cylinder (e.g. Eisner [70], Fage [73], Fage and Falkner [75], Achenbach [1], Bearman [24], Achenbach and Heinecke, [5], Farell and Blessmann [76], Schewe [208, 209], Almosnino and McAlsiter [17], Higuchi *et al.* [98], Fujita *et al.* [84], Singh and Mittal [223], Vaz *et al.* [262], Lehmkuhl *et al.* [131], Miau *et al.* [145], Rodríguez *et al.* [194]). The exact values of both bounding Reynolds numbers strongly depend even on the smallest variations in the values of the influencing parameters, listed at the beginning of this chapter, owing to which a rather large scatter in the data is observed among the different studies. Following the argumentation presented by Schewe [209], the onset of this flow condition is initiated by the appearance of critical, low-frequency fluctuations in the microstructure of the flow that locally perturb the free shear layer on one side of the cylinder and invoke a transition to turbulence in this free shear layer. In his experiments on a perfectly smooth circular cylinder, he showed that the side at which the LSB appears is arbitrary, as it depends on the location in the oncoming flow at which the first disturbances are present that trigger the transition to turbulence (Schewe [209, 210]). After reattachment of the turbulent free shear layer onto the cylinder surface, the presence of the LSB leads to an acceleration of the flow on this side of the cylinder, whereas a flow deceleration occurs on the opposite side that induces a delay of the transition to turbulence. In combination with a relocation of the stagnation point away from the bubble (Kamiya *et al.* [119], Schewe [208]), which leads to a longer laminar surface boundary layer up to its separation from the surface on the bubble side and a shorter one on the other side, this results not only in a stable laminar separation bubble, but also in a delay of the formation of a (second) separation bubble on the opposite side. Hence, although the separation bubble may randomly occur at either side of the cylinder, once formed, it locally stabilises and fixes the asymmetric flow field. Because there are two stable states with
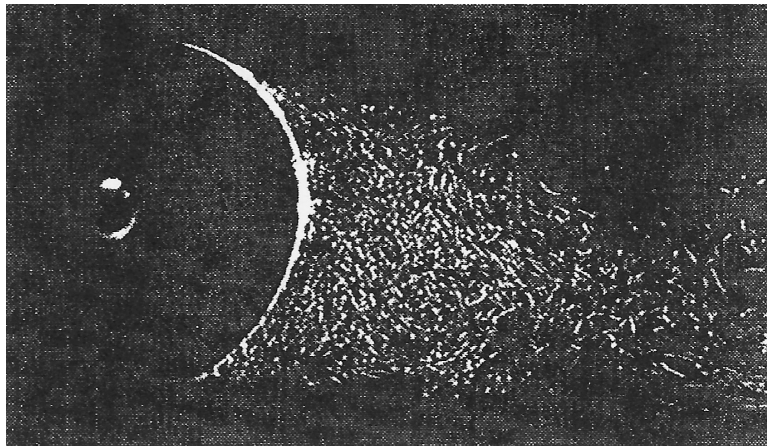
Figure 2.9: Flow visualisation of the near wake behind a smooth circular cylinder in a steady flow at $Re_D = 3.38 \times 10^5$ within the *bistable* flow regime (Almosnino and McAlsiter [17]).

a nearly equal probability of occurrence, this flow state is called the *bistable asymmetric flow state*. Bearman [24], on the other hand, reported that in his experiments the laminar separation bubble appeared each time at the same side of the cylinder. Although he mentioned that he was not aware of any obvious asymmetry in his experimental test setup, it can be argued that there must have been some sort of asymmetry present that caused the persistent occurrence of the LSB at one particular side of the circular cylinder. The presence of cells along the span of the circular cylinder results furthermore in a variation of the bubble occurrence and spanwise length over neighbouring sections (Schewe [209]). The large difference in angular positions at which the upper (turbulent) and lower (laminar) boundary layer separate from the surface results in a distinct asymmetric and narrower near wake compared to the previous *subcritical* flow regime, as shown in Figures 2.9 and 2.10(a).

The strong sensitivity of this bistable flow state to the Reynolds number is noticed clearly when the value of the latter is only slightly increased. Schewe [209] noted that the upper boundary of the *critical* flow regime is marked by the re-appearance of critical, low-frequency fluctuations in the microstructure of the flow. Hence, on that side of the cylinder on which the flow behaviour was essentially still *subcritical* in the *critical* flow regime, the laminar free shear layer is from this instant on also locally perturbed. This leads to a transition to turbulence in this laminar free shear layer just after separation from the cylinder surface as well, owing to which a laminar separation bubble is also formed on that side of the cylinder. Since a separation bubble is now present at both sides of the cylinder, the cylinder experiences a symmetric flow field (Bearman [24], Schewe [209]). However, Lehmkuhl *et al.* [131] reported that at a Reynolds number of 3.8×10^5 (Figure 2.10(b)), i.e. well within the *critical* flow regime, "*the combined effects of flow separation, transition to turbulence and the increase in the shear-stresses, makes the flow to reattach causing the formation of (two) asymmetric LSBs and delaying the final separation of the flow*". With a small further increase in the Reynolds number, the flow instabilities close to the surface and the two separation bubbles both become increasingly symmetric (Figure 2.10(c)), until the point is reached at which all topological changes of the flow around the smooth circular cylinder from *subcritical* to *supercritical* have been accomplished and the critical flow transition has thus been completed (Figures 2.10(d)). Their observation of the appearance of two (slightly) asymmetric LSBs at the end of the *critical* flow regime is most probably caused by an artefact of their numerical scheme, as it clearly contradicts the experi-

(a) Reynolds number: $2.5{\times}10^5$

(b) Reynolds number: $3.8{\times}10^5$

(c) Reynolds number: $5.3{\times}10^5$

(d) Reynolds number: $6.5{\times}10^5$
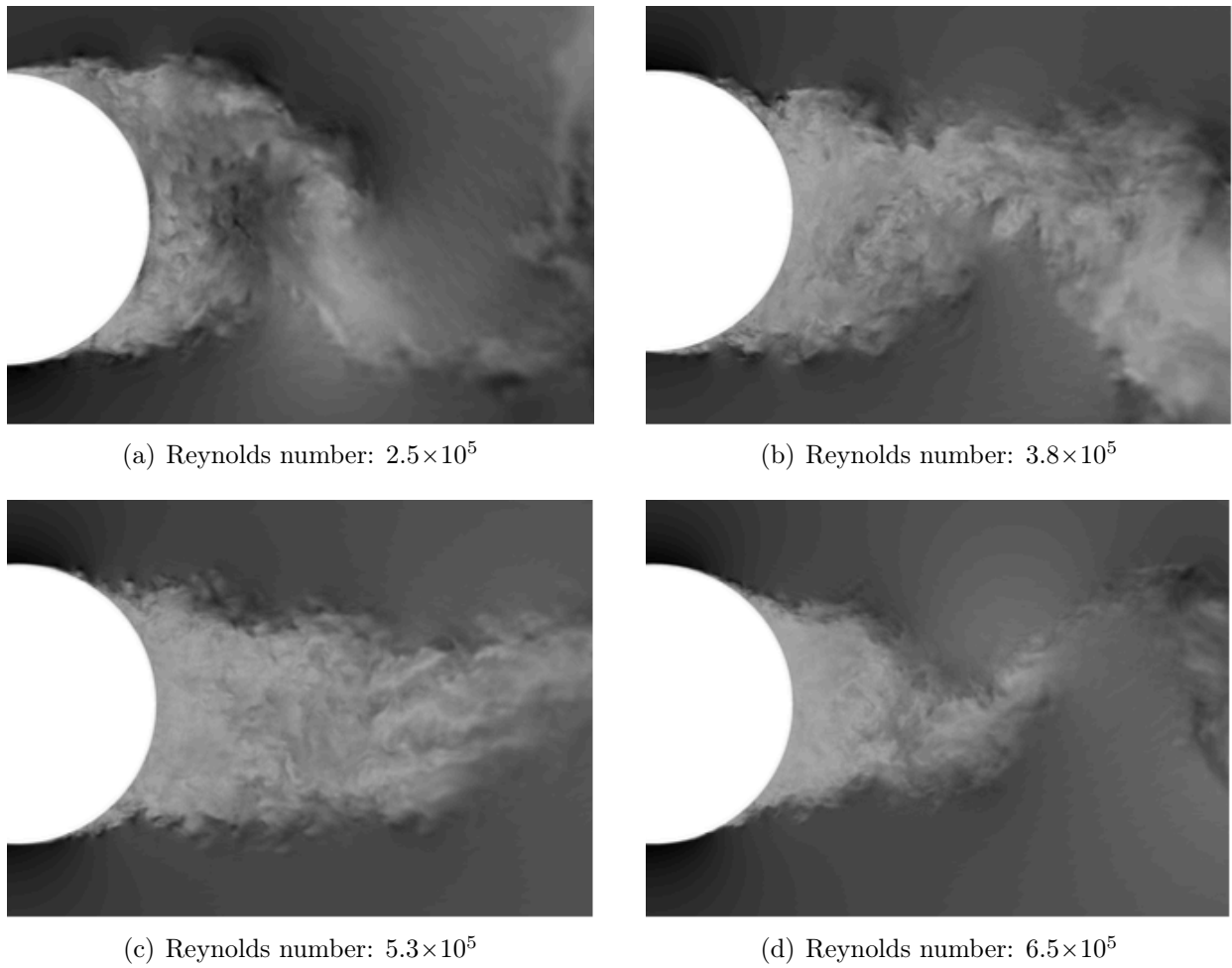
Figure 2.10: Instantaneous velocity magnitude profiles in the near wake behind a smooth circular cylinder at Reynolds numbers in the range of $2.5{\times}10^5$–$6.5{\times}10^5$ (Lehmkuhl *et al.* [131]). *(a)*: $Re_D = 2.5{\times}10^5$; *(b)*: $Re_D = 3.8{\times}10^5$; *(c)*: $Re_D = 5.3{\times}10^5$; *(d)*: $Re_D = 6.5{\times}10^5$.

mental results by Bearman [24] and Schewe [209].

As soon as symmetric conditions between both sides of the cylinder have been regained, the *supercritical* flow regime starts. It continues up to a Reynolds number of approximately $Re_D = 1.5{\times}10^6$ and is characterised by, among other things, both a smaller recirculation zone behind the cylinder and near-wake width in comparison to the *subcritical* flow regime. The cause of the latter results from a combination of the presence of both separation bubbles and the state of the reattached surface boundary layer, which is now turbulent up to the moment of its secondary separation from the cylinder surface. Contrary to a laminar boundary layer, which ceases to exist soon after it experiences a positive external pressure gradient, a turbulent boundary layer has the ability to sustain a high adverse pressure gradient over a long circumferential distance before its separation takes place. Because of the strong velocity fluctuations both in flow and cross-flow direction in this turbulent boundary layer, the continuous mixing of fluid elements promotes the interchange of momentum between the upper and lower regions of the boundary layer. Not only produces this mixing process a faster increase in thickness of the turbulent boundary layer compared to a laminar one, but high-energy fluid elements are in this way also transported from the outer flow regions to the regions close to the surface and therefore

continuously supply new kinetic energy to the fluid particles near the wall. Hence, the mean flow velocity of those fluid particles possesses a higher tangent component. The resultant larger velocity gradient directly at the surface of the cylinder enables the thick turbulent boundary layer to counteract the adverse pressure gradient over a longer distance. Its separation from the surface of the cylinder therefore shifts to a position further downstream, i.e. well past the maximum thickness of the cylinder, as can be clearly observed by comparison of the flow fields in the Figures 2.7(b) (high subcritical) and 2.10(d) (low supercritical). Interestingly, the process of laminar boundary layer separation, transition in the free shear layer, and reattachment onto the cylinder surface induces additional velocity fluctuations in cross-flow direction in the turbulent boundary layer upon reattachment. The boundary layer can therefore withstand an even stronger pressure increase over a longer circumferential distance along the cylinder surface compared to a "normal" laminar-turbulent transition in the attached boundary layer (Roshko [198]). The final separation is therefore postponed to the highest possible angular positions on the leeward side of the cylinder and generates in that way a small recirculation zone and a narrow near- and far-wake.

In the following state of the flow over a smooth circular cylinder, the so-called *upper transition*, that exists up to a Reynolds number of approximately $4.5{\times}10^6$, the location of the transition to turbulence pursues its migration along the surface of the cylinder in upstream direction with increasing Reynolds number. This leads to a continuous decrease in size of both laminar separation bubbles, which then successively become unstable, disrupt and fragment along the span of the cylinder as the transition reaches the primary laminar separation line (Bearman [24], Loiseau and Szechenyi [135]). With each further increase in Reynolds number, the transition location creeps further upstream along the surface, thereby overtaking the primary separation, upon which the laminar separation bubbles vanish, and a "normal" laminar-turbulent transition takes place in the attached boundary layer. The boundary layer can therefore no longer withstand the strong pressure increase on the downstream-directed face of the cylinder and the primary boundary-layer separation locations advance towards both shoulders of the cylinder. The recirculation zone behind the cylinder becomes wider and the near wake opens again. Similar to the *critical flow state*, this flow transformation occurs in an asymmetric manner between the upper and lower sides of the cylinder. The amount of asymmetry is once more strongly affected by the values of the influencing parameters, which results in a rather large scatter in the measurement data. In addition, the highly three-dimensional, irregular state of the turbulent free shear layers can cause a suppression of the regular eddy shedding process in the wake of the cylinder at certain Reynolds numbers (Bearman [24]).

For Reynolds numbers above $4.5{\times}10^6$, the flow field around the smooth circular cylinder is characterised by a relatively wide recirculation zone and near-wake region, as well as by a regular vortex shedding (Roshko [197], Cincotta *et al.* [52], Loiseau and Szechenyi [136], Schewe [209]). The laminar-turbulent transition is situated between the stagnation and separation points in the attached boundary layer and slowly, but steadily continues its motion towards the stagnation point for increasing Reynolds numbers. This implies, that the complete wake, the free shear layers, and large amounts of the boundary layer are turbulent in this ultimate *transcritical* flow regime. The two separation locations on the cylinder are located over the shoulders and show only minor variations with Reynolds numbers. The latter therefore also counts for the widths of the base region and the near- and far wake.

2.1.2 Fluid dynamic forces on smooth circular cylinders

In the preceding section, the variation of the state of the flow over a circular cylinder with changing Reynolds number was discussed in detail. With the exception of the *Stokes flow* for $Re_D \leqslant 5$, the cylinder experiences in each of the flow regimes a total drag force that results from the asymmetric pressure distribution on the windward and leeward side of the cylinder and the viscous friction force – the latter induced by the wall shear stress along the surface – that both act on the cylinder surface. Since in this monograph the primary focus is placed on the range of Reynolds numbers of $10^5 < Re_D < 10^7$, i.e. from high *subcritical* up to moderate *transcritical*, the component of the viscous friction force on the resultant fluid dynamic force on the cylinder is low. Achenbach [1], for example, showed that at these Reynolds numbers less than 3% of the total drag experienced by a circular cylinder in a steady cross-flow results from friction forces on the cylinder surface. The friction force component can therefore be omitted without introducing large errors. In the following discussion on the fluid-dynamic forces, only the drag component by the pressure force on the cylinder is therefore taken into account.

Upon the final separation of the laminar or turbulent boundary layer from the cylinder surface, the flow region that is formed immediately downstream of the base of the cylinder contains reversed flow and is characterised by a relatively low, but constant pressure (Figure 2.2). This circulation zone or near wake is bounded by the cylinder surface and the free shear layers. In this zone, eddies are formed alternatingly on both sides of the cylinder as a result of the interplay between the reversed and forward-directed flows that induces a roll-up of the shear layers. During the formation of such an eddy, portrayed schematically in Figure 2.11, it is fed by circulation from its connected shear layer, and can thus gradually increase both in strength and size. Once its strength is sufficiently large, the eddy draws the opposing free shear
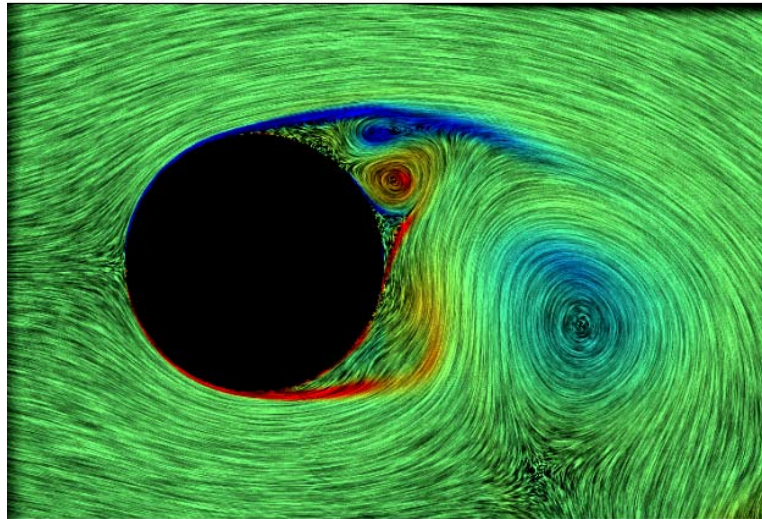
Figure 2.11: Instantaneous vorticity and velocity field around a smooth circular cylinder in a steady cross-flow (Shirayama and Ohta [221]). The shear layer roll-up and the eddy formation region can clearly be recognised.

layer across the near wake. The latter therefore starts to roll up into an eddy as well and, since it is simultaneously fed by vorticity, it also grows in strength and size. Once this approaching and oppositely rotating eddy is strong enough, it cuts off the further supply of circulation of the former eddy. As a consequence, the latter thereupon detaches from the surface and has now
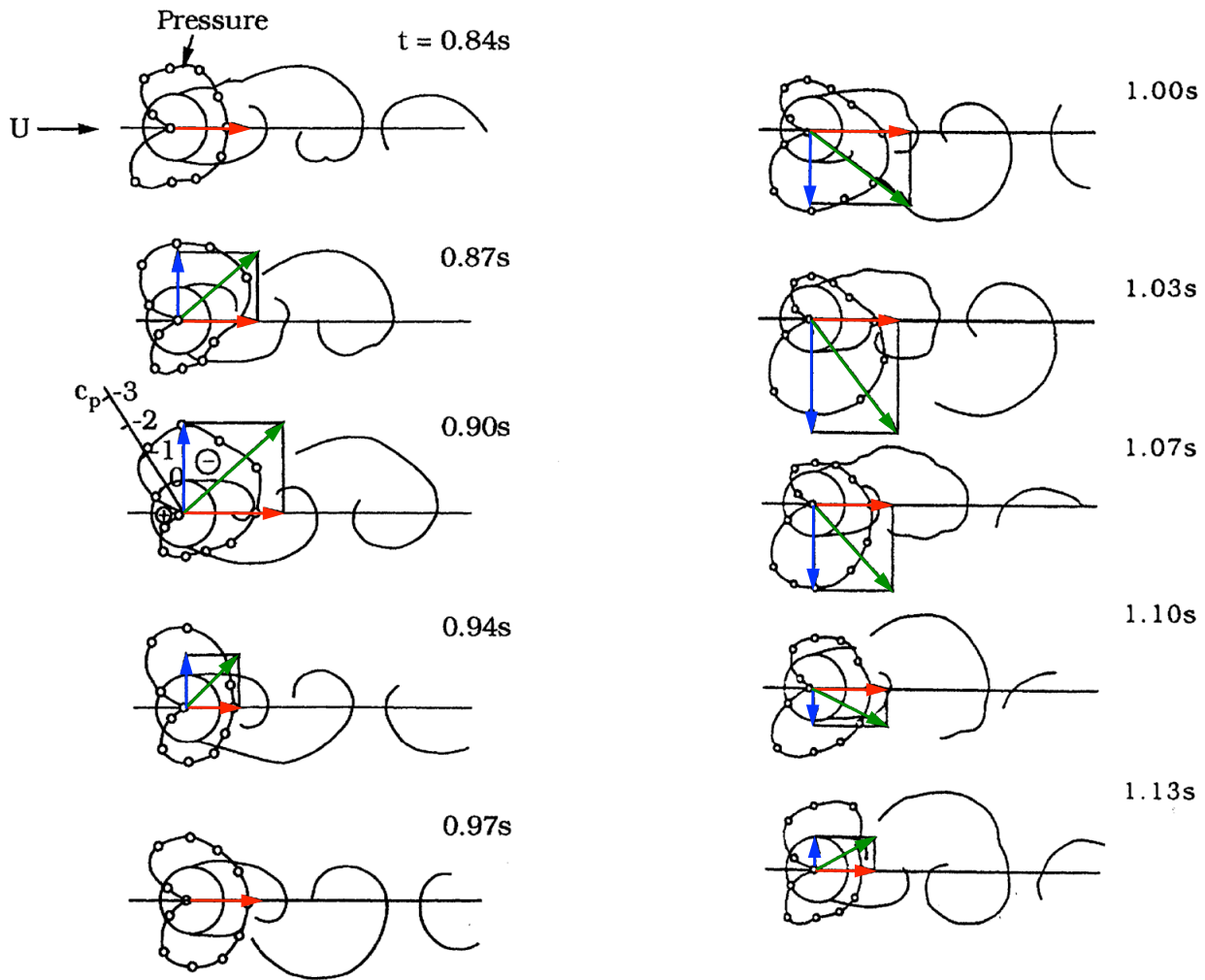
Figure 2.12: Variation of surface pressure coefficient C_p, as well as lift (blue arrow), drag (red arrow), and resultant force (gree arrow) on a circular cylinder in a steady cross-flow during one shedding cycle at $Re_D = 1.1 \times 10^5$ (Drescher [63]).

become a distinct vortex. This so-called eddy shedding generally takes place in an alternating manner between the sides of the cylinder. Upon formation and shedding of the eddy, each distinct vortex is convected downstream by the flow and gradually decays along the (far) wake, thereby forming in this way the well-known *Kármán vortex street*.

The process of the alternating shedding of counter-rotating eddies introduces a regular fluctuation of the pressure distribution on the cylinder surface that leads to a similar regular variation in the lift and drag component – for the former both in direction and amplitude, for the latter solely in amplitude – of the resultant fluid-dynamic force, shown in Figure 2.12. From this figure it becomes evident that the frequency of the lift force equals the Kármán vortex shedding frequency, whereas the drag force fluctuates with a dominant frequency that equals twice that value. It is therefore not surprising, that the same ratio in frequencies exists between the transverse and in-line vortex-induced vibrations experienced by an elastically-mounted circular cylinder in a steady flow.

2.1.2.1 Mean drag and lift forces

The distribution of the mean, i.e. time-averaged, surface pressure coefficient, defined as

$$C_p = \frac{p - p_\infty}{\frac{1}{2}\rho U_\infty^2} \tag{2.2}$$

where p equals the mean local static pressure on the surface and p_∞ the static pressure in the free stream, are presented in Figure 2.13 for different Reynolds numbers from *subcritical* up to *transcritical*. The characteristic pressure distributions on the windward side of the cylinder

(a) *Subcritical* to *supercritical* flow regimes

(b) *Subcritical* to *transcritical* flow regimes
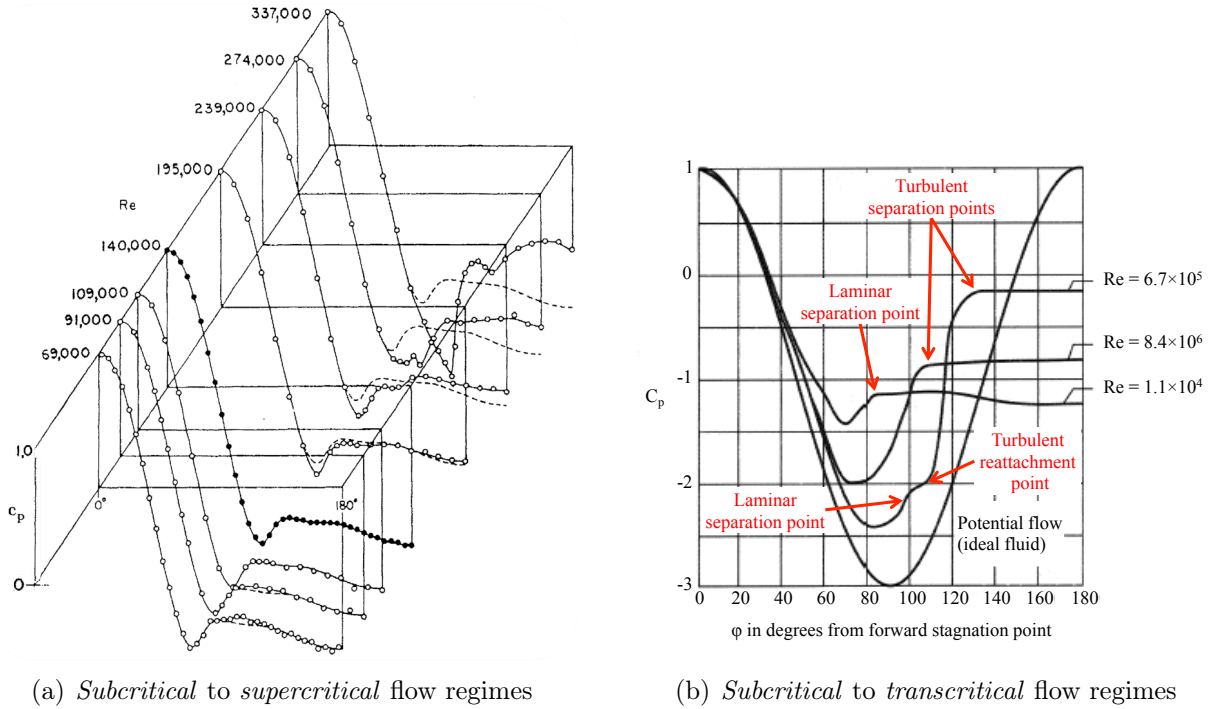
Figure 2.13: Cross-sectional mean pressure distribution on the surface of a circular cylinder for different Reynolds numbers in the *subcritical* to *transcritical* flow regimes. *(a)*: experimental data by Cantwell [41] (from Zdravkovich [294]); *(b)*: adapted from Nakayama [154].

show only minor variations with increasing Reynolds number and neatly follow the pressure distribution obtained from the potential flow theory, given by

$$C_{p,pot} = 1 - 4sin^2\varphi \tag{2.3}$$

where φ is the circumferential angle. On the rear side of the cylinder a strong deviation from the potential flow theory occurs as a result of the separation of the flow from the cylinder surface. The presence of a recirculation zone adjacent to the base of the cylinder with a relatively flow velocity induces the plateau of the surface pressure coefficient across the cylinder wake. With growing Reynolds number, the value of the mean minimum pressure coefficient $C_{p,min}$ gradually lowers in the *subcritical* flow regime ($Re_D \leqslant 2.39{\times}10^5$ in Figure 2.13(a)), subsequently drops drastically in the *critical* flow regime ($Re_D = 2.74{\times}10^5$ and $3.37{\times}10^5$, Figure 2.13(a)), shows a gradual recovery in the *upper transition*, and finally settles at a relatively constant *transcritical* value of about $C_{p,min} = -2$ ($Re_D = 8.4{\times}10^6$ in Figure 2.13(b)). The drastic fall in $C_{p,min}$ over the *critical* flow regime is combined with a steep increase in the adverse pressure recovery

along the cylinder circumference directly downstream of the angular location at which $C_{p,min}$ occurs, as well as an increase of the plateau of C_p at the base of the cylinder. This becomes clearly visible in Figure 2.13(b) when comparing the pressure distributions at $Re_D = 1.1 \times 10^4$ (subcritical) and $Re_D = 6.7 \times 10^5$ (supercritical).

Based on the mean surface pressure distribution, the mean (two-dimensional) cross-sectional pressure drag and lift coefficient, C_d and C_l, respectively, can be determined according to

$$C_d = \frac{d}{\frac{1}{2}\rho U_\infty^2 L_{ref}} = \int_0^{2\pi} \frac{C_p sin\varphi}{L_{ref}} d\varphi = \frac{1}{L_{ref}} \int_s C_p n_X ds = \frac{1}{L_{ref}} \sum_{i=1}^m C_{p,i} n_{X,i} ds_i \qquad (2.4a)$$

$$C_l = \frac{l}{\frac{1}{2}\rho U_\infty^2 L_{ref}} = \int_0^{2\pi} \frac{C_p cos\varphi}{L_{ref}} d\varphi = \frac{1}{L_{ref}} \int_s C_p n_Z ds = \frac{1}{L_{ref}} \sum_{i=1}^m C_{p,i} n_{Z,i} ds_i \qquad (2.4b)$$

where d and l equal the mean cross-sectional drag and lift force on the cylinder, φ the angular coordinate, s the circumferential location on the cylinder surface, n the local normal vector on the cylinder surface, and X and Z the directed axes in downstream and cross-flow (positive upward) direction, respectively, with respect to the centre location of the cylinder. Figure 2.14 presents a compilation of experimental data of the cross-sectional drag coefficient C_d for $Re_D \geqslant 10^5$. As expected from the behaviour of the mean surface pressure distribution, the drag coefficient possesses a very clear and distinct Reynolds-number dependent variation as well.
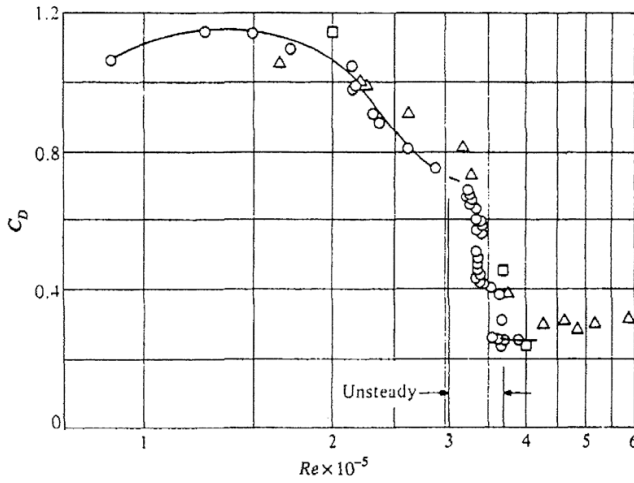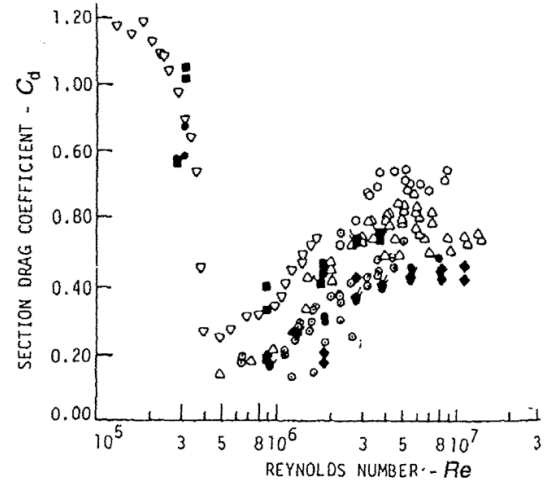
(a) *Subcritical* to *supercritical* flow regimes (b) *Subcritical* to *transcritical* flow regimes

Figure 2.14: Evolution of the mean cross-sectional drag coefficient for *subcritical* to *transcritical* Reynolds numbers (Zdravkovich [294]). *(a)*: □: Bearman [24], △: Güven *et al.* [91], ○: Farell and Blessmann [76]; *(b)*: ▽: Polhamus [186], ○: Roshko [197], ⊙: Schmidt [214], △: Jones *et al.* [116], full symbols: James *et al.* [114].

For *subcritical* Reynolds numbers up to about 1×10^5 to 2×10^5 the mean drag coefficient is practically constant with a value of around 1.2. The laminar boundary layer separates around an angular position of $\varphi_S = 80°$, i.e. upstream of each shoulder of the cylinder (Figure 2.15). As a consequence, a strong deflection of the streamlines and a distinct spreading of the free shear layers in cross-flow direction occur. The eddies are therefore formed relatively close to the base surface of the cylinder, which is mirrored in a high negative base pressure coefficient in the range of $C_{pb} = -1.0$ to -1.2, as illustrated in Figure 2.16(a). At the end of the *subcritical*
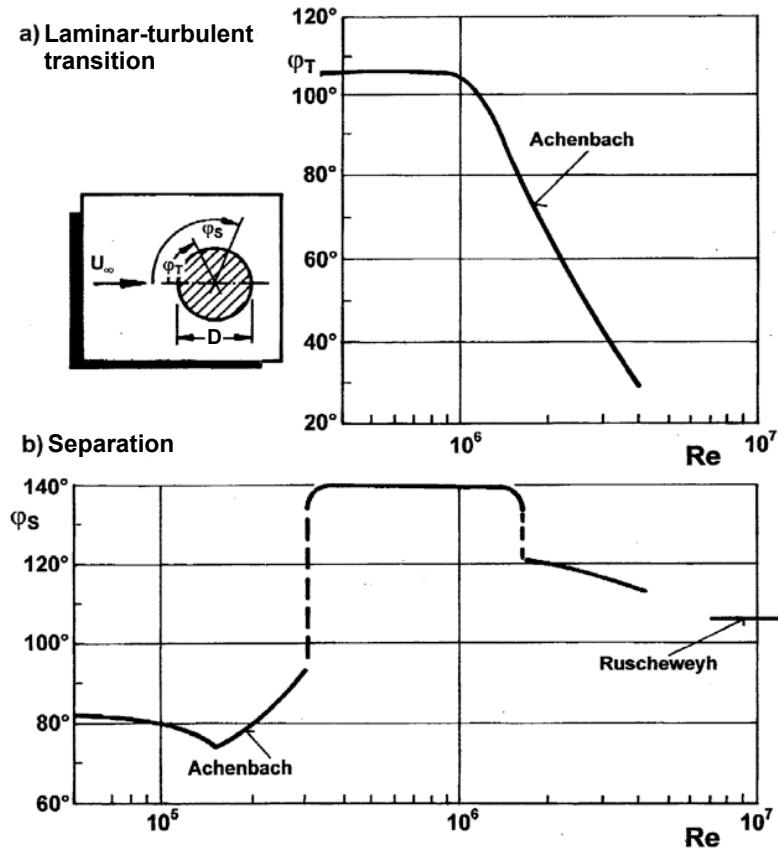
Figure 2.15: Behaviour of the attached boundary layer on a circular cylinder in cross-flow for $6{\times}10^4 \leqslant Re_D \leqslant 4{\times}10^6$ (Zdravkovich [294]). *(a)*: Angular location of the laminar-turbulent transition (Achenbach [4]); *(b)*: Angular separation location (Achenbach [1], Ruscheweyh [199]).
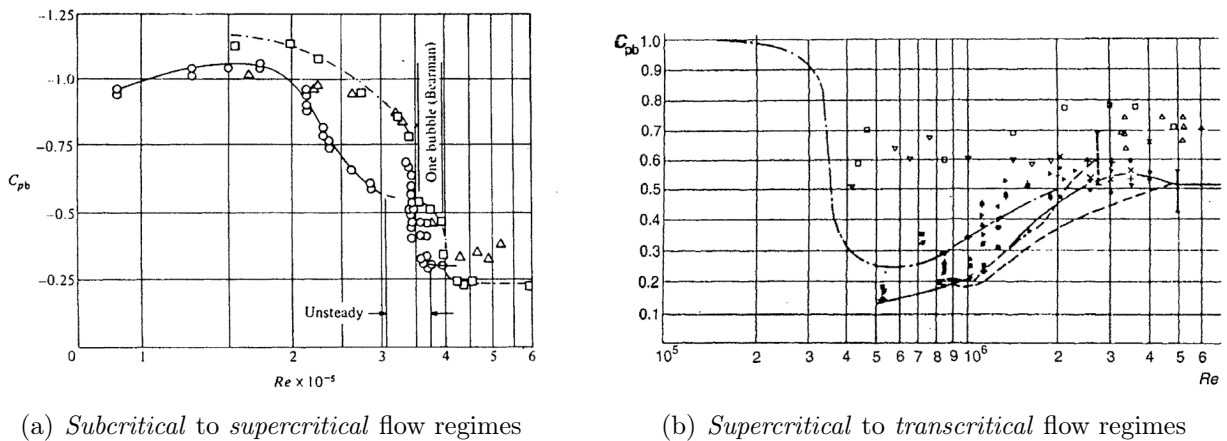
(a) *Subcritical* to *supercritical* flow regimes   (b) *Supercritical* to *transcritical* flow regimes

Figure 2.16: Dependency of the mean cross-sectional base pressure coefficient for *subcritical* to *transcritical* Reynolds numbers (Zdravkovich [294]). *(a)*: □: Bearman [24] △: Güven *et al.* [91], ○: Farell and Blessmann [76]; *(b)*: all symbols: Warschauer and Leene [267].

flow regime, a gradual, but steady decrease of the drag coefficient is obtained. It results from the elongation of the low-pressure region, situated adjacent to the base of the cylinder, in which the eddies are formed (Peltzer [185]). This leads to a decrease in the negative mean base pressure coefficient (Figure 2.16(a)) and a shift of the angular separation location of the laminar boundary layer from the windward to the leeward side of the cylinder shoulders (Figure 2.15). The latter demonstrates, that the near wake does not only gradually become longer, but at the same time also somewhat smaller at those Reynolds numbers.

The formation of the laminar separation bubbles, first at one side of the cylinder, subsequently also at the other side in the *critical* flow regime induces a strong drop of the mean drag coefficient that includes two discontinuous downward steps. These two discontinuities in the mean drag coefficient occur at those Reynolds numbers at which either the first or the second LSB does appear. The main driving parameter behind the sharp decrease in C_d is the combination of the relocation of the final separation location of the attached boundary layer from $\varphi_S = 95°$–$100°$ at $Re_D = 3\times10^5$ to $\varphi_S = 140°$ at $Re_D = 3.5\times10^5$ and the state of the boundary layer at separation that changes from laminar to turbulent. As a result of displayed secondary separation, the near wake becomes increasingly smaller, which leads to a sharp decrease of the negative base pressure coefficient (Figure 2.16(a)) and thus a major and abrupt decrease in the drag force experienced by the cylinder. In the discussion of the *critical* flow regime in section 2.1.1, it was mentioned, that although the single separation bubble may randomly occur at either side of the cylinder, once formed, it locally stabilises and fixes the asymmetric flow field within the narrow *bistable asymmetric flow state.* The resultant asymmetric mean surface pressure distribution introduces a mean steady lift force on the cylinder. Kamiya *et al.* [119] obtained in their experiments a mean cross-sectional lift coefficient of $C_L = 0.8$ and 1.2, the value being dependent on whether they passed this *bistable flow state* by increasing or decreasing the Reynolds number (Figure 2.17(a)). The steady increase/decrease of C_L at the beginning and the end are an indication for the presence of a light asymmetry in their experimental test setup. Schewe [208, 209], on the other hand, measured a spanwise-integrated mean lift coefficient of $C_L = 1.3$ which was independent of the Reynolds-number sequential order (Figure 2.17(b)). In
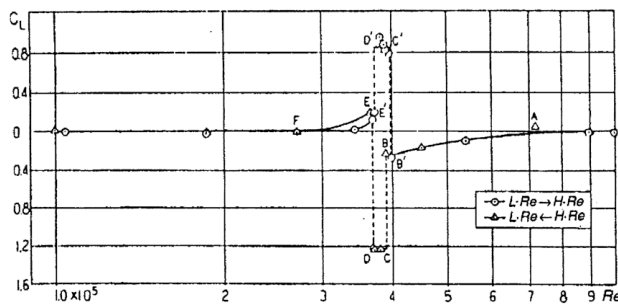
(a) Steady mean cross-sectional lift coefficient
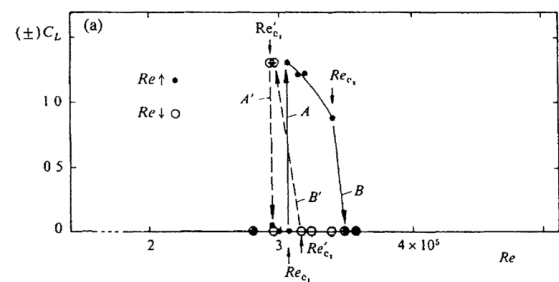
(b) Steady mean spanwise-integrated lift coefficient

Figure 2.17: Steady mean lift coefficient on a circular cylinder in cross-flow for Reynolds numbers in the *bistable* flow state. *(a)*: cross-sectional lift coefficient (Kamiya *et al.* [119]); *(b)*: spanwise-integrated lift coefficient (Schewe [209]).

addition, both authors observed a clear hysteresis in the abrupt appearance and subsequent disappearance of the steady mean lift force with increasing or decreasing Reynolds numbers. This demonstrates, that the sequential formation of the two laminar separation bubbles takes place at two somewhat higher Reynolds numbers than the burst of both LSBs when the Reynolds

number is successively decreased from *supercritical* to *subcritical* values.

The lowest, relatively constant mean cross-sectional drag coefficient of approximately $C_d = 0.2$ is obtained throughout the *supercritical* flow regime (Figure 2.14). At most of the *supercritical* Reynolds numbers, i.e. up to about 1×10^6, the transition to turbulence along the span of the cylinder is located within the separation bubble around $\varphi_T = 106°$. Only at the end of this flow regime, near to the beginning of the *upper transition*, a gradual upstream motion of the transition location in the attached surface boundary layer can be seen to commence (Figure 2.15). The presence of the two laminar separation bubbles leads to a high value of the adverse pressure recovery, defined as $C_{pb} - C_{p,min}$, in comparison to those at *subcritical* Reynolds numbers, as shown in Figure 2.13(b). Güven [91] measured, for example, a strong jump of a factor 10 for the value of the adverse pressure recovery over the *critical* flow regime. Following the mechanism of laminar-turbulent transition over the separation bubble, the reattached turbulent boundary layer can withstand this strong adverse pressure gradient on the leeward side of the cylinder over a long circumferential distance along the cylinder surface, owing to which the secondary separation location remains at a steady angular value of $\varphi_S = 140°$. The following short and narrow recirculation zone behind the cylinder and the near wake keep the negative mean base pressure coefficient at a low negative value of $C_{pb} = -0.2$ to -0.25 (Figure 2.16), which results in the low mean drag coefficient.

In the last portion of the *supercritical* flow regime a discontinuous step in the separation angle to $\varphi_S = 125°$ was measured by Achenbach [1], that is followed by a continuous decrease towards $\varphi_S = 115°$ in the subsequent *upper transition* (Figure 2.15). This decrease in φ_S results from the shrinkage and subsequent disappearance of the two laminar separation bubbles, owing to which a "normal" laminar-turbulent transition takes place in the attached boundary layer. During its steady shift along the surface of the cylinder in the direction of the stagnation point with increasing Reynolds number, Figure 2.15, the transition location overtakes the angular location of the primary turbulent separation. The boundary layer can no longer withstand the large adverse pressure gradient on the downstream-directed face of the cylinder, the primary separation location thus has to advance upstream, thereby approaching both shoulders of the cylinder, but with a much lower angular velocity than the transition point. The upstream motion of the separation leads to a widening of the recirculation zone behind the cylinder and an increase of the negative mean base pressure (Figure 2.16(b)). The magnitude of the adverse pressure recovery decreases (Achenbach [1], Roshko [197], Jones [116], Güven [91]) and the near wake opens itself again. All of these factors combined cause the increase in the mean drag coefficient, as presented in Figure 2.14(b). The scatter of the experimental data for C_d and C_{pb} in this *upper transition*, as well as the scatter of the Reynolds number at which this flow regime starts and the value of C_d that is reached at its upper bounding Reynolds number result from the different values of the influencing parameters in the listed tests.

In the final *transcritical* flow regime for $Re_D > 4.5 \times 10^6$, the laminar-turbulent transition is situated in the attached boundary layer in the vicinity of the stagnation point. Ruscheweyh [199] measured a separation of the turbulent boundary layer around a steady angle of $\varphi_S = 105°$ at high *transcritical* Reynolds numbers of 10^7. Since the separation occurs at the leeward sides of both cylinder shoulders, the nearly regular near wake is for these Reynolds numbers smaller as the laminar near wake in the *subcritical* flow regime. This reflects in lower, but highly Reynolds-number independent values of C_{pb} and thus also of C_d at *transcritical* Reynolds numbers.

2.1.2.2 Fluctuating drag and lift forces

As already discussed at the beginning of this section, the process of alternating roll-up of the free shear layers into eddies at either side of the cylinder in the base region and the subsequent shedding of the distinct counter-rotating vortices introduces a regular change of the pressure distribution on the surface of the cylinder (Figure 2.12). The circular cylinder experiences thereupon a resultant fluid-dynamic force that varies regularly with time and can be split up into a its lift and drag force components. The characteristic Reynolds-number-dependent variation of the mean parts of the lift and drag force has been discussed in detail in the previous section, where it was shown, that a circular cylinder with a smooth surface experiences a mean non-zero lift force only in a very small range of Reynolds numbers within the *critical* and *upper transition* flow regimes. However, from Figure 2.12 it becomes evident, that, independent of the Reynolds number, this same cylinder experiences regular fluctuations in both lift and drag – even when the mean lift force equals zero – over each shedding cycle, provided that a (regular) eddy shedding does actually take place in the near wake behind the cylinder at that specific Reynolds number.

A compilation by Hallam *et al.* [93] of the magnitude of the oscillating (RMS) parts of the cross-sectional lift and drag force on a circular cylinder, denoted by $\sqrt{(\overline{C_l'^2})}$ and $\sqrt{(\overline{C_d'^2})}$, respectively, are presented in Figure 2.18 as function of the Reynolds number. It has to be mentioned at this point, that there exist many different methods to measure the RMS values of the lift and drag forces. One must distinguish between sectional forces, for which the considered segment length l in spanwise direction on which the forces are measured is small compared to the total span L of the cylinder, and global forces that act on the complete span of the cylinder. Since the coherence of the flow structures (or sectional forces) is decreasing in spanwise direction, the integration of the measured forces over the spenwise section leads to lower RMS values when L/D is increased. From this figure, it is obvious that the trends of the RMS values of both

(a) Fluctuating cross-sectional lift coefficient (b) Fluctuating cross-sectional drag coefficient
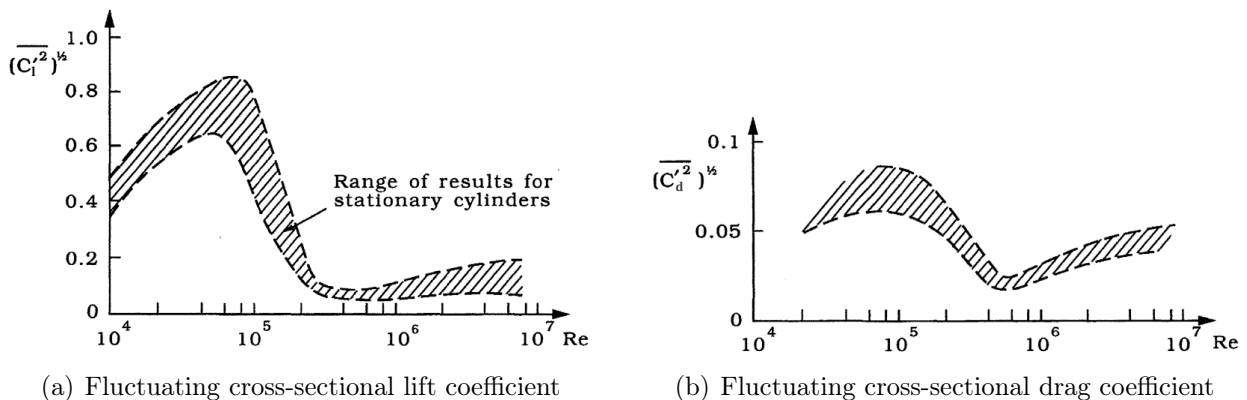
Figure 2.18: Fluctuating cross-sectional force coefficients (RMS) on a smooth circular cylinder in a steady cross-flow (Hallam *et al.* [93]). *(a)*: cross-sectional lift coefficient; *(b)*: cross-sectional drag coefficient.

C_l and C_d follow the general curve of the mean drag coefficient with Reynolds number given in Figure 2.14: the highest values are obtained in the *subcritical* flow regime, followed by a drastic change with a large and steep decrease over the *critical* flow regime, before attaining extremely low values at *supercritical* Reynolds numbers. In the subsequent *upper transition*, a

gradual increase in both $\sqrt{(\overline{C_l'^2})}$ and $\sqrt{(\overline{C_d'^2})}$ takes place, whereby the latter parameter shows a stronger recovery than the former and thus obtains higher nearly constant values in the final *transcritical* flow regime. The combination of an extremely high boundary layer separation angle of $\varphi_S = 140°$ at *supercritical* Reynolds numbers (Figure 2.15) and the fact that this boundary layer is turbulent at its final separation results in a weak interaction between the eddies in the very narrow recirculation zone at the base of the cylinder. The induced pressures on the surface of the circular cylinder show therefore only small fluctuations over each shedding cycle, which explains the extremely small RMS values in the *supercritical flow state*. Their values and variations in the other flow regimes can be explained in a similar manner by reference to the pressure distributions in Figure 2.13, the transition and separation angles given in Figure 2.15, and the state of the boundary layer at separation.

The values of the $\sqrt{(\overline{C_l'^2})}$ and $\sqrt{(\overline{C_d'^2})}$ can be considered a measure of the influence of the eddies on the fluidelastic behaviour of the circular cylinder. The higher the values, the stronger the eddies interact with the base of the cylinder in the recirculation zone and the larger the vortex-induced oscillations. The difference of about a factor 10 between the RMS values of the lift and the drag force over all flow regimes furthermore explains the much higher amplitude of the vortex-induced vibration in transverse (i.e. lift) direction that an elastically-mounted smooth 2D circular cylinder experiences in a steady cross-flow, as has already been mentioned in Section 1.2.2.

2.1.2.3   Strouhal number

The power spectral densities (PSD) of the time-dependent signals of the lift and drag forces, obtained with piezoelectric platform dynamometers, of the velocity fluctuations, measured with hot wires, or of the surface pressure signals can be used to extract the main frequency or frequencies of the eddy shedding process. The resultant normalised eddy shedding frequencies in cross-flow and flow direction, denoted hereafter as the Strouhal numbers St_L and St_D, respectively, are defined as

$$St_L = \frac{f_{s,L} L_{ref}}{U_\infty} \tag{2.5a}$$

$$St_D = \frac{f_{s,D} L_{ref}}{2U_\infty} \tag{2.5b}$$

where $f_{s,L}$ and $f_{s,D}$ are the main frequencies in the PSDs in flow and cross-flow direction, respectively. Figure 2.19 illustrates the variation of the Strouhal number St_L with Reynolds number for a smooth circular cylinder. Following an initial increase of the Strouhal number from $St_L = 0.1$ at $Re_D = 40$ to a value of about 0.2 around $Re_D = 300$, i.e. at the lower bound of the *subcritical* flow regime, its value remains nearly constant throughout this latter flow regime. As shown in paragraph 2.1.2.1, the separation angle of the laminar boundary layer shifts at the end of this flow regime from the windward ($\varphi_S \approx 75°$) to the leeward ($\varphi_S = 95°-100°$) side of both shoulders of the cylinder, which indicates a slight lateral convergence of the two free shear layers in the near wake (Figure 2.15). A small increase in the value of the Strouhal number would thus be expected, which is contradicted by the experimental data in Figure 2.19 though. The cause is found in the simultaneous increase of the length of the near wake, L_f, that counteracts the induced effect by the approaching shear layers in the near wake and keeps the Strouhal number in that way at a relatively constant value (Peltzer [185]).

The formation of the laminar separation bubble at one side of the cylinder in the *ciritcal* flow regime and the resultant shift of the secondary, final separation of the turbulent boundary
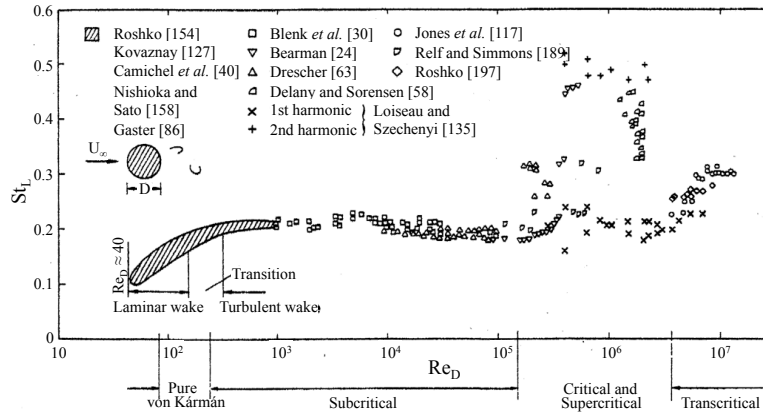
Figure 2.19: Variation of the Strouhal number St_L for a smooth circular cylinder in a steady cross-flow (Adapted from Naudascher and Rockwell [155]). The Strouhal number is computed with the main eddy shedding frequency in the power spectral density.

layer to $\varphi_S = 140°$ at that cylinder side introduce an asymmetric near wake (Figures 2.9 and 2.10(a)). The reduction of the spacing between both free shear layers leads to a sudden jump in the Strouhal number to $St_L = 0.32$. With the appearance of the LSB at the other cylinder side around $Re_D = 3.5 \times 10^5$, a second jump in the $St_L(Re_D)$ curve occurs to the high value of $St_L = 0.45$ to 0.5, upon which it remains at this value over a large part of the following *supercritical* flow regime. The extremely narrow near wake and the resultant proximity of both shear layers in this region result in a higher interaction rate between the two shear layers, which explains the high shedding frequency. Although the rate of interaction between both shear layers is high at these *supercritical* Reynolds numbers compared to the *subcritical* flow regime, the lowest values of the RMS of C_l and C_d in the *supercritical* flow regime (Figure 2.18) demonstrate that the strengths of the resultant vortices are low, being the result of the downstream displacement of the near wake.

The cross-over from the *supercritical* flow regime to the *upper transition* around $Re_D = 1.5 \times 10^6$ is characterised by another discontinuity in the $St_L(Re_D)$ curve and is caused by the step in the separation angle φ_S from 135° to 120° (Figure 2.15). In section 2.1.1, it has been mentioned, that in the *upper transition* ($1.5 \times 10^6 < Re_D < 4.5 \times 10^6$) the transformation of the flow field around the smooth circular cylinder from *supercritical* – with the presence of a separation bubble on each side of the cylinder over which the transition to turbulence occurs – to *transcritical* – where a "normal" laminar-turbulent transition takes place in the attached boundary layer – may develop asymmetrically between both cylinder sides. If this is the case, the asymmetry has then also an effect on the final separation location on the surface at both sides, which in turn affects the symmetry of the eddy formation in the near wake. In combination with the highly three-dimensional, irregular state of the turbulent free shear layers, their interaction is only weakly and partially. The result is an irregular eddy shedding throughout the complete *upper transition*, as well as a partial suppression of the regular eddy shedding process in the wake of the cylinder.

A highly regular eddy shedding marks the start of the *transcritical* flow regime. Constant, highly Reynolds-number-independent Strouhal numbers of $St_L = 0.25$–0.30 are obtained at these high Reynolds numbers.

2.1.3 Surface roughness and Reynolds number as alternating governing parameters

The previous section has demonstrated, that the flow around a smooth circular cylinder mainly depends on the locations of the laminar-turbulent transition and the primary (and secondary) separation of the laminar or turbulent boundary layer from the surface of the cylinder. Not only do they determine the instantaneous pressure distribution on the cylinder surface and thus the resultant mean and fluctuating lift and drag forces, they also characterise the size of the recirculation region adjacent to the cylinder base, the complete process of eddy formation and shedding taking place within this zone, and the flow pattern in the near- and far-wake. In case of a smooth circular cylinder in a steady laminar oncoming flow, the classification of the characteristic flow regimes, presented in section 2.1.1, clearly demonstrate the Reynolds number as the primary governing parameter. At the beginning of this chapter, the surface roughness has been designated as one of the various possible *influencing parameters* that can disturb the flow to a certain extent as well. The boundary layer thickness δ, in the case of a laminar boundary layer, is defined by Schlichting and Gersten [213] as

$$\frac{\delta_{lam}}{L_{ref}} = \mathcal{O}\big(Re^{-1/2}\big) \tag{2.6}$$

The influence of an intentionally applied or natural surface roughness on the flow around a circular cylinder now becomes evident. At a constant Reynolds number, an increase in surface roughness height will progressively intensify the perturbation of the boundary layer from the inside. Once the roughness height value lies in the vicinity of the boundary layer thickness, it is effective in triggering transition to turbulence, thereby altering the Reynolds number at which the transition takes place. At that moment it has thus become a governing parameter as well. The other way around, an increase in the Reynolds number leads to a gradual thinning of the laminar surface boundary layer (eq. (2.6)) on a circular cylinder with a fixed surface roughness texture. Hence, as soon as the boundary layer thickness approaches or subceeds the surface roughness height, the latter is once again a governing parameter. The advantage of a turbulent boundary layer is its more than twice as large thickness in comparison to its laminar counterpart at an equal Reynolds number

$$\frac{\delta_{turb}}{L_{ref}} = \mathcal{O}\big(Re^{-1/5}\big) \tag{2.7}$$

This means that a much higher surface roughness with respect to the thickness of the boundary layer is required before its influence on the laminar-turbulent transition and thus on the fluid dynamics of the circular cylinder becomes noticeable. Referring to section 1.3.1, this connection between boundary layer state – and resultant thickness – on the one hand and surface roughness height on the other is in particular important in case the latter is intentionally applied on a cylindrical structure for utilisation as a passive flow control method to reduce the vortex-induced vibrations by a delayed separation of the turbulent boundary layers from the surface in the perceived range of Reynolds numbers.

In no other industry sector has surface roughness and its influence on the flow over cylindrical structures been studied as intensively as in the offshore industry. The immersed foundation elements of offshore constructions like wind turbines or oil and gas drilling rigs are colonised over the years by a bright variety of marine fouling microorganisms (e.g. Forteath *et al.* [82], Langhamer *et al.* [129], Kerckhof *et al.* [123], Fitridge *et al.* [78]). Consequently, the flow around

these parts is steadily being altered during their lifetime. Although they actually function in this way as artificial reefs, bio colonisation has a number of effects on the hydrodynamic properties of the immerged slender structures that can eventually result in large economical and technical problems.

The settlement of biofouling leads, for example, to an increased structural diameter that not only induces larger mean and fluctuating lift and drag forces (Wolfram and Theophanatos [275]), but also increases both the actual structural weight and the hydrodynamic added mass. Combined, these phenomena can lead to a massive hydrodynamic overloading of the foundation of offshore platforms (Theophanatos [245], Jusoh and Wolfram [118], Schoefs and Boukinda [215], Shi et al. [219]). They can furthermore give rise to a considerable decrease of the tendon force on vertical taut mooring lines, resulting in the so-called slack tendon event, at which point a tendon loses all tension and undesirable snap loading can occur (Wright et al. [277]). Is the latter harmonic event present over a longer period of time, it drastically lowers the fatigue life of the mooring lines (Yang et al. [285]). The weight increase, in combination with the larger hydrodynamic added mass, furthermore lowers the natural frequency of the structure (Henry et al. [97], Jahjouh [113]). Once again particularly for mooring lines, with their relatively small diameters compared to the main columns of the floating structure, this can move their structural responses to resonance (Spraul et al. [237]). The added surface roughness also affects the mechanism of eddy formation, thereby increasing both the vortex strength and their spanwise coherence, thus giving rise to even higher regular lift forces (Wolfram [276]) which may lead to a further increase of the susceptibility towards vortex-induced vibrations.

The three main categories of marine growth that can be distinguished are hard growth (e.g. oysters, tubeworms, mussels), soft growth, like sponges, anemones, algae, sea-squirts, sea-weeds, and kelp growth, a long flapping weed (Langhamer et al. [129], Kerckhof et al. [123]) Special reference should also be made to the very detailed overview by Theophanatos [245]. One way of representing hard marine fouling in wind tunnel, water tunnel, or towing tank experiments is by covering the outer surfaces of the (scaled) structure with a roughness which is characterised through its non-dimensional equivalent sand-grain surface roughness k_s/L_{ref} (Adams et al. [7]). On a critical note, it must right away be pointed out as well, that Theophanatos [245] discussed in his Ph.D. thesis, that the characterisation of hard marine growth by a single parameter k/L_{ref} (or k_s/L_{ref}) is not the most suitable solution. His experiments have shown, that other parameters, like the limitation of roughness scaling to model sizes, the percentage of coverage, overall thickness and element size of the simulated fouling, the non-uniformity of the thickness, the axial distribution, and the orientation to the direction of the oncoming flow all have a large influence on the hydrodynamic loading and thus on the resultant fluid-structure interactions.

The influences of the texture, relative height, and/or location of the surface roughness on the fluid-dynamic behaviour of 2D circular cylinders in a steady cross-flow have been examined in numerous experimental and numerical studies, whereby the main emphasis was put on the dynamic loading experienced by those cylinders and the flow topology around them (Fage and Warsap [74], Achenbach [2], Batham [23], Szechenyi [239], Achenbach [3], Güven et al. [91], Achenbach and Heinecke [5] , Buresti [39], Nakamura and Tomonari [153], Basu [22], Niemann and Hölscher [156], Zdravkovich [293], Ribeiro [190], Bearman and Harvey [27], Shih et al. [218], Adachi [6], Yamagishi and Oki [281–283], Behara and Mittal [28]). However, in the majority of these well-documented fundamental studies, the applied surface roughness was in fact only used as a passive instrument to provoke a triggering of the laminar-turbulent transition in the surface boundary layer. In that way, it gave the authors the possibility to artificially simulate
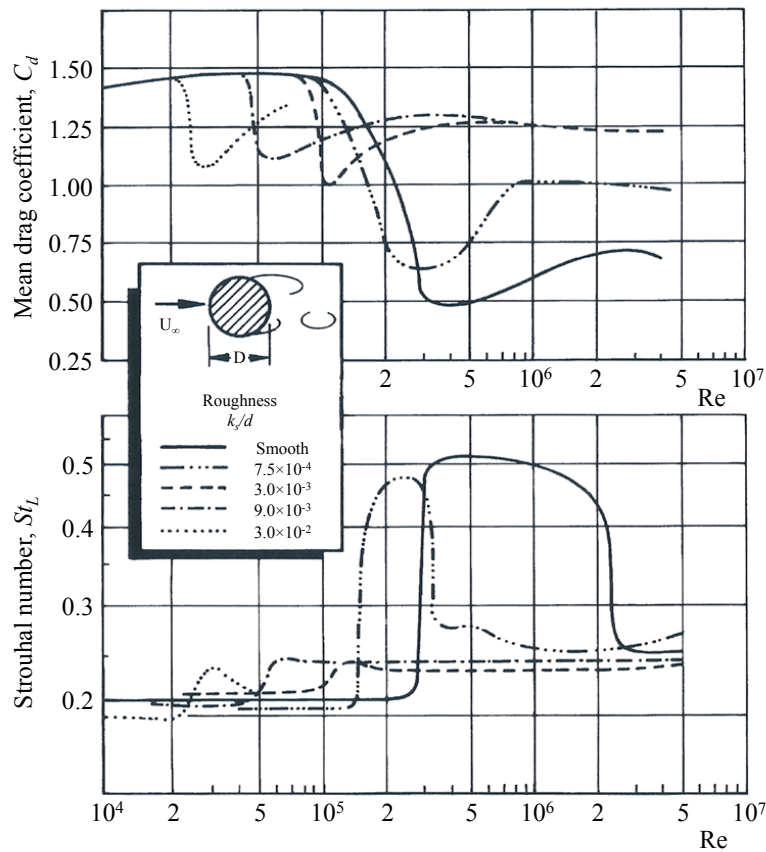
Figure 2.20: Effect of the surface roughness height on the mean cross-sectional drag coefficient (upper graph) and the Strouhal number (lower graph) as function of the Reynolds number for a circular cylinder in a steady cross-flow (Adapted from Achenbach and Heinecke [5]).

and investigate high-Reynolds-number flow phenomena at physically low Reynolds numbers in low-speed wind and water tunnel experiments.

Fage and Warsap [74] were one of the first to experimentally investigate how surface roughness influenced the drag on a circular cylinder. They observed that with increasing surface roughness height the occurrence of the *drag crisis* (paragraph 2.1.2.1) in the *critical* flow regime was progressively shifted to smaller Reynolds numbers. They attributed this phenomenon to the increased retardation of the boundary layer by the roughness elements that results in a forward motion of the separation points, as a consequence of which the drag of the cylinder is increased. By applying uniformly distributed dimples and grooves at the cylinder surface, Achenbach [2,3], Achenbach and Heinecke [5], Bearman and Harvey [27], Adachi [6], and Yamagishi and Oki [281–283] investigated the effect of those roughness elements on the flow behaviour over a circular cylinder up to the *supercritical / upper transition* flow regime. In most of these studies, the main focus was put on the change in the values of the mean drag force and the eddy shedding frequency. Their findings showed that also for circular cylinders with an increased surface roughness height the same characteristic flow regimes could be identified. Whereas the *subcritical* flow regime seemed to be unaffected by the roughness height, both the minimum value of the mean drag coefficient $C_{d,min}$ at the cross-over from the *critical* to the *supercritical* flow regime and the constant *transcritical* mean drag coefficient were both found to highly depend on the roughness conditions (Figure 2.20). For $k_s/D \geqslant 3 \times 10^{-3}$, the switching from one flow regime to another furthermore occured in a very short range of Reynolds numbers. They

attributed these changes to the behaviour of the boundary layer induced by the relocation of the transition and separation points on the cylinder surface. These trends were later confirmed in experimental wind tunnel studies by Buresti [39] and Niemann and Hölscher [156]. They furthermore observed that, compared to the results for a smooth cylinder, the length of the *critical*, *supercritical*, and *upper transition* flow regimes decreased with increasing roughness. In addition, the unstable and bistable flow states, which characterise the *critical* flow regime for smooth cylinders, disappeared for larger roughness heights.

Besides the mean drag coefficient, the eddy shedding frequency also shows a significant dependence not only on the Reynolds number, but also on the value of the surface roughness height. In their experimental data for five different values of k_s/D in the range of "smooth" up to "very rough" ($k_s/D = 3 \times 10^{-2}$), presented in Figure 2.20, Achenbach [2] and Achenbach and Heinecke [5] observed a strong decrease in the distance of the jump in the Strouhal number within the *critical* flow regime (Figure 2.20). At high roughness values, only a very weakly developed jump could still be identified without the cessation of the eddy shedding. The experiments performed by Buresti [39] shows an equal behaviour of both fluid-dynamic quantities. He observed a disappearance of the peak in the frequency spectra between the low values of the Strouhal number in the *subcritical* flow regime and high values in the *supercritical* flow regime for $3 \times 10^{-3} < k_s/D \leqslant 7 \times 10^{-3}$. No suppression of the shedding frequency was observed for $k_s/D = 1.2 \times 10^{-2}$, though.

Ribeiro [190] placed sand paper, wire mesh screens, or span-wise roughness stripes, the latter either at a single angular position or at multiple circumferential angles, on the cylinder surface to investigate "*which types of surface roughness are more efficient in triggering a transition of the flow so as to simulate the mean and fluctuating pressures occurring at ultra-critical Reynolds numbers*". He concluded, that, among those roughness elements, the use of ribs as a transition-triggering mechanism led to mean force and surface pressure coefficients that were the most comparable to those obtained for a smooth circular cylinder. Regarding the fluctuating parts of the force components, the ribs model was still the most favourable one, although the RMS values of the lift and drag forces were found to be higher than for the smooth counterpart in equal flow regimes. In a later numerical study by Behara and Mittal [28] a roughness element, similar to the ribs model by Ribeiro [190], was used to promote early transition of the boundary layer on the upper half of a smooth cylinder. It should be pointed out, however, that the three-dimensional flow domain in their simulations only covered one cylinder diameter in spanwise direction and was built up by 11 uniformly spaced sections of the two-dimensional mesh. To reach higher Reynolds numbers in their experiments, Fage and Warsap [74], Batham [23], Szechenyi [239], and Güven *et al.* [91] covered the complete cylinder surface with solid particles, like glass beads, or with large sheets of glass or sand paper. The data of all of these studies clearly show, that not only the (ir)regular texture and the relative height of the surface roughness, but also its location on the surface has a significant effect on the loading on circular cylinders, in particular in the *critical* and *supercritical* flow regimes.

2.2 Flows around prisms with sharp-edged square cross-sections

Whereas cylindrical bluff bodies with their continuous, finite surface curvature can be found at one outer boundary of the wide spectrum of possible cross-sectional shapes, prisms with square (or rectangular) cross-sections and sharp edges (hence, an "infinite" surface curvature) are positioned at the exact opposite outer boundary. Similar to the circular cylinder, the flow

topology around and the fluid-dynamic loading on this particular kind of prisms exhibit distinct characteristics with a variation of the Reynolds number. Hence, flows over two-dimensional square-section prisms are governed by the Reynolds number as well. In the following paragraph, it will be presented, that, in contrast to flows over circular cylinders, the governing influence of Re_D is limited to relatively low Reynolds numbers up to about $Re_D = 10^4$ only. This limitation results from the fixed location of the primary separation at the sharp leading edges of the prism at an incidence angle of $\alpha = 0°$ for higher Reynolds numbers, which has been demonstrated by the many different experimental and numerical studies by, among others, Delany and Sorensen [58], Vickery [263], Bearman and Trueman [25], Lee [130], Okajima [174], Norberg [159], Lyn *et al.* [143], Tamura and Miyagi [242], Dutta *et al.* [69], van Oudheusden *et al.* [260, 261], Huang *et al.* [106], and Huang and Lin [105].

Independent of the Reynolds number and in contrast to the circular cylinder flow, the stable separation of the wall boundary layer at the windward sharp edges of these prisms introduces an additional influencing flow parameter on their fluid-dynamic behaviour, namely the dependency on the orientation of the prism to the free-stream velocity vector, e.g. Delany and Sorensen [58], Polhamus [186], Bearman and Trueman [25], Lee [130], Norberg [159], Luo *et al.* [142], Dutta *et al.* [69], van Oudheusden *et al.* [260, 261], Huang *et al.* [106], and Huang and Lin [105], Yen and Yang [286], Carassale *et al.* [45], Sohankar *et al.* [233]. As has been mentioned at the beginning of this chapter, an influencing parameter can become a governing one once it has exceeded a certain lower threshold value. Regarding the angle of incidence of square-section prisms, no such lower threshold is present though. As soon as its value equals non-zero, the influence of α on the surface pressure distribution, the instability and development of the separated free shear layers, and the shedding process of the eddies is so pronounced that the incidence angle can be defined as an additional governing parameter. For Reynolds numbers above 10^4, it even becomes the sole governing parameter, as the former loses from that point on its governing influence on the fluid dynamics altogether.

2.2.1 Classification of the characteristic flow regimes based on sharp-edged square-section prisms

Based on extensive and detailed experimental and numerical investigations (see for example [20] and references therein) on the characteristic Reynolds-number-dependent trends of various flow parameters of square-section prisms with sharp edges at an incidence angle of $0°$, Bai et al. [20] distinguished between five main flow regimes.

The first one is named the *steady* flow regime and spreads up to $Re_D < 50$. Similar to the flow around circular cylinders for $5 < Re_D < 40$ (Figure 2.4), a closed near-wake region is formed behind the prism, in which two fixed, counter-rotating eddies are captured (Erturk and Gökçöl [71]). The formation of a Kármán vortex shedding street in the wake is therefore prevented. The streamwise length of the two-dimensional steady recirculation zone increases steadily from $L_r = 0.6D$ to $3.5D$ with growing Reynolds number (Figure 2.21). The value of the base pressure therefore becomes less negative, which results in a gradual decrease of the mean drag coefficient experienced by the prism (Figure 2.22).

The subsequent *laminar wake* regime exceeds from $Re_D = 50$ up to about $Re_D = 160$. It is characterised by an unsteady laminar flow over the cross-section plane of the square-section prism, a boundary layer separation from both trailing edges for $Re_D < 120$ and from both leading edges at $Re_D > 120$, an alternating roll-up of the free shear layers in the recirculation zone behind the prism, and a Kármán vortex shedding street in the wake. In addition, the eddy formation length in the near-wake region decreases rapidly from $L_f = 5D$ to $2.2D$ with
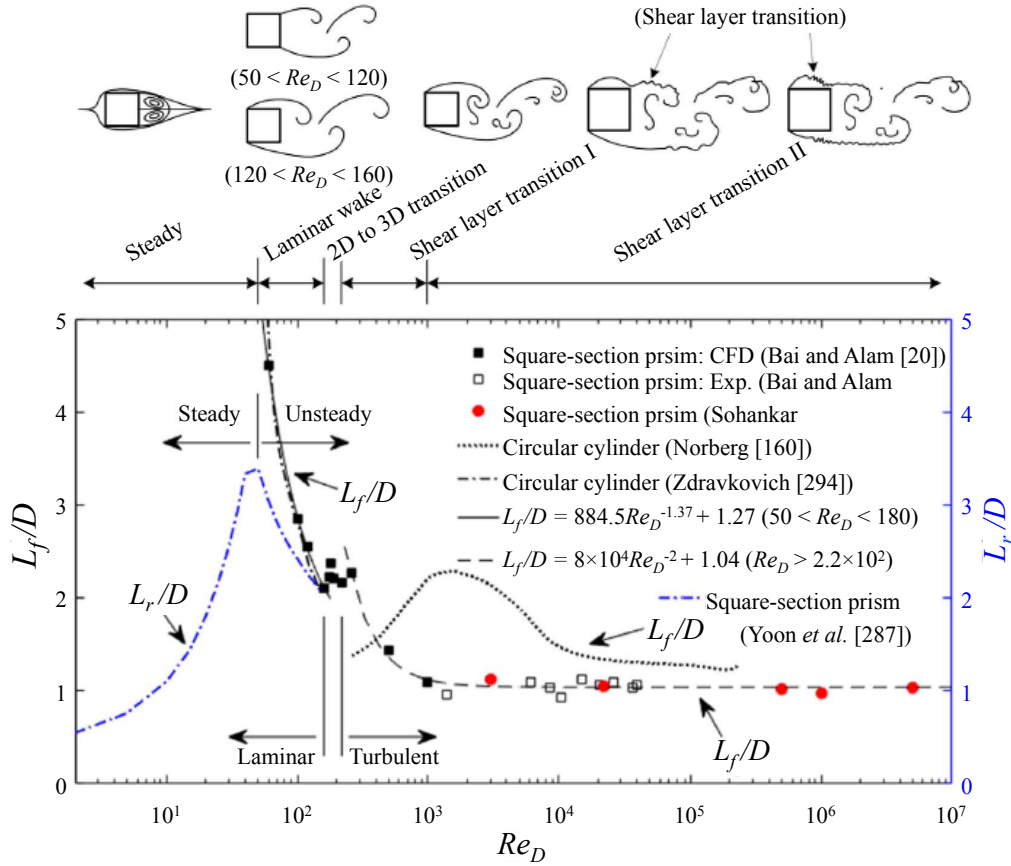
Figure 2.21: Variation of the eddy formation length L_f and streamwise length of steady recirculation zone L_r with Reynolds number for a square-section prism with sharp edges in a steady cross-flow (Adapted from Bai and Alam [20]).

increasing Reynolds number (Figure 2.21). The width of the near wake shrinks as well, but its decline is less vigorous, i.e. from $W = 1.5D$ to $0.95D$, and spread over the complete range of Reynolds numbers (Figure 2.23). The combined decrease of those two characteristic lengths leads to an increasing interaction between the eddies that are formed alternately on both sides of the prism in the base region, which is mirrored in the steady increase of the Strouhal number from $St_L = 0.11$ to 0.16 between $Re_D = 50$ and 160 (Figure 2.24). Meanwhile, the mean drag coefficient continues its steady decline in this *laminar wake* regime (Figure 2.22), driven by the decrease of the wake width W. At the same time, the coefficients of the fluctuating lift and drag forces experience both an exponential increase, whereby the former has a steeper rate than the latter (Sohankar [228]).

The appearance of spanwise instability modes A and B, the first on at the critical Reynolds number of about $Re_{D,cr1} = 160$ and the second one at $Re_{D,cr2} = 220$, mark the two boundaries of the following *two- to three-dimensional transition* flow regime (Robichaux *et al* [192], Sohankar *et al.* [236], Saha *et al.* [202], Luo *et al.* [138]). The transition from two- to three-dimensionality occurs in the near wake behind the prism. Streamwise vortices arise with spanwise wavelengths of around $5D$ in the mode A instability at $Re_{D,cr1}$ and of a reduced value of $1.2D$ in the mode B instability at $Re_{D,cr2}$. Luo *et al.* [138] confirmed a similarity between the vortical structures in the modes A and B for a square-section prism and a circular cylinder. They therefore concluded, that the instabilities are in both cases generated by similar mechanisms, although their appear-
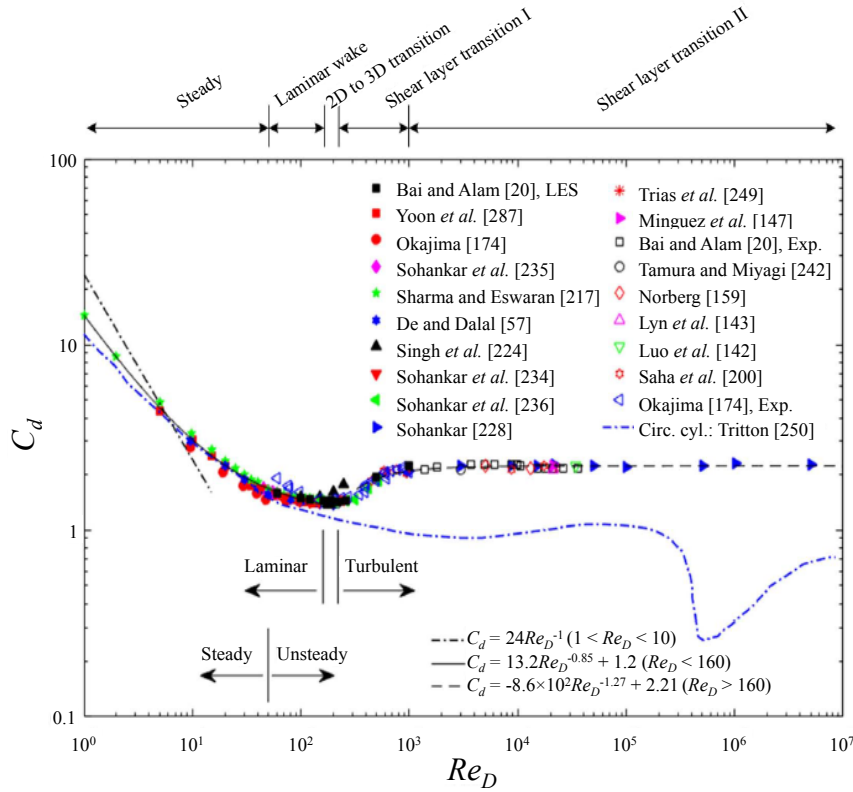
Figure 2.22: Dependence of the mean cross-sectional drag coefficient C_d on the Reynolds number for a square-section prism with sharp edges in a steady cross-flow (Adapted from Bai and Alam [20]).

ances occur at higher Reynolds numbers for a circular cylinder, as has been mentioned in the discussion on the *upper transition* and *lower transition* regimes (Zdravkovich [294]) in section 2.1.1. The eddy formation length remains constant at about $L_f = 2.2D$ (Figure 2.21), while the wake width and the mean drag coefficient both reach their minimum values of $W = 0.95D$ and $C_d = 1.4$ to 1.5 , see Figures 2.23 and 2.22, respectively. As a result, the Strouhal number tips at its maximum of $St_L = 0.14$–0.165 (Figure 2.24). In contrast, the exponential increase of the RMS values of C_l and C_d that started in the *laminar wake* regime remains unchanged (Sohankar [228]).

The occurrence of the instability mode B marks the cross-over to the *shear layer transition I* regime, which extends over a range of Reynolds numbers of $220 < Re_D < 1 \times 10^3$ (Okajima [174], Sohankar *et al.* [236], Saha *et al.* [200, 202], Luo *et al.* [138, 141]). At the beginning of this flow regime, the laminar-turbulent transition appears far downstream of the base surface of the prism at about $L_t = 2.2D$, where L_t is measured from the spanwise centre axis of the two-dimensional prism (Figure 2.25). Similar to what can be observed for a circular cylinder flow, the transition location progressively wanders with growing Reynolds number along the free shear layers in upstream direction in the direction of the boundary layer separation points on the surface of the prism (Figure 2.25). At $Re_D = 1 \times 10^3$, i.e. the upper boundary of the current flow regime, L_t has declined exponentially to a value of $0.5D$, indicating that the transition has reached the base surface of the prism. This induces an alternating reattachment of the free shear layers at the sharp trailing edges of the prism. The increase in C_d with Reynolds number from its absolute minimum at $Re_D = 220$ up to $C_d = 2.2$ at $Re_D = 1 \times 10^3$, clearly evident from Figure
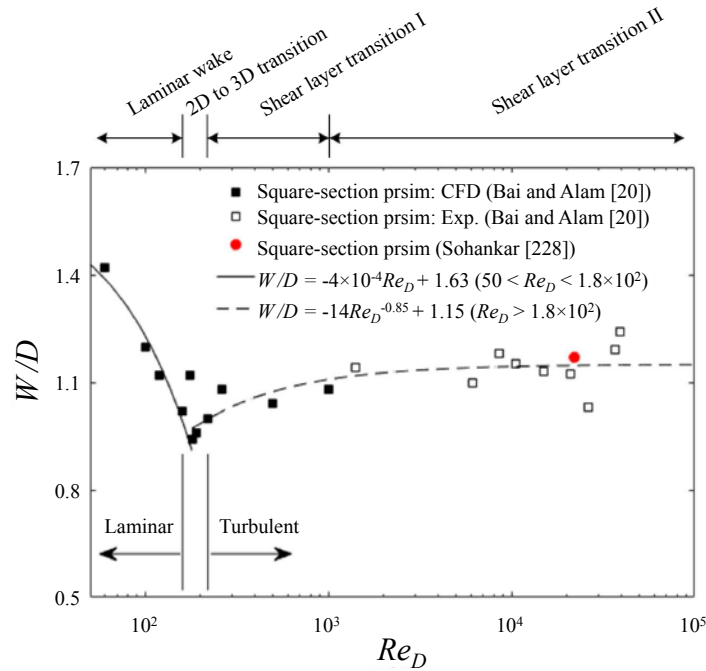
Figure 2.23: Effect of the Reynolds number on the width of the near wake W behind a square-section prism with sharp edges in a steady cross-flow (Adapted from Bai and Alam [20]).
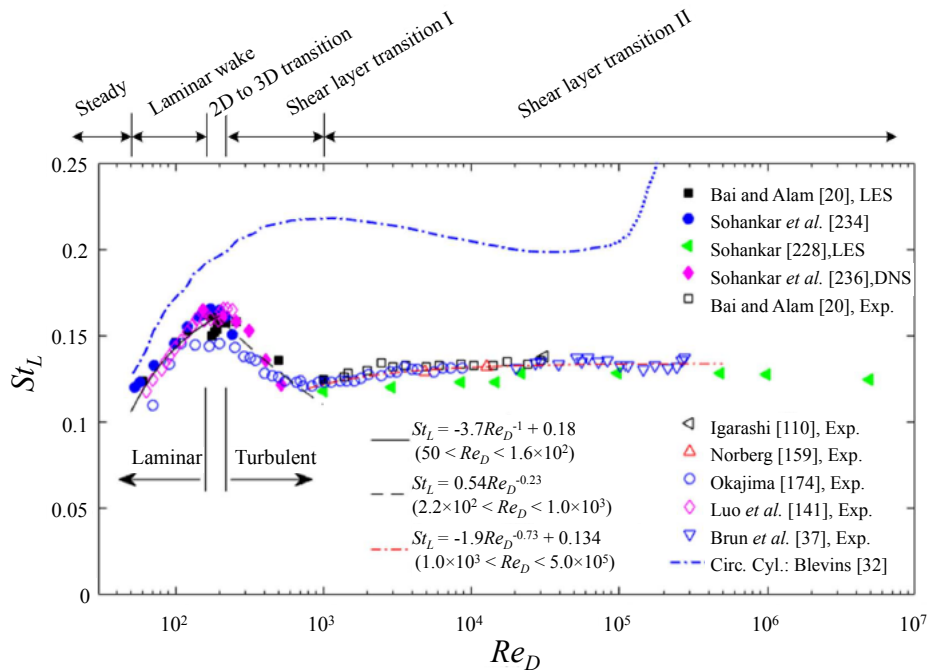
Figure 2.24: Variation of the Strouhal number St_L for a square-section prism with sharp edges in a steady cross-flow (Adapted from Bai and Alam [20]).

2.22, is a direct consequence of the combination of a progressive increase of W from 0.95D to 1.15D (Figure 2.23) and a sharp decrease of L_f towards a value of about 1D at the end of this flow regime (Figure 2.21). The continuous decrease of the Strouhal number from its maximum value in the range of $St_L = 0.14$ to 0.165 down to 0.13 at the upper boundary of the flow regime
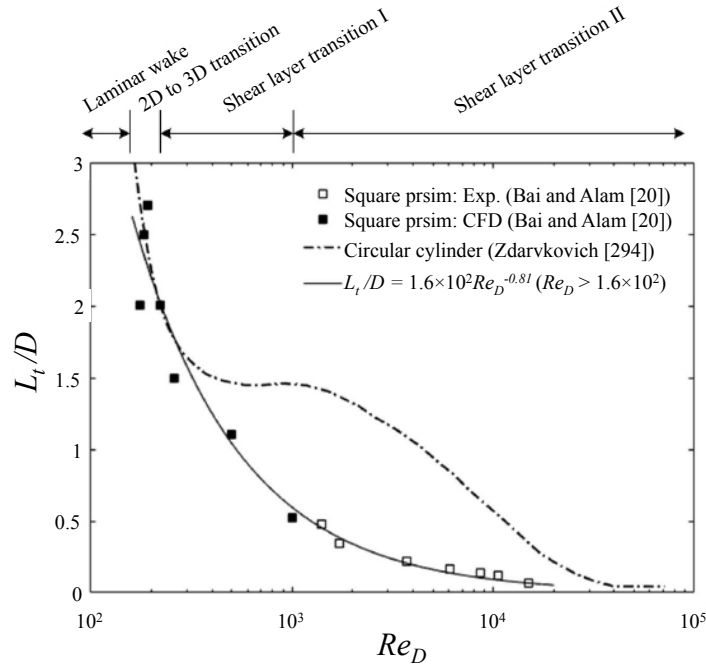
Figure 2.25: Variation of the laminar-turbulent transition location in the free shear layer L_t as function of the Reynolds number for a square-section prism with sharp edges in a steady cross-flow (Adapted from Bai and Alam [20]). L_t is defined as the streamwise distance between the spanwise centre axis of the prism and the transition location.

in Figure 2.24 is therefore apparent as well. The RMS values of C_l and C_d show in this flow regime the steepest increase, the former from $\sqrt{(\overline{C_l'^2})} = 0.2$ at $Re_D = 220$ to approximately 1.4 at $Re_D = 1 \times 10^3$, while the latter grows from about $\sqrt{(\overline{C_d'^2})} = 0.015$ to 0.23 (Sohankar [228]).

The final *shear layer transition II* regime exists for $Re_D > 10^3$. In this flow regime, the transition to turbulence occurs upstream of both sharp trailing edges ($L_t < 0.5D$) and is located in the first portion of the free shear layers above the side surfaces of the prism. This allows the free shear layers to reattach alternately on those side surfaces. The turbulent wake of the square-section prism is therefore fully developed. Figure 2.25 shows that, with increasing Reynolds number, the transition pursues its upstream shift in the direction of the primary separation locations of the boundary layer at both windward-directed sharp edges with increasing Reynolds number. In comparison to the *shear layer transition I* regime, the reduction rate of L_t slows down at $Re_D > 1 \times 10^3$ and approaches its asymptotic value of 0 at Reynolds numbers larger than 4×10^4. The decrease of the vortex formation length decelerates as well, upon which an asymptotic value of about $L_f = 1D$ is reached around $Re_D = 1 \times 10^4$ (Figure 2.21). At about the same Reynolds number, both W and C_d also attain approximately constant values, i.e. $W \approx 1.15D$ and $C_d \approx 2.2$ (Figures 2.23 and 2.22). The coefficient of the fluctuating lift reaches its maximum value of $\sqrt{(\overline{C_l'^2})} = 1.55$ to 1.60 around $Re_D = 1 \times 10^4$ and shows a subsequent slight decrease towards $Re_D = 5 \times 10^4$, before obtaining a relatively constant plateau at about 1.5 to 1.6. The magnitude of the oscillating part of the drag force has settled at $\sqrt{(\overline{C_d'^2})} = 0.23$ at the end of the *shear layer transition I* regime and remains unchanged throughout the *shear layer transition II* regime (Sohankar [228]). In the range $Re_D = 1.0 \times 10^3$ to 4.0×10^3, a slight recovery of the Strouhal number is seen to take place, be-

fore also this parameter reaches its constant value of $St_L \approx 0.13$, as shown in Figure 2.24. Since for $Re_D > 4 \times 10^4$ the various flow parameters have thus all reached approximately constant values, it can be argued, that the Reynolds number ceases to exist as being a governing parameter.

It is this last flow regime that has been extensively investigated in the last couple of decades, in particular for flows at intermediate Reynolds numbers of $\mathcal{O}(10^4)$ to $\mathcal{O}(10^5)$. Brun *et al.* [37] and Minguez *et al.* [147] carried out measurements with Laser Doppler Velocimetry (LDV) at $Re_D = 2 \times 10^4$ to 3×10^5 and $Re_D = 1.4 \times 10^4$, respectively, to analyse the fluctuating behaviour of the flow in the vicinity of the prism with square cross-section. The development of the coherent structures in the separated shear layer above the side surfaces of the prism, in particular the small-scale Kelvin-Helmholtz type vortical structures, and the large-scale von Kármán vortex street in the near wake were observed in detail. Accompanying Large Eddy Simulations (LES) at relatively low Reynolds numbers of $500 \leqslant Re_D \leqslant 2000$ were carried out by Brun *et al.* [37,38] to describe the Reynolds-number-dependent behaviour of these Kelvin-Helmholtz structures in the separated shear layers more precisely. Experiments on the variation of the eddy shedding frequency were performed by Okajima [174] in the Reynolds-number range of 70 to 2×10^4, whereas Durão *et al.* [68] conducted LDV measurements in a water tunnel at $Re_D = 1.4 \times 10^4$ to quantify the turbulent, hence random, and regular, non-turbulent motions of the near-wake flow. Lyn *et al.* [143] obtained the ensemble-averaged statistics at constant phase of the turbulent near-wake flow, the differences in the length and velocity scales of the flow in the base region on one hand and in the near wake on the other, and the characterisation of the vorticity saddles and streamline saddles at $Re_D = 2.14 \times 10^4$, using the LDV technique in a water tunnel as well. Based on these detailed reference studies, a large amount of research effort has been put into numerical simulations of the small- and large-scale flow structures at this specific Reynolds number of $Re_D = 2.2 \times 10^4$, using either high-order LES approaches by Minguez *et al.* [147] and Cao and Tamura [42], Direct Numerical Simulations (DNS) by Saha *et al.* [201] and Trias *et al.* [249], or by Reynolds Averaged Navier-Stokes (RANS) and hybrid LES/RANS simulations (e.g. by Ke [122]). Furthermore, the fluctuating and time- and phase-averaged characteristics of the flow structures in the base region and in the near and far wake, like the velocity distributions in flow and cross-flow direction, the various length scales of the eddy-formation region, the eddy shedding frequency, the two-dimensional distributions of the vorticity, turbulent kinetic energy and the Reynolds stresses, were reported for a wide range of Reynolds numbers of $Re_D = 1 \times 10^3$ to 5×10^6 using experimental techniques like Hot-Wire Anemometry (Saha *et al.* [200], Hacişevki and Teimourian [92], Bahrami and Hacişevki [19]), Particle Image Velocimetry (Hu *et al.* [104]), or a combination of those two measurement techniques (Bai and Alam [20]), or through numerical simulations based on DNS (Sohankar *et al.* [236]) or LES (Sohankar *et al.* [231], Sohankar [228], Li *et al.* [133]).

2.2.2 Incidence angle of the square-section prism as governing parameter

The majority of numerical and experimental studies on the effect of a variation of the incidence angle on the fluid dynamics of prisms with square cross-sections and sharp edges in cross-flow describes two main aspects. On the one hand, investigations have focussed on the loading on the prism at incidence, like the surface pressure distributions, the (resultant) mean and fluctuating lift and drag forces, and the shedding frequency of the eddies. The formation of the eddies and their shedding process in the near-wake region, as well as the characteristics of both the near and far wake, such as the topology and instantaneous and time- and phased-averaged

velocity distributions, were then again analysed by others.

Early measurements of the Strouhal number as function of the angle of incidence by Lee [130], Rockwell [193], Obasaju [168], and Knisely [126] show, that a minimum mean cross-sectional drag coefficient in combination with a sharp rise of the Strouhal number to its maximum value occurs around the critical angle of incidence. The latter was found to be located within a limited range of incidence angles of $\alpha = 13°$ to $17°$, its exact value being dependent on the free-stream turbulence level and the (low) Reynolds number (Lee [130] and Chen and Liu [47]). Both observed phenomena are related to a reattachment of the separated shear layer onto the downstream portion of the windward-directed side face close to its sharp trailing edge (Figure 2.26). This reattachment causes a strong pressure recovery on this side face (Chen and Liu [47]) that leads to a strong asymmetric flow field around the prismatic body. The resultant deflection of the shear layer induces the formation of a weaker eddy – in comparison to those formed at lower angles of incidence – in the base region. The negative base pressure reaches a lower value and the drag force on the prism reduces, while the eddy shedding frequency increases. These observations have later been confirmed by Dutta *et al.* [69] through wind tunnel

(a) $\alpha = 13°$ (b) $\alpha = 15°$

(c) $\alpha = 20°$ (d) $\alpha = 22.5°$
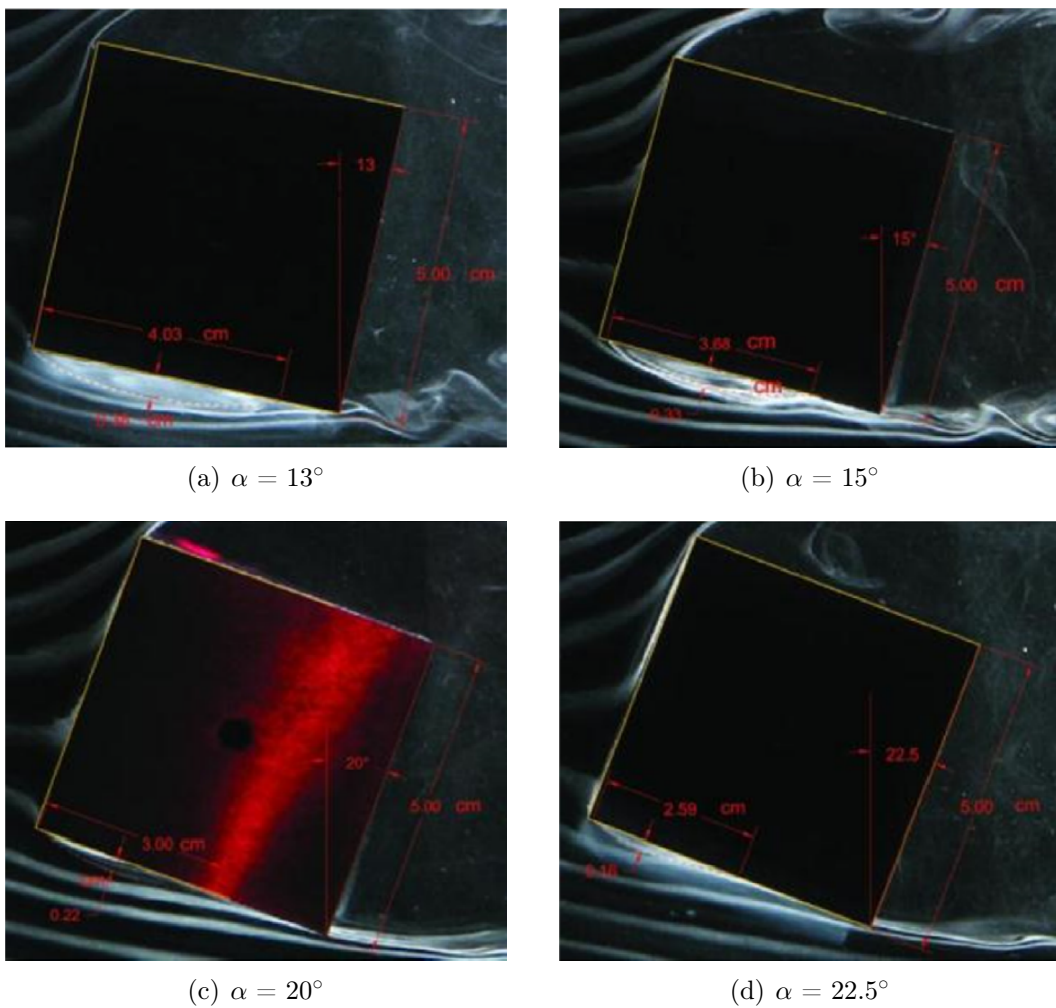
Figure 2.26: Visualisation of the change in size of the separation bubble on the windward-directed side face with increasing incidence angle ($13° \leqslant \alpha \leqslant 22.5°$) of a sharp-edged square-section prism in a steady cross-flow of $Re_D = 6776$ (Sohankar *et al.* [233]).

experiments on the flow topology around a square-section prism and the two component time-varying velocity in its wake for angles of incidence between 0° and 60° and Reynolds numbers of 1340, 4990, and 9980 by application of Hot-Wire anemometers and the smoke-wire visualisation technique. They concluded, that for $\alpha > 0°$ a downstream shift of the separation points and a widening of the wake in combination with a reduction of the eddy formation length take place. This leads then to a reduction of the mean cross-sectional drag coefficient and an increase in the Strouhal number. The eddy shedding frequency furthermore dominates the velocity spectrum.

By making use of the PIV-technique, the instantaneous vorticity, as well as its phased- and time-averaged values, the mean streamline pattern, and the two-dimensional distributions of the mean and fluctuating velocities in the near wake of a square prism in cross-flow have been resolved by Van Oudheusden *et al.* [260] for $\alpha = 0°$, 5°, 10°, and 15° and by Ozgoren [178] for $\alpha = 0°$ and 45°. Eddy-formation lengths in the base region were discussed, while Van Oudheusden *et al.* additionaly applied the Proper Orthogonal Decomposition (POD) technique to the instantaneous PIV-images to extract the characteristics of the coherent large-scale flow unsteadiness associated with the eddy shedding process and the effect of the angle of incidence upon it.

Igarashi [108] used a combination of the surface oil-flow visualisation technique and smoke visualisation to study the flow pattern around a sharp-edged square-section prism at angles of incidence of 0° to 45°. The Reynolds number was varied between $Re_D = 3.85 \times 10^3$ and 7.7×10^4, hence, all tests were performed in the *shear layer transition II* regime. Based on the smoke images and the trends of multiple aerodynamic parameters with increasing angle of incidence, his classification of the flow over the prism according to the incidence angle between $\alpha = 0°$ and 45° is the following:

(1.) *subcritical* or *perfect separated* flow regime for $\alpha < \alpha_{cr} = 12°$–15°. The forward boundary layer separation is in this flow regime pinpointed at both leading sharp edges of the prism. He divided this regime further into two subcategories:

(1a.) *symmetric flows* for $\alpha = 0°$ to 5° (Figures 2.27(a) and 2.27(b)), and

(1b.) *asymmetric flows* for 5° $< \alpha <$ 12° to 15° (Figures 2.27(c) and 2.27(d)).

Igarashi observed, that in the former subcategory the free shear layers, having separated from the two leading edges of the prism, "*rolled up, reattached on the rear face, passed around the trailing edge corners further, and then reattached on the side faces*". At those small incidence angles, a high symmetry in the flow around the prism, as well as in the mean and fluctuating pressures on the prism surface remains. In the latter subcategory, no such reattachment of the separated shear layer on the upper side face of the prism could be detected in the oil-flow-pattern images.

(2.) *reattachment* or *separation* flow regime, which extends from a lower bounding incidenc angle of about $\alpha = 12°$ to 15° up to the upper boundary of $\alpha = 35°$. It is characterised by the formation and subsequent gradual decrease in size of a recirculation bubble on the prism's side face exposed to the wind as a result of the one-sided reattachment of the free shear layer following its separation from the leading edge of this side face (Figure 2.26 and Figures 2.27(e) to 2.27(g)). The flow around the prism and the mean and fluctuating pressures on the prism faces are highly asymmetric.

(a) $\alpha = 0°$

(b) $\alpha = 5°$

(c) $\alpha = 10°$

(d) $\alpha = 15°$

(e) $\alpha = 20°$

(f) $\alpha = 25°$

(g) $\alpha = 30°$

(h) $\alpha = 45°$
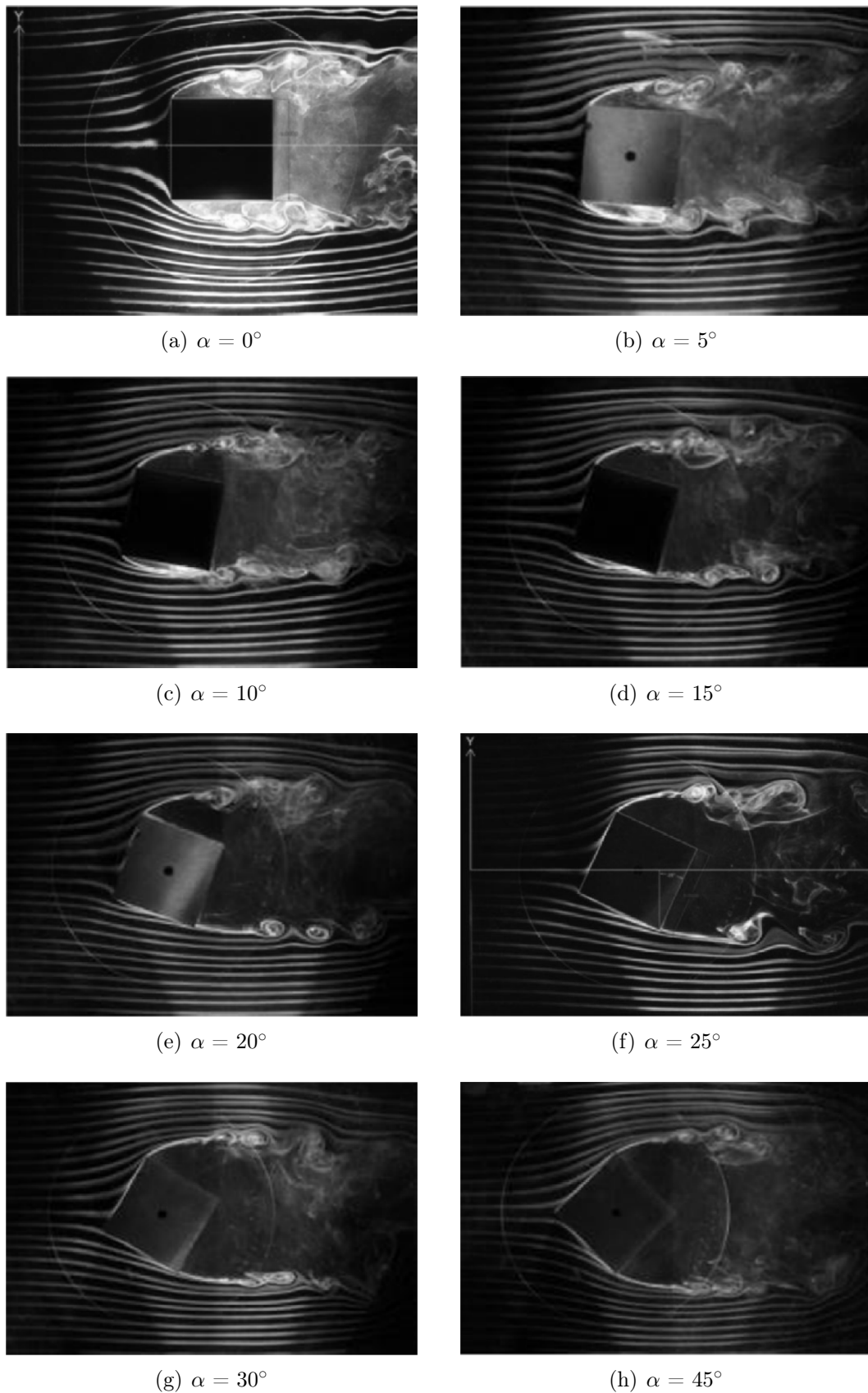
Figure 2.27: Visualisation of instantaneous flow patterns over a sharp-edged square-section prism at an angle of incidence between $\alpha = 0°$ and $45°$ in a steady cross-flow of $Re_D = 6776$ (Sohankar *et al.* [233]).

(3.) *wedge* or *attached* flow regime for $\alpha > 35°$, where an attached flow is present on both upstream-directed faces of the prism and the boundary layer primary separation occurs at their trailing edges. With increasing incidence angle towards 45°, symmetry in both the flow and the surface pressures is gradually restored (Figure 2.27(h)).

Huang *et al.* [106] and Yen and Yang [286] performed detailed studies on the flow behaviour on the four faces of a square prism in cross-flow and the flow characteristics around the prisms at angles of incidences from 0° to 45° within the *shear layer transition II* regime at Reynolds numbers of $Re_D = 1.3 \times 10^4$ to 9.4×10^4 and $Re_D = 4.0 \times 10^3$ to 3.6×10^4, respectively. The purpose of the wind tunnel tests was to study the physical mechanism occurring in the vicinity of the critical angle of incidence and the associated effects on the wake properties. Through a combination of the surface pressure distribution and several flow visualisation techniques to obtain the prominently different features of the topological flow patterns they could identify the same flow regimes as had been observed by Igarashi [108] three decades earlier. In addition, they could link the characteristics of the cross-sectional lift and drag coefficients, the Strouhal number, and the base pressure coefficient as function of the angle of incidence to the various flow regimes. In the *perfect separated* flow regime ($\alpha < \alpha_{cr}$) the fluctuating and mean cross-sectional lift coefficient (Figure 2.28(b)), the mean cross-sectional drag coefficient (Figure 2.28(a)), and the mean base pressure coefficient all possessed a negative slope and reached their minimum values around α_{cr}, whereas the Strouhal (Figure 2.29) and the longitudinal length of the eddy formation region both increased with increasing incidence angle and obtained their maximum values around the critical angle of incidence. This was followed by a steady increase of the fluid-dynamic coefficients, a moderate decrease of the Strouhal number, and only a small recovery of the eddy formation length in the *reattachment* or *separation bubble* flow regime, before each of them reached a relatively constant value in the *wedge* or *attached* flow regime (Norberg [159], Luo *et al.* [142], Chen and Liu [47], Tamura and Miyagi [242], Van Oudheusden *et al.* [261], Huang *et al.* [106], Yen and Yang [286], Carassale *et al.* [45]).

(a) Mean cross-sectional drag coefficient   (b) Mean cross-sectional lift coefficient
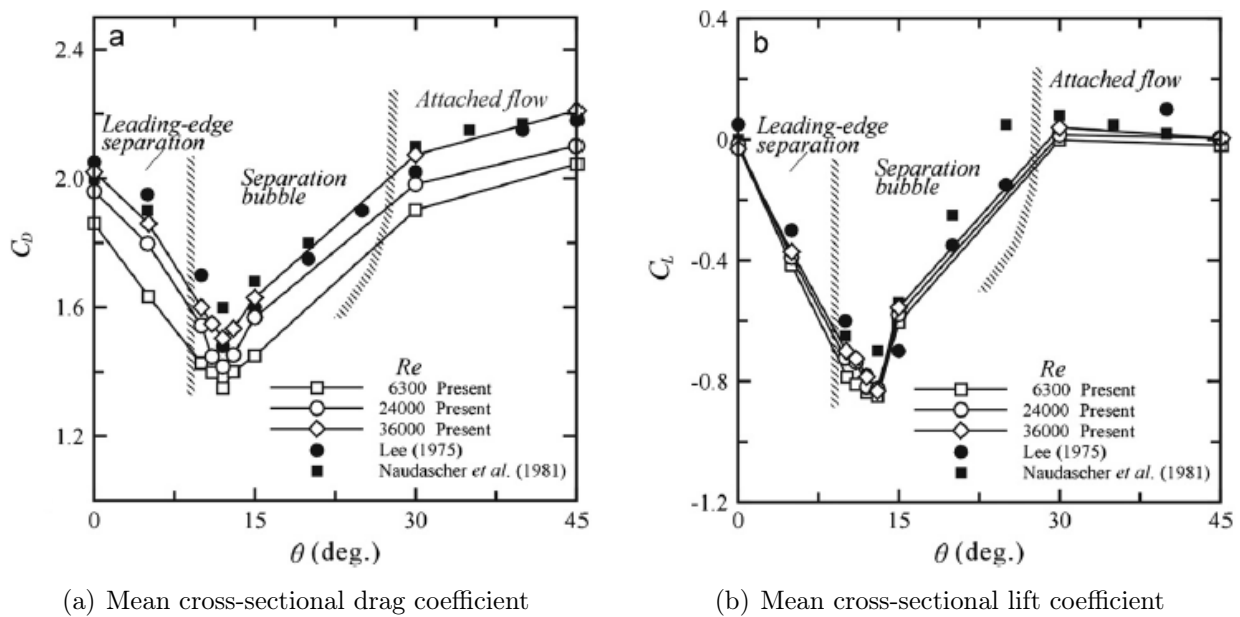
Figure 2.28: Effect of a variation in incidence angle between $0° \leqslant \alpha \leqslant 45°$ on the mean cross-sectional force coefficients of a sharp-edged square-section prism in a steady cross-flow (Yen and Yang [286]). *(a)*: mean cross-sectional drag coefficient; *(b)*: mean cross-sectional lift coefficient.
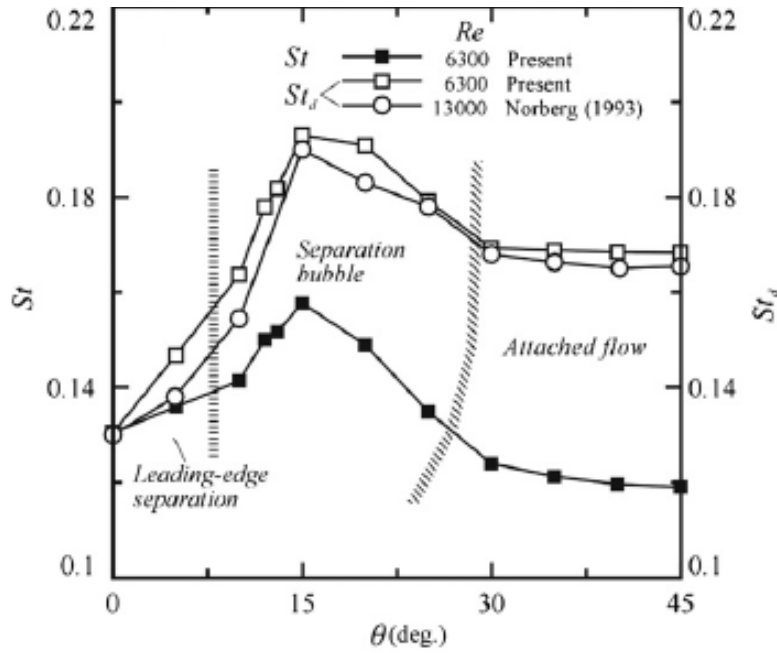
Figure 2.29: Variation of the Strouhal number ($St = (f_{s,L}L_{ref})/U_\infty$) and projected (hence, based on the frontal wetted area) Strouhal number ($St_d = (f_{s,L}L_{ref,proj})/U_\infty$) as function of the angle of incidence of a square-section prism with sharp edges in a steady cross-flow (Yen and Yang [286]).

2.3   Résumé Chapter 2

The aim of this chapter was to present in detail the fluid-dynamic properties of rigid, two-dimensional, stationary bluff bodies in a steady cross-flow. As cross-sections of those isolated structures, those two were selected which lie at the two opposite extremes of the whole spectrum of possible cross-sectional shapes: circular and square with sharp edges of $90°$.

The curved and smooth surface shape of circular cylinders allows a continuous meandering of the transition points, the primary boundary layer separation locations, and – if applicable – the reattachment points of the free shear layers and the secondary separation points on the surface of the cylinder. This introduces a flow over the cylinder which is therefore very sensitive to a variation in the Reynolds number. A change of Reynolds number from $Re_D \sim 0$ to its theoretically maximum value of $Re_D \to \infty$ causes the fluid dynamics of a smooth circular cylinder to pass through a total of nine different flow regimes, from the *creeping* or *Stokes flow* for extremely low Reynolds numbers of $Re_D < 5$ to the *transcritical flow* regime for high to ultra-high values of $Re_D > 4 \times 10^6$. Their properties are mainly determined by the local state, i.e. partially or fully laminar or turbulent, of the surface boundary layer and the free shear layers. This namely influences not only the position of the primary boundary layer separation, but also whether a reattachment of the free shear layers and a subsequent secondary separation occurs and at which angular positions on the surface they are located. The resultant surface pressure distribution and the extent of two- and three-dimensionality of the flow over the cylinder in the spanwise direction define the values of the mean and fluctuating loads on the cylinder, the size of the recirculation zone adjacent to the base of the cylinder in which the free shear layers alternatingly roll up on both sides of the cylinder and form eddies, the frequency with which these eddies are shed, and the flow topology of the near and far wake.

In contrast, the "infinitely curved" sharp edges of prisms with square cross-sections fixes the primary separation points at their windward-directed edges. Nevertheless, even for this type of bluff body, there is a variation of the flow over the prism with increasing Reynolds number at an angle of incidence of $\alpha = 0°$. Up to a Reynolds number of about 4×10^4, the fluid dynamics of sharp-edged square-section prisms goes through five different flow regimes. Above this value, however, all fluid-dynamic coefficients have reached approximately constant values at a constant incidence angle, so that from that point on the Reynolds number ceases to exist as a governing parameter. The angle of incidence – non-existent as an influencing parameter for flows over smooth circular cylinders – plays a major role in the mean and fluctuating loading on the prism, the shedding frequency of the eddies, and the flow topology around the prism and in its near and far wake. Between $\alpha = 0°$ and $45°$, four different "angle-based" flow regimes can be distinguished , in which the flow changes from symmetric at α $0°$ in the *subcritical* or *perfect separated* flow regime to highly asymmetric in the *reattachment* or *separation* flow regime ($\alpha_{cr} = 12°$–$15° \leqslant \alpha \leqslant 35°$) as a result of the occurrence of a recirculation bubble on the prism's side face exposed to the wind, and back to symmetric for $\alpha > 35°$ in the *wedge* or *attached* flow regime. Depending on its exact value in combination with the Reynolds number, the incidence angle behaves either as a pure influencing parameter, as an additional governing parameter besides the Reynolds number, or as the sole governing parameter when the Reynolds number is in the *shear layer transition II* regime, i.e. for $Re_D > \mathcal{O}(10^4)$.

Chapter 3

Cross-sectional edge roundness of isolated square-section prisms

In the previous chapter, the strong dependence of the flow over two-dimensional circular cylinders on the Reynolds number was presented. It was discussed, that the resultant mean and fluctuating forces on the cylinder, as well as the strengths of the eddies and the frequency with which they are shed from the cylinder therefore all show large variations with changing Reynolds number. At *subcritical* Reynolds numbers, for example, a circular cylinder experiences a high global mean drag force of about $C_D = 1.2$ and large force fluctuations in cross-flow direction of in the range of $\sqrt{(\overline{C_L'^2})} = 0.35$ to 0.45, the latter occurring with a low non-dimensional frequency of $St_L = 0.2$, though (Schewe [209]). In the *supercritical* flow regime exactly the opposite is found: the mean drag and fluctuating lift forces are low, $C_D = 0.2$ and $\sqrt{(\overline{C_L'^2})} = 0.02$, respectively, while the non-dimensional shedding frequency of the eddies has reached its maximum value of $St_L = 0.47$. Cylindrical constructions that are placed in a uniform flow with a constant velocity can be structurally optimised in such a way, that not only the best combination of mean and fluctuating loading and shedding periodicity is obtained, but also its proneness to vortex-induced vibrations is reduced to a minimum. In case of its placement in a flow with large velocity fluctuations, like in the earth boundary layer or in the ocean, such passive or active countermeasures as described in section 1.3 are mostly only partly effective, since they are commonly tuned on those flow velocity ranges that prevail over time.

For Reynolds numbers above $\mathcal{O}(10^4)$, prisms with square cross-sections and longitudinal sharp edges, placed in a steady cross-flow at $0°$ angle of incidence, possess constant fluid-dynamic parameters: a high global mean drag coefficient of $C_D = 2.15$ to 2.2, fluctuating lift and drag values of about 1.0 and 0.1 to 0.15, respectively, and a Strouhal number of 0.11 to 0.13. Their independence on the Reynolds number is in strong contrast to the distinct flow alteration they experience with changing angle of incidence, though. Similar to circular cylinders, they are susceptible to vortex-induced vibrations. However, as discussed in Chapter 1, they possess an additional proneness to self-excited translational or plunge *galloping*, a motion-induced vibration that has the potential of being much more harmful to the structure than VIV (see section 1.2.2) because of the linear increase of the vibration amplitude of limit cycle oscillation of the structure with growing reduced velocity, see section 1.2.2. Since VIV and *galloping* appear at completely different and thus fully separated ranges of the reduced velocity, a huge effort has to be invested to alter the internal and external structural properties of prismatic structures with sharp-edged square cross-sections in such a way that both classes of flow-induced vibrations are fully suppressed. Referring once again to oncoming flows with large velocity fluctuations,

the modification of the structure should therefore mainly focus on the prevention of *galloping*, thereby taking into account that vortex-induced vibrations may still occur occasionally.

The interesting question that naturally rises at this stage, is whether it is be possible to combine the positive fluid-dynamic effects of each of the two bluff bodies and eliminate (part of) the negative ones through an optimisation of the aero- or hydrodynamic structural design. Adding a finite roundness to the edges of non-circular cross-sections of prisms is nowadays a common means to lower not only their proneness to the aforementioned types of flow-induced vibrations, but also the experienced mean and fluctuating fluid-dynamic loads. Because this cross-section can be seen as transition geometry between the two extreme cases, it is evident that the behaviour of the flow around square-section prisms with rounded longitudinal edges is a combination of the flow over circular cylinders and sharp-edged square-section prisms, whereby the extent to which the edges are rounded plays an important role. Hence, contrary to the two latter cross-sectional shapes, an edge roundness introduces a flow dependence on both the Reynolds number and the angle of incidence.

Pioneering work in the field of flows over prismatic structures with rounded longitudinal edges was performed in the fifties of the last century by Delany and Sorensen [58] and Polhamus [186]. They presented wind tunnel data on the mean cross-sectional drag and lift coefficients, together with Strouhal numbers of two-dimensional cylindrical and prismatic bluff bodies, the latter with various cross-sectional shapes, for a wide range of Reynolds numbers up to 2×10^6. Regarding the square-section prism, they reported that an increase in the non-dimensional cross-sectional edge radius results in the appearance of the *critical* flow regime with its characteristic *drag crisis* and hysteresis effects, both well-known from studies on circular cylinders in cross-flow. In addition, their data show, that apart from the *transcritical* flow regime, the trend of the $C_D(Re_D)$ curve is similar to the one found for a circular cylinder. The *critical* flow regime, however, shifts to lower Reynolds number with increased r/D values, and particular in the *critical* and *supercritical* flow regimes a reduction of the mean cross-sectional drag coefficient can be observed. The latter phenomenon has at a later stage been confirmed for various flow regimes in an experimental and numerical study by Tamura *et al.* [241] ($r/D = 0$ and 0.167 at $Re_D = 10^4$ and 10^6) and through CFD simulations by Dalton and Zheng [54] ($r/D = 0.125$, $Re_D = 250$ and 1000). In addition, they demonstrated that this increase in the mean cross-sectional drag coefficient is accompanied by a shift of the fluctuating lift force to higher values, both of which they attributed to a decrease of the mean pressure in the near-wake region. They furthermore observed, that with increasing Reynolds number a narrowing of the wake behind the square-section prism takes place. Consequently, a better communication of the separated shear layers in the near wake occurs, giving rise to higher eddy shedding frequencies (Bokaian and Geoola [34], Hu *et al.* [104]). The data obtained through wind tunnel tests on square-section prisms by Carassale *et al.* [44, 45] revealed, that by increasing the edge radius the aerodynamic behaviour of these prisms can be strongly modified as a result of the promoted flow reattachment on the lateral faces. They observed an increase of the Strouhal number over the complete investigated range of incident angles of $0°$ to $45°$. An increase in Reynolds number in the *supercritical* flow regime for $Re_D \geqslant 1 \times 10^5$ results furthermore in a shrinkage of the separation bubbles at both side surfaces towards the leading edge and a recovery of the base pressure at $\alpha = 0°$. Tamura and Miyagi [242], Letchford and Mason [132], Carassale *et al.* [44, 45] all measured, that for higher free-stream turbulence levels a larger edge radius promotes the reattachment of the separated shear layers on the side surfaces even at an angle of incidence of $0°$.

The previous overview shows, that the emphasis of most studies has been placed on a proper determination of the edge roundness effect on the fluid dynamics of square-section prisms at low to moderate Reynolds numbers. To date, the investigations by Delany and Sorensen [58], Polhamus [186], and Tamura *et al.* [241] are the only ones in which the Reynolds number was increased up to values of $Re_D = \mathcal{O}(10^6)$. Hence, little attention has been directed to the range of Reynolds numbers above one to two million, i.e. covering the *supercritical* to *transcritical* flow regimes, which is actually quite surprising, as it is of considerable relevance to many applications in, for example, the marine, aeronautical, and civil engineering fields.

3.1 Effect of edge roundness of square-section prisms at $\alpha = 0°$ for Reynolds numbers up to 10^7

3.1.1 Experimental setup

Low-speed experiments at different pressure levels were conducted in the Göttinger-type High-Pressure wind tunnel facility (HDG) at the German Aerospace Center in Göttingen. The main purpose of this unique test facility is the realisation of maximum Reynolds numbers of $\mathcal{O}(10^7)$ in model-scale tests through a combination of an internal pressurisation of the HDG up to $p_0 = 10$ MPa and a variation of the free stream velocity in the range $4 \leqslant U_\infty \leqslant 35$ m/s (Försching [80], Försching *et al.* [81]). The closed test section has a square cross-section of 0.6×0.6 m^2 ($= 10 L_{ref} \times 10 L_{ref}$) and measures 1 m ($= 16.67 L_{ref}$) in length (Figure 3.1). It can be removed out of and put back into the wind tunnel by means of an airlock system, in that way allowing the modification or exchange of the model and instrumentation outside the wind tunnel without the need of de- and re-pressurisation of the tunnel itself. The relative dynamic pressure variation across the working section at the model's position is below 0.3%.

The properties of the studied smooth cylindrical and prismatic models are listed in Table 3.1. Each model was mounted horizontally in the test section and spanned its complete width from one side wall to the other, whereby both free model ends passed through the side walls of the test section (Figure 3.1). A labyrinth seal was used to minimise the amount of flow leakage through the small ring gaps between the model and the sidewalls. The time-dependent global lift and drag forces on the model, $L(t)$ and $D(t)$, respectively, were obtained by two rigid piezoelectric platform dynamometers, one at each model's end (Schewe [209]). In com-

Table 3.1: Structural properties of the investigated smooth cylindrical and prismatic wind tunnel models.

Parameter	Edge roundness, r/L_{ref}			
	0	0.16	0.29	0.50[†]
Material		stainless steel		
Length, L / m		0.6		
Reference length, L_{ref} (face width or diameter) / m		0.06		
Aspect ratio, AR		10		
Geometric blockage ratio at $\alpha = 0°$, L_{ref}/h_{test_sec} (%)		10		
Equivalent sand-grain surface roughness, k_s/L_{ref}	$40\pm4\times10^{-6}$	$4.5\pm0.7\times10^{-6}$	$4.5\pm0.7\times10^{-6}$	$\mathcal{O}(10^{-5})$
Natural frequency in lift direction, $f_{n,L}$ / Hz	340	298	298	–
Natural frequency in drag direction, $f_{n,D}$ / Hz	316	312	312	385

[†] data by Schewe [209].
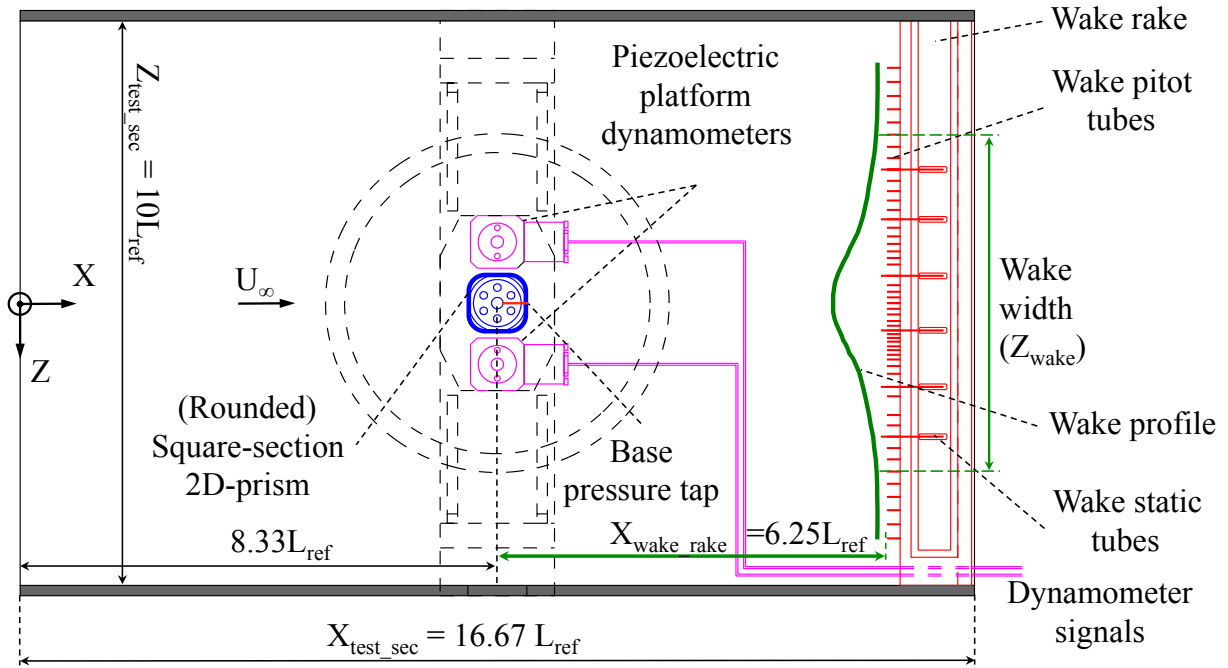
Figure 3.1: Experimental setup in the High-Pressure wind tunnel facility for isolated 2D-model tests: side view of test section with model, piezoelectric platform dynamometers, and wake rake (Adapted from Van Hinsberg [257]).

parison the balances based on strain gauges, the piezoelectric platform dynamometers have the huge advantage of a very high stiffness. Their resultant high natural frequencies in flow and cross-flow direction allow the measurement of high eddy shedding frequencies. The values of $L(t)$ and $D(t)$ were used to determine the global time-mean and fluctuating quantities of the lift and drag coefficients. A brief reminder to the reader, that all measured RMS values of C_L and C_D presented hereafter are based on the total spanwise length of the investigated bluff bodies, hence, $L = 0.6$ m. From the PSDs of the time series of the lift force, the main eddy shedding peaks and corresponding shedding frequencies were derived. A vertical pressure rake with 6 static pressure tubes and 52 Pitot pressure tubes was installed at $6.25 L_{ref}$ behind the model's spanwise centre axis to obtain the non-dimensional mean pressure loss in the near wake, as shown in Figure 3.1. This quantity is defined as $\Delta p = (p_0 - p_i)/q_\infty$, where p_i equals the total pressure at the tube location i $(= 1, 2,..., 51, 52)$ in the near wake. The shape of the curve was analysed to extract the qualitative measure of both the (a)symmetry of the wake flow with respect to the model's horizontal spanwise axis and of the width of the near wake at this location. The latter is defined as the distance between the two most outer Pitot pressure tubes for which the value of the non-dimensional pressure loss lies above the threshold of 4% of the maximum non-dimensional pressure loss, hence $\Delta p_{thr} = 0.04 \Delta p_{max}$.

The initial pressure level inside the wind tunnel of $p_0 = 0.35$ MPa was increased in seven steps with various increments ($\Delta p_0 = 500$ kPa, 1 MPa, and 2 MPa) up to the final pressure level of $p_0 = 10$ MPa. At each of these constant pressure levels, the flow velocity was increased from 4 m/s up to 34 m/s by increments of 1 m/s. In that way, the complete range of Reynolds numbers between 10^5 and 10^7 was covered. For the detailed investigation of the hysteresis in the fluid dynamics for increasing and decreasing Reynolds numbers that cover the transition

from the *subcritical* to *supercritical* flow regime and vice versa, the increments of the velocity were reduced to $\Delta U_\infty = 0.3$ m/s at a constant pressure level, which corresponds to a change in Reynolds number of about $\Delta Re_D = 1 \times 10^4$ for both increasing and decreasing Reynolds numbers. Per measurement point a constant integration time of $T = 30$ s was set for all recorded signals. The global aerodynamic forces were thereby scanned with a sampling frequency of $f_{scan} = 5$ kHz at a resolution of 16 bit.

3.1.2 Mean fluid-dynamic loads

Beginning with the mean fluid-dynamic loads, the distributions of the mean global drag coefficient C_D and the mean cross-sectional, hence local, base pressure coefficient at the mid-section of the prism C_{pb} with increasing Reynolds number are shown in Figure 3.2 for square-section prisms with edge roundness values r/D of 0, 0.16, and 0.29 at an incidence angle of $\alpha = 0°$. In addition, the global drag coefficients of a smooth circular cylinder, obtained by Schewe [209] in the same wind tunnel under equal boundary and flow conditions as listed in table 3.1, have been included in this figure for both comparison reasons and completeness.
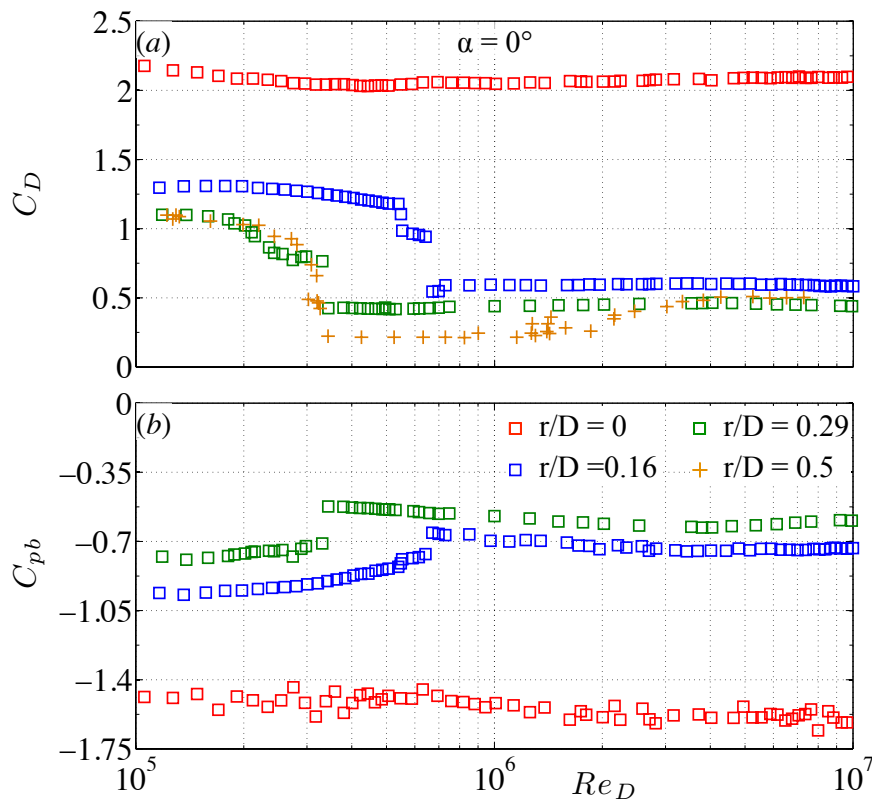
Figure 3.2: Effect of edge roundness r/D on the mean global drag coefficient (a) and mean cross-sectional base pressure coefficient (b) of a 2D square-section prism at $\alpha = 0°$ for Reynolds numbers in the range of 1×10^5 to 1×10^7 (Van Hinsberg *et al* [254], Van Hinsberg [258]). Reference: $+$ Schewe [209] ($r/D = 0.5$).

The direct comparison of the different curves in both graphs clearly shows that the trends and the values of the two mean aerodynamic coefficients are not only predominated through the Reynolds number, but in an equal manner also through the edge roundness value, the latter

thus clearly having changed from an influencing to a governing parameter. While the curve of C_D for the sharp-edged square section prism is characterised by a complete independency on the Reynolds number up to 10^7 (i.e. $C_D = 2.08\pm0.04$), a distinct variation in the drag coefficient with increasing Reynolds number is observed for the two square-section prisms with $r/D = 0.16$ and 0.29. Interestingly, both latter curves show a similar behaviour: relatively constant and high drag coefficient values in the *subcritical* flow regime, a clear *drag crisis* with a sharp drop in C_D in the *critical* flow regime, a discontinuous step at the cross-over from the *critical* to the *supercritical* flow regime, and a flat plateau at a low drag coefficient that reaches up to $Re_D = 10^7$. The absolute values of C_D, the Reynolds number at which the discontinuous step in C_D occurs, and the boundaries of the various flow regimes all steadily shift to significantly lower values with increasing edge roundness. In other words, the $C_D(Re_D)$ curve gradually approaches the curve of the circular cylinder for increasing r/D. For $r/D = 0.29$, even a clear overlap appears with the curve for $r/D = 0.5$ at low Reynolds numbers of $Re_D < 3\times10^5$ and at high Reynolds numbers above approximately 3 million. For $2\times10^5 < Re_D < 3\times10^5$ within the lower of those two ranges that are both bounded at one end only, the mean global drag that is experienced by the square prism with $r/D = 0.29$ is even slightly smaller than that one obtained for the circular cylinder. This means, that for $\alpha = 0°$ the effect of the edge radius on the global mean drag coefficient weakens the closer the cross-section of the prism resembles a circle.

For the three square-section prisms, the same, but inverted trend of the $C_{pb}(Re_D)$ curve with respect to the corresponding curve of the global mean drag coefficient is obtained at $\alpha = 0°$, as shown in Figure 3.2b. Furthermore, for both non-zero edge roundness values a discontinuous step in the mean base pressure coefficient appears at the cross-over from the *critical* to the *supercritical* flow regime; hence, at the exact same Reynolds numbers as for C_D in Figure 3.2a. This common behaviour of both aerodynamic coefficients is not really surprising, though, as a change in the (mean) base pressure alters the net (mean) pressure force that acts on the prism in flow direction. A higher suction at the base may thus lead to a larger mean drag force, whereas a decrease in the mean base pressure may induce a smaller mean drag force on the prism.

The variation of the global mean drag and cross-sectional mean base pressure coefficients with Reynolds number for the square-section prisms with edge roundness vales of $r/D = 0$, 0.16, and 0.29 are presented once more in Figure 3.3, together with the experimental and numerical drag coefficient and base pressure data from many reference studies on two-dimensional smooth square-section prisms with sharp and rounded edges and circular cylinders. The values of C_D of the sharp-edged square-section prism for the present investigation are in good agreement with the data of both Lee [130] and Letchford and Mason [132], but slightly higher than those of Li *et al.* [133] and Vickery [263] as well as lower than the numerical results by Sohankar [228]. The reference data for square-section prisms with non-dimensional edge radii close to zero – i.e. with $r/D = 0.021$ (Delany and Sorensen [58]) and $r/D = 0.0937$ to 0.011 (James and Vogel [115]) – are also found to be Reynolds-number independent and lie between $C_D = 1.86$ and 2.0 for $1.10\times10^5 \leqslant Re_D \leqslant 1.24\times10^6$. The previously described trend of the global mean drag coefficient with increasing non-dimensional edge roundness for the present investigation, presented in Figure 3.2a, fits well in the overall image that is obtained from Figure 3.3a. A near to perfect match is achieved between the present drag coefficient values for $r/D = 0.16$ and the data by Delany and Sorensen [58] for their square-section prism with edge radius of $r/D = 0.167$ for *subcritical* and low *supercritical* Reynolds numbers. The same holds for the value of the *critical* Reynolds number at about $Re_D = 6.4\times10^5$. Interestingly, an additional coverage exists with the
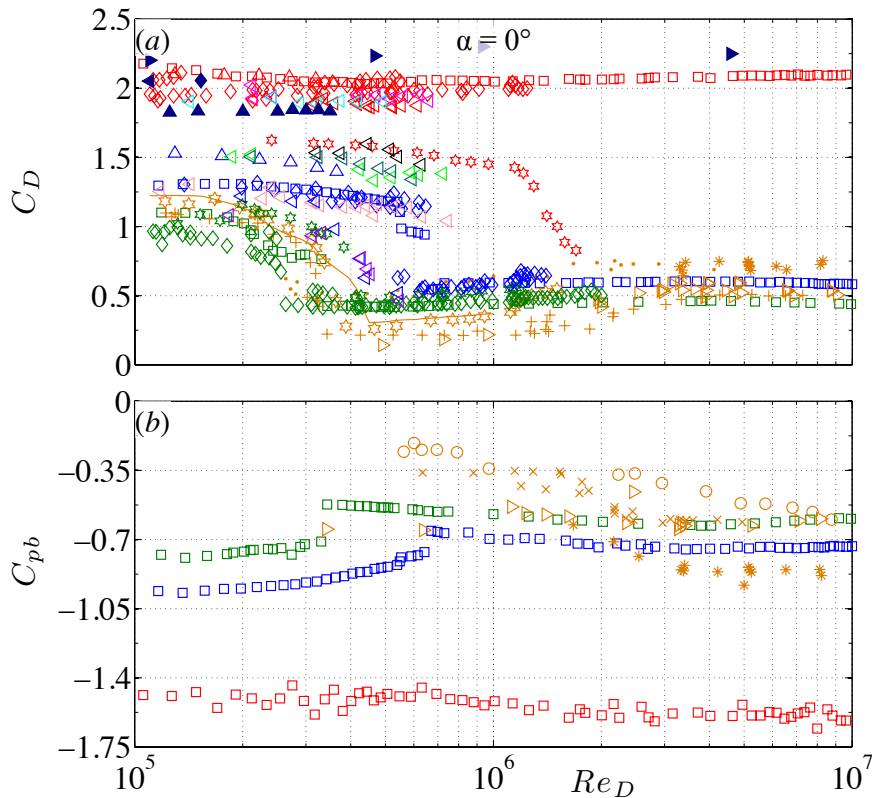
Figure 3.3: Dependence of the mean global drag coefficient (a) and mean cross-sectional base pressure coefficient (b) on the Reynolds number for 2D square-section prisms at $\alpha = 0°$ with edge roundness values between $r/D = 0$ (sharp-edged) and 0.5 (circular cylinder). Van Hinsberg *et al* [254] and Van Hinsberg [258]: □: $r/D = 0$; □: $r/D = 0.16$; □: $r/D = 0.29$. References: • Achenbach and Heinecke [5] ($r/D = 0.5$), ◇ Delany and Sorensen [58] (◇: $r/D = 0.021$; ◇: $r/D = 0.167$; ◇: $r/D = 0.333$), ◁ James and Vogel [115] (◁: $r/D = 0.00937$; ◁: $r/D = 0.0109$; ◁: $r/D = 0.011$; ◁: $r/D = 0.0625$; ◁: $r/D = 0.0729$; ◁: $r/D = 0.075$; ◁: $r/D = 0.125$; ◁: $r/D = 0.15$; ◁: $r/D = 0.1875$), ▷ Jones *et. al* [117] ($r/D = 0.5$), ◆ Lee [130] ($r/D = 0$), △ Letchford and Mason [132] (△: $r/D = 0$; △: $r/D = 0.12$), ▲ Li *et al.* [133] ($r/D = 0$), ★ Polhamus [186] (★: $r/D = 0.08$; ★: $r/D = 0.245$; ★: $r/D = 0.5$), ✳ Roshko [197] ($r/D = 0.5$), + Schewe [209] ($r/D = 0.5$), × Schmidt [214] ($r/D = 0.5$), ○ Shih *et al.* [218] ($r/D = 0.5$), ▶ Sohankar [228] ($r/D = 0$), ◀ Vickery [263] ($r/D = 0$), – Wieselberger [270] ($r/D = 0.5$).

drag curves of the square-section prisms with $r/D = 0.125$ and 0.15 by James and Vogel [115] for $Re_D \leqslant 5.25 \times 10^5$ and 3.18×10^5, respectively. The $C_D(Re_D)$ curves for $r/D = 0.245$ and $r/D = 0.333$ by Polhamus [186] and Delany and Sorensen [58], respectively, nicely enclose the mean drag coefficient of the present square-section prism with edges of $r/D = 0.29$.

At a given Reynolds number, the measured and simulated data in Figure 3.3a show a large variation with changing edge roundness. A prediction of the C_D value for a square-section prism with a certain edge roundness other than those presented by interpolation may therefore be not as accurate as desired, in particular in the *critical* flow regime in which the largest effect of r/D occurs. In conformity with the suggestion by Polhamus [186], an empirical factor of $(r/D)^{1.31}$ has been applied to the Reynolds number to force the *drag crisis* of the various curves to overlap, as shown in Figure 3.4. With the exception of the curves for the sharp-edged square-section prisms and circular cylinders, the curves for all edge roundness values between $r/D = 0$ and 0.5 show a rather good overlap of their *critical* flow regimes. The spreading of
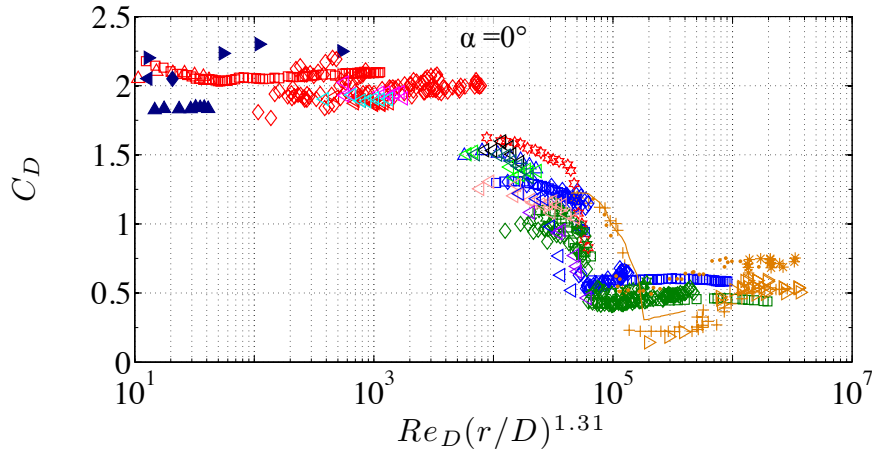
Figure 3.4: Effect of Reynolds number – based on edge roundness of $r/D = 0$ to 0.5 – on the mean global drag coefficient of 2D square-section prisms at $\alpha = 0°$. Van Hinsberg *et al* [254] and Van Hinsberg [258]: □: $r/D = 0$; □: $r/D = 0.16$; □: $r/D = 0.29$. References: • Achenbach and Heinecke [5] $(r/D = 0.5)$, ◇ Delany and Sorensen [58] (◇: $r/D = 0.021$; ◇: $r/D = 0.167$; ◇: $r/D = 0.333$), ◁ James and Vogel [115] (◁: $r/D = 0.00937$; ◁: $r/D = 0.0109$; ◁: $r/D = 0.011$; ◁: $r/D = 0.0625$; ◁: $r/D = 0.0729$; ◁: $r/D = 0.075$; ◁: $r/D = 0.125$; ◁: $r/D = 0.15$; ◁: $r/D = 0.1875$), ▷ Jones *et. al* [117] $(r/D = 0.5)$, ◆ Lee [130] $(r/D = 0)$, △ Letchford and Mason [132] (△: $r/D = 0$; △: $r/D = 0.12$), ▲ Li *et al.* [133] $(r/D = 0)$, ✷ Polhamus [186] (✷: $r/D = 0.08$; ✷: $r/D = 0.245$), ✳ Roshko [197] $(r/D = 0.5)$, + Schewe [209] $(r/D = 0.5)$, ▸ Sohankar [228] $(r/D = 0)$, ◂ Vickery [263] $(r/D = 0)$, – Wieselberger [270] $(r/D = 0.5)$.

the data, partly also at an equal prism's edge roundness value, results from the variation in the influencing parameters between the different reference studies. The graph shows that the value for C_D at any edge radius between sharp-edged and circular can be obtained with a rather good accuracy by vertical interpolation.

The high global mean drag coefficient of $C_D = 2.08 \pm 0.04$ (Figure 3.2a) for the sharp-edged prism is due to a combination of three phenomena: (*1*) the fixed separation of the laminar boundary layer on the prism's surface at both windward-directed sharp edges, (*2*) a distinct lateral spacing of the resultant free shear layers (presented, among others, in Luo *et al.* [142], Van Oudheusden *et al.* [260], Sohankar [228,233], Cao and Tamura [42], Bai and Alam [20], and Cao *et al.* [43] for various Reynolds numbers) that leads to an even larger effective aerodynamic blockage ratio than the geometric blockage ratio of 0.10 (Table 3.1), and (*3*) the relatively high negative cross-sectional base pressure coefficients of $C_{pb} = -1.50 \pm 0.06$ (Figure 3.2b). A clear indication for the occurrence of the second phenomenon is given by the wake width that is defined as the vertical distance in between those two points $Z_{1,2}/L_{ref}$ at which the total pressure decay along the wake rake equals 4% of the maximum occurring total pressure decay, hence $(p - p_0)/(p_{min} - p_0) = 0.04$ with p the static pressure at the locations $Z_{1,2}$, p_0 the total pressure, and p_{min} the minimum occurring static pressure at the specific Reynolds number. For the sharp-edged prism at $\alpha = 0°$, a large and constant value of the wake width of $Z/L_{ref} = 6$ is still present even at a distance of $5.75L_{ref}$ downstream of the prism's base surface, as shown in the Figures 3.5a and 3.5b. Polhamus [186] stated that the decrease of both C_D and the *critical* Reynolds number $Re_{D,cr}$, the latter marking the cross-over from the *critical* to the *supercritical* flow regime, is caused by the promotion of a smoother separation of the boundary layers as a result of an increased severity of the adverse pressure gradients along the rounded surface of
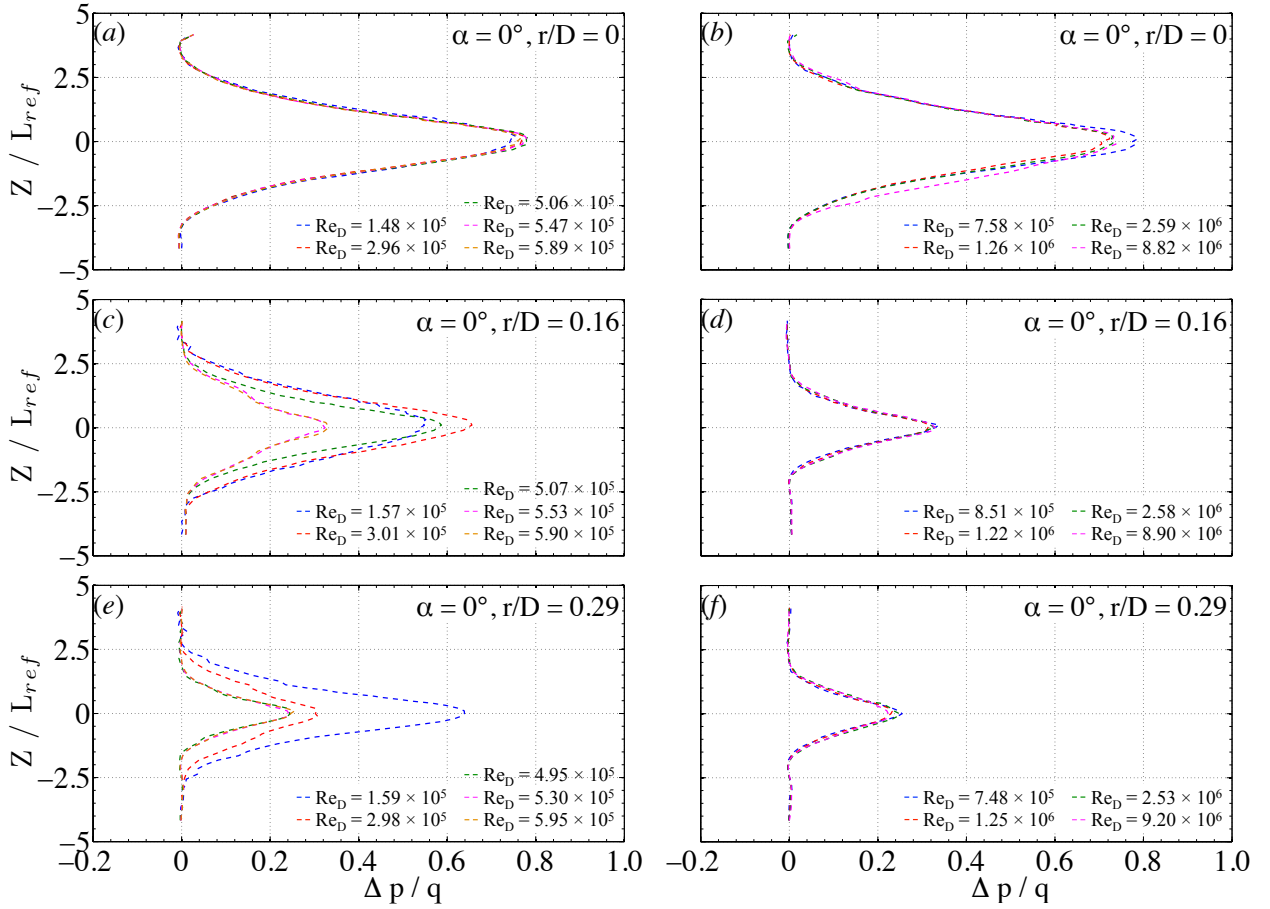
Figure 3.5: Effect of Reynolds number on the mean vertical wake profiles at $X/L_{ref} = 6.25$ behind the mid-span of two-dimensional square-section prisms at $\alpha = 0°$. (a)-(b): $r/D = 0$; (c)-(d): $r/D = 0.16$; (e)-(f): $r/D = 0.29$.

the prism for enlarged edge radii. This interpretation was later confirmed by Hu *et al.* [104] who studied the vortex behaviour in the near wake of square-section prisms with different edge radii in the range of $r/D = 0$ to 0.5 by using PIV and LDA. Although the Reynolds number in their test was much lower ($Re_D = 6000$) than in the study by Polhamus, they also observed that an increase in edge radius leads to a lower lateral movement of the separated shear layers and thus a weaker deflection of the streamlines along both side faces of the square-section prism. This is due to the continuously curved surface at the edges of the prism that allows – similar to the flow around circular cylinders – a downstream motion of the boundary layer separation location along both upwind rounded edges with increasing Reynolds number in the *critical* flow regime. This is confirmed by the wake profiles in Figure 3.5c to f for $r/D = 0.16$ and 0.29, for which a clear shrinkage of the near wake with growing edge radius is seen to take place for increasing Reynolds numbers from the *subcritical* to the *supercritical* flow regime. In combination with a progressive upstream wandering of the transition location along the free shear layers in the direction of the boundary layer separation points, a reattachment of the free shear layers at the two downstream rounded edges can occur at the *critical* Reynolds number. The subsequent secondary separation of the turbulent boundary layer at those two edges initiates a sharp decrease in the width of the near wake, as a result of which the negative value of the base pressure is lowered (Figure 3.2b). Owing to this decrease of C_{pb} for larger edge roundness values, the separated boundary layers are less rapidly immersed into the prism's base

region, i.e. a weaker interaction of the forming eddies takes place at the base. In combination with a lower spreading of the separated shear layers, this leads to a growth of both the eddy formation length and the wake closure length. A longer, but smaller near wake is thus formed, which then again results in a sharp reduction of the drag coefficient at the end of the *critical* flow regime (Hu *et al.* [104]). Since the positions of the primary and secondary separation on the surface of the prism are rather fixed in the subsequent *supercritical* flow regime, only minor variations in C_D, C_{pb}, the mean vertical wake profile, and the mean wake width occur within the *supercritical* flow regime.

3.1.3   Fluctuating fluid-dynamic loads

Figure 3.6a presents the variation of the coefficient of the global fluctuating lift, $\sqrt{(\overline{C_L'^2})}$, with Reynolds number for a 2D square-section prism with various edge roundness values ($r/D = 0$, 0.16, and 0.29) and for the 2D circular cylinder. Note once more that the presented RMS-values are based on the global forces that are obtained by integration along the complete span of the prisms and of the circular cylinder, i.e. $L = 10D$. Regarding both the trend of each curve with increasing Reynolds number and the overall trend of the RMS-values of the lift coefficient with respect to an increasing r/D-value, a very similar behaviour to the $C_D(Re_D)$ curves, presented
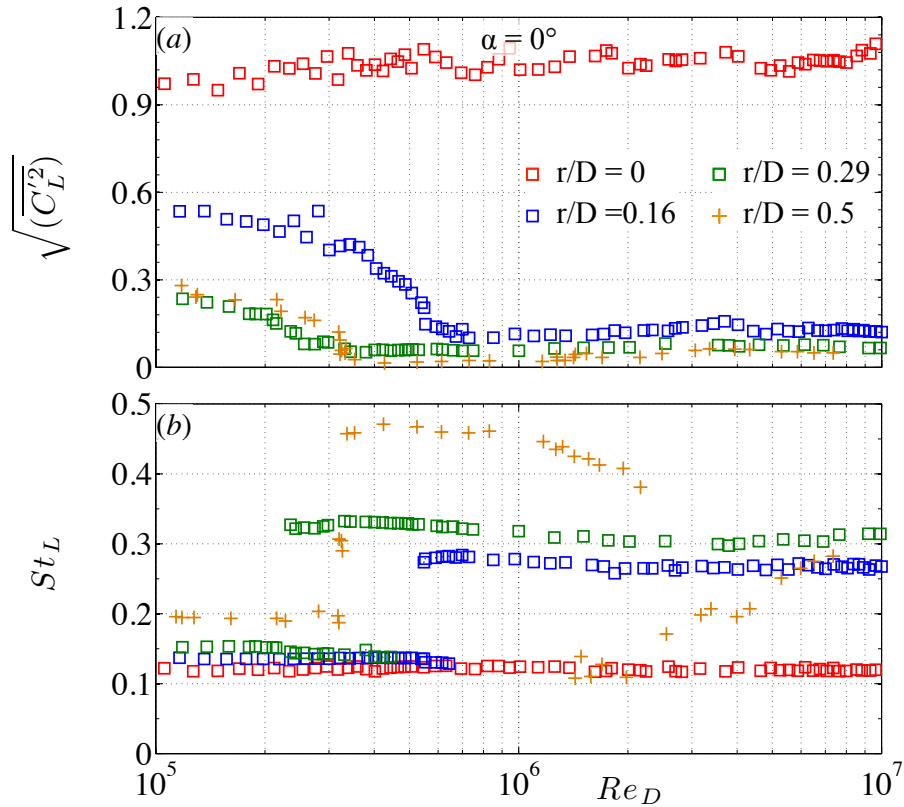
Figure 3.6: Effect of edge roundness r/D on the fluctuating global lift coefficient (a) and the lift-based Strouhal number (b) of a 2D square-section prism at $\alpha = 0°$ for Reynolds numbers in the range of 1×10^5 to 1×10^7 (Van Hinsberg *et al* [254], Van Hinsberg [258]). Reference: + Schewe [209] ($r/D = 0.5$). In case of the occurrence of two peaks in the power spectra at a Reynolds number, the more dominant Strouhal number is indicated by an open symbol, whereas a dot within the symbol belongs to the secondary peak.

in Figure 3.2a, can be identified. Hence, constant high values of the fluctuating lift at $r/D = 0$ and a decreasing trend with increasing edge roundness at an arbitrary fixed Reynolds number. For $r/D > 0$, each curve is characterised by a steady decrease within the *subcritical* and *critical* flow regime, that is followed by a plateau of low $\sqrt{(\overline{C_L'^2})}$ values at *supercritical* Reynolds numbers, being relatively strong Reynolds-number independent up to $Re_D = 10^7$ for $r/D = 0.16$ and 0.29. For the circular cylinder, a light increase in the fluctuating lift occurs in the *upper transition*, thereby reaching a second plateau with relatively constant values in the subsequent *transcritical* flow regime.

A comparison with experimental and numerical data from various references for two-dimensional sharp-edged square-section prisms and circular cylinders in Figure 3.7a shows two interesting points. Regarding the data for circular cylinders, a common behaviour with increasing Reynolds
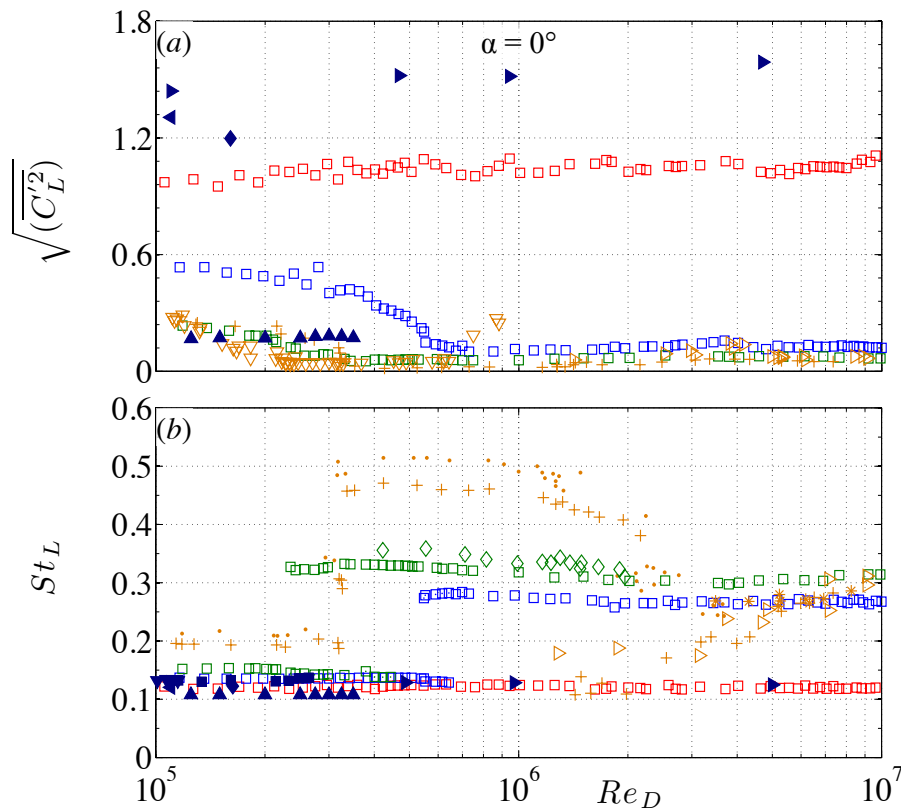
Figure 3.7: Dependence of the fluctuating global lift coefficient (a) and non-dimensional eddy shedding frequency (b) on the Reynolds number for 2D square-section prisms at $\alpha = 0°$ with edge roundness values between $r/D = 0$ (sharp-edged) and 0.5 (circular cylinder). Van Hinsberg *et al* [254] and Van Hinsberg [258]: □: $r/D = 0$; □: $r/D = 0.16$; □: $r/D = 0.29$. References: • Achenbach and Heinecke [5] ($r/D = 0.5$), ■ Brun *et al.* [37] ($r/D = 0$), ◇ Delany and Sorensen [58] ($r/D = 0.333$), ▾ Huang *et al.* [106] ($r/D = 0$), ▷ Jones *et. al* [117] ($r/D = 0.5$), ◆ Lee [130] ($r/D = 0$), ▲ Li *et al.* [133] ($r/D = 0$), ✳ Roshko [197] ($r/D = 0.5$), + Schewe [209] ($r/D = 0.5$), ▸ Sohankar [228] ($r/D = 0$), ◂ Vickery [263] ($r/D = 0$), ▽ Zan and Matsuda [289] ($r/D = 0.5$).

number is present; nonetheless, a non-negligible variation in the fluctuating lift can be observed at a given Reynolds number, which is in particular in the *critical* flow regime quite significant. Leading the attention to the data of sharp-edged square-section prisms, a very wide spreading can be observed. Most reference data show an overprediction of the fluctuating lift, except for

the data by Li *et al.* [133] that are as much as a factor 6 lower than the present values.

While the lift fluctuations can be seen as a measure of the intensity of the eddy shedding process in the direct wake behind the bluff body, the Strouhal number expresses the frequency at which those eddies are alternatingly formed and shed on the upper and lower surface of the body. Figure 3.6b shows the relation of the Strouhal number, St_L, with Reynolds number for the same four square-section prisms with edge values of $r/D = 0$, 0.16, 0.29, and 0.5. The presented Strouhal numbers are based on the main and, when applicable, also the secondary frequency peak in the PSDs of the time series of the lift $L(t)$, presented in Figure 3.8 for various Reynolds numbers from 1×10^5 to 1×10^7. For the sharp-edged prism, the location of the main peak of
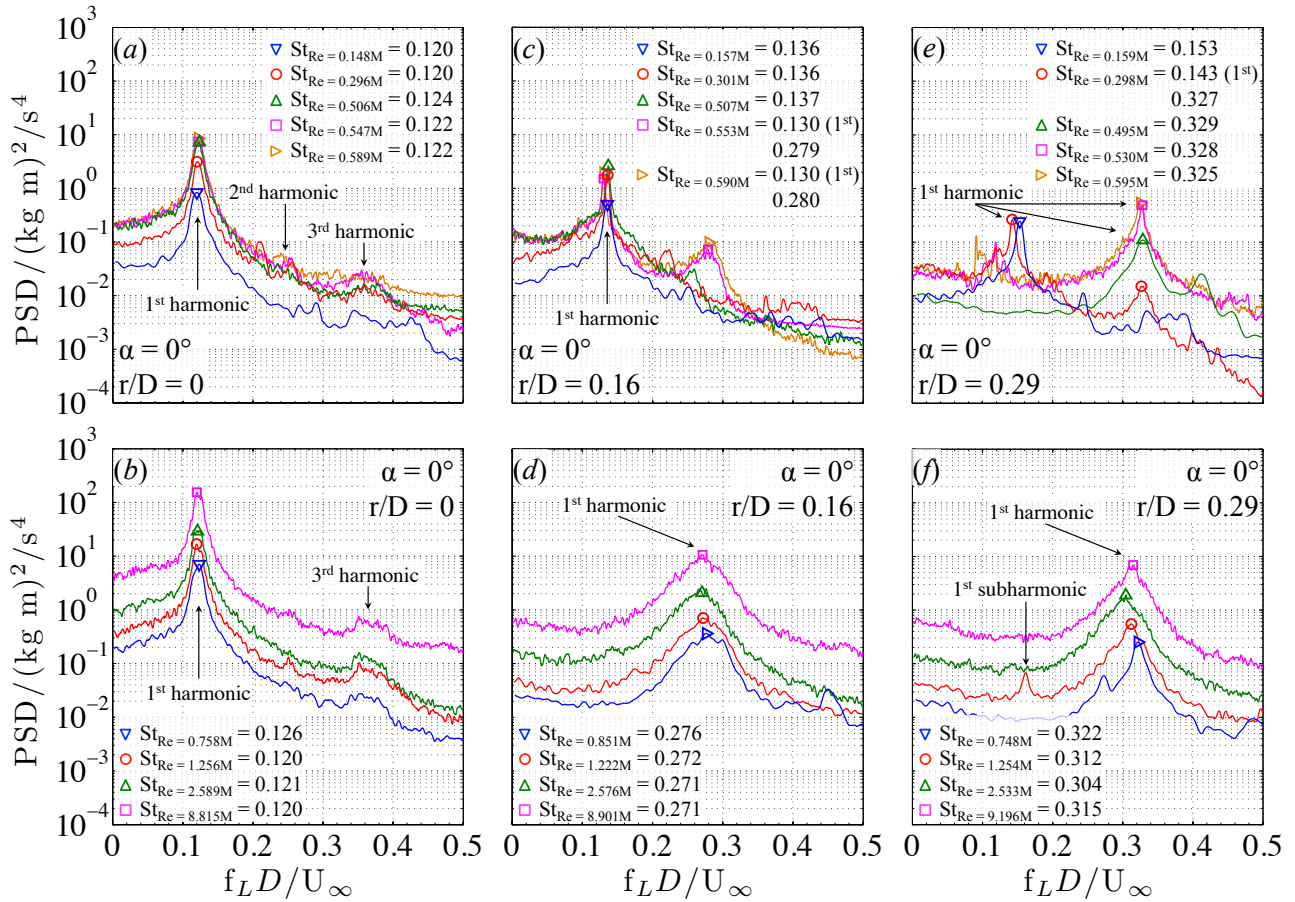
Figure 3.8: Power spectral density of the time series of the global lift force on two-dimensional square-section prisms at $\alpha = 0°$ at selected Reynolds numbers between 1×10^5 and 1×10^7. (a)-(b): $r/D = 0$; (c)-(d): $r/D = 0.16$; (e)-(f): $r/D = 0.29$. The corresponding Strouhal numbers are indicated by the symbols on the curves and the numbers inside each graph. In case of multiple occurring Strouhal numbers at equal Reynolds number, the dominant Strouhal number is indicated by (1st) and is followed by the Strouhal number of the secondary peak. M in the Reynolds number equals "million".

each power spectrum in the Figures 3.8a and 3.8b is found at $f_L D/U_\infty = St_L = 0.123 \pm 0.003$. Both this Reynolds-independent behaviour of the non-dimensional eddy-shedding frequency and the values of the Strouhal number agree well with data by other references in Figure 3.7b. With decreasing bluffness, i.e. larger r/D-values, of the prism, an increasing range in Strouhal numbers is covered within the Reynolds-number range of 10^5 to 10^7. The occurrence of only

three flow regimes for the square-section prisms with $r/D = 0.16$ and 0.29 becomes once more clearly visible in the corresponding $St_L(Re_D)$ curves. The *subcritical* flow regime is characterised by low Strouhal numbers, their values showing only weak changes with increasing r/D. The interesting phenomenon in the subsequent *critical* flow regime is the occurrence of two Strouhal numbers at one single Reynolds number: $St_L = 0.13$ and 0.28 for $r/D = 0.16$ and $St_L = 0.14$ and 0.32 to 0.33 (dependent on the exact Reynolds number) for $r/D = 0.29$. The Strouhal number that belongs to the higher and thus more dominant peak in each spectrum in Figure 3.8c to 3.8f is represented by an open symbol in Figure 3.6b, whereas the open symbols with an inner dot belong to the secondary peaks. Since the lower of the two occurring Strouhal numbers can be linked to the *subcritical* flow regime and the higher one to the *supercritical* flow regime, a clear indication is given that at those *critical* Reynolds numbers the flow around the prism jumps continuously back and forth between both flow regimes. Interestingly, for $r/D = 0.16$ the *subcritical* flow regime is the more dominant one of the two flow regimes, while for $r/D = 0.29$ the *supercritical* flow regime dominates. The alternating flow behaviour extends up to the end of the *critical* flow regime, at which a permanent cross-over to the *supercritical* flow regime takes place and the Strouhal number settles at a relatively flat *supercritical* plateau of $St_L = 0.31$ and 0.27 for $r/D = 0.16$ and 0.29, respectively. In good agreement with the general trend of the Strouhal number with increasing edge roundness, the latter value is slightly lower than those obtained by Delany and Sorensen [58] for their square-section prism with $r/D = 0.333$ at low *supercritical* Reynolds numbers. The most pronounced variation of the Strouhal number with Reynolds number is obtained for the circular cylinder, since all five flow regimes from *subcritical* to *transcritical* occur in the shown range of Reynolds number in Figure 3.6b. The trend of this curve has been described in detail by Schewe [209] and in paragraph 2.1.2.3. A comparison with data from other references in Figure 3.7b confirms the general trend, although a large scatter – being the result of different values for the various influencing parameters – is observed for $1 \times 10^6 < Re_D < 3 \times 10^6$ in the *upper transition*.

Durão *et al.* [68], Lyn *et al.* [143], and Van Oudheusden *et al.* [260] presented that the highest activity of the RMS of the horizontal and vertical velocity fluctuations in the flow field around sharp-edged square-section prisms at $\alpha = 0°$ occur along the separated shear layers and at the wake centreline just downstream of the four-way wake saddle point at which both wake division streamlines meet, respectively. As a consequence of the large-scale eddy shedding in the near wake, maximum velocity fluctuation levels as high as 60% for u_{rms}/U_∞ and 80% to 90% for v_{rms}/U_∞ were measured. These strong velocity fluctuations in cross-flow direction in the base region enhance the entrainment of fluid into the wake during the eddy formation process and cause large periodic changes in the lift force on the prism, e.g. $\sqrt{(\overline{C_L'^2})} = 1.02 \pm 0.07$ in Figure 3.6. This high value agrees well with the results obtained by Carassale *et al.* [45]. In addition, the large lateral spacing of the free shear layers promotes a strong interaction between the alternatingly shed eddies in the base region that leads to a low shedding frequency, i.e. low Strouhal numbers.

Because the parameter $\sqrt{(\overline{C_L'^2})}$ can be seen as a measure of the vigorousness of the eddy shedding process, it becomes clear that the major reduction in the fluctuating lift when varying the prism's cross-section from one extreme (hence, squared with sharp edges) to the other (i.e. circular) is associated with a much weaker interaction of each eddy with the base flow at the opposite base side from which it has separated, as well as the interaction between each two subsequent counter-rotating eddies. This is also the cause for the increase in the eddy shedding frequency for larger edge roundness values at equal Reynolds numbers. The latter is consistent with the experimental data by Tamura and Miyagi [242] and Hu *et al.* [104] for

steady prisms and by Ajith Kumar *et al.* [11] for transversely oscillating prisms. Although the investigated Reynolds numbers in these references are much lower, i.e. $\mathcal{O}(10^3)$ to $\mathcal{O}(10^4)$, the relation between the edge radius and the Strouhal number is identical, owing to which it is arguable that similar underlying physical phenomena in the flow are responsible.

3.2 Effect of edge roundness of square-section prisms at $\alpha = 45°$ for Reynolds numbers up to 10^7

This section deals with the influence of the edge roundness of two-dimensional smooth square-section prisms positioned at the second "symmetric" incidence angle of 45°. Besides the mean and fluctuating fluid-dynamic loading on those bluff bodies and the non-dimensional eddy-shedding frequency in their near wake for the equal range of Reynolds numbers as in the previous section for $\alpha = 0°$, a detailed analysis of the flow behaviour in the *critical* flow regime is presented. It is shown, that within this flow regime not only circular cylinders possess an asymmetry in the surrounding flow field with a distinct non-zero lift force, but that a similar fluid-dynamic behaviour also appears for square-section prisms when rounding their longitudinal edges. The same counts for the hysteresis effects that become visible for increasing or decreasing *critical* Reynolds numbers.

3.2.1 Mean fluid-dynamic loads

In comparison to $\alpha = 0°$, the square-section prism with sharp edges experiences at $\alpha = 45$ merely a 6% higher global mean drag (Figure 3.9a). Apparently, the large increase in the geometric blockage ratio from $L_{ref}/h_{test\_sec} = 10\%$ at $\alpha = 0°$ to 14.5% at $\alpha = 45°$ is to a great extent compensated by the change of the flow field around the prism. After separation of the surface boundary layer from the upper and lower edge of the prism, the shear layers experience a wide spreading in cross-flow direction (e.g. Dutta *et al.* [69], Ozgoren [178], Huang *et al.* [106], Yen and Yang [286], Sohankar *et al.* [233]) that induces an even larger effective aerodynamic blockage ratio and larger eddies in the near wake than at $\alpha = 0°$ (Huang *et al.* [106], Yen and Yang [286]). The data by Huang *et al.* [106] reveal that for $Re_D \leqslant 7.7 \times 10^4$ the wake width at a distance of about $0.5 L_{ref}$ downstream of their sharp-edged prism is $1.25D$ and $1.67D$ for $\alpha = 0°$ and 45°, respectively. Using the smoke visualisation technique in their wind tunnel experiments, Sohankar *et al.* [233] obtained similar values at $D/4$ downstream of their sharp-edged prism for Reynolds numbers between 6.8×10^3 and 8.2×10^3. Interestingly, at a location of $X/L_{ref} = 6.25$ behind the mid-span of the present sharp-edged square-section prism this difference in lateral spreading of the free shear layers between both incidence angles no longer exists, as the equal mean vertical wake profiles at $\alpha = 0°$ (Figures 3.5a and 3.5b) and 45° (Figures 3.10a and 3.10b) clearly demonstrate. Figure 3.9b presents the behaviour of the coefficient of the suction force at the base of the prism with varying Reynolds number for 45° angle of incidence. With a constant mean value of $C_{pb} = -1.19$ for $Re_D = 1 \times 10^5$ to 1×10^7, it has reduced by as much as 21% compared to $\alpha = 0°$. It can thus be pinpointed as being primarily responsible for the compensation of the large effective aerodynamic blockage ratio and thus the merely small rise of C_D.

With increasing edge roundness, the mean global drag coefficient progressively approaches the values for circular cylinders. Contrary to their counterparts at $\alpha = 0°$, the shapes of both $C_D(Re_D)$ curves for $r/D = 0.16$ and 0.29 possess a limited *supercritical* flow regime that is subsequently followed by an *upper transition* and a left-bounded *transcritical* flow regime, the
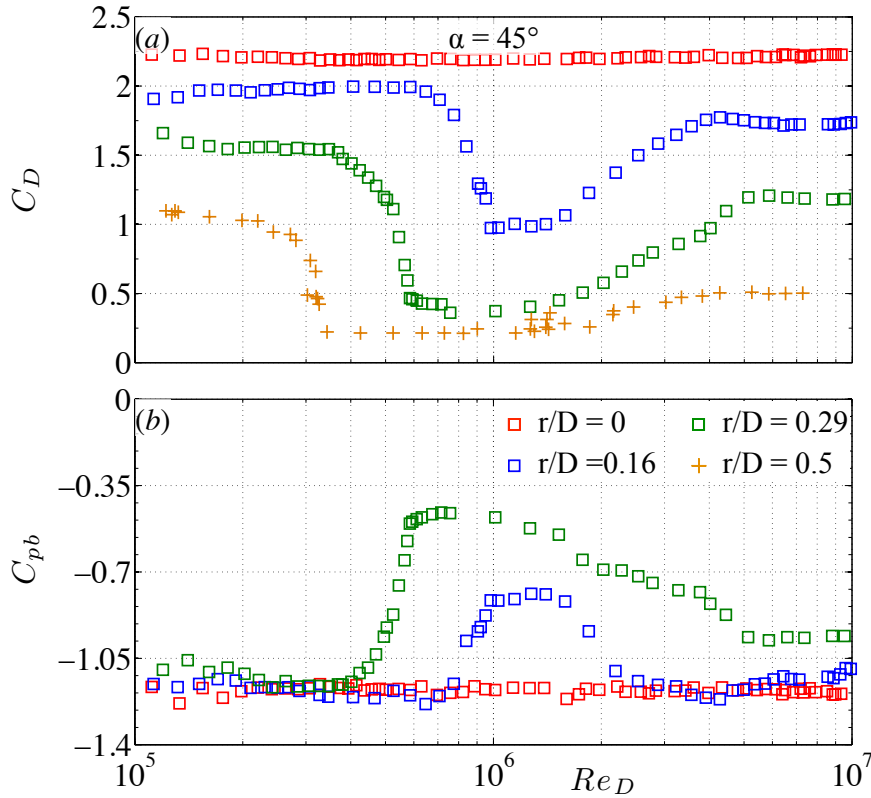
Figure 3.9: Effect of edge roundness r/D on the mean global drag coefficient (a) and mean cross-sectional base pressure coefficient (b) of a 2D square-section prism at $\alpha = 45°$ for Reynolds numbers in the range of 1×10^5 to 1×10^7 (Van Hinsberg et al [254], Van Hinsberg [258]). Reference: $+$ Schewe [209] ($r/D = 0.5$).

last one characterised by constant high values of C_D that have approached the *subcritical* level.

The main reason behind this different shapes of the $C_D(Re_D)$ curves between $\alpha = 0°$ and $45°$ is the change in the position on the rounded edges at which the laminar or turbulent boundary layer separates from the prism's surface. At an incidence angle of $45°$, the decreasing curvature of the upper and lower (shoulder) edges of the prism allows a stronger meandering of the primary – and, in the case of a laminar separation bubble, also of the secondary – separation positions along those rounded edges with a variation of the Reynolds number. Similar to what is known for flows over circular cylinders, the *critical* flow regime of the prisms with $r/D = 0.16$ and 0.29 exhibits a drastic *drag crisis* that is initiated by the steady wandering of the primary separation locations from the windward-directed section towards to leeward-directed part of both shoulder edges. This relocation of the separation points leads to a reduction of the width of the near wake (Figure 3.10c to 3.10f), which then again lowers the suction force at the base of the prism. Within a narrow band of Reynolds numbers, an *asymmetric* flow state appears, being the result of the formation of a laminar separation bubble over one of the two rounded shoulder edges only. The resultant asymmetric mean pressure distribution on the surface of the prism introduces a mean steady lift force, as presented in Figure 3.11. Two interesting points can be derived from this figure: for a larger edge roundness value (*1*) the limited range of Reynolds numbers at which a steady non-zero lift force occurs both shifts to lower values and decreases in width, and (*2*) the maximum peak of $|C_L|$ increases. Both phenomena are relatively obvious, as the whole *critical* flow regime shifts to lower Reynolds numbers for larger r/D-values (e.g. Figure 3.9) and a larger laminar separation bubble can be formed on a sur-
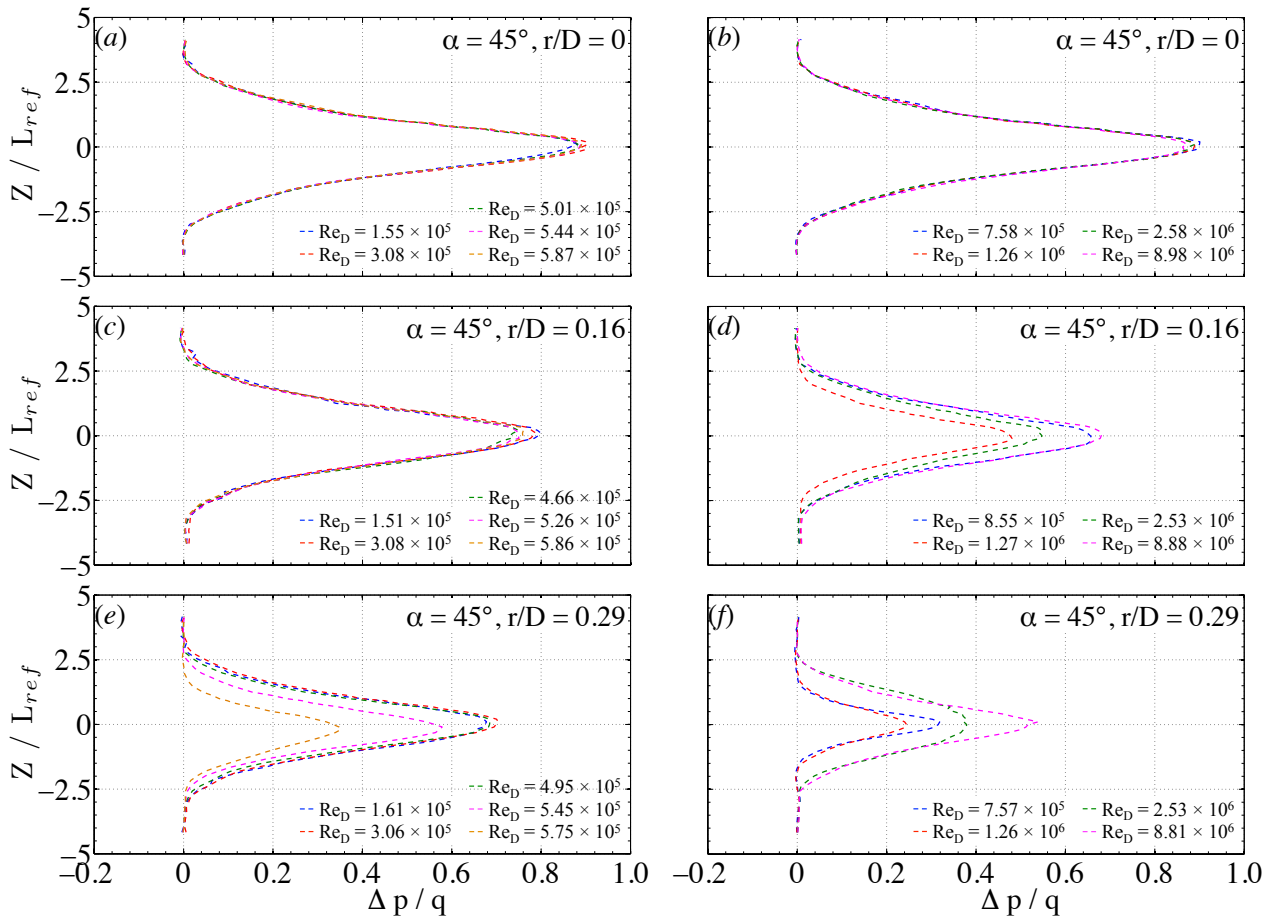
Figure 3.10: Effect of Reynolds number on the mean vertical wake profiles at $X/L_{ref} = 6.25$ behind the mid-span of two-dimensional square-section prisms at $\alpha = 45°$. (a)-(b): $r/D = 0$; (c)-(d): $r/D = 0.16$; (e)-(f): $r/D = 0.29$.
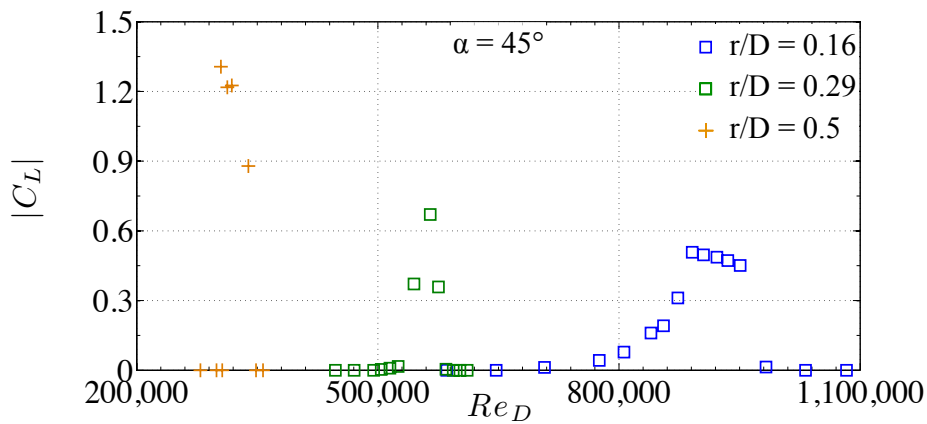
Figure 3.11: Effect of edge roundness on the absolute value of the mean global lift coefficient of 2D square-section prisms at $\alpha = 45°$ for Reynolds numbers from 1×10^5 up to 1×10^7. Reference: $+$ Schewe [209] $(r/D = 0.5)$.

face that possesses a longer curvature. The latter induces a stronger asymmetric pressure field around the bluff body and thus a higher lift force.

Based on the data for C_D, C_{pb}, and the mean vertical wake profile, it can be argued that similar variations in the flow behaviour around both rounded square-section prisms at $\alpha = 45°$ as for circular cylinders are transited one after another with increasing Reynolds numbers in the *supercritical* to *transcritical* flow regime. It is assumed that at *supercritical* Reynolds numbers a laminar separation bubble has firmly settled over both rounded shoulder edges and a secondary separation of the turbulent boundary layer occurs further downstream on both leeward-directed faces of the prism. The more the edge roundness approaches the value of $r/D = 0.5$, the further downstream this secondary separation takes place. This not only lowers the effective aerodynamic blockage ratio, but it also induces a small and short near wake (Figures 3.10d and 3.10f) that reduces in size with increasing r/D-value. As a result, low negative base pressure coefficients are obtained, as presented in Figure 3.9b, which are then mainly responsible for the lowest C_D-values in the *supercritical* flow regime. The increase in the mean global drag coefficient in the following *upper transition* is the outcome of the steady shift of the transition location upstream over both shoulder edges, which leads to a subsequent progressive size reduction and – at the moment the transition overtakes the primary separation location – the disappearance of both LSBs with increasing Reynolds number. With the absence of those laminar separation bubbles, the turbulent boundary layer separates earlier at both shoulder edges, the lateral spreading of the separated shear layers in the near wake increases, and the high suction force on the two downstream-directed faces of the prism re-appears. In the final *transcritical* flow regime, the boundary layer separation points mainly remain at a fixed position. Only very light fluctuations in both the shape of the mean vertical wake profile and the width of the near wake at $X/L_{ref} = 6.25$ can be observed, the effective aerodynamic blockage ratio can thus be expected to be constant, which explains the constant values for C_{pb} and C_D. Their values in Figure 3.9 furthermore show that the smaller the value of the edge roundness, the higher the plateau of both coefficients in the *transcritical* flow regime and the more these values approach the *subcritical* plateau.

The Figures 3.12 and 3.13 present the same data as in Figure 3.9a; this time, however, complemented with data for square-section prisms with $0 \leqslant r/D < 0.5$ and for circular cylinders from other reference studies. In contrast to the first of both figures, the second shows the behaviour of C_D as function of the Reynolds number multiplied by an empirical factor of $(r/D)^{1.31}$ (Polhamus [186]). The present values of the mean global drag coefficient for the sharp-edged prism coincide well with the data by Lee [130], but are underpredicted by those of Letchford and Mason [132]. Regarding the *subcritical* flow regime, the present data fit relatively well within the overall trend of the $C_D(Re_D)$ curves for increasing r/D-value. Unfortunately, the amount of reference data for the other flow regimes is too scarce to obtain an accurate and sound comparison. Several conclusions can nevertheless be drawn from those data. The drag coefficients for $r/D = 0.167$ by Delany and Sorensen [58] are, for example, significantly higher than the present ones for $r/D = 0.16$. They furthermore remain at a relative constant high level up to $Re_D = 1.25 \times 10^6$, while the present data for $r/D = 0.16$ show a distinct *drag crisis* in the range of approximately $7 \times 10^5 \leqslant Re_D \leqslant 1 \times 10^6$ and subsequent low values at *supercritical* Reynolds numbers. Regarding their data for $r/D = 0.333$, it is observed that the trend of the $C_D(Re_D)$ curve agrees well with those of $r/D = 0.16$ and 0.29, but also for this configuration drag coefficients were measured by Delany and Sorensen [58] that lie above those of the present prism configuration with $r/D = 0.29$. On the other hand, the experimental data by James and Vogel [115] for $r/D = 0.15$ and 0.1875 not only significantly underpredict the present drag
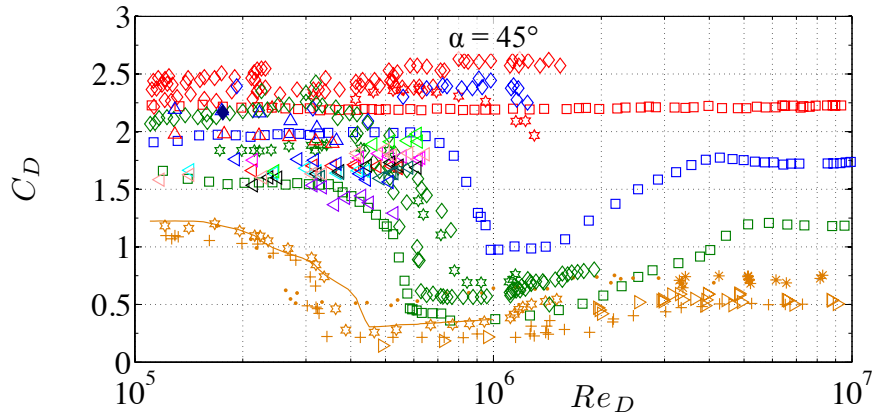
Figure 3.12: Dependence of the mean global drag coefficient on the Reynolds number for 2D square-section prisms at $\alpha = 45°$ with edge roundness values between $r/D = 0$ (sharp-edged) and 0.5 (circular cylinder). Van Hinsberg *et al* [254] and Van Hinsberg [258]: □: $r/D = 0$; □: $r/D = 0.16$; □: $r/D = 0.29$. References: ● Achenbach and Heinecke [5] ($r/D = 0.5$), ◇ Delany and Sorensen [58] (◇: $r/D = 0.021$; ◇: $r/D = 0.167$; ◇: $r/D = 0.333$), ◁ James and Vogel [115] (◁: $r/D = 0.00937$; ◁: $r/D = 0.0109$; ◁: $r/D = 0.011$; ◁: $r/D = 0.0625$; ◁: $r/D = 0.0729$; ◁: $r/D = 0.075$; ◁: $r/D = 0.125$; ◁: $r/D = 0.15$; ◁: $r/D = 0.1875$), ▷ Jones *et. al* [117] ($r/D = 0.5$), ◆ Lee [130] ($r/D = 0$), △ Letchford and Mason [132] (△: $r/D = 0$; △: $r/D = 0.12$), ★ Polhamus [186] (★: $r/D = 0.08$; ★: $r/D = 0.245$; ★: $r/D = 0.5$), ✳ Roshko [197] ($r/D = 0.5$), + Schewe [209] ($r/D = 0.5$), – Wieselberger [270] ($r/D = 0.5$).

Figure 3.13: Effect of Reynolds number – based on edge roundness of $r/D = 0$ to 0.5 – on the mean global drag coefficient of 2D square-section prisms at $\alpha = 45°$. Van Hinsberg *et al* [254] and Van Hinsberg [258]: □: $r/D = 0$; □: $r/D = 0.16$; □: $r/D = 0.29$. References: ● Achenbach and Heinecke [5] ($r/D = 0.5$), ◇ Delany and Sorensen [58] (◇: $r/D = 0.021$; ◇: $r/D = 0.167$; ◇: $r/D = 0.333$), ◁ James and Vogel [115] (◁: $r/D = 0.00937$; ◁: $r/D = 0.0109$; ◁: $r/D = 0.011$; ◁: $r/D = 0.0625$; ◁: $r/D = 0.0729$; ◁: $r/D = 0.075$; ◁: $r/D = 0.125$; ◁: $r/D = 0.15$; ◁: $r/D = 0.1875$), ▷ Jones *et. al* [117] ($r/D = 0.5$), ◆ Lee [130] ($r/D = 0$), △ Letchford and Mason [132] (△: $r/D = 0$; △: $r/D = 0.12$), ★ Polhamus [186] (★: $r/D = 0.08$; ★: $r/D = 0.245$; ★: $r/D = 0.5$), ✳ Roshko [197] ($r/D = 0.5$), + Schewe [209] ($r/D = 0.5$), – Wieselberger [270] ($r/D = 0.5$).

coefficients for $r/D = 0.16$, the data for $r/D = 0.1875$ even coincide almost perfectly with those for $r/D = 0.29$. Last, but not least it should be mentioned that the values of C_D for $r/D = 0.245$ (Polhamus [186]) are not only flanked by the present data for $r/D = 0.16$ and 0.29, but all three curves also possess a similar trend with Reynolds number.

Despite the large scatter of the data, the additionally applied empirical factor of $(r/D)^{1.31}$ allows a rather good overlap of the *critical* flow regime, as presented in Figure 3.13. In contrast to $\alpha = 0°$, the large scatter of the data at $\alpha = 45°$ does unfortunately not allow a sound vertical interpolation of the data at a fixed Reynolds number to obtain an accurate prediction of the drag coefficient for a square-section prism with an arbitrary edge roundness.

3.2.2 Fluctuating fluid-dynamic loads

The fixed, and therefore Reynolds-number independent position of the separation of the surface boundary layer at both sharp shoulder edges induces a wide and long near wake behind the base surface of the prism with $r/D = 0$ at $45°$ angle of incidence. Although the shape of the mean vertical wake profile in the Figures 3.10a and 3.10b resembles at each Reynolds number the respective curve at $\alpha = 0°$ (Figures 3.5a and 3.5b), the higher maximum value of $\Delta p/q$ and the smaller negative values of C_{pb} (Figure 3.9b) at $45°$ angle of incidence are an indication that the recirculation regions have shifted further downstream, i.e. away from the two base faces of the prism. The reason for this is most probably the turning of one of the two side faces of the prism into the wake. The two leeward-directed faces can be seen as an afterbody that is extruded downstream into the base region. It is assumed that its presence not only shifts the region with the highest vertical components of the velocity fluctuations on the wake centreline in downstream direction, but also causes a decrease in the amount of fluid that is entrained into the wake. The combined effect leads to a weaker intensity with which the eddies are shed from the prism, which explains the smaller periodic changes in the lift force on the prism of $\sqrt{(\overline{C'^2_L})} = 0.47 \pm 0.05$ (Figure 3.14a) to 1.04 ± 0.07 (Figure 3.6a) for $\alpha = 45°$ and $0°$, respectively. The Figures 3.15a and 3.15b present the power spectra of the time-dependent lift force at nine Reynolds numbers between $Re_D = 10^5$ and 10^7, together with values of the Strouhal numbers that belong to the main peak in each spectrum. The frozen separation location of the surface boundary layer is clearly recognised in the immobile position of the main peak at $St_L = 0.11$.

A reduction of the prism's bluffness by increasing the roundness of its edges introduces a gradually increasing variation of both fluid-dynamic parameters with Reynolds number, whereby for larger r/D-values the curves for $\sqrt{(\overline{C'^2_L})}$ and St_L progressively approach those ones of the circular cylinder. While only small variations with r/D occur in the *subcritical* and *transcritical* flow regimes, distinct changes take place in the flow regimes in-between. Both for $r/D = 0.16$ and 0.29, the *critical* flow regime is characterised by a sharp decrease of the fluctuating lift and a rise of the shedding frequency in two steps. Similar to the circular cylinder flow, the intermediate, short plateau of approximately constant Strouhal numbers of $St_L = 0.15$ to 0.16 at $Re_D = 8.6 \times 10^5 – 9.1 \times 10^5$ for $r/D = 0.16$ and $St_L = 0.2$ at $Re_D = 5.7 \times 10^5 – 5.8 \times 10^5$ for $r/D = 0.29$ results from the formation of a laminar separation bubble over one of the two rounded shoulder edges only. At these Reynolds numbers, a clear asymmetrical flow exists over the prism that influences both the strengths of the eddies – and thus the fluctuating lift – and the frequency with which these eddies are shed. The latter is evident from the shift of the main peak in the PSDs in the Figures 3.15c to 3.15f. The simultaneous existence of two Strouhal numbers at one single *critical* Reynolds number is limited to the prism with $r/D = 0.16$ and appears only at both outer regions of the *asymmetric* flow state, as is shown in the following
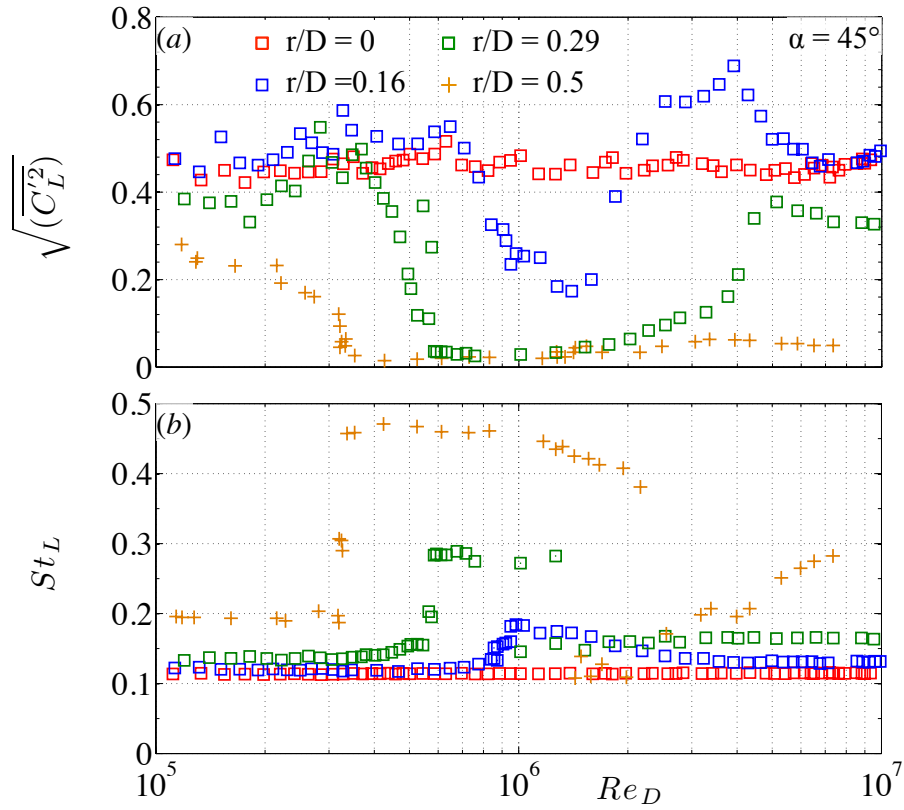
Figure 3.14: Effect of edge roundness r/D on the fluctuating global lift coefficient (a) and Strouhal number (b) of a 2D square-section prism at $\alpha = 45°$ for Reynolds numbers in the range of 1×10^5 to 1×10^7 (Van Hinsberg *et al* [254], Van Hinsberg [258]). Reference: $+$ Schewe [209] ($r/D = 0.5$).

section together with the occurrence of hysteresis effects for increasing or decreasing *critical* Reynolds numbers.

  The presence of a laminar separation bubble over both shoulder edges and the resultant narrow near wake at *supercritical* Reynolds numbers are responsible for the lowest occurring coefficients of the fluctuating lift and the highest Strouhal numbers. As expected, the higher the value of r/D, the nearer the *supercritical* values of both fluid-dynamic parameters are located to the curve of the circular cylinder. Interesting to note at this point is the even almost perfect overlap of the *supercritical* parts of the fluctuating lift curves for $r/D = 0.29$ and 0.5, while the values of St_L still differ significantly at those Reynolds numbers.

  As soon as the laminar-turbulent transition location overtakes the separation points of the surface boundary layer in the *upper transition*, the separation location of the turbulent boundary layer migrates upstream along the shoulder edges and the near wake gradually widens again. This process is accompanied with a significant increase in $\sqrt{(\overline{C_L'^2})}$ for $r/D = 0.16$ and 0.29 towards the *subcritical* plateau, although the manner in which this increase occurs differs remarkably between both configurations, whereby the sharp rise of the curve for $r/D = 0.16$ up to $\sqrt{(\overline{C_L'^2})} = 0.69$ at $Re_D = 3.9 \times 10^6$ and subsequent decrease are the most remarkable phenomena. The behaviour of the Strouhal number with increasing Reynolds number differs as well between both r/D values in this flow regime. Whereas the $St_L(Re_D)$ curve for $r/D = 0.29$ possesses a discontinuous step down to $St_L = 0.15$–0.16 at the cross-over from the *supercritical* flow regime to the *upper transition* and subsequently remains at this level throughout the
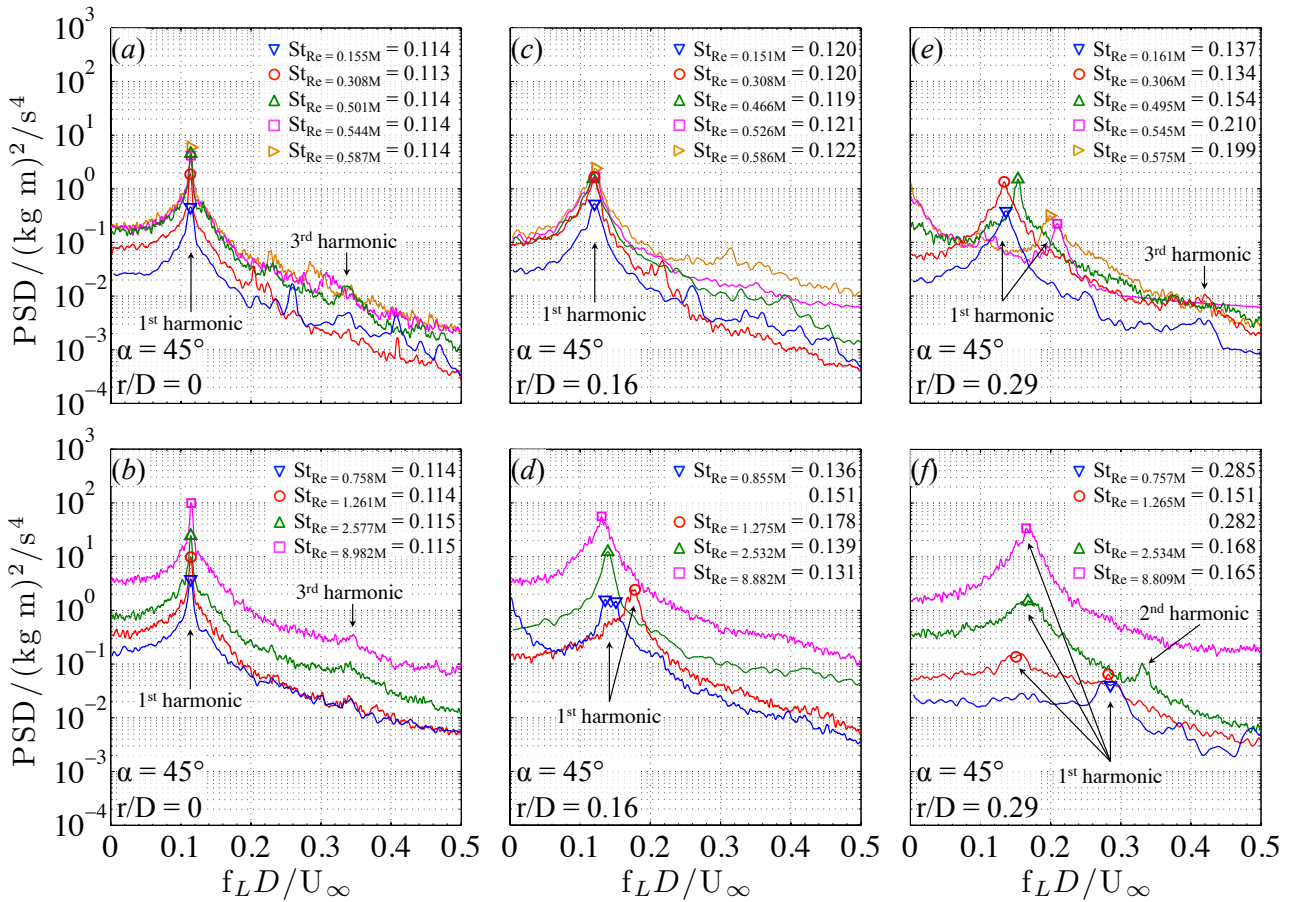
Figure 3.15: Power spectral density of the time series of the global lift force on two-dimensional square-section prisms at $\alpha = 45°$ at selected Reynolds numbers between 1×10^5 and 1×10^7. (a)-(b): $r/D = 0$; (c)-(d): $r/D = 0.16$; (e)-(f): $r/D = 0.29$. The corresponding Strouhal numbers are indicated by the symbols on the curves and the numbers inside each graph. In case of multiple occurring Strouhal numbers at equal Reynolds number, the dominant Strouhal number is mentioned first, followed by the Strouhal number of the secondary peak. M in the Reynolds number equals "million".

complete *upper transition* and adjacent *transcritical* flow regime, a steady, gradual decrease characterises the $St_L(Re_D)$ curve for $r/D = 0.16$.

In contrast to circular cylinder flows, the amount of reference data for sharp-edged and rounded square-section prisms at $\alpha = 45°$ for $Re_D \geqslant 10^5$ is extremely scarce, so that a comparison with the present data is hardly possible. While no such reference data exist at all for the fluctuating lift, as presented in Figure 3.16a, reference data for the Strouhal number have been included in Figure 3.16b for prisms with $r/D = 0$ (Huang *et al.* [106] and Lee [130]) and 0.333 (Delany and Sorensen [58]). The present Strouhal numbers for the sharp-edged prism agree well with those by Huang *et al.* [106] and Lee [130], although their data unfortunately cover a range of Reynolds numbers of $Re_D = 1 \times 10^5$–2×10^5 only. Regarding the Strouhal numbers of the present rounded prism with $r/D = 0.29$, a reasonable match with those by Delany and Sorensen [58] for $r/D = 0.333$ is obtained for Reynolds numbers from high *subcritical* up to the end of the *supercritical* flow regime.
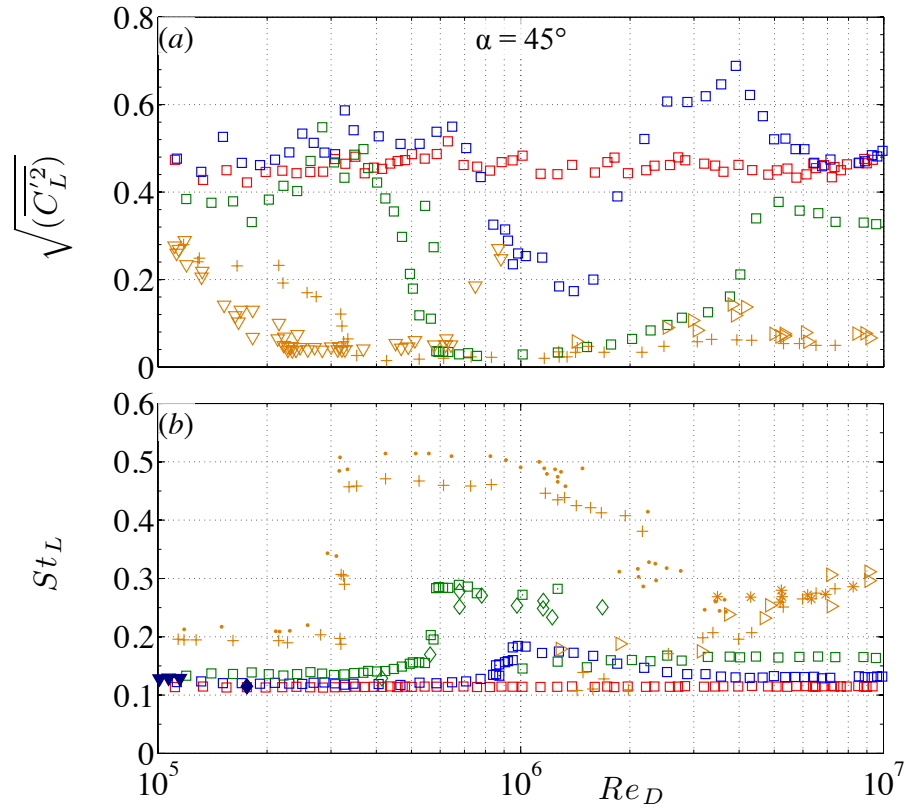
Figure 3.16: Dependence of the fluctuating global lift coefficient (a) and non-dimensional eddy shedding frequency (b) on the Reynolds number for 2D square-section prisms at $\alpha = 45°$ with edge roundness values between $r/D = 0$ (sharp-edged) and 0.5 (circular cylinder). Van Hinsberg *et al* [254] and Van Hinsberg [258]: □: $r/D = 0$; □: $r/D = 0.16$; □: $r/D = 0.29$. References: ● Achenbach and Heinecke [5] ($r/D = 0.5$), ◇ Delany and Sorensen [58] ($r/D = 0.333$), ▼ Huang *et al.* [106] ($r/D = 0$), ▷ Jones *et. al* [117] ($r/D = 0.5$), ◆ Lee [130] ($r/D = 0$), ✳ Roshko [197] ($r/D = 0.5$), + Schewe [209] ($r/D = 0.5$), ▽ Zan and Matsuda [289] ($r/D = 0.5$).

3.2.3 Hysteresis in the fluid-dynamic loads and Strouhal number for increasing and decreasing Reynolds numbers in the *critical* flow regime

In the previous section, reference was already made to the appearance of hysteresis effects when comparing the fluid dynamics of rounded square-section prisms at $\alpha = 45°$ while passing through the *drag crisis* with increasing or decreasing Reynolds numbers. Figure 3.17 presents the outcomes of the mean global drag force, absolute mean global lift coefficient, and Strouhal number for the present square-section prisms with $r/D = 0.16$ and 0.29, as well as the reference data by Schewe [209] for the circular cylinder obtained in the same High-Pressure wind tunnel facility. For each shown model configuration, the branches of rising and declining Reynolds numbers cover the range between the upper part of the *subcritical* flow regime and the lower part of the *supercritical* flow regime.

The various graphs show that each of the three configurations experiences a hysteresis; however, the extent of this hysteresis on the presented fluid-dynamic quantities differs significantly among them. The square-section prism with rounded edges of $r/D = 0.16$ experiences only a very weak hysteresis effect that is limited to both boundaries of the *asymmetric* flow state.
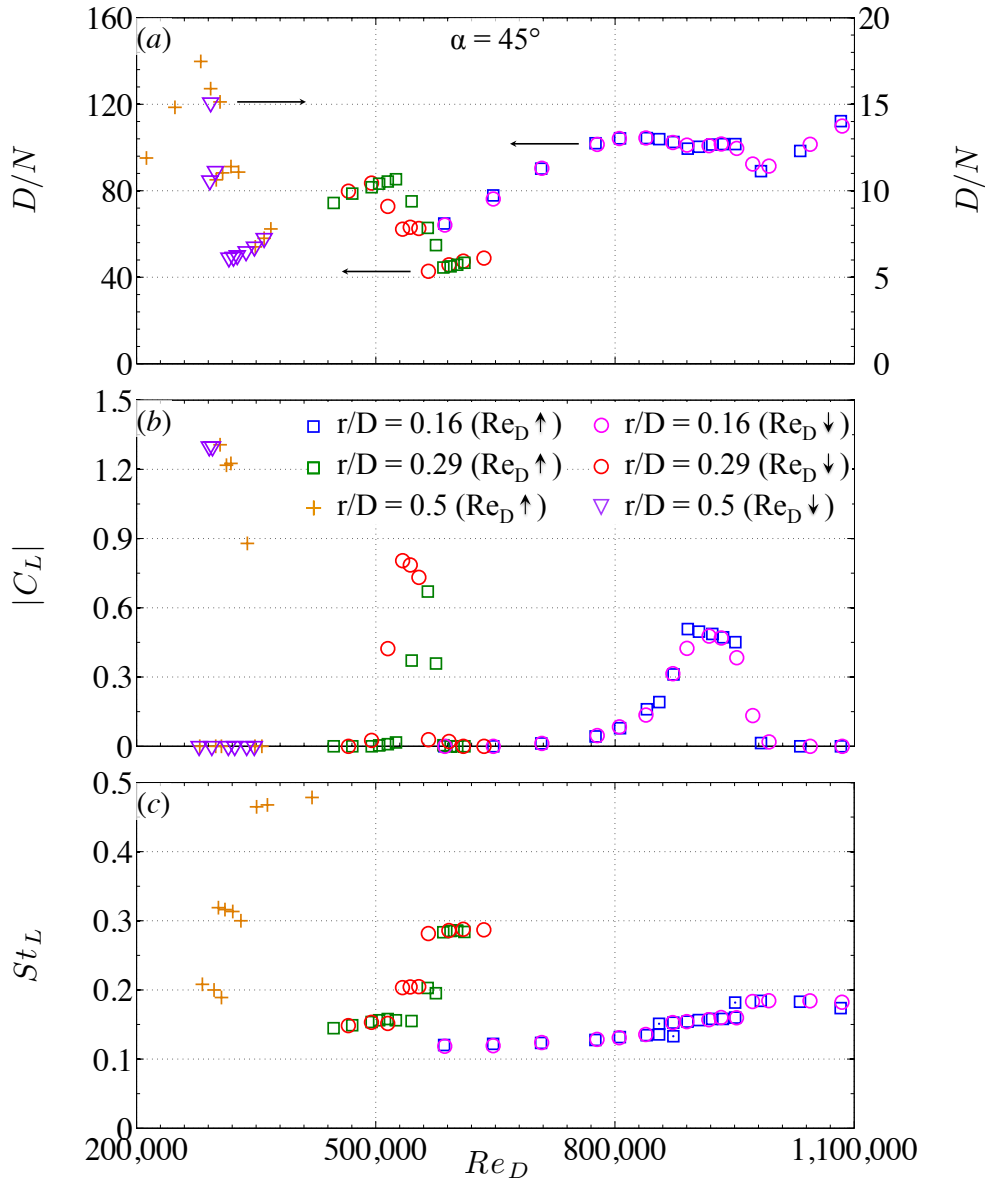
Figure 3.17: Hysteresis effects for the transition from the *subcritical* flow regime to the *supercritical* flow regime (increasing Re_D) and vice versa (decreasing Re_D) on the mean global drag force D in Newton (a), absolute mean global lift coefficient (b), and Strouhal number (c) of 2D square-section prisms with edge roundness at an incidence angle of $\alpha = 45°$. Reference: $+$ and $\triangledown$ Schewe [209] ($r/D = 0.5$).

Small differences in the values of D and $|C_L|$ between the two branches can be recognised at $Re_D = 8.9 \times 10^5$ and 9.5×10^5. Increasing the radius of the prism edges to 0.29 and 0.5 leads to the appearance of a much more pronounced hysteresis. In particular the shift towards lower values of the two Reynolds numbers (on the decreasing branch) at which a transition from a symmetric flow state into an asymmetric one and back to the symmetric case takes place, are clearly visible. Interestingly, the values of D, $|C_L|$, and St_L in the *asymmetric* flow state and in both bounding symmetric flow regimes are hardly affected by the hysteresis.

In the following, a detailed review of the hysteresis effects of the smooth square-section prism with $r/D = 0.29$ at $\alpha = 45°$ is presented. The reader should take notice, that the observations

83

described hereafter depend to a large extend on the roughness of the prism's faces. A different value of the equivalent sand-grain surface roughness than the present one of $k_s/L_{ref} = 4.5 \times 10^{-6}$ not only modifies the pressure distribution on the prism's surface and thus the values of all fluid-dynamic parameters, but also shifts the various flow regimes to different Reynolds numbers. These aspects are part of a thorough analysis in section 4.2 for square-section prisms with edge roundness values of $r/D = 0$ to 0.5.

Figure 3.18 presents the changes in the experimentally obtained values of C_D, Z_w/L_{ref}, St_L, and $|C_L|$ with both increasing and decreasing Reynolds number within and in the direct vicinity of the *drag crisis*. In the top graph, the two branches are accompanied by lower case letters
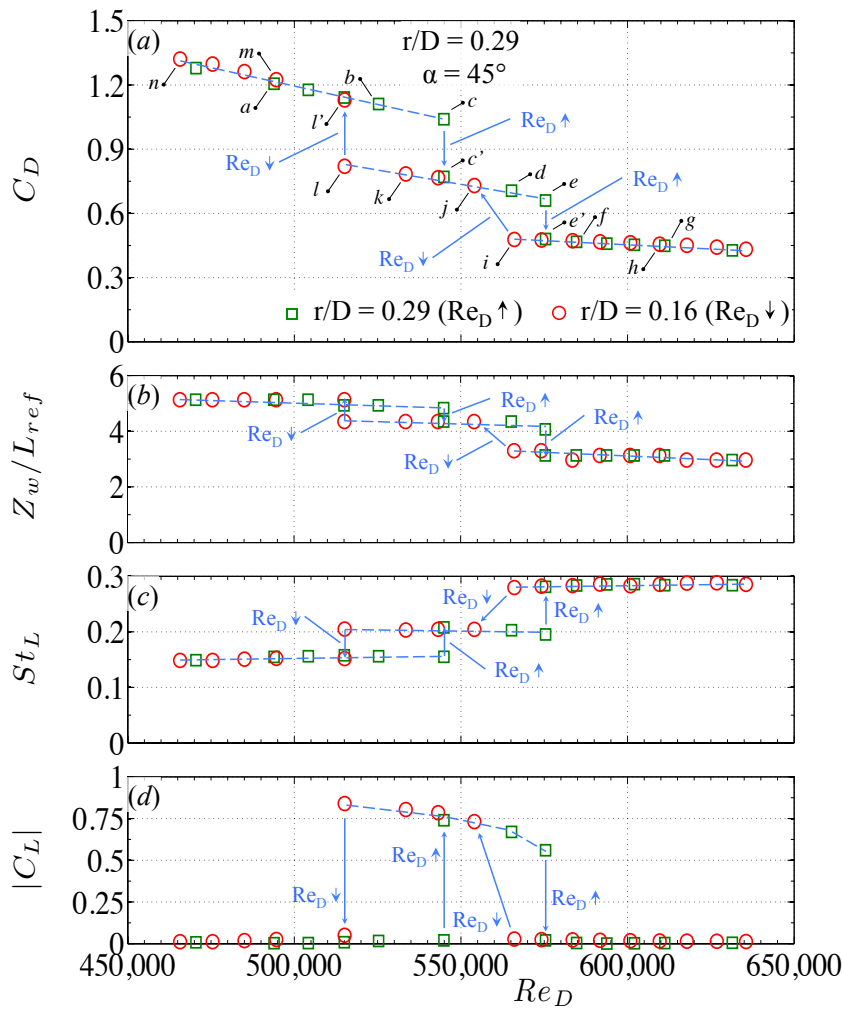
Figure 3.18: The individual stages within the *critical* flow regime with hysteresis effect for a 2D square-section prism with rounded edges of $r/D = 0.29$ at an incidence angle of $\alpha = 45°$ (Adapted from Van Hinsberg *et al.* [254]). *(a)*: mean global drag coefficient; *(b)*: non-dimensional mean wake width at $X/L_{ref} = 6.25$; *(c)*: Strouhal number based on the lift fluctuations; *(d)*: absolute mean global lift coefficient. □: increasing Reynolds number; ○: decreasing Reynolds number. The lower case letters in graph *(a)* denote the individual stages of the flow state with *a-g* being the transition from the *subcritical* flow regime to the *super-critical* flow regime and *h-n* the transition from the *supercritical* flow regime to the *subcritical* flow regime).

that mark several specific stages of the flow. The letters *a-g* characterise the gradual transition

from the *subcritical* to the *supercritical* flow regime, the letters *h-n* correspond to the declining branch. To understand the physical phenomena that appear and disappear when traversing form one stage to another along one of the two branches, the corresponding probability density distributions and power spectra of the lift fluctuations are displayed in the Figures 3.19 and 3.20. With the exception of the distribution of the absolute mean lift coefficient, the three
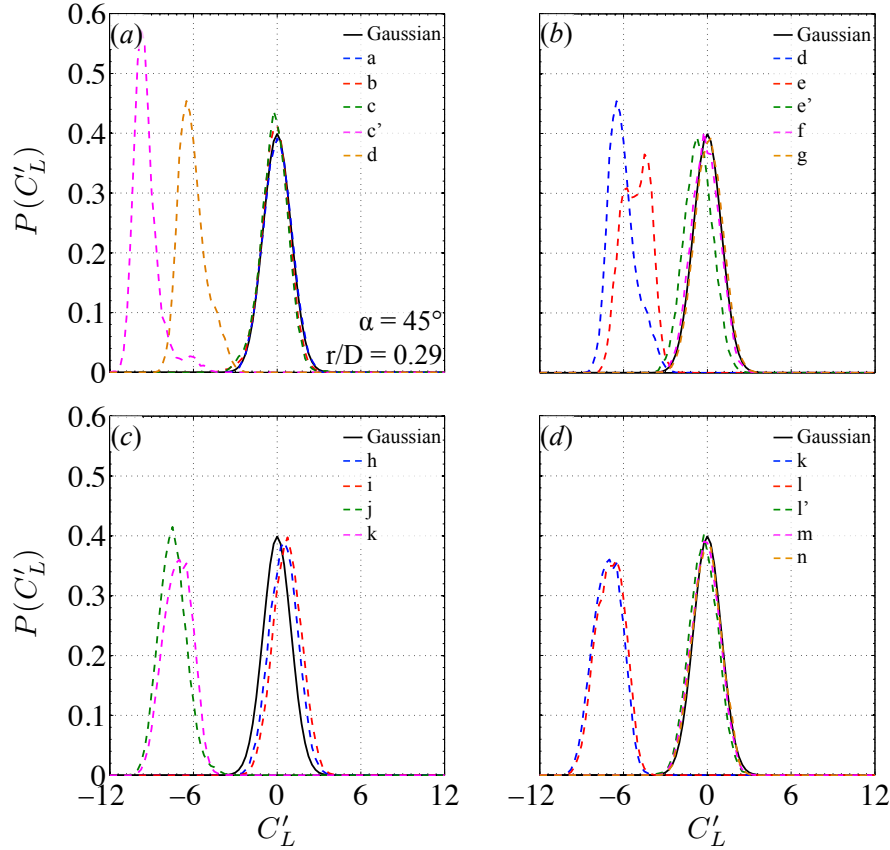
Figure 3.19: Probability density distributions of the lift fluctuations in the *critical* flow regime with hysteresis effect for a two-dimensional square-section prism with rounded edges of $r/D = 0.29$ at $\alpha = 45°$ (Adapted from Van Hinsberg *et al.* [254]). The lower case letters in each graph correspond to the individual stages of the flow state in Figure 3.18a. The letters *a-g* characterise the transition from the *subcritical* flow regime to the *supercritical* flow regime and *h-n* the transition from the *supercritical* flow regime to the *subcritical* flow regime. The solid black line represents the Gaussian distribution.

plateaus (marked as dashed lines) that correspond to the *subcritical* flow regime, the *asymmetric* flow state, and the *supercritical* flow regime can clearly be identified in Figure 3.18. Since a non-zero mean lift force only exists in the *asymmetric* flow state, only two clearly separated levels can be recognised for this coefficient. Points *a* and *b* both represent the *subcritical* flow regime, although small differences are obtained between both stages. Passing from *a* to *b*, the decrease in C_D and the slightly smaller width of the near wake indicate a small repositioning in downstream direction of the primary separation points along the surface of both rounded shoulder edges. Although the probability density functions for *a* and *b* in Figure 3.19a match the Gaussian distribution well, the increasing deviation of the skewness and excess kurtosis values for point *b* from the values for a perfect Gaussian distribution in Table 3.2 reveal a change in the flow around the prism. The combination of the appearance and growth of the
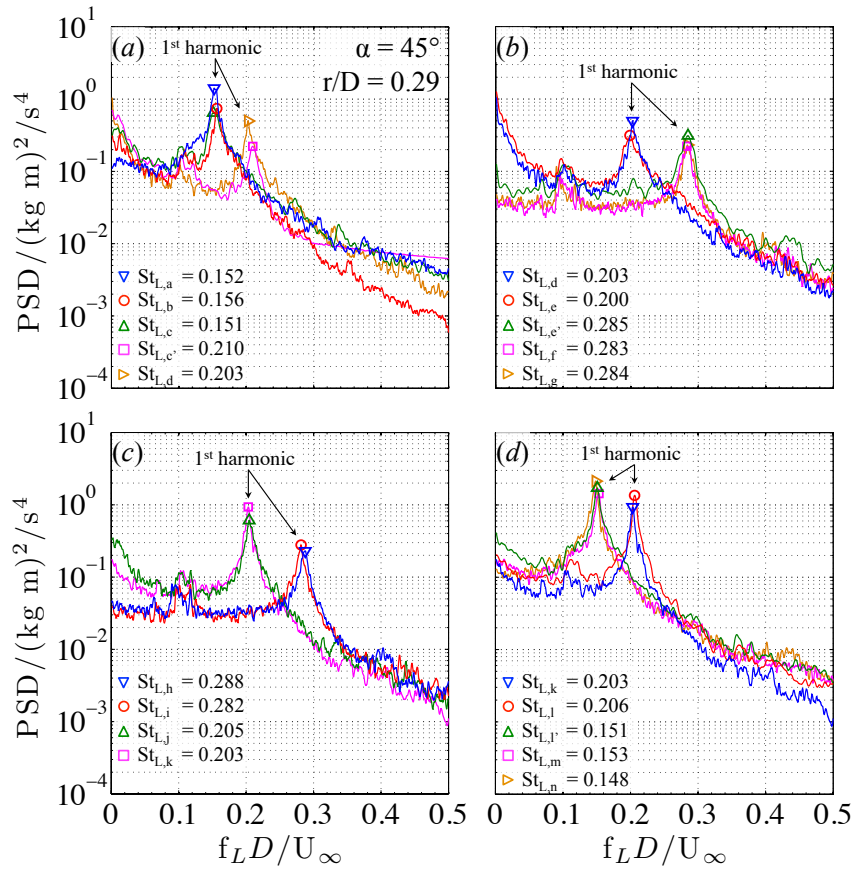
Figure 3.20: Power spectra of the lift fluctuations in the *critical* flow regime with hysteresis effect for a two-dimensional square-section prism with rounded edges of $r/D = 0.29$ at $\alpha = 45°$. The lower case letters correspond to the individual stages of the flow state in Figure 3.18a with *a-g* characterising the transition from the *subcritical* flow regime to the *supercritical* flow regime and *h-n* the transition from the *supercritical* flow regime to the *subcritical* flow regime.

broadband low-frequency critical fluctuations and the decrease of the main peak in the PSD of point *b* in Figure 3.20a furthermore reveal that the state of the flow progressively gets unstable.

Figure 3.21 portrays the experimentally obtained temporal distribution of the global lift coefficient on the prism for the individual flow stages *b* to *e*. While the lift coefficient fluctuates in point *b* ($Re_D = 5.25 \times 10^5$) around its mean value of $C_L = 0$, a sudden and sharp jump in C_L down to a mean value of $C_L = -0.74$ occurs at about $t = 15.4$ s (i.e. $TU_\infty/D = 7120$) in the times serie for point *c*, after which it remains at this new level. At this stage a small disturbance in the oncoming flow (e.g. a tiny increase of its velocity) is apparently enough to tackle the flow in a definite way and induce a stable asymmetric flow condition. This step marks the transition of the flow from *subcritical* to the stable *asymmetric state* at $Re_D = 5.45 \times 10^5$, initiated by the formation of a local laminar separation bubble over the upper rounded shoulder edge, thereby introducing an highly asymmetric pressure field on the prism's surface. This change in the state of the flow is reflected in a sudden reduction of the mean global drag coefficient from $C_D = 1.04$ (point *c*) to $C_D = 0.77$ (point *c'*), and a decrease of the wake width by 10%. By comparing the power spectra at the points *c* and *c'* in Figure 3.20a, an increased peak at low frequencies and a distinct shift of the main peak from $f_L D/U_\infty = St_L = 0.151$ to 0.210 can be identified. A similar observation is made for the respective probability density distribution (Figure 3.19a)

Table 3.2: Skewness and excess kurtosis of the probability density distribution at the stages a-g (increasing Reynolds number) and h-n (decreasing Reynolds number) in the hysteresis range of the smooth square-section prism with $r/D = 0.29$ at $\alpha = 45°$.

Stage	Reynolds number	Skewness	Excess kurtosis
a	$4.94{\times}10^5$	0	–0.21
b	$5.25{\times}10^5$	–0.26	0.55
c	$5.45{\times}10^5$	–0.28	0.81
c'	$5.45{\times}10^5$	1.50	3.62
d	$5.65{\times}10^5$	0.69	0.27
e	$5.75{\times}10^5$	–0.04	–0.65
e'	$5.75{\times}10^5$	0.01	–0.16
f	$5.85{\times}10^5$	0.01	–0.17
g	$6.11{\times}10^5$	0	–0.09
h	$6.10{\times}10^5$	0.02	–0.19
i	$5.66{\times}10^5$	0.02	–0.12
j	$5.54{\times}10^5$	0.31	0.29
k	$5.34{\times}10^5$	–0.09	–0.44
l	$5.15{\times}10^5$	–0.11	–0.49
l'	$5.15{\times}10^5$	–0.03	0.07
m	$4.95{\times}10^5$	–0.04	–0.23
n	$4.66{\times}10^5$	–0.02	–0.34
Gaussian	–	0	0

that changes from a centric distribution around $C'_L = 0$ (point c) to a strong asymmetric distribution around $C'_L = -9.7$ (point c'). The values of the skewness ($sk = 1.50$) and excess kurtosis ($ex.kt = 3.62$) for point c' are even higher than those known from circular cylinder experiments. It can be argued that the appearance of a second intermediate *asymmetric flow stage* around $C_L = -0.4$, occurring around the time steps $t = 17.5$ s, $t = 20$ s, $t = 24$ s, and $t = 27$ s in Figure 3.21b, is responsible for these high values of sk and $ex.kt$. At this intermediate asymmetric stage, the LSB at the upper side of the prism covers most probably not the complete span of the prism. It is assumed that the flow over the prism is highly three-dimensional, whereby part of the flow over the upper two faces of the prism jumps back into the *subcritical* flow regime for a limited time period of only a couple of milliseconds, which can explain the short occurrence of a smaller negative lift coefficient. This results in a probability density distribution being asymmetric with a tail at its right side and higher values for the skewness and excess kurtosis (Table 3.2). The time series for points d and e illustrate that – within the *asymmetric* flow state – an increase in the Reynolds number augments both the number of occurrences of this intermediate stage and their durations. At point e at the upper boundary of the *asymmetric* flow state, the probability density distribution even possesses a double peak (i.e. a small bimodal shape) around its centre at $C'_L = -5.2$, with both peaks having unequal heights (Figure 3.19b).

Upon formation of the LSB over the upper rounded shoulder, the steady decrease of the four
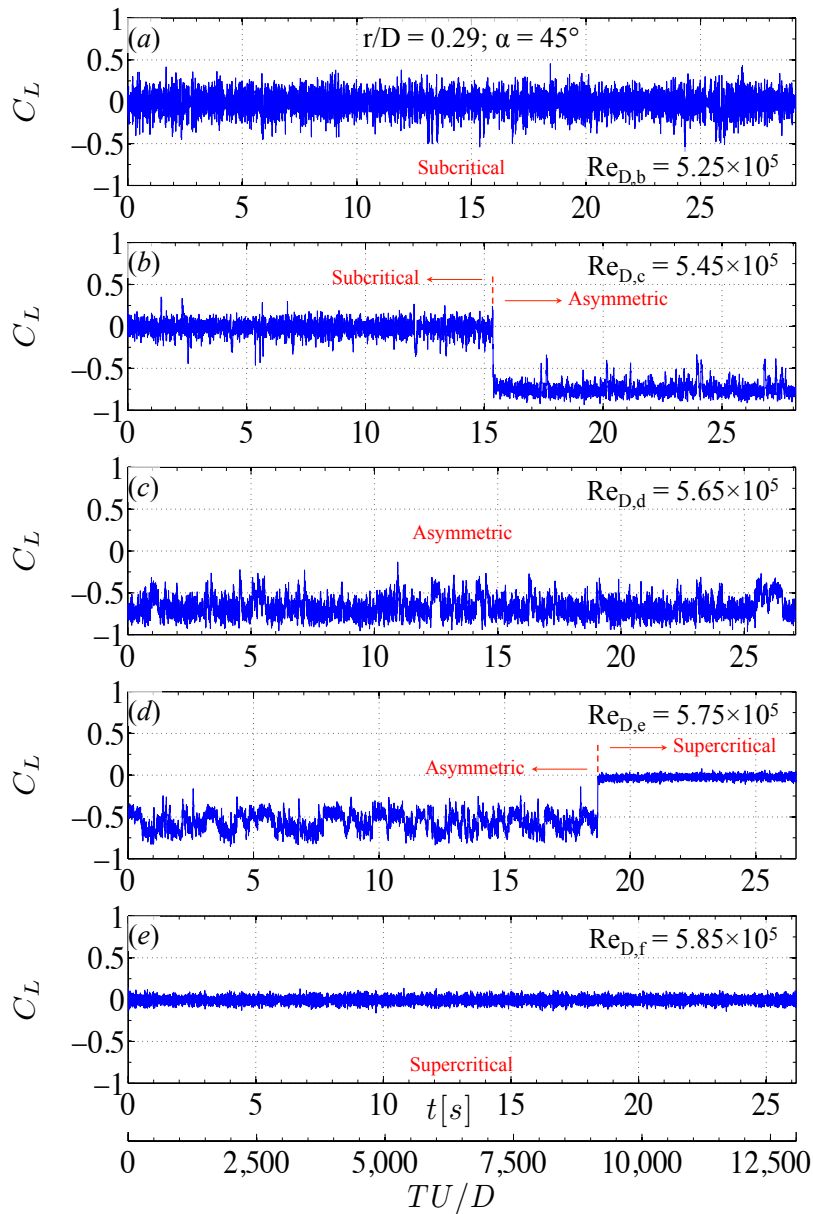
Figure 3.21: Time series of the lift coefficient for a two-dimensional square-section prism with rounded egdes of $r/D = 0.29$ at $\alpha = 45°$ at various stages in the *critical* flow regime that correspond to Figure 3.18a (Adapted from Van Hinsberg *et al.* [254]). The non-dimensional timescale TU_∞/D is valid for all curves. (a): stage b, $Re_D = 5.25\times10^5$; (b): stages c and c', $Re_D = 5.45\times10^5$; (c): stage d, $Re_D = 5.65\times10^5$; (d): stages e and e', $Re_D = 5.75\times10^5$; (e): stage f, $Re_D = 5.85\times10^5$.

fluid-dynamic quantities between the points c' and e in Figure 3.18 indicates a gradual, but continuous decrease of the amount of asymmetry between the flow over the upper and the lower faces of the prism. A confirmation of this process is given by the probability density distribution that gradually shifts from a strong asymmetric distribution around $C'_L = -9.7$ towards a more centric distribution around $C'_L = 0$ and the decline of the corresponding values for the skewness and excess kurtosis of those curves in Table 3.2. The shape of the mean vertical wake profile for point d in Figure 3.22 clearly shows that at this *asymmetric* flow state a *subcritical* flow (point b) is still present over both lower faces of the prism, whereas over the upper two prism
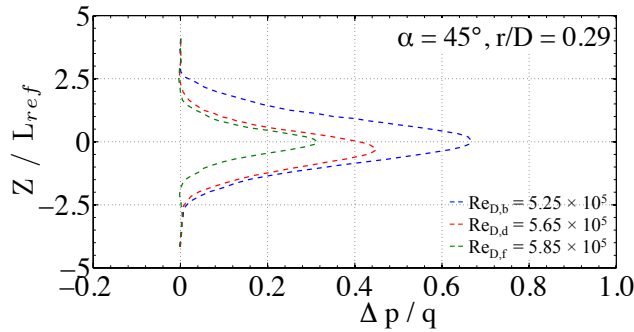
Figure 3.22: Mean vertical wake profile at $X/L_{ref} = 6.25$ behind the mid-span of two-dimensional square-section prisms at $\alpha = 45°$ for the stages b, d, and f in the *critical* flow regime according to Figure 3.18a (Adapted from Van Hinsberg *et al.* [254]).

faces the local flow has transitioned already into the *supercritical* flow regime (point f).

With increasing Reynolds number in the direction of the second transition at point e, the low-frequency critical fluctuations steadily grow in strength. At the upper bounding Reynolds number of the *asymmetric* flow state, $Re_D = 5.75 \times 10^5$, the flow around the prism is once more highly unstable and jumps locally back and forth between two subsequent flow states. The boundary layer on the lower side of the prism that remained separated in the *asymmetric* flow state, now becomes unstable and locally reattaches as well, thereby forming also a laminar separation bubble over the lower rounded shoulder. This leads to the termination of the *asymmetric* flow state and the appearance of the *supercritical* flow regime, the latter being the second symmetric flow state. As previously mentioned, the probability density distribution of point e in Fig. 3.19b has a small bimodal shape, the cause of which can be explained by studying the temporal distribution of the global lift coefficient as presented in Figure 3.21d. The first 18.7 seconds, up to about $TU_\infty/D = 9550$, of the measured signal belong to the *asymmetric* flow state. In this part, the flow around the prism jumps back and forth between the *asymmetric* flow state with $C_L = -0.75$ and the *intermediate asymmetric* flow state with $C_L = -0.4$. In the probability density distribution, each of the two flow states is mapped as a single distinct peak, whereby the height of the peak denotes the probability of occurrence in this part of the total signal of C_L. At $t = 18.7$ s, the global lift coefficient switches sharply to values close to $C_L = 0$ and resides at this level over time. Hence, the second transition of the flow from *asymmetric* to *supercritical* has just taken place. This shorter, second part of the signal is characterised by narrowband fluctuations of the global lift coefficient, owing to which only one sharp and narrow peak appears in the probability density function of the lift fluctuations at point e' in Figure 3.19b. The sudden occurrence of a steady reattachment of both free shear layers along the complete span of the prism and the associated secondary separation of the turbulent boundary layer on both downstream-directed faces of the prism at $Re_D = 5.75 \times 10^5$ leads to a discontinuity in each curve in Figure 3.18. Both the width of the near wake and the mean global drag coefficient decrease by about 25%, while the Strouhal number jumps up from $St_L = 0.2$ at point e to 0.285 at point e' as a result of the shift of the main peak in the power spectra of the fluctuating lift (Figure 3.20b). Within the following *supercritical* flow regime, the shape of the probability density distributions for the points f and g in Figure 3.19b are once again nearly Gaussian with values for the skewness and excess kurtosis close to zero. As described in the previous sections, the values of all fluid-dynamic parameters remain stable over the complete *supercritical* flow regime.

The hysteresis of the flow around this prism manifests itself in a shift of the *critical* Reynolds numbers at which the transitions from one flow stage to another occur from $Re_{D,cr} = 5.45 \times 10^5$ and 5.75×10^5 of the increasing Reynolds-number branch towards $Re_{D,cr} = 5.15 \times 10^5$ and 5.65×10^5 for the decreasing branch. This implies, that for decreasing Reynolds numbers the *supercritical* flow regime and *asymmetric* flow state can be maintained at lower Reynolds numbers. The data in Figure 3.18 show that perfectly equal values for the shown fluid-dynamic quantities are obtained at the three flow stages for increasing and decreasing Reynolds numbers. This clearly demonstrates, that the fine structures that subsequently take place from point h towards point n are not only identical to those described above for increasing Reynolds numbers, but also take place in an equal, albeit inverted manner when passing the *drag crisis* in reversed order.

3.3   Résumé Chapter 3

The present chapter has aimed at providing a deep insight into the separate and combined influences of the Reynolds number and the edge roundness on the steady-state performance of two-dimensional square-section prisms. In order to determine the unsteady and mean fluid-dynamic behaviour of this type of bluff bodies, wind tunnel experiments were performed on smooth square-section prisms with non-dimensional edge radii of $r/D = 0$ (i.e. sharp edges), 0.16, and 0.29. They were placed in a cross-flow at the two "symmetric" angles of incidence of $\alpha \in \{0°, 45°\}$. Regarding the Reynolds number, the focus was on a limited range of 10^5 to 10^7. In combination with the experimental data by Schewe [209] for a smooth circular cylinder in cross-flow, obtained in the same wind tunnel facility and under equal boundary conditions, a comparative analysis of the various governing and influencing parameters on the fluid dynamics of the prism was performed. It allows a first modest estimation of the influence of the prism's cross-sectional shape on the transverse vibrations to be expected at a certain Reynolds number in the case of the occurrence of the flow-induced excitations on an identical, but flexibly mounted prism.

It has been demonstrated that a drastic reduction in the global mean drag force on a rounded square-section prism at $\alpha = 0°$ is achieved by increasing the Reynolds number into or beyond the *drag crisis*. The change in edge roundness is noted to cast an additional positive effect on C_D, because the lower the applied edge curvature of the prism (i.e. the more its cross-sectional shape resembles a circle), the more this *drag crisis* shifts to lower Reynolds numbers, which is in close agreement with other reference studies. Hence, the sooner the *supercritical* flow regime – characterised by the lowest possible global drag force and manifesting itself even up to $Re_D = 10^7$ for $r/D = 0.16$ and 0.29 – is reached when increasing the Reynolds number. Within the *supercritical* flow regime, the largest gain in global drag reduction is then again achieved for small values of the non-dimensional edge roundness, while for $0.16 \leqslant r/D \leqslant 0.5$ only small additional changes in the global drag force are obtained. A clear exception is the sharp-edged prism configuration, which not only has the highest global drag at all Reynolds numbers, but its value is also constant for all Reynolds numbers above 10^4.

At an incidence angle of $45°$, the complete drag curve shifts to lower values as the edges of the prism are rounded. Also at this incidence angle, the greatest gain in drag reduction is achieved at *supercritical* Reynolds numbers. However, in contrast to $\alpha = 0°$, this Reynolds-number regime is now limited and followed by a significant recovery of the drag force for Reynolds numbers $\rightarrow 10^7$. The trend of the curves has shown that a gradual increase of the edge roundness leads to a steady approach of the mean drag force towards a *subcritical* level at those very large Reynolds numbers.

The fluid-dynamic parameters related to the eddy shedding process, i.e. the fluctuating lift and the Strouhal number, show opposite trends that emerge at both incidence angles. The changes in the fluctuating lift with increasing Reynolds number as well as with increasing edge roundness closely resemble those for the global mean drag force. The eddy shedding frequency, on the other hand, has a constant low level that is hardly dependent on the edge roundness at *subcritical* Reynolds numbers, which is followed by a discontinuous jump to a high plateau in the *critical* flow regime and remains there up to $Re_D = 10^7$ for $\alpha = 0°$. The height of this second *supercritical* plateau increases for larger roundness values. Deviations from this overall trend are found for both outer boundaries of the entire spectrum of possible cross-sectional shapes. While the sharp-edged square-section prism exhibits a constant low Strouhal number over the complete Reynolds-number range of 10^5 to 10^7, pronounced changes with large jumps up and down in the eddy shedding frequency characterise the flow around circular cylinders during the transition from one Reynolds-number regime to the next. This latter behaviour of the Strouhal number is also found for all prism configurations with non-zero edge-roundness values at $\alpha = 45°$, albeit in a slightly lesser extent with weaker sudden steps in the eddy shedding frequency. Corresponding to the mean global drag and the fluctuating lift forces, the Strouhal number attains at extremely high Reynolds numbers of $Re_D = 10^7$ similar values as those around 10^5, i.e. in the *subcritical* flow regime.

The identification of the level of rise and plunge of the eddy shedding frequency and the Reynolds numbers at which they occur as function of the edge roundness of the square-section prism at each one of the two "symmetric" incidence angles is important information. Obviously, it is essential to be aware of these jumps with respect to a possible vortex-induced excitation of the structure. At *subcritical*, i.e. "low" Reynolds numbers, a flexibly supported prism, which is allowed to oscillate freely in the direction transverse to the oncoming flow, will most likely oscillate harmonically at a relatively low frequency (i.e. low values for St_L) that is hardly affected by the bluffness of the prism's cross-section. However, the excitation amplitude is in that case expected to be quite significant, as can be derived by the high values of the fluctuating lift force, and will most probably increase as the edges become sharper.

During the transition from the *critical* flow regime to higher Reynolds numbers, e.g. at higher wind speeds or water currents, a severe drag reduction is obtained, but also the vibration properties possess sharp changes, with most probably a significant reduction in oscillation amplitude that is combined with a sudden jump to much higher vibration frequencies. While for $\alpha = 0°$ exactly this vibration state persists at least up to $Re_D = 10^7$, a recovery of the *subcritical* vibration state occurs at *transcritical* Reynolds numbers for $\alpha = 45°$. It is thus obvious that the fluid-elastic response of rounded square-section prisms actually results from an interplay of mainly the mean drag, the fluctuating lift, and the eddy shedding frequency, with both the Reynolds number and the edge roundness as governing parameters. Therefore, already during the design of a structure, a trade-off has to be made and compromises have to be found between the maximum acceptable vibration amplitude on the one hand and the vibration frequency on the other at all possible flow conditions that may occur over time.

Chapter 4

Surface-roughness effects on isolated square-section prisms with rounded edges at incidence

It is a common assumption in existing literature that surface roughness passively modifies the flow over 2D circular cylinders in such a way that post-critical, i.e. *supercritical* to even *transcritical* values of the fluid-dynamic parameters, belonging to 2D smooth circular cylinders, are obtained at physically low Reynolds numbers. The idea and physical mechanism behind this theory is that the transition from a laminar to a turbulent boundary layer is now triggered by the surface roughness at (significantly) smaller Reynolds numbers than is the case for the cylinder configuration with a smooth surface, provided, of course, that the height of the surface roughness is sufficiently large to actually influence the state of the boundary layer. In this way, the various flow regimes are shifted to lower Reynolds numbers; hence, as discussed in section 2.1.3, the right-bounded flow regimes appear already at relatively low Reynolds numbers that can still be achieved in low-speed wind and water tunnel facilities without the need for a modification of, for example, the diameter of the cylinder. The latter could, in fact, result in large geometric and effective aerodynamic blockage ratios and undesired wall effects, which then have to be corrected for in the post-processing of the measurement data, as well as a reduction in the cylinder's aspect ratio, thereby jeopardising the two-dimensional flow around the cylinder.

The interchangeability in effect between Reynolds number and surface roughness, which is often given as a justification for examining high-Reynolds number flow phenomena, is, however, questionable and should therefore be taken with caution. Particularly in the *critical*, *supercritical* and *upper transition* flow regimes is the outcome of a measurement sensitive to even the smallest disturbances in the flow conditions and in the local model surface topology (Schewe [210], Niemann and Hölscher [156], Zdravkovich [293]). This is for example the case for the transition and separation positions of the boundary layer on the surface of the cylinder, the resultant surface pressure distribution, and the three-dimensionality of the flow along the span of the cylinder. Because of their dependence on those quantities, the overall induced fluid-dynamic forces, the eddy formation in the base region, and the subsequent shedding in the near wake are also affected and altered.

This chapter addresses the effects of the presence and height of surface roughness on the fluid dynamics of not only 2D circular cylinders, but also of 2D sharp-edged and rounded square-section prisms, all of them placed in a steady cross-flow at Reynolds numbers ranging form 10^5 to 10^7. All measurements were once more performed in the High-Pressure wind tunnel

facility by using exactly the same test setup as described in section 3.1.1. Hence, except for the height of the surface roughness, none of the other boundary conditions were changed. In the previous chapter, it has been shown that the flow over smooth square-section prisms with edge roundness values of $r/D = 0.16$ or 0.29, placed at $\alpha = 45°$ or smooth circular cylinders has reached the *transcritical* regime well before $Re_D = 10^7$. This means that, in contrast to most reference studies, no changes in one or more boundary conditions need to be made during the experiments to be able to physically reach this flow regime at low-subsonic velocities and for low geometric blockage ratios. This made it possible to study the mere effect of a change in Reynolds number on one side and of the surface roughness height on the other in one single experiment as a fully decoupled system. The focus of the experimental investigations – of which the results are presented and discussed hereafter – could therefore be placed solely on the actual physical influence of the surface roughness on the fluid dynamics of these kinds of bluff bodies. In the area of offshore wind engineering and maritime engineering, this enables, for example, the analysis of the impact of biofouling (i.e. soft and hard marine growth) and its accumulation in time on the unsteady and mean flow around foundation elements of floating structures over all flow regimes from *subcritical* to *transcritical*.

Three different aspects are addressed hereafter. Section 4.1 demonstrates the impact of a variation in the surface roughness height on the global mean and fluctuating force coefficients and on the shedding frequency of the eddies in the near wake of a square-section prism with a fixed edge roundness of $r/D = 0.16$. The non-dimensional equivalent sand-grain surface roughness height has therefore been varied in the range of $k_s/D = 10^{-6}$ (hereafter denoted as "smooth") up to 10^{-3} ("very rough"). It is presented that in this case the Reynolds number and the roughness height can both be treated as governing parameters, since they both have a strong effect on the behaviour of the flow around the prism at the two "symmetric" angles of incidence, i.e. $\alpha \in \{0°, 45°\}$. The discussion of the results is accompanied by a first explanation of the physical background of the flow changes induced by those two parameters through analysis of the cross-sectional pressure distribution on the surface of the prism.

In Chapter 3, it was shown that the spanwise edge rounding of smooth square-section prisms has a distinct effect on their fluid-dynamic behaviour. Based on the outcomes of the preceding experimental study on the effect of k_s/D on the flow over a rounded square-section prism with $r/D = 0.16$, presented in section 4.1, the roughness height of $k_s/D = 1 \times 10^{-3}$ (hereafter denoted as "rough") has been selected and applied on the surface of each of the previous four prismatic and cylindrical bluff bodies. Depending on the combination of the amount of edge rounding and the incidence angle, the rough configurations experience different fluid-dynamic loads and eddy-shedding frequencies compared to their smooth counterparts, in particular in the *supercritical* up to *transcritical* flow regimes. These results are presented in section 4.2.

Finally, section 4.3 discusses the combined effect of variations in both the Reynolds number and the incidence angle on the fluid dynamics of a square-section prism with $r/D = 0.16$ and $k_s/D = 4.5 \times 10^{-4}$ (hence, "slightly rough") for angles of incidence in the range of $-3.25°$ to $45°$. A thorough analysis of the cross-sectional surface pressure distribution gives insight into the behaviour of the boundary layer on the prism and of the free shear layers. The stability criterion by Den Hartog for a susceptibility to transverse *galloping* and the criterion for torsional *galloping*, both presented in section 1.2.2, are applied to the measurement data. It is shown that, according to the two criteria that are based on the quasi-steady theory, this specific square-section prism is expected to be prone to both motion-induced vibrations in specific single- or double-bounded ranges of Reynolds numbers.

4.1 From smooth to very rough: influence of surface roughness height on the fluid dynamics of a square-section prism with $r/D = 0.16$ at $\alpha = 0°$ and $45°$

4.1.1 Mean loading

Figure 4.1a presents the variation of C_D, C_{pb}, and $|C_L|$ with Reynolds number for an isolated 2D prism with rounded edges of $r/D = 0.16$ at $\alpha = 0°$ and $45°$. The value of the surface roughness height was varied between $k_s/D = 4.5 \times 10^{-6}$ ("smooth") and 1.4×10^{-3} ("very rough"). The curves for the smooth prism have already been discussed in Chapter 3 and are therefore taken as reference. A distinct effect of the surface roughness on the fluid-dynamic coefficients is found for both incidence angles. However, the way in which those coefficients are influenced by a variation in k_s/D strongly differs between the two angles of incidence. At both angles, an increase in the roughness height induces a common shift of the various flow regimes towards lower Reynolds numbers in combination with a decrease of their widths, i.e. the covered Reynolds-number
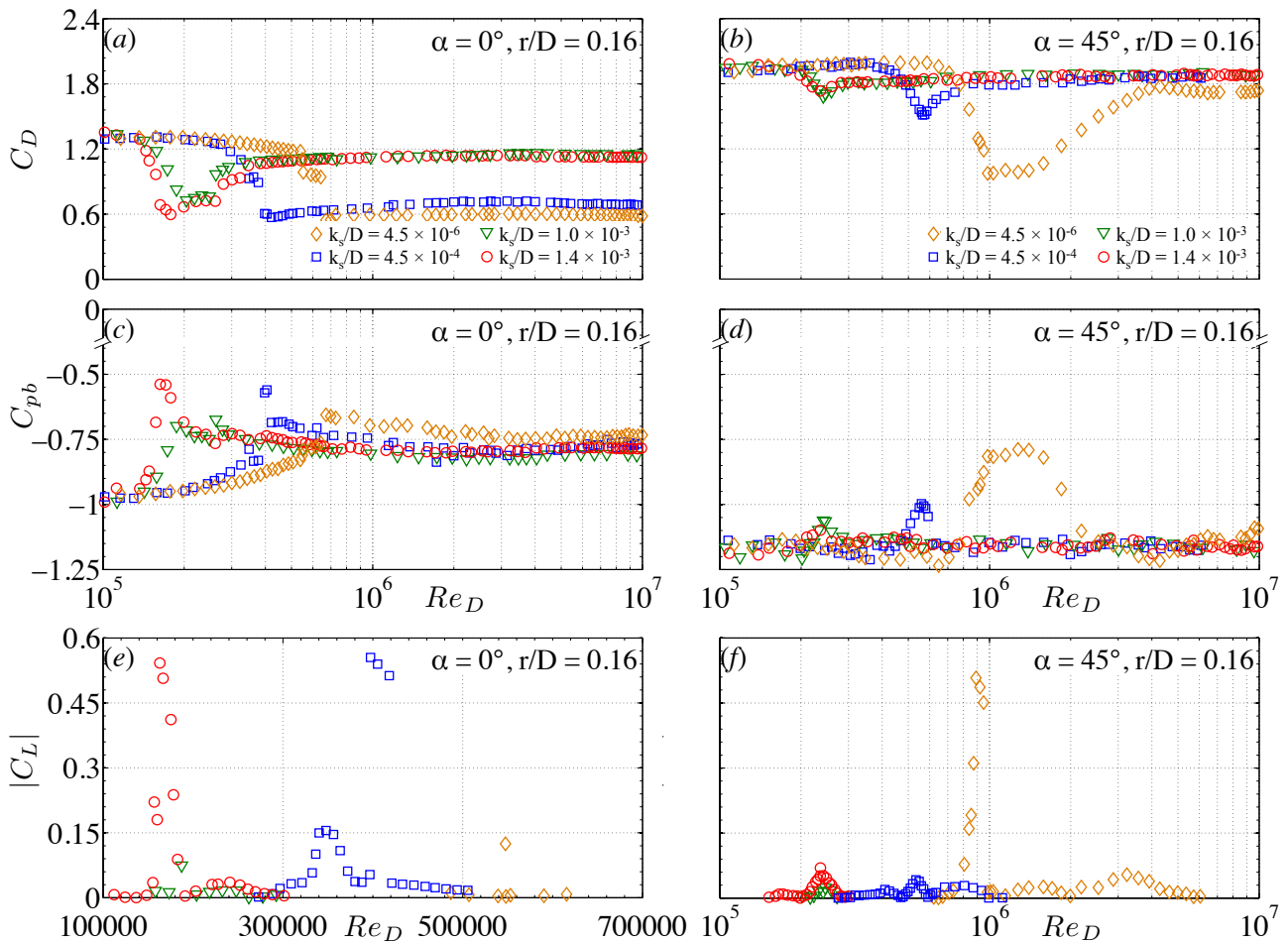
Figure 4.1: Impact of increasing non-dimensional equivalent sand-grain surface roughness height on the mean global drag (upper row), mean cross-sectional base pressure (centre row), and absolute mean global lift (lower row) coefficients for a 2D square-section prism with edge roundness of $r/D = 0.16$ at $\alpha = 0°$ and $45°$ at Reynolds numbers between 10^5 and 10^7 (Van Hinsberg *et al.* [254, 255], Van Hinsberg [257]).

range per flow regime. This leads to the interesting phenomenon, that Reynolds numbers which belong to the *subcritical* flow regime for the smooth prism have shifted to the *transcritical* flow regime for $\mathcal{O}(10^{-3})$. These trends are in good agreement with the changes in flow behaviour over circular cylinders with increased surface roughness height, as presented in section 2.1.3. At $\alpha = 45°$, this similarity in flow behaviour between the rounded prism and the circular cylinder covers also the independence of C_D and C_{pb} on the roughness height in the *subcritical* flow regime, the continuous increase of the minimum value of the mean global drag coefficient $C_{D,min}$ and of the mean cross-sectional base pressure coefficient $C_{pb,min}$ with increasing k_s/D at the cross-over from the *critical* to the *supercritical* flow regime, and their constant *transcritical* values that extend over a very long range of Reynolds numbers. The same holds for the gradual decrease of the mean steady lift force that appears in the short *asymmetric* flow state within the *critical* flow regime, see Figure 4.1f. All of these changes indicate an increasing independence of the flow around the prism on the Reynolds number. This trend is also visible by a direct comparison of the shapes of the mean vertical wake profile at selected *subcritical* to *transcritical* Reynolds numbers for all four surface roughness heights, shown in the right column of Figure 4.2. With increasing Reynolds number, significant changes in $\Delta p/q$ along the complete vertical plane, as well as in the derived mean non-dimensional wake width Z_w/D and in the maximum total non-dimensional pressure loss $\left(\Delta p/q\right)_{max}$ (listed in Table 4.1) occur for the smooth prism. In contrast, only minor changes in the values of $\left(\Delta p/q\right)_{max}$ around $Z/L_{ref} = 0$ and of Z_w/D occur with increasing Reynolds number for larger surface roughness heights. The status of the Reynolds number as a governing parameter thus reduces with increasing surface roughness height, thereby showing the increased influence of the latter parameter which gradually transitions from an influencing parameter to the main governing one. Interestingly, this is, however, not the case at $\alpha = 0°$. At this incidence angle, an increase of the surface roughness height by a factor of 100 (i.e. from "smooth" to "slightly rough") has practically no influence on the values of C_D, C_{pb}, and $|C_L|$ in the *subcritical*, *critical*, and *supercritical* flow regimes (Figure 4.1). The same holds for the mean vertical wake profile in Figure 4.2 (left column), the mean non-dimensional width, and the maximum total non-dimensional pressure loss (Table 4.1). For both surface-roughness values, the cross-over from the *critical* to the *supercritical* flow regime is accompanied by a sudden step in the $C_D(Re_D)$ and $C_{pb}(Re_D)$ curves, in contrast to the respective curves at $\alpha = 45°$ for which no such plunge of both coefficients is visible. A further doubling of the value of k_s/D from "slightly rough" to "rough" leads then again to the appearance of an upper bound of the *supercritical* flow regime and the occurrence of both an *upper transition*, characterised by a strong recovery of both C_D and C_{pb}, and subsequent *transcritical* flow regime. This results in an increased Reynolds-number dependence of the various fluid-dynamic quantities for $1.4 \times 10^5 \leqslant Re_D \leqslant 3.8 \times 10^5$. The most striking difference with the results for $\alpha = 45°$ is that the roughness height itself has barely any effect on $C_{D,min}$ and $C_{pb,min}$, on the absolute values of the fluid-dynamic quantities at *subcritical* and *supercritical* Reynolds numbers, and on the strong changes associated with the *drag crisis* in the *critical* flow regime. Surprisingly, the mean cross-sectional base pressure coefficient depends only weakly on k_s/D for $Re_D \geqslant 3 \times 10^6$, regardless of the actual flow regime at those Reynolds numbers. For both incidence angles, an increase of k_s/D beyond 1×10^{-3} has little to no additional impact on the fluid dynamics and wake properties of this rounded square-section prism. This indicates that around $k_s/D = \mathcal{O}(10^{-3})$ the upper threshold has been reached where the surface boundary layer on the prism is still modified by an increasing roughness height. Achenbach [3] found in his experimental study on the loading on 2D smooth and rough circular cylinders a similar behaviour. He related this independence on the surface roughness to the fact that at very high roughness values the tops of the roughness elements are

located outside of the surface boundary layer and therefore generate no additional disturbing effect.

4.1.2 Fluctuating loads due to eddy formation and shedding

The fluid-dynamic coefficients associated with the shedding of the eddies in the near wake, i.e. the fluctuating global drag and lift that act on the prism and the Strouhal number, possess qualitatively similar trends with increasing surface roughness height over all flow regimes as
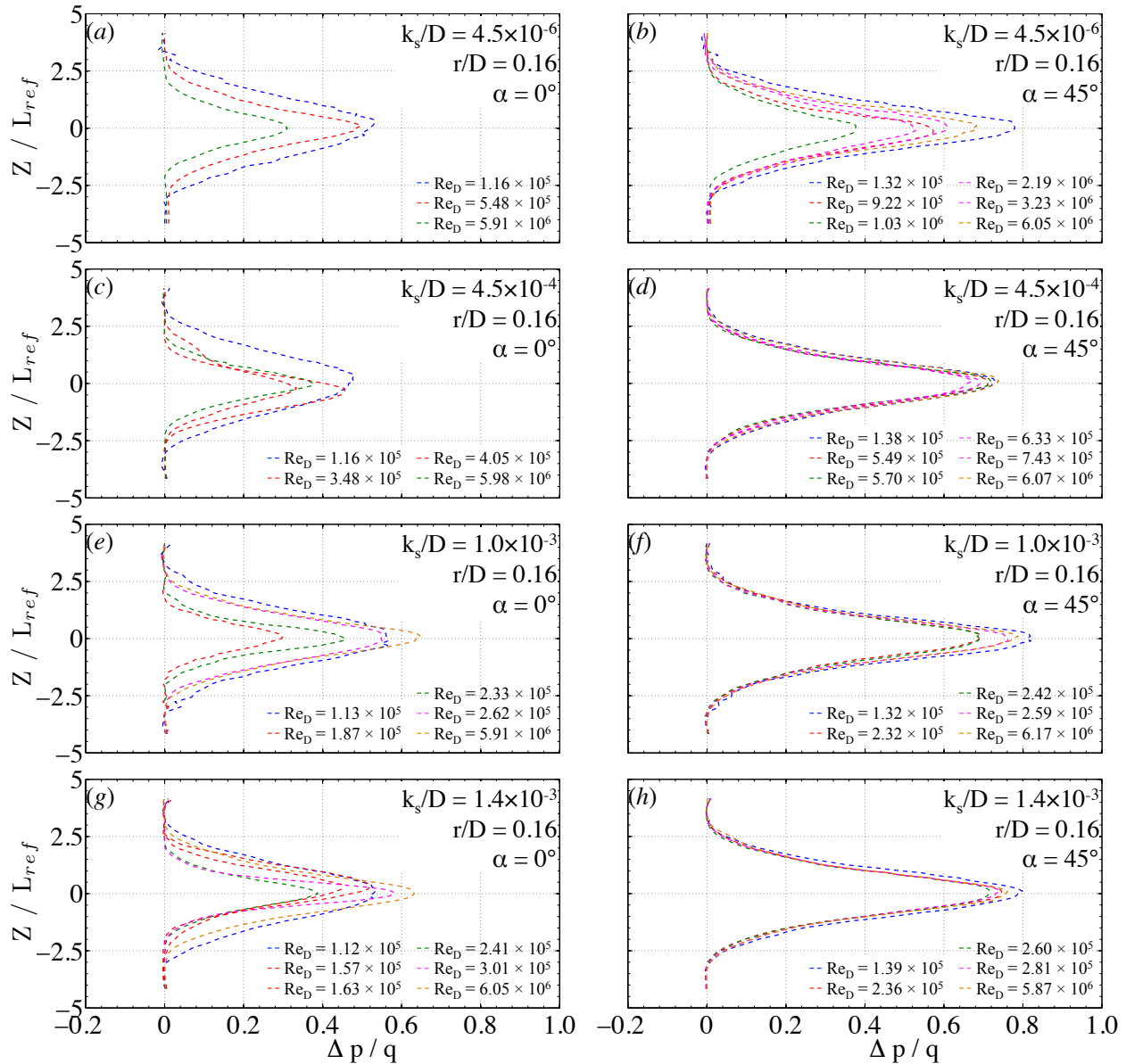
Figure 4.2: Effect of non-dimensional equivalent sand-grain surface roughness height on the mean vertical wake profile at $X/L_{ref} = 6.25$ behind the mid-span of a two-dimensional square-section prism with edge roundness of $r/D = 0.16$ for selected Reynolds numbers in the various flow regimes. Left column: $\alpha = 0°$; right column: $\alpha = 45°$. --: *subcritical* flow regime; --: *critical* flow regime; --: *supercritical* flow regime; --: *upper transition*; --: *transcritical* flow regime.

Table 4.1: Mean non-dimensional width Z_w/D and maximum total non-dimensional pressure loss $\left(\Delta p/q\right)_{max} = (p_0 - p_{max})/q_\infty$ of the wake at 6.25 prism widths downstream of the spanwise centre axis of a square section prism ($r/D = 0.16$, $k_s/D = 4.5{\times}10^{-6}$ to $1.4{\times}10^{-3}$, $\alpha = 0°$ and $45°$) at Reynolds numbers belonging to the various flow states.

Incidence angle α / °	Dimensionless surface roughness height k_s/D	Flow regime	Reynolds number Re_D	Mean wake width Z_w/D	Maximum total non-dimensional pressure loss $\left(\Delta p/q\right)_{max}$
0	$4.5{\times}10^{-6}$	subcritical	$1.16{\times}10^5$	6.0	0.53
		critical	$5.48{\times}10^5$	5.1	0.50
		supercritical	$5.91{\times}10^6$	3.8	0.31
	$4.5{\times}10^{-4}$	subcritical	$1.16{\times}10^5$	5.8	0.48
		critical	$3.48{\times}10^5$	$4.5^\dagger$	0.33
		critical	$4.05{\times}10^5$	$3.9^\dagger$	0.46
		supercritical	$5.98{\times}10^6$	3.8	0.38
	$1.0{\times}10^{-3}$	subcritical	$1.13{\times}10^5$	6.2	0.57
		critical	$1.87{\times}10^5$	3.0	0.30
		supercritical	$2.33{\times}10^5$	3.8	0.46
		upper transition	$2.62{\times}10^5$	4.7	0.55
		transcritical	$5.91{\times}10^6$	5.1	0.65
	$1.4{\times}10^{-3}$	subcritical	$1.12{\times}10^5$	6.0	0.53
		critical	$1.57{\times}10^5$	$4.3^\dagger$	0.45
		critical	$1.63{\times}10^5$	$4.0^\dagger$	0.52
		supercritical	$2.41{\times}10^5$	3.8	0.39
		upper transition	$3.01{\times}10^5$	3.3	0.58
		transcritical	$6.05{\times}10^6$	4.9	0.63
45	$4.5{\times}10^{-6}$	subcritical	$1.32{\times}10^5$	5.5	0.78
		critical	$9.22{\times}10^5$	5.1	0.57
		supercritical	$1.03{\times}10^6$	4.7	0.38
		upper transition	$2.19{\times}10^6$	5.3	0.53
		upper transition	$3.23{\times}10^6$	5.5	0.61
		transcritical	$6.05{\times}10^6$	5.5	0.68
	$4.5{\times}10^{-4}$	subcritical	$1.38{\times}10^5$	5.5	0.73
		critical	$5.49{\times}10^5$	5.1	0.71
		supercritical	$5.70{\times}10^5$	5.1	0.72
		upper transition	$6.33{\times}10^5$	5.3	0.69
		upper transition	$7.43{\times}10^5$	5.5	0.67
		transcritical	$6.07{\times}10^6$	5.5	0.74
	$1.0{\times}10^{-3}$	subcritical	$1.32{\times}10^5$	5.8	0.82
		critical	$2.32{\times}10^5$	5.5	0.69
		supercritical	$2.42{\times}10^5$	5.5	0.69
		upper transition	$2.59{\times}10^5$	5.5	0.76
		transcritical	$6.17{\times}10^6$	5.5	0.79
	$1.4{\times}10^{-3}$	ssubcritical	$1.39{\times}10^5$	5.5	0.80
		critical	$2.36{\times}10^5$	5.3	0.75
		supercritical	$2.60{\times}10^5$	5.1	0.72
		upper transition	$2.81{\times}10^5$	5.5	0.74
		transcritical	$5.87{\times}10^6$	5.5	0.76

† *asymmetric* flow state with one-sided separation bubble.

were obtained for C_D and C_{pb} at the two "symmetric" incidence angles (Figure 4.3). At $\alpha = 0°$, particularly noteworthy are once more the strong overlap between the curves for the two smallest roughness heights, the significant changes that occur when increasing the surface roughness from $k_s/D = 4.5{\times}10^{-4}$ to $1.0{\times}10^{-3}$, and the near-perfect overlap of the curves for the rough and very rough prism configurations. In addition, the independence on k_s/D of the *subcritical* flow regime at both incidence angles also shows up in the results of both fluctuating fluid-dynamic
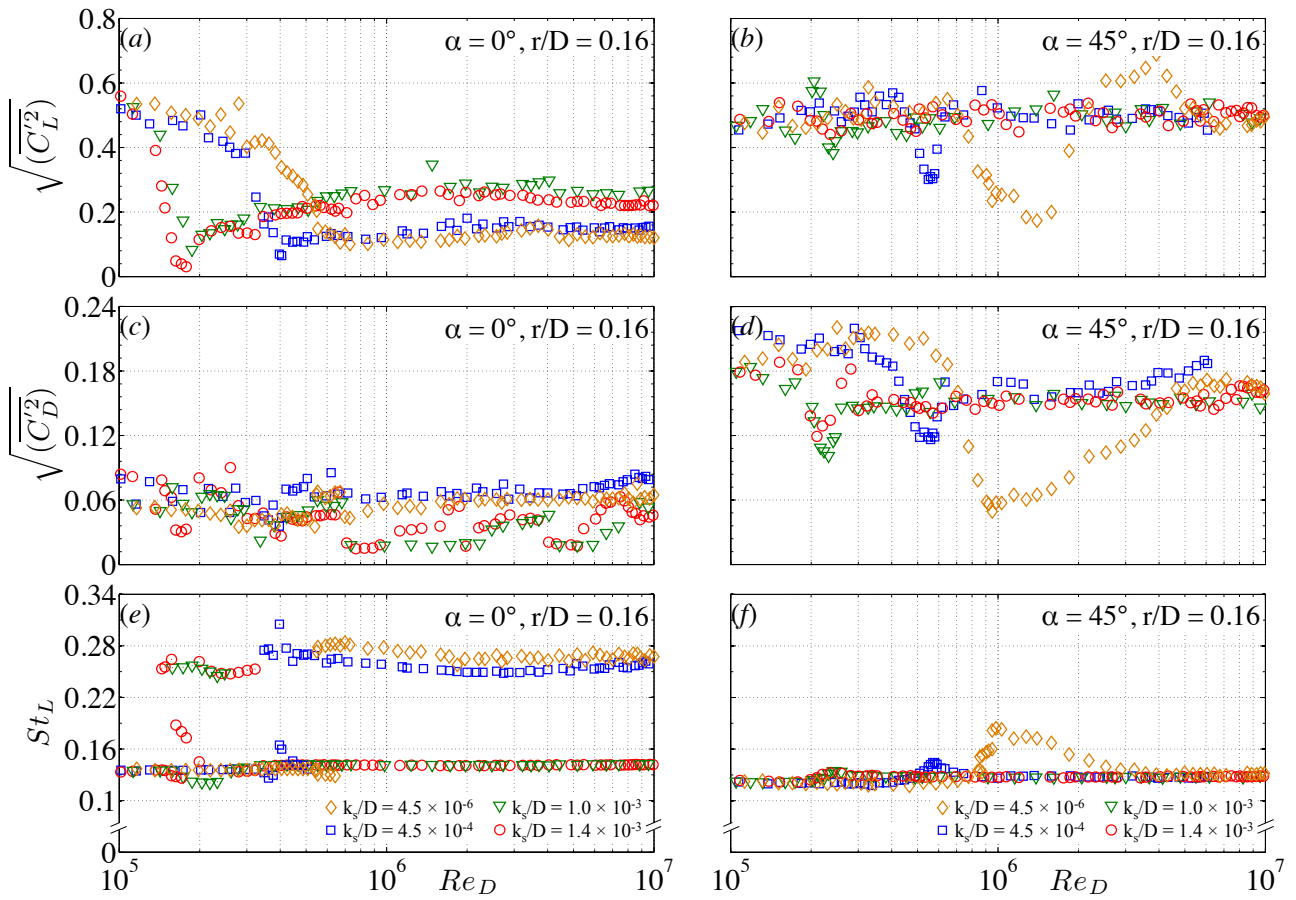
Figure 4.3: Impact of increasing non-dimensional equivalent sand-grain surface roughness height on the Reynolds-number-dependent fluctuating global lift (upper row) and drag (centre row) coefficients, as well as the Strouhal number (lower row) for a 2D square-section prism with edge roundness of $r/D = 0.16$ at $\alpha = 0°$ and $45°$ (Van Hinsberg *et al.* [254,255], Van Hinsberg [257]).

forces and the Strouhal number. Moreover, the same can be said about the minimum values of the fluctuating global forces at the cross-over from the *critical* to the *supercritical* flow regime and their subsequent *supercritical* values, both at $\alpha = 0°$. Subtle differences with the previously described trends of C_D and C_{pb} with Reynolds number and surface roughness height do nonetheless emerge. For instance, the steep drops that occur in various $C_D(Re_D)$ curves in the *critical* flow regime in Figure 4.1a are in the corresponding curves of the fluctuating global drag and lift coefficients (Figures 4.3a and 4.3c) either only moderate or even non-existent at the same Reynolds numbers. The same applies to the somewhat weaker steps that appear in the *upper transition* for the rough and very rough prism configurations, as well as the recovery of $\sqrt{\overline{(C_L'^2)}}$ in this same flow regime that is much less pronounced compared to C_D. Interestingly, the influence of k_s/D on the fluctuating global drag is only weak at $\alpha = 0°$. An exception forms the *transcritical* flow regime where stronger variations with both k_s/D and Re_D take place. The nearly perfect match of the values of the fluctuating global lift coefficient and Strouhal number for the smooth and slightly rough prism and for the rough and very rough one can be explained by looking at the underlying power spectra of the time series of the global lift forces at selected Reynolds numbers in the Figures 4.4a to 4.4d. Per prism pair, very similar spectral distributions with a main peak at a nearly equal value of $f_L D/U_\infty$ (see also Table 4.2) and with similar heights have been obtained for each flow regime. Hence, not only the shedding

frequencies of the eddies coincide, but also the intensity with which they are shed as the latter can be derived from the values of the fluctuating lift and drag forces.

Compared to $\alpha = 0°$, much larger fluctuations in the global lift and drag forces occur for all
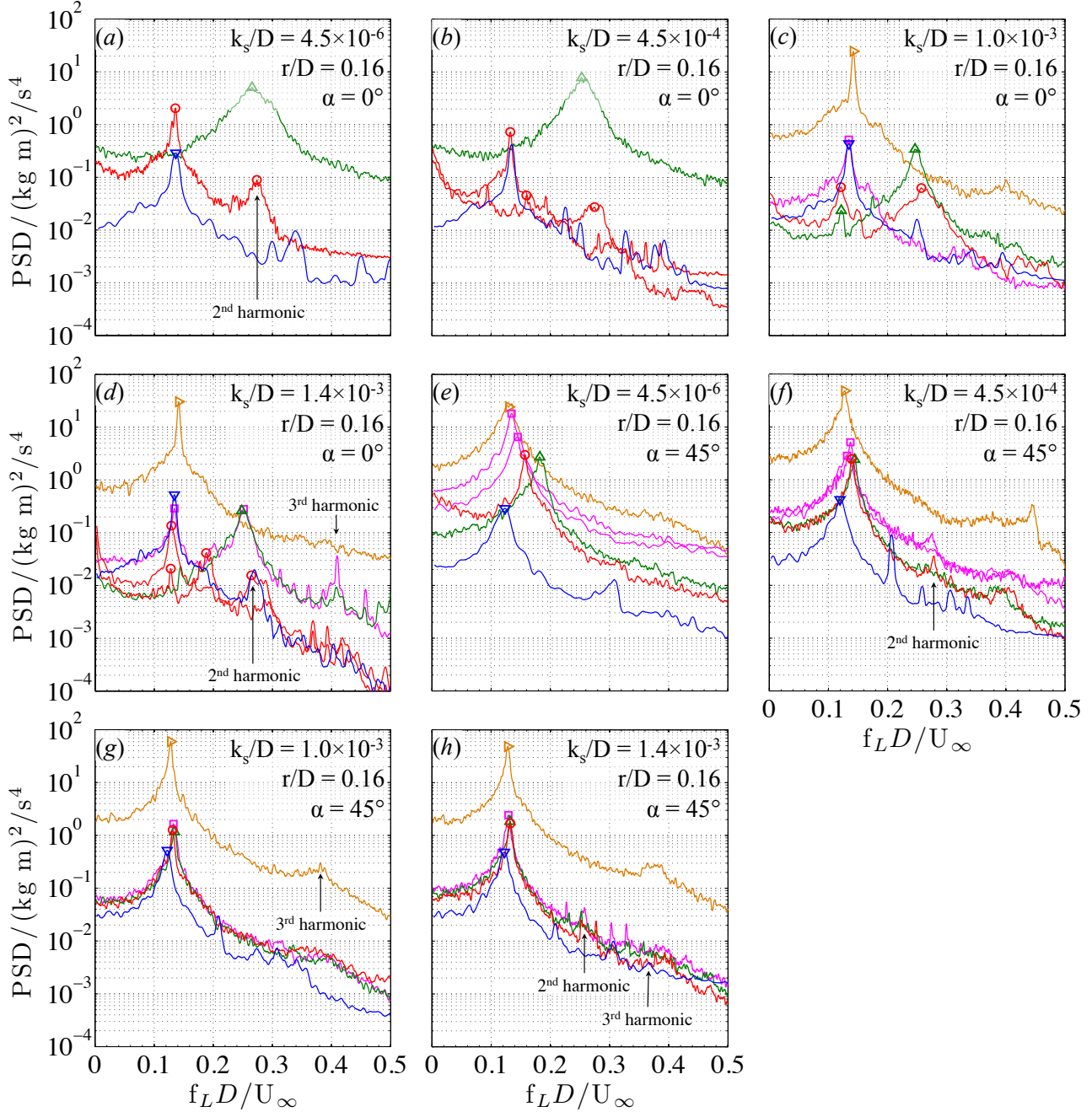
Figure 4.4: Effect of non-dimensional equivalent sand-grain surface roughness height on the PSD of the time series of the global lift force for a two-dimensional square-section prism with edge roundness of $r/D = 0.16$ for selected Reynolds numbers in the various flow regimes (Partially adapted from Van Hinsberg [256]). (a)-(d): $\alpha = 0°$; (e)-(h): $\alpha = 45°$. ——: *subcritical* flow regime; ——: *critical* flow regime; ——: *supercritical* flow regime; ——: *upper transition*; ——: *transcritical* flow regime. The corresponding Strouhal numbers are indicated by symbols on the curves and listed in Table 4.2. In case of the occurrence of two Strouhal numbers at equal Reynolds number, both have been highlighted in the graphs.

Table 4.2: Values of the Strouhal numbers – based on the main, and when applicable also the secondary, frequency peak in the PSDs of the time series of the lift $L(t)$ in Figure 4.4 – for selected Reynolds numbers in the various flow regimes. Properties of the square-section prism: $r/D = 0.16$, $4.5{\times}10^{-6} \leqslant k_s/D \leqslant 1.4{\times}10^{-3}$, and $\alpha = 0°$ and $45°$.

Edge roundness r/D	Incidence angle α / $°$	Surface roughness height k_s/D	Flow regime	Reynolds number Re_D	Strouhal number(s)[†]	
					$St_{L,1}$	$St_{L,2}$
0.16	0	$4.5{\times}10^{-6}$	subcritical	$1.16{\times}10^5$	0.136	–
			critical	$5.48{\times}10^5$	0.136	0.274
			supercritical	$5.91{\times}10^6$	0.266	–
		$4.5{\times}10^{-4}$	subcritical	$1.16{\times}10^5$	0.135	–
			critical	$3.48{\times}10^5$	0.132	0.257
			critical	$4.05{\times}10^5$	0.160	–
			supercritical	$5.98{\times}10^6$	0.253	–
		$1.0{\times}10^{-3}$	subcritical	$1.13{\times}10^5$	0.135	–
			critical	$1.87{\times}10^5$	0.121	0.257
			supercritical	$2.33{\times}10^5$	0.246	0.122
			upper transition	$2.62{\times}10^5$	0.134	–
			transcritical	$5.91{\times}10^6$	0.142	–
		$1.4{\times}10^{-3}$	subcritical	$1.12{\times}10^5$	0.134	–
			critical	$1.57{\times}10^5$	0.129	0.264
			critical	$1.63{\times}10^5$	0.188	0.128
			supercritical	$2.41{\times}10^5$	0.248	–
			upper transition	$3.01{\times}10^5$	0.134	0.251
			transcritical	$6.05{\times}10^6$	0.141	–
	45	$4.5{\times}10^{-6}$	subcritical	$1.32{\times}10^5$	0.123	–
			critical	$9.22{\times}10^5$	0.157	–
			supercritical	$1.03{\times}10^6$	0.182	–
			upper transition	$2.19{\times}10^6$	0.145	–
			upper transition	$3.23{\times}10^6$	0.135	–
			transcritical	$6.05{\times}10^6$	0.130	–
		$4.5{\times}10^{-4}$	subcritical	$1.38{\times}10^5$	0.120	–
			critical	$5.49{\times}10^5$	0.139	–
			supercritical	$5.70{\times}10^5$	0.144	–
			upper transition	$6.33{\times}10^5$	0.137	–
			upper transition	$7.43{\times}10^5$	0.132	–
			transcritical	$6.07{\times}10^6$	0.127	–
		$1.0{\times}10^{-3}$	subcritical	$1.32{\times}10^5$	0.122	–
			critical	$2.32{\times}10^5$	0.131	–
			supercritical	$2.42{\times}10^5$	0.135	–
			upper transition	$2.59{\times}10^5$	0.133	–
			transcritical	$6.17{\times}10^6$	0.128	–
		$1.4{\times}10^{-3}$	subcritical	$1.39{\times}10^5$	0.122	–
			critical	$2.36{\times}10^5$	0.132	–
			supercritical	$2.60{\times}10^5$	0.132	–
			upper transition	$2.81{\times}10^5$	0.129	–
			transcritical	$5.87{\times}10^6$	0.128	–

[†] $St_{L,1}$ and $St_{L,2}$ correspond to the dimensionless vortex-shedding frequencies at the main and secondary peak, respectively.

surface roughness heights at $\alpha = 45°$. The decreased dependence on the Reynolds number with increasing surface roughness height, previously discussed for C_D and C_{pb}, is also clearly visible in the curves for the fluctuating global lift and drag coefficients and the Strouhal number in Figure 4.3. While for the smooth prism large changes occur over a wide range of Reynolds numbers that covers the *critical* to *upper transition* flow regimes, only a small (fluctuating global lift) to moderate (fluctuating global drag) dip in the curves appears in the same flow regimes for

the very rough prism configuration. The same is true for the $St_L(Re_D)$ curves: the "hill" over those flow regimes at $k_s/D = 4.5\times10^{-6}$ has diminished to a wake bump at $k_s/D = 1.4\times10^{-3}$. The underlying power spectra at selected Reynolds numbers in Figure 4.4e for the smooth prism show both a shift of the main peak and a variation in its height among the various flow regimes. With increasing roughness height, the range of non-dimensional frequencies in which the main peak wanders shrinks gradually – i.e. the variation in the Strouhal number with Reynolds number reduces, as is also listed in Table 4.2 – and only a variation of the peak height remains. This explains the clear changes in the values of the fluctuating lift and drag forces with Reynolds number that still occur even for the very rough prism within $Re_D = 2\times10^5$ to 3×10^5 in Figure 4.3b and 4.3d. The recovery of the fluctuating global lift coefficient over the *upper transition* is then again much more pronounced at $\alpha = 45°$ than at $\alpha = 0°$, resulting in *transcritical* values that correspond to those present in the *subcritical* flow regime.

4.1.3   Mean surface pressure distributions

In the previous section, the very weak dependence on the surface roughness height of the various fluid-dynamic coefficients and wake parameters (i.e. the shape of the mean vertical wake profile and the associated mean non-dimensional wake width, as well as the maximum total non-dimensional pressure loss) for *subcritical* to *supercritical* Reynolds numbers at $\alpha = 0°$, together with the values of $C_{D,min}$, $C_{pb,min}$, $\sqrt{(\overline{C_L'^2})}_{min}$, and $\sqrt{(\overline{C_D'^2})}_{min}$ at the cross-over from the *critical* to the *supercritical* flow regime were addressed. The underlying cause becomes visible by a closer inspection of the mean pressure distribution over the mid-span cross-section of the prism. Figure 4.5 presents a quantitative and qualitative (i.e. scaled vectorial) distribution of the mean cross-sectional surface pressure coefficients for the slightly rough and very rough prism at three exemplary Reynolds numbers that belong to the *subcritical, critical*, and *supercritical* flow regimes. A direct comparison between the mean surface pressure distributions on both prisms shows a remarkable similarity in each flow regime, despite the shift of the Reynolds numbers towards lower values for the very rough prism. This includes not only the height of the plateaus of C_p in the base region of both prisms, but even more remarkably also the shape(s) and maximum value(s) of the negative pressure peak(s) at $s/D = 0.98$ (i.e. on the rounded edge between the surfaces *I* and *II*) and $s/D = 3.67$ (i.e. on the rounded edge between the surfaces *I* and *IV*) in the *critical* and *supercritical* flow regimes. These pressure peaks on the upstream-directed edges are associated with the formation of a separation bubble further downstream on the side surface(s) *II* and/or *IV*. It implies a highly surface-roughness-independent behaviour of (*1*) the positions at which the boundary layer separates from the surface over both windward-directed rounded edges, (*2*) the reattachment locations of the free shear layers on the side faces *II* and *IV*, and (*3*) the positions of the following secondary separation of the attached boundary layer on the leeward rounded edges. It is thus not surprising that the resultant mean and fluctuating fluid-dynamic forces, the eddy-shedding frequency, and the (near-)wake properties are also only weakly influenced by an increase of the surface roughness height at those flow regimes.

The independence of the fluid-dynamic coefficients on k_s/D at *subcritical* Reynolds numbers is actually well known from the many experimental and numerical studies on the flow around smooth and (slightly) rough 2D circular cylinders, e.g. Achenbach [2, 3], Güven *et al.* [91], Buresti [39], Niemann and Hölscher [156], Zdravkovich [293], Lehmkuhl *et al.* [131], and Rodríguez *et al.* [195]. In this flow regime, the attached laminar boundary layer has a large thickness with respect to the height of the surface roughness and is therefore relatively unaffected by an increase in roughness height – up to a certain upper threshold – up to separation
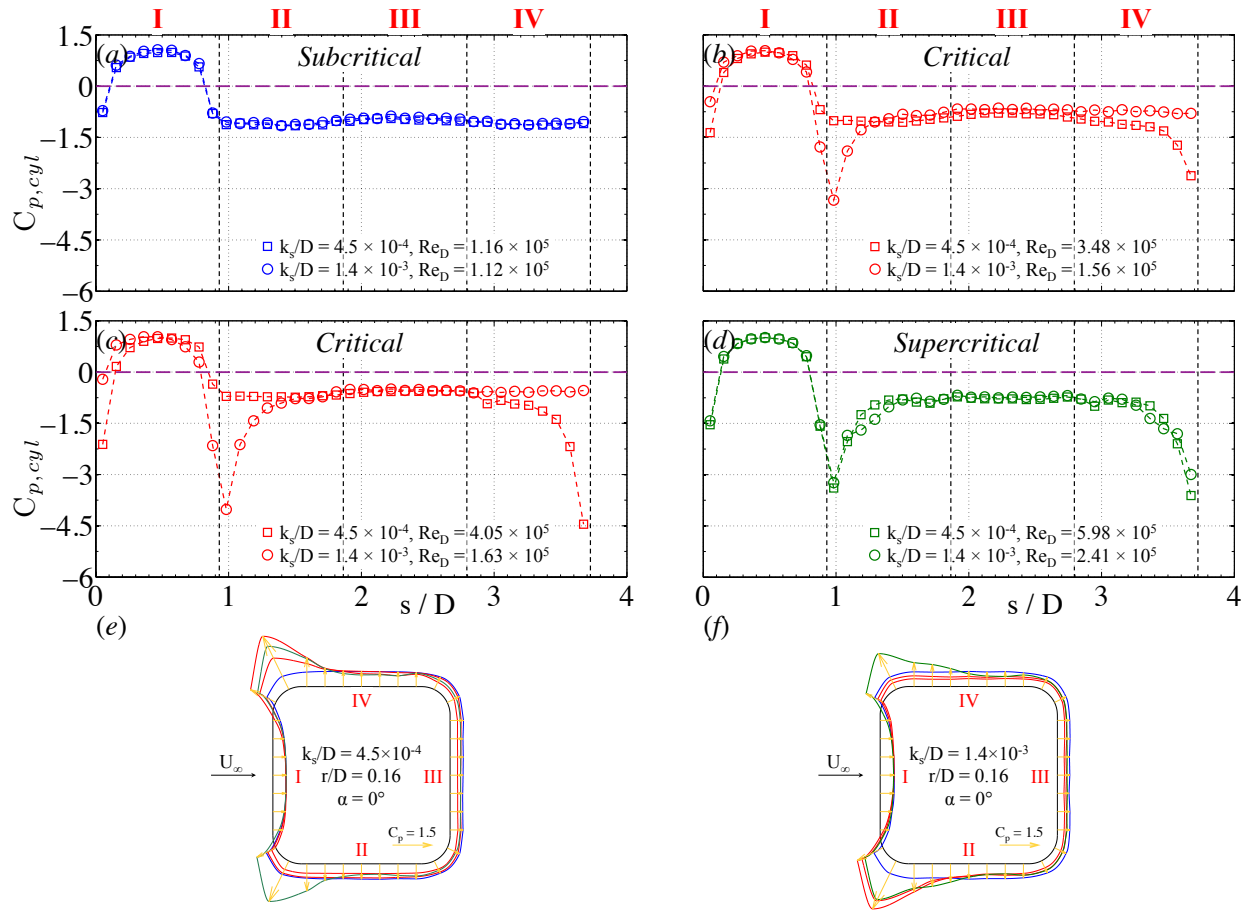
Figure 4.5: Comparison of the mean cross-sectional pressure distribution over the mid-span of a slightly rough ($k_s/D = 4.5 \times 10^{-4}$) and highly rough ($k_s/D = 1.4 \times 10^{-3}$) two-dimensional square-section prism with edge roundness values of $r/D = 0.16$, placed at $\alpha = 0°$ (Adapted from Van Hinsberg [256]). (a): *subcritical* flow regime; (b)-(c): *critical* flow regime; (d): *supercritical* flow regime; (e): qualitative scaled vectorial representation for the slightly rough prism; (f): qualitative scaled vectorial representation for the highly rough prism. —: *subcritical* flow regime; —: *critical* flow regime; —: *supercritical* flow regime.

from the cylinder. In experimental studies on 2D smooth and (slightly) rough circular cylinders in cross-flow by Fage [73], Achenbach [2], Okajima and Nakamura [175], and Adachi [6], it was furthermore proven that a continuation of this weak influence of the surface-roughness height also exists throughout the *critical* and even in the ensuing *supercritical* flow regime as long as k_s/D remains smaller than 5×10^{-4}. Above this threshold, a flattening of the curves of C_D, $C_{p,b}$, and St_L with Reynolds number was observed in combination with a decrease of the *critical* Reynolds number at which $C_{D,min}$, $C_{pb,min}$, and $St_{L,max}$ take place. This latter behaviour corresponds to the currently obtained trends of these three and other fluid-dynamic parameters for the rounded square-section prism at $\alpha = 45°$ in the Figures 4.1 and 4.3. Similar to the circular cylinder flow, the boundary layer is attached to the windward-directed surfaces *I* and *II*, its primary separation occurs over or slightly downstream of the rounded shoulder edges and the (local) continuous surface allows a migration of the separation position along this surface with changing Reynolds number (Figures 4.6c, 4.6d, 4.6g, and 4.6h). It can therefore be expected, that an increase in surface roughness height has a similar effect on the boundary

103

layer and thus also on the resultant fluid dynamics as known from flows over circular cylinders.

Figure 4.6 presents the mean cross-sectional surface pressure distributions on the slightly rough and very rough prisms at selected *subcritical* to *transcritical* Reynolds numbers for both incidence angles. For a clear qualitative visualisation of these distributions, the scaled vectorial representations have been included as well. Based on these surface pressure distributions in combination with the results presented in the Figures 4.1 to 4.4, the following behaviour of and changes in the flow field around the rounded square-section prisms can be derived when passing from one flow regime to the next:

(a.) $\alpha = 0°$

(1.) *Subcritical* flow regime
The attached boundary layer on the windward-directed surface I separates over both rounded edge between the faces I and II and between I and IV of the prism, independent of the height of the roughness on both faces. The relatively flat pressure distributions on the two side faces II and IV imply the absence of a reattachment of both free shear layers on them. In addition, the negative pressure values indicate the presence of two large recirculation regions in between these faces and the free shear layers. From the many experimental and numerical studies on the flow around sharp-edged square-section prisms, it is known that these backflow regions force a strong lateral spreading of the two free shear layers and the outer streamlines along the side faces (e.g. Figure 2.27(a)). The occurrence of this large deflection for the smooth and (slightly) rough rounded square-section prisms is confirmed by the large mean wake width of $Z_w/D = 5.8$ to 6.2 at a location of $X = 5.75D$ downstream of the base of the prism (Figure 4.2 and Table 4.1) and the high mean global drag coefficients of $C_D \approx 1.3$ at *subcritical* Reynolds numbers in Figure 4.1a for all four investigated prism configurations. The strong fluctuations of C_L in Figure 4.3a furthermore indicate an intense interaction of both free shear layers in the base region during the process of rolling up into eddies, which results in a high suction at the base (i.e. $C_{pb} = -0.97$ in Figure 4.1c), whereas the fluctuations in flow direction remain small (Figure 4.3c). The narrow main peak in the power spectra of the unsteady lift force in Figure 4.4 reveals a strong periodic shedding of the eddies at a main dimensionless frequency of $St_L = 0.13$–0.14.

(2.) *Critical* flow regime
The gradual (partly asymmetric) reduction of the mean wake width Z_w/D implies a decrease of the lateral spreading of the free shear layers and thus a shrinkage of the recirculation regions above the two side faces. The latter is confirmed by the gradual decrease of the negative value of the pressure coefficients on these surfaces. The resultant lower effective aerodynamic blockage ratio, together with the sharp rise of the mean base pressure coefficient, explain the decrease of C_D (Figure 4.1). Studies on flows over circular cylinders at *subcritical* and *critical* Reynolds numbers have demonstrated that those flow changes are mainly caused by a shift of the transition location along both free shear layers in the direction of the primary separation location. The steep decrease of the fluctuating lift in Figure 4.3, in combination with the reduced suction on the prism's base face, are evidence of a weaker interaction of both shear layers in the base region of the prism. The passage of the *asymmetric* flow state is characterised by the appearance of a distinct asymmetric
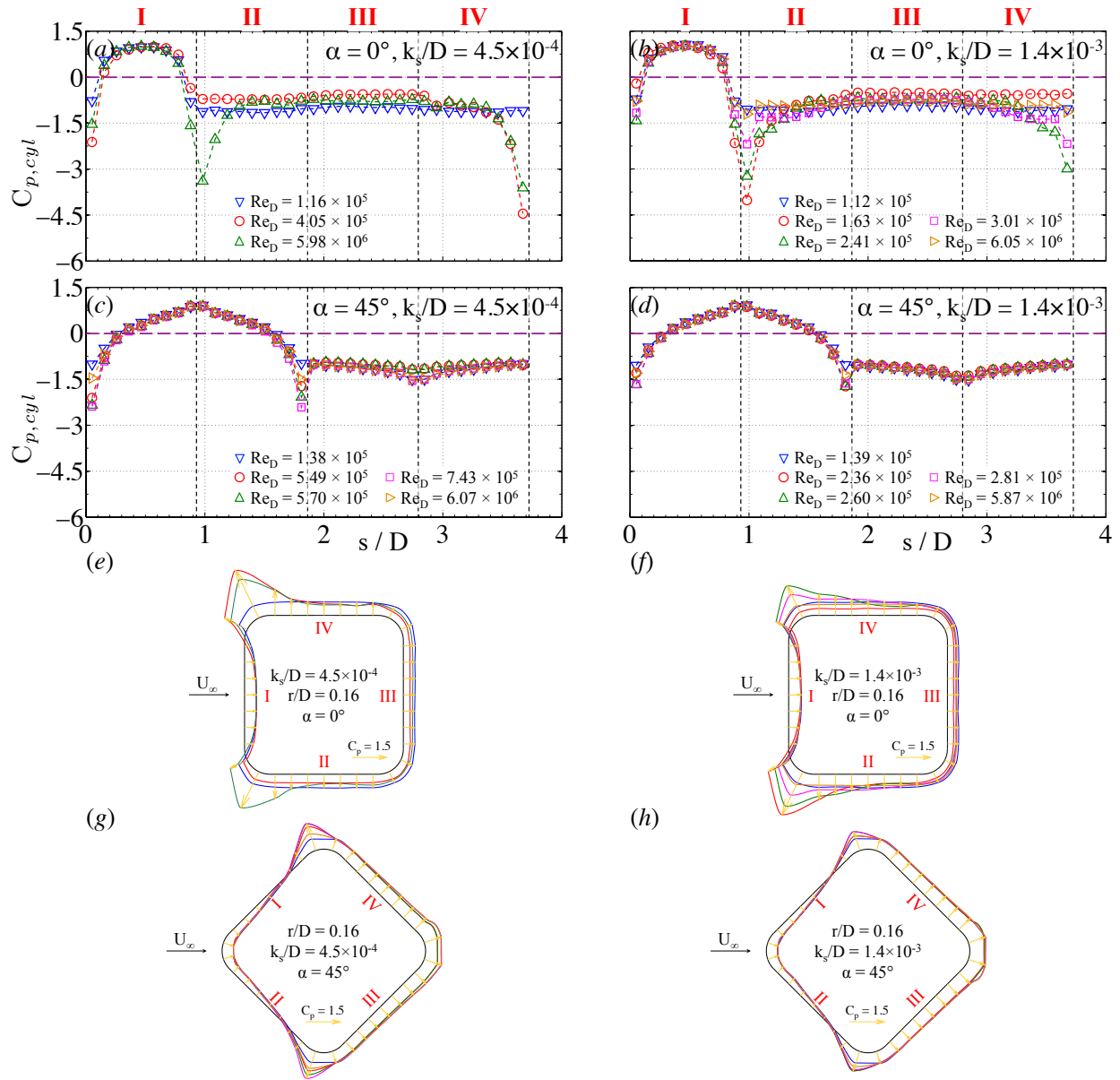
Figure 4.6: Comparison of the mean cross-sectional pressure distribution over the mid-span of a slightly rough ($k_s/D = 4.5\times10^{-4}$) and highly rough ($k_s/D = 1.4\times10^{-3}$) two-dimensional square-section prism with edge roundness values of $r/D = 0.16$, placed at $\alpha = 0°$ or $45°$ to the oncoming flow (Adapted from Van Hinsberg [256]). (a)-(b): $\alpha = 0°$; (c)-(d): $\alpha = 45°$; (e): qualitative scaled vectorial representation for the slightly rough prism at $\alpha = 0°$; (f): qualitative scaled vectorial representation for the highly rough prism at at $\alpha = 0°$; (g): qualitative scaled vectorial representation for the slightly rough prism at $\alpha = 45°$; (h): qualitative scaled vectorial representation for the highly rough prism at at $\alpha = 45°$; left column: $k_s/D = 4.5\times10^{-4}$; right column: $k_s/D = 1.4\times10^{-3}$. ——: *subcritical* flow regime; ——: *critical* flow regime; ——: *supercritical* flow regime; ——: *upper transition*; ——: *transcritical* flow regime.

surface pressure distribution that is caused by the formation of a laminar separation bubble on one of the two side faces slightly downstream of the windward-directed rounded edge and the upstream portion of the side face (Figures 4.6b and 4.6c). The re-separation of the attached turbulent boundary layer occurs further down-

105

stream over the leeward-directed edge of the prism, induced by the strong pressure increase in the surface boundary layer over that curved surface. The free shear layer at the opposite side of the prism remains fully separated up to the base region, as the energy of the flow is not yet sufficiently high to force a reattachment at that side of the prism as well. Interesting to note is that the one-sided reattachment of the free shear layer on the side face IV (for the prism with a surface roughness of $k_s/D = 4.5{\times}10^{-4}$) or II ($k_s/D = 1.4{\times}10^{-3}$) in Figure 4.6 is still clearly visible in the asymmetric vertical wake profiles in the Figures 4.2c and 4.2g. In particular at the *critical* Reynolds numbers $Re_D = 3.48{\times}10^5$ ($k_s/D = 4.5{\times}10^{-4}$) and $Re_D = 1.57{\times}10^5$ ($k_s/D = 1.4{\times}10^{-3}$) the wake profiles are composed of a *subcritical* branch at the side at which no reattachment of the free shear layer has occurred yet and a *supercritical* branch at the opposite side, both of which overlap relatively well with the mean wake profiles at their respective flow regime at lower or higher Reynolds numbers. As a result of the different positions of the boundary layer separation on the prism, a much weaker communication of the two shear layers in the base region of the prism takes place, as is projected by a sharp decrease of the fluctuating lift force. The mean suction at the base decreases thereupon further, which, in combination with an increased reduction of the effective aerodynamic blockage ratio, results in a sharp drop of the mean drag force. The appearance of two main peaks in the power spectra of the unsteady lift force at all four prism configurations in the Figures 4.4a to 4.4d demonstrates that the flow around each prism and thus the topology of its near wake is quite dynamic, as it switches at this specific *critical* Reynolds number continuously back and forth between the *subcritical* and the *supercritical* flow regimes. The height of each peak is a measure of the occurrence of that respective stage during the measurement. With increasing surface roughness height, both the start of the *critical* flow regime and the final cross-over from the *critical* to the *supercritical* flow regime are shifted to lower Reynolds numbers. At the cross-over the flow around the prism regains its symmetry, as both free shear layers can reattach to their respective side faces. A sharp drop in the curves of the mean drag, mean lift, and fluctuating lift coefficients, as well as a step to a lower negative mean base pressure coefficient are all evidence of this event.

(3.) *Supercritical* flow regime

The presence of a strong adverse pressure recovery region at the upstream part of both side faces right downstream of the windward-directed edges in Figure 4.6 implies a firm settlement of the two laminar separation bubbles on these side surfaces. The narrow near wake of less than 4 prism widths and the lowest values of the fluctuating lift force and mean base pressure coefficient hint on the presence of a small recirculation region behind the prism in which only a weak interaction between the opposite free shear layers takes place. It is therefore not surprising that the lowest mean global drag force is achieved in this flow regime. Compared to the previous two flow regimes, a relatively broad main peak around $St_L = 0.25$–0.27 is present in the power spectra of the unsteady lift force. The nearly constant surface pressure distributions and the plateaus of the various fluid-dynamic coefficients for the smooth and slight rough prisms demonstrate that the flow around these two prisms is stable up to a Reynolds number of at least $\mathcal{O}(10^7)$.

(4.) *Upper transition* and *transcritical* flow regime

The appearance of the *upper transition* and *transcritical* flow regimes for the rough

and very rough prism results from the increased ratio of the height of the surface roughness to the boundary layer thickness. The roughness elements most probably protrude into regions of higher velocity inside the boundary layer, thereby inducing an even more rapid growth and amplification of the instabilities in the boundary layer. This disturbs the laminarity and leads to an earlier (i.e. more upstream) transition to turbulence. The *upper transition* is characterised by a gradual decrease of the height of the two negative pressure peaks and a related reduction of the adverse pressure recovery region (and thus most probably also of the laminar separation bubble and the strength of the enclosed recirculating flow) on both side faces, as is exemplary shown for the very rough prism at $Re_D = 3.01 \times 10^5$ in the Figures 4.6b and 4.6f. The gradual widening of the near wake, the increase in the value of the maximum total pressure loss $(\Delta p/q)_{max}$ (Figure 4.2), and the steady recovery of all fluid-dynamic parameters is not only proof for a gradual increase of the lateral spacing between both turbulent free shear layers that depart from the trailing edges, but also for a more intense interaction of both free shear layers in the base region. Similar to the flow transition in the *critical* flow regime, two main peaks are present in the power spectra of the unsteady lift force, of which each one corresponds with one of the two bounding flow regimes.

The cross-sectional mean surface pressure distributions at the final *transcritical* flow regime strongly resemble those obtained at *subcritical* Reynolds numbers, as the negative pressure peaks and adverse pressure recovery regions have fully disappeared (Figure 4.6). The mean width of the near wake is slightly lower than its *subcritical* value, which implies a somewhat smaller lateral deflection of the two free shear layers and the outer streamlines along the side faces. This is in agreement with the appearance of a slightly lower mean suction on these faces, which implies a weaker backflow region in between the faces *II* and *IV* and the free shear layers. The higher mean value of $(\Delta p/q)_{max}$ in the *transcritical* flow regime is an indication for a recirculation region behind the base of the prism that extends further in downstream direction compared to the *subcritical* flow regime. Although similar Strouhal numbers are obtained in the *subcritical* and *transcritical* flow regime, the values of the fluctuating lift force in Figure 4.3 suggest that the intensity of the free shear layer interaction in the recirculation region is in the latter flow regime much lower. This explains the much lower suction at the prism's base and the resultant slightly smaller values of the mean global drag force.

(b.) $\alpha = 45°$

While at $0°$ angle of incidence very distinct changes in the mean surface pressure distribution occur with increasing Reynolds number for slightly and very rough rounded square-section prisms, the surface pressures on these prisms at $\alpha = 45°$ in Figure 4.4 show only small variations in the negative pressure peaks at $s/D = 0.98$ and 3.67 (i.e. at both rounded shoulder edges) and in the pressures at the two base faces *III* and *IV*. A direct comparison of the pressure distributions on both prisms reveals a reduction in magnitude of those variations with increasing surface roughness height. Analogue to circular cylinder flows, an increase in surface roughness height reduces the shifts of the transition and main separation locations along the surface of the prism, as well as those of the reattachment and secondary separation points in the case of the existence of laminar separation bubbles. This explains the growing Reynolds-number independence of the fluid dynamics – in particular with respect to the *critical* flow regime up to the *upper transition*

– of the prism with increasing k_s/D from smooth to very rough. The same counts for the *asymmetric* flow state in which only the smooth prism experiences a distinct asymmetric flow with a resultant maximum steady lift force of $|C_L| = 0.51$, as shown in Figure 4.1f. Independent of the Reynolds number and surface roughness height, the main separation of the attached boundary layer on the windward-directed surfaces *I* and *II* is most probably situated on both rounded shoulders. The negative pressure peaks that occur for *critical* up to *transcritical* Reynolds numbers are sharp and narrow. Hence, the downstream adverse pressure recovery is only weak and short. The relatively large mean width of the near wake of $Z_w/D \geqslant 4.7$ over all flow regimes for each prism configuration implies a large separation in cross-flow direction between both free shear layers. The afterbody that is extruded downstream into the wake leads to a strong interaction of both shear layers with the two bases faces *III* and *IV* and results in high fluctuating lift and drag forces and a strong suction on both faces. The resultant shedding frequency is relatively low, as pointed out by the low Strouhal numbers.

4.2 From square with sharp edges to circular: combined influences of edge roundness and surface roughness on the fluid dynamics of prismatic bluff bodies at $\alpha = 0°$ and $45°$

The results in the previous chapter on the flow over rounded square-section prisms with smooth surfaces have shown that the highest drag reduction is achieved in the *supercritical* flow regime for both "symmetric" incidence angles. The presence of a laminar separation bubble on both side surfaces in combination with a secondary separation further downstream on the prism's surface leads at these Reynolds numbers to a low suction force at the base, a narrow wake, and thus a small effective aerodynamic blockage. Starting with a squared prism with sharp edges, the largest gain in global drag reduction over the full range of edge roundness values – hence, from $r/D = 0$ (squared with sharp-edged) to $r/D = 0.5$ (circular cylinder) – is accomplished for a relatively small non-dimensional edge roundness, whereas only modest additional benefits for C_D are obtained for $0.16 \leqslant r/D \leqslant 0.5$. The eddy shedding at those *supercritical* Reynolds numbers is characterised by the lowest intensity, but occurring at the highest frequency. While at $\alpha = 0°$ these flow characteristics remain stable up to Reynolds numbers of at least $\mathcal{O}(10^7)$, an increase in the Reynolds number results at $\alpha = 45°$ in a gradual recovery towards their respective *subcritical* levels. Hence, the final *transcritical* flow regime is marked by high mean and fluctuating forces and a low Strouhal number.

The past section of the current chapter revealed a distinct effect of the surface roughness height on the flow around square-section prisms with edge roundness values of $r/D = 0.16$. Independent of the height of the surface roughness, the lowest drag is also at this angle of incidence obtained in the *supercritical* flow regime, but the flow regime itself has shrunk to only a very small range of Reynolds numbers. While at $\alpha = 0°$ the low *supercritical* drag values are hardly affected by the roughness height, a sharp increase in C_D is observed at $\alpha = 45°$. Similar trends were observed for the fluctuating lift and drag forces and the Strouhal number. The surface roughness introduces an upper boundary of this flow regime at $\alpha = 0°$ as well, thereby causing a recovery of the fluid-dynamic properties of the prism at high *transcritical* Reynolds numbers at both incidence angles. In particular at $\alpha = 45°$, the values of the fluid-dynamic quantities in the *transcritical* flow regime are similar to the *subcritical* flow regime.

The current section places the focus on the combined influence of both parameters. The wind tunnel experiments were performed on square-section prisms having edge roundness values of $r/D = 0$, 0.16, or 0.29, and on a circular cylinder. Based on the outcomes of the preceding section, two surface roughness values were selected: $k_s/D = 4.5{\times}10^{-6}$ ("smooth") and $1{\times}10^{-3}$ ("rough"). The studied range of Reynolds numbers was kept constant, i.e. from 0.1 million up to 10 million, and the incidence angles of the square-section prisms equalled $0°$ and $45°$.

It is hardly surprising that the surface roughness height has no influence on the fluid dynamics of the sharp-edged square-section prism: neither the mean quantities C_D, C_{pb}, Z_w/D, and $\left(\Delta p/q\right)_{max}$ in the Figures 4.7 and 4.8, nor those associated with the eddy-shedding process, hence $\sqrt{(\overline{C_L'^2})}$, $\sqrt{(\overline{C_D'^2})}$, and St_L (Figure 4.9) at both $\alpha = 0°$ and $45°$ are affected. Even the heights of the main peaks in the PSDs of the time series of the lift, presented in Appendix A for various selected Reynolds nunbers between 10^5 and 10^7, are independent of the height of the surface roughness. The boundary layer separation remains frozen at the two windward-directed (for $0°$ incidence angle) or the two shoulder (at $\alpha = 45°$) sharp edges and the increased roughness height does not lead to a reattachment of the free shear layers on the downstream faces.

In contrast to the sharp-edged square-section prism, the curves of the 2D circular cylinder show a significant alteration with increased roughness height, thereby closely following the trends that are known from literature and presented in section 2.1.3. Those include, among others, a narrowing of the *subcritical* up to *upper transition* flow regimes coupled with a shift of their bounding Reynolds numbers to lower values. In addition, the absolute mean global lift coefficient that appears in the *asymmetric bistable* flow state strongly reduces, as shown in Figure 4.10b. This implies the occurrence of a much smaller one-sided laminar separation bubble with a substantially weaker enclosed recirculating flow, owing to which the asymmetry in the cross-sectional surface pressure distribution is much less pronounced. The range of Reynolds numbers that cover the *supercritical* flow regime reduces even to a single value. The value of C_D at this Reynolds number increases, while those of C_{pb} and St_L decrease. Not only does this demonstrate, that the secondary separation points must be located closer to the (most probably smaller) laminar separation bubbles at the upper and lower surfaces of the rough circular cylinder than is the case for the smooth cylinder case. Simultaneously, a much more rapid migration of the transition location in upstream direction occurs, first on the free shear layers above the laminar separation bubbles and – after having overtaken the primary separation points – along the surface of the prism, with increasing Reynolds number while passing through the *upper transition*. At common *transcritical* Reynolds numbers near 10^7 the increased surface roughness height has induced a 60% increase in the mean global drag force on the circular cylinder, as well as a reduction of the eddy shedding frequency by 20% in combination with a tremendous gain in strength of the eddies that is reflected in an increase in the fluctuating lift of more than 250%.

The fluid-dynamic quantities of the two rough prisms with rounded edges, placed at $\alpha = 0°$, generally follow the trends as described above for the circular cylinder. Since the baseline situation of those two prisms is a different one than of the smooth circular cylinder, various small-scale differences are nevertheless obtained. Small deviations in the trends are also found among the two square-section prisms and related to the different value of the edge roundness. Regarding the square-section prism with rounded edges of $r/D = 0.16$, the effect of the increased roughness height on the various fluid-dynamic quantities has already been outlined in detail in the previous section for both incidence angles. In a nutshell, the higher surface roughness induces a narrowing of the flow regimes together with a shift of the bounding Reynolds
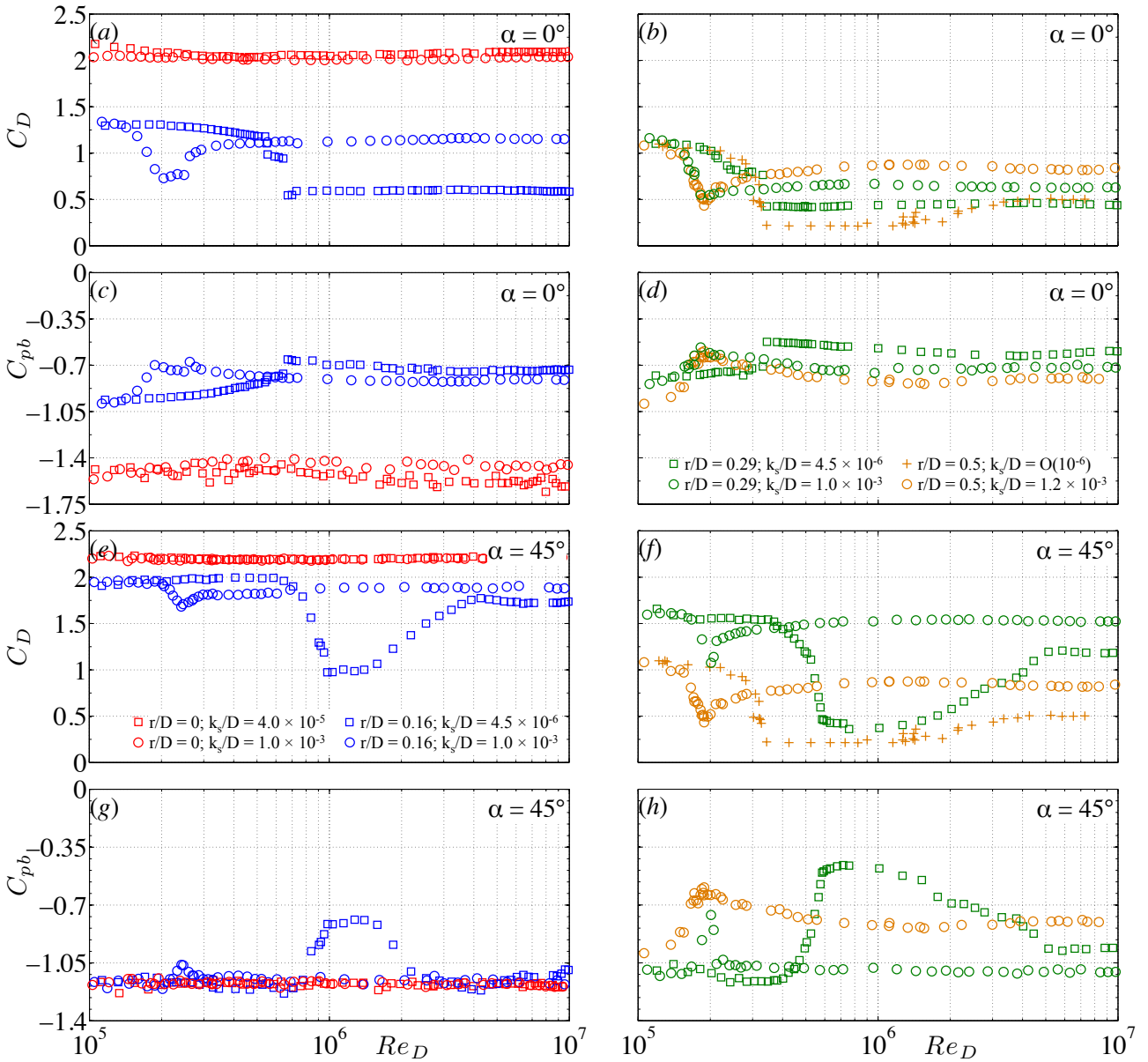
Figure 4.7: Combined effects of edge roundness r/D, non-dimensional equivalent sand-grain surface roughness height k_s/D, and Reynolds number Re_D on the mean global drag coefficient and mean cross-sectional base pressure coefficient of 2D square-section prisms at incidence. (a)-(d): $\alpha = 0°$; (e)-(h): $\alpha = 45°$; left column: $r/D = 0$ and 0.16; right column: $r/D = 0.29$ and 0.5 (Van Hinsberg [253, 258], Van Hinsberg et $al.$ [254, 255]). Reference: $+$ Schewe [209] $(r/D = 0.5$ and $k_s/D = \mathcal{O}(10^{-6}))$.

numbers to lower values. For the smooth prism configuration, the left-bounded $supercritical$ flow regime is open to the right at $\alpha = 0°$. As for its rough counterpart, approximately equal levels of the mean global drag, the mean cross-sectional base pressure, the fluctuating lift, and the Strouhal number are obtained in this flow regime. This implies, that for both roughness values the transition, primary and secondary separation, and the reattachment points are located at nearly equal positions on the surface of the prism at this incidence angle. Hence, both prisms thus experience a similar overall effective flow field. The sharp increase of the absolute mean global lift coefficient in the $asymmetric$ flow state in Figure 4.10a implies a
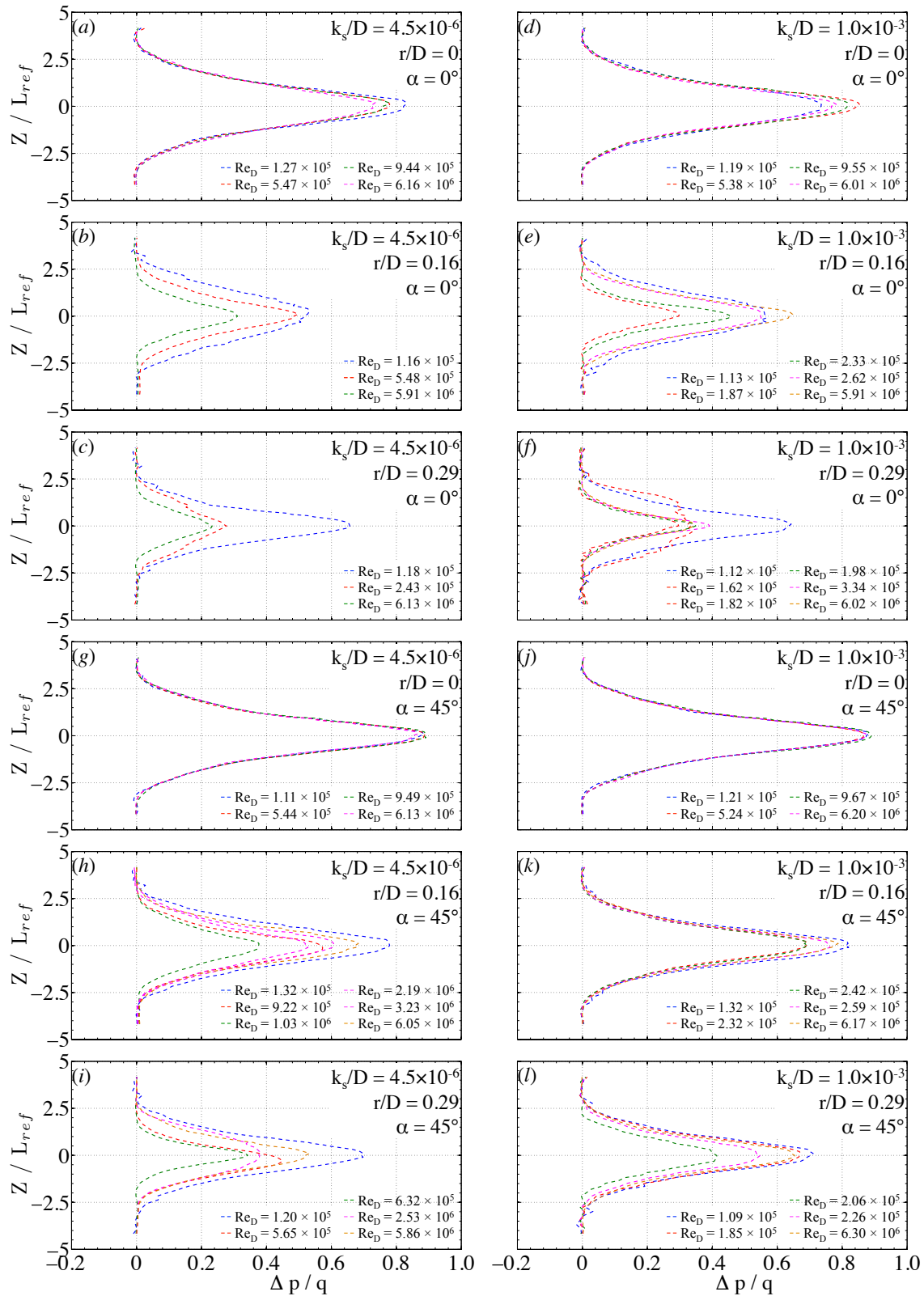
Figure 4.8: Combined effect of non-dimensional equivalent sand-grain surface roughness height and prism's edge roundness value on the mean vertical wake profile at $X/L_{ref} = 6.25$ behind the mid-span of a two-dimensional square-section prism for selected Reynolds numbers in the various flow regimes. (a)-(f): $\alpha = 0°$; (g)-(k): $\alpha = 45°$; left column: $k_s/D = 4.5 \times 10^{-6}$; right column: $k_s/D = 1.0 \times 10^{-3}$. $\mathbf{--}$: *subcritical* flow regime; $\mathbf{--}$: *critical* flow regime; $\mathbf{--}$: *supercritical* flow regime; $\mathbf{--}$: *upper transition*; $\mathbf{--}$: *transcritical* flow regime.

111
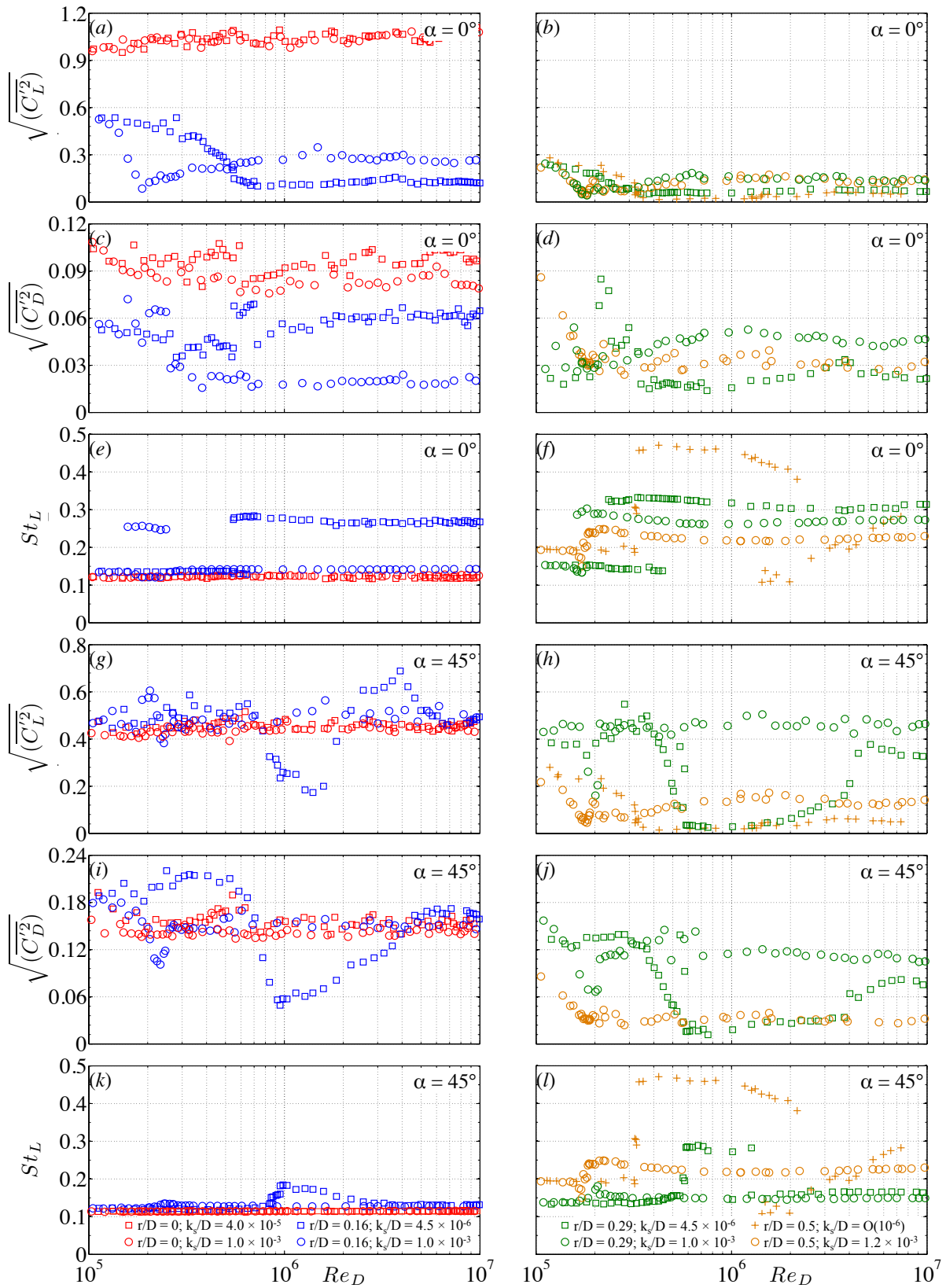
Figure 4.9: Combined effects of edge roundness r/D, non-dimensional equivalent sand-grain surface roughness height k_s/D, and Reynolds number Re_D on the fluctuating global lift and drag coefficients, as well as the Strouhal number of 2D square-section prisms at incidence (Van Hinsberg [253, 258], Van Hinsberg *et al.* [254, 255]). (*a*)-(*f*): $\alpha = 0°$; (*g*)-(*l*): $\alpha = 45°$; left column: $r/D = 0$ and 0.16; right column: $r/D = 0.29$ and 0.5. Reference: $+$ Schewe [209] ($r/D = 0.5$ and $k_s/D = \mathcal{O}(10^{-6})$).
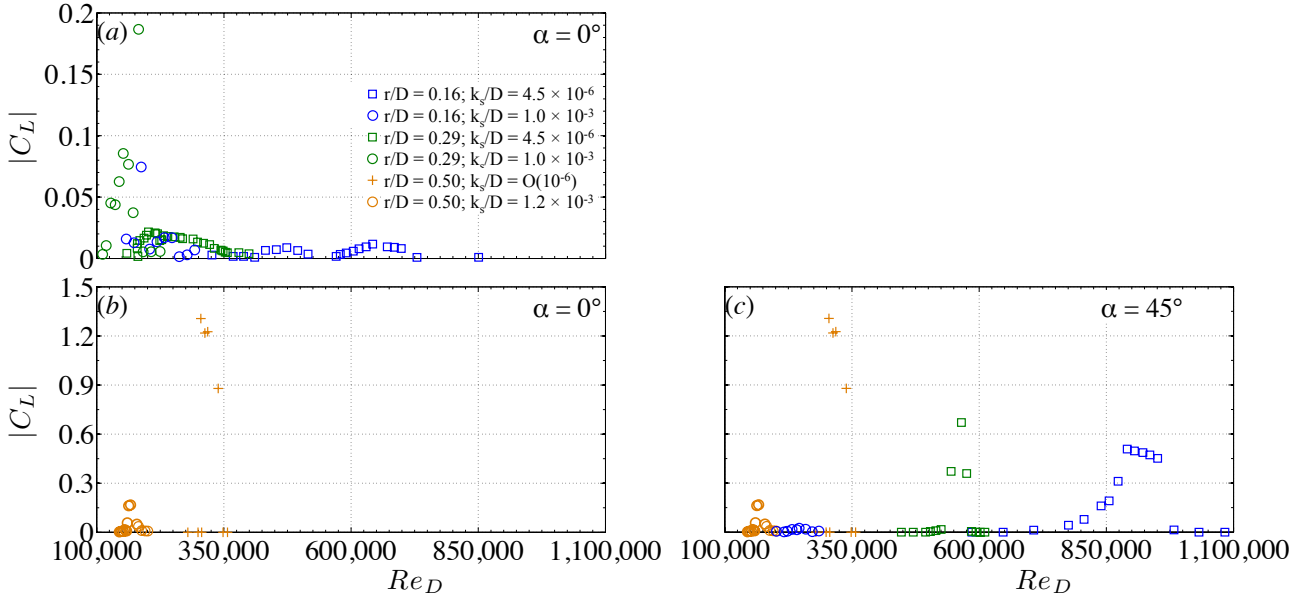
Figure 4.10: Combined effects of edge roundness r/D, non-dimensional equivalent sand-grain surface roughness height k_s/D, and Reynolds number Re_D on the absolute value of the mean global lift coefficient of 2D square-section prisms at incidence and a circular cylinder. (*a*): $r/D = 0.16$ and 0.29 at $\alpha = 0°$; (*b*): $r/D = 0.5$; (*c*): $r/D = 0.16$, 0.29, and 0.5 at $\alpha = 45°$. Reference: + Schewe [209] ($r/D = 0.5$ and $k_s/D = \mathcal{O}(10^{-6})$).

distinct asymmetry in the cross-sectional surface pressure distribution on the rough prism at these Reynolds numbers. Surprisingly, the same two phenomena are also found for the prism with $r/D = 0.29$ at $\alpha = 0°$, but not for the 2D circular-cylinder case. Whereas for the smooth prism with $r/D = 0.16$, these points remain at their respective locations up to $Re_D = 10^7$, the appearances of an upper-bounding Reynolds number of the *supercritical* flow regime and of the subsequent *upper transition* and *transcritical* flow regime with increased surface roughness demonstrates a gradual, but steady migration of in particular the transition location (and in a lesser extend also the reattachment and secondary separation points) with increasing Reynolds number in upstream direction towards the stagnation point. Both laminar separation bubbles on the side face of the prism in the vicinity of the forward-directed edges decrease thereupon in size, before eventually disappearing at a sufficiently high Reynolds number, caused by the laminar boundary layer that undergoes transition before separation. During this flow transition from the *supercritical* to the *transcritical* flow regime, the majority of the fluid-dynamic quantities shows a recovery of their values in the direction of their respective *subcritical* levels. The only exception forms the fluctuating drag force in Figure 4.9c, which shows a sharp decrease in the *upper transition*, as a result of which the absolute lowest level is obtained in the *transcritical* flow regime.

A similar overall development of the flow with increased k_s/D-value is obtained for the square-section prism with curved edges of $r/D = 0.29$. Subtle differences in the change of the flow behaviour for both rounded prisms can nevertheless be observed in the Figures 4.7 and 4.9. A first discrepancy to $r/D = 0.16$ concerns the *supercritical* flow regime, which shrinks from left-bounded and open to the right side for the smooth prism configuration to a single Reynolds number for the rough counterpart. In addition, the *upper transition* is characterised by a very weak recovery of the various fluid-dynamic quantities. As a consequence, their *transcritical* values nearly equal those of the *supercritical* flow regime. This is reflected in the virtually identical

113

shapes of the mean vertical wake profile and the associated values for the mean non-dimensional wake width and maximum mean total non-dimensional pressure loss at the selected *supercritical* to *transcritical* Reynolds numbers in Figure 4.8f. These two phenomena are quite similar to the results obtained for the circular cylinder, although less pronounced. The alteration of the flow around the rough square-section prism with $r/D = 0.29$ for increasing Reynolds numbers can thus be seen as a mixture of the trends of the previous two bluff bodies. This becomes particularly clear when looking at the curves of the Strouhal numbers in the Figures 4.9e and 4.9f, in combination with the underlying power spectra at selected Reynolds numbers in Appendix A.1. Two clearly separated Strouhal numbers, each one either associated with the *subcritical* or with the *supercritical* flow regime, were acquired at multiple *critical* Reynolds numbers for both rounded square-section prisms. In the *upper transition* though, a gradual reduction of the Strouhal number without the appearance of two peaks in the power spectra is found for the rough square-section prism with $r/D = 0.29$, therefore closely following the $St_L(Re_D)$ curve of the rough circular cylinder.

At $\alpha = 45°$, the trends of the curves of the various fluid-dynamic quantities that belong to both square-section prisms with non-zero edge roundness agree to a large extend to those of the circular cylinder. This encompasses (*1*) a narrowing of the *subcritical* to *upper transition* flow regimes and their migration to lower Reynolds numbers with increased roughness height, (*2*) a significant increase of both $C_{D,min}$ and $C_{pb,min}$ at the cross-over from the *critical* to the *supercritical* flow regime, (*3*) the appearance of a very low mean steady lift force in the short *asymmetric* flow state that is even non-existent for $r/D = 0.29$, and (*4*) a weaker dependence of the flow around the two rounded prisms on the Reynolds number. The combination of all of these developments results in deviations in the values of the fluid-dynamic quantities between the smooth and the rough versions of both prisms at common *transcritical* Reynolds numbers. While the shedding frequency of the eddies in the near wake decreases, higher values for all other mean and fluctuating coefficients are obtained. The graphs furthermore show that a decrease in bluffness (i.e. a higher r/D-value) leads to larger differences between the smooth and rough prism.

4.3 From one "symmetric" incidence angle to the other: influence of the incidence angle of the oncoming flow on the fluid dynamics of a slightly-rough square-section prism with $r/D = 0.16$.

Not only the cross-sectional shape and the surface roughness are examples of influencing parameters that can become governing ones. The incidence angle of non-circular bluff bodies is another important one that severely alters the behaviour of the flow around them. In particular structures with bluff cross-sections that have been placed in the ocean or in the planetary boundary layer experience in the vast majority of cases a water or air flow from all possible directions. Under unsteady flow conditions, such as atmospheric turbulence or storms with strong wind gusts, large directional and spatial variations in wind shear, or strong impacting waves, large and rapid fluctuations in both the Reynolds number and incidence angle may take place.

While the combined effects of edge roundness and angle of incidence on the aerodynamics, the flow topology, and the heat transfer of square-section prisms has been subject of extensive

research for Reynolds numbers up to $\mathcal{O}(10^3)$, see for example Alam *et al.* [13] and the many references therein, only few studies have actually focussed on the high to very high Reynolds-number range. So performed Tamura *et al.* [241] a numerical study on the three-dimensional incompressible flow around square-section prisms with sharp, chamfered, and rounded ($r/D = 1/6$) edges at $\alpha = 0°$ and $Re_D = 10^4$. Their results showed that a 60% decrease in drag could be obtained by rounding the edges of the prism compared to its sharp-edged counterpart. In a follow-up experimental study at a Reynolds number of $3{\times}10^4$ it was shown that an edge roundness of $r/D = 1/6$ resulted in lower drag coefficients and higher Strouhal numbers for all angles of incidence between –5° and 30°, as well as in a reduction of the lift fluctuations by about 50% compared to the values for the sharp-edged square-section prism at small angles of incidence [242]. The critical angle at which both the slope of the $C_L(\alpha)$ curve changed from negative to positive and the Strouhal number reached its maximum value, shifted from 12° for prisms with $r/D = 0$ to 5° for those with $r/D = 1/6$, and was induced by an earlier reattachment of the separated shear layer on the side face exposed to the wind. Similar conclusions were drawn in the studies by Carassale *et al.* [44,45] for two-dimensional square-section prisms with rounded edges of $r/D = 0$, $1/15$, and $2/15$ in the Reynolds-number range of $1.7{\times}10^4$ to $2.3{\times}10^5$. Their surface pressure data at the prism's mid-section demonstrated that around $\alpha = \alpha_{cr}$, being 12°, 7°, and 5° for $r/D = 0$, $1/15$, and $2/15$, respectively, an increase in the suction near the leading edge of the side face exposed to the oncoming free stream and a decrease close to its trailing edge occurred, thus proving the formation of a separation bubble through reattachment of the free shear layer on this face. A further increase in angle of incidence led to a shrinkage of both the length and height of this separation bubble towards the windward-directed edge, in agreement with the observations by Huang *et al.* [106] for a square-section prism with sharp edges. This latter behaviour can be subscribed to the steady migration of the reattachment point along the side face towards its leading edge with increasing angle of incidence towards $\alpha = 45°$, as has been described in detail in section 2.2.2.

The results of the wind tunnel experiment on a slightly rough and rounded square-section prism ($k_s/D = 4.5{\times}10^{-4}$, $r/D = 0.16$) at incidence are presented in this section. Eleven incidence angles between –45° and +3.25° were selected and at each one of them, the fluid dynamics over the full range of Reynolds numbers from 0.1 million up to 8 million was investigated.

4.3.1 Mean global and cross-sectional fluid-dynamic coefficients

Figure 4.11 presents the variations of the mean lift and drag coefficients C_D and C_L and the mean cross-sectional pitch moment and base pressure coefficients C_m, and C_{pb} with respect to the angle of incidence at multiple Reynolds numbers between $Re_D = 2.0{\times}10^5$ (*subcritical*) and $Re_D = 6.0{\times}10^6$, i.e. either *supercritical* at $\alpha = 0°$ or *transcritical* at all other incidence angles. For a Reynolds number up to $Re_D = 3.0{\times}10^5$, i.e. up to the end of the *subcritical* flow regime, a decrease in C_D takes place as the incidence angle decreases from $\alpha = 0°$ to –6.5°. At the latter incidence angle, a sign inversion of the slope of the $C_D(\alpha)$ curve from positive to negative is seen to occur, followed by a steady increase of C_D with further decreasing incidence angle and a flattening of the $C_D(\alpha)$ curve for $\alpha \to -45°$. The sign inversion implies that the angle of $\alpha = -6.5°$ either corresponds or lies close to the critical angle of incidence, α_{cr}, at which the detached flow reattaches close to the trailing edge of the upper lateral face that has been turned into and is thus exposed to the oncoming flow. This value is slightly higher than $\alpha_{cr} = 5°$ found by Carassale *et al.* [45] and $\alpha_{cr} = 4°$–5° obtained by Tamura and Miyagi [242] for a square-section prism with $r/D = 2/15$ at $Re_D = 2.7{\times}10^4$ and $r/D = 0.167$, respectively, in a smooth
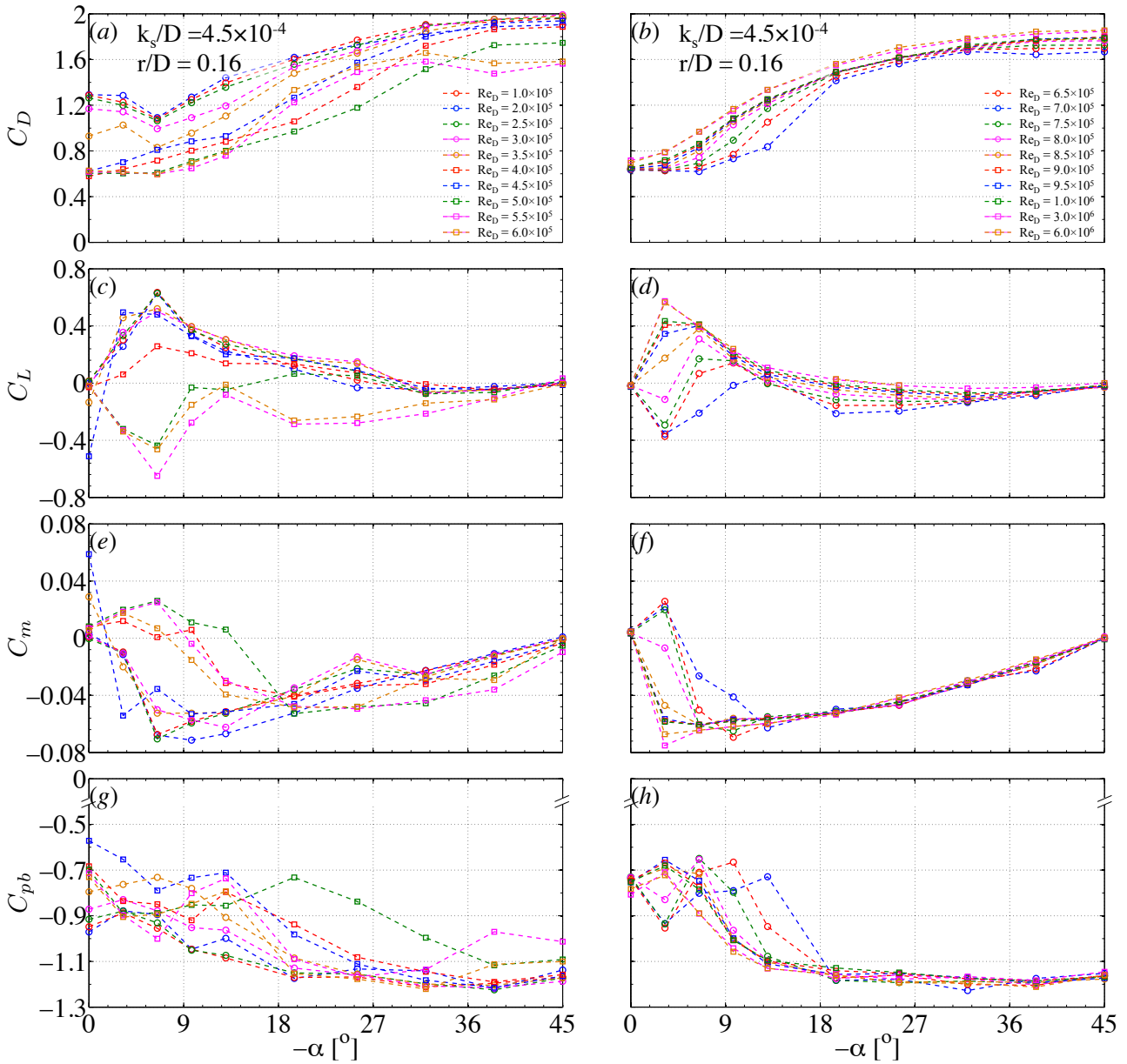
Figure 4.11: Combined effects of incidence angle α and Reynolds number Re_D on the mean global drag and lift coefficients and on the mean cross-sectional pitch moment and base pressure coefficients of a 2D square-section prism with edge roundness of $r/D = 0.16$ and non-dimensional equivalent sand-grain surface roughness height of $k_s/D = 4.5 \times 10^{-4}$. (a)-(b): C_D; (c)-(d): C_L; (e)-(f): C_m; (g)-(h): C_{pb}. Left column: $Re_D = 1.0 \times 10^5$ to 6.0×10^5; right column: $Re_D = 6.5 \times 10^5$ to 6.0×10^6.

flow with turbulence intensities below 0.3. Interestingly, the Figures 4.11a and 4.11b show that for Reynolds numbers ranging from 5.0×10^5 to 8.5×10^5 the mean global drag coefficient either starts its steady increase straight away from $\alpha = 0°$ or its value remains relatively constant at low negative angles of incidence (i.e. down to $\alpha = -3.25°$ or $\alpha = -6.5°$) before commencing its continuous increase. At these Reynolds numbers, no distinct critical incidence angle can thus be derived from the trend of the corresponding $C_D(\alpha)$ curves. The curve at $Re_D = 3.5 \times 10^5$ forms the transition between both trends at low negative incidence angles: for $-3.25° \leqslant \alpha \leqslant 0°$ the

drag slope is negative and thus consistent with the curves at $Re_D \geqslant 4\times10^5$, whereas $dC_D/d\alpha$ > 0 for $-6.5° \leqslant \alpha \leqslant -3.25°$, i.e., equal to the trend of the curves at $Re_D \leqslant 3\times10^5$. Although the behaviour of the mean base pressure coefficient C_{pb} is directly coupled to the mean drag coefficient, as the latter has a direct influence on the value of the former, the aforementioned two exact opposite trends of C_D with increasing Reynolds number in the range of $-6.5° \leqslant \alpha \leqslant 0°$ cannot be seen in the behaviour of C_{pb} in figures 4.11g and 4.11h. Based on these latter curves, the appointment of the exact value of the critical angle of incidence is therefore also less accurate. In comparison to C_D, a somewhat wider spreading of the C_{pb}-values can furthermore be observed at low absolute angles of incidence for $Re_D = 4\times10^5$–8×10^5. This larger spreading is caused by the relatively deep and bright dip in the corresponding $C_{pb}(Re_D)$ curves for $\alpha = -$ 3.25° to -13° in that range of Reynolds numbers. The deviation of the trend of the base pressure curves for $Re_D = 5.5\times10^5$ and 6.0×10^5 for $\alpha \geqslant -38.5°$ is then again in close agreement with C_D.

The curves of the mean global lift and the mean cross-sectional pitch moment coefficients as function of the incidence angle in the Figures 4.11c to 4.11f possess two main trends that appear alternately and are separated at each cross-over by a transition curve at a certain Reynolds number. For relatively low Reynolds numbers up to about 4.0×10^5, C_L shows a steady increase with decreasing incidence angle down to $\alpha_{cr} \approx -6.5°$ (Figure 4.11c). This is followed by a continuous decrease with a slope $dC_L/d\alpha$ that is highly independent of the Reynolds number, a cross-over to a negative mean global lift coefficient in between $\alpha = -25.5°$ and $-32°$ and a moderate recovery towards $C_L = 0$ for $\alpha \rightarrow -45°$. A relatively similar, but opposite behaviour is found for C_m for $Re_D \leqslant 3.5\times10^5$ in Figure 4.11e: a steep decrease of its value with decreasing incidence angle down to $\alpha = -6.5°$ that is followed either directly by a steady increase of C_m towards $C_m = 0$ at $\alpha = -45°$ or by an intermediate and short plateau with rather constant values of C_m for incidence angles between $-6.5°$ and $-13°$ prior to the gradual recovery towards $C_m = 0$ at $\alpha = -45°$.

At the first transitional Reynolds number of $Re_D = 4.5\times10^5$ for C_L and $Re_D = 4.0\times10^5$ for C_m, a deviation in absolute values of the $C_L(\alpha)$ curve is seen to occur at angles of incidence smaller than $-19.5°$ and of the $C_m(\alpha)$ curve at angles of incidence below $-6.5°$, whereby this deviation is clearer for the former than for the latter coefficient. In the following range of Reynolds numbers that prolongs up to $Re_D = 7.5\times10^5$, both curves have swapped trends and therefore keep their mirrored image. Down to an incidence angle of either $-6.5°$ ($5.0\times10^5 \leqslant Re_D \leqslant 6.0\times10^5$) or $-3.25°$ ($6.5\times10^5 \leqslant Re_D \leqslant 7.5\times10^5$) the mean global lift coefficient shows a strong negative trend, whereas the mean cross-sectional pitch moment coefficient becomes increasingly positive in the exact same range of incidence angles. This is followed by a steep recovery of C_L to values that lie close to $C_L = 0$ and at several Reynolds numbers C_L even switches sign and reaches a positive lift force. In contrast, the $C_m(\alpha)$ curves show either a steady and moderate (Figure 4.11e) or a steep (Figure 4.11f) decrease for larger incidence angles, whereby a sign change appears at all Reynolds numbers. Beyond the second common transitional Reynolds number of $Re_D = 8.0\times10^5$, the individual curves of both coefficients regain their "*subcritical*" shapes.

4.3.2 Fluctuating global fluid-dynamic coefficients and Strouhal number

The trends of the fluid-dynamic quantities $\sqrt{(\overline{C_L'^2})}$, $\sqrt{(\overline{C_D'^2})}$, and St_L with decreasing incidence angle are shown in Figure 4.12 for the same 20 Reynolds numbers in the range of $Re_D = 1\times10^5$ to 6×10^6. At small negative incidence angles, there is a striking resemblance between the be-
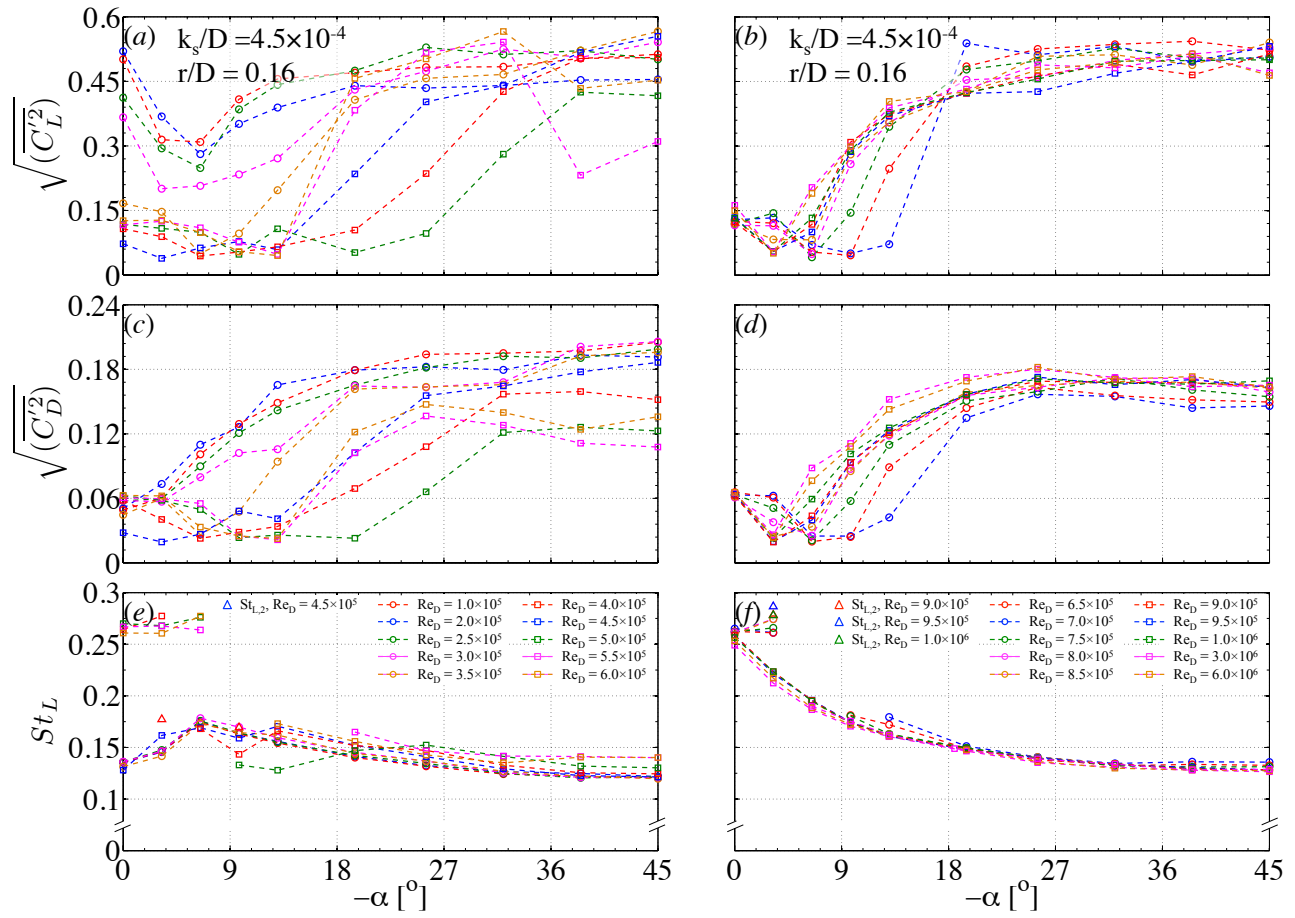
Figure 4.12: Influence of incidence angle and Reynolds number on the fluctuating global lift and drag coefficients and the Strouhal number of a 2D square-section prism with edge roundness of $r/D = 0.16$ and covered with a non-dimensional equivalent sand-grain surface roughness of $k_s/D = 4.5 \times 10^{-4}$. (a)-(b): $\sqrt{(\overline{C_L'^2})}$; (c)-(d): $\sqrt{(\overline{C_D'^2})}$; (e)-(f): St_L. The open triangles correspond to the secondary peak in the power spectra in Figure B.1. Left column: $Re_D = 1.0 \times 10^5$ to 6.0×10^5; right column: $Re_D = 6.5 \times 10^5$ to 6.0×10^6.

haviour of both fluctuating force coefficients at each Reynolds number, while distinct differences in the trends are obtained at combinations of high negative incidence angle and relatively low Reynolds number up to $Re_D = 3.0 \times 10^5$, i.e. up to the point at which the cross-over between the *subcritical* and the *critical* flow regimes takes place. At these *subcritical* Reynolds numbers, the values of both fluctuating force coefficients show a steady increase with decreasing angle of incidence that levels off at intermediate negative incidence angles, before reaching a plateau that remains relatively constant towards $\alpha = -45°$. The only discrepancy in the trends between the two coefficients is observed at incidence angles close to $0°$, for which the curves of the fluctuating lift show a sharp drop instead.

The curve at $Re_D = 3.5 \times 10^5$ can be assigned as transitional, justified by the first appearance of a bright valley between $\alpha = 0°$ and $-13°$ with a minimum value of $\sqrt{(\overline{C_D'^2})} = 0.03$ and $\sqrt{(\overline{C_L'^2})} = 0.05$ at $\alpha = -6.5°$. Beyond this transitional Reynolds number, the curves possess initially two plateaus, of which the first one spreads down to $\alpha = -6.5°$ and the second one continues to angles of incidence as low as $\alpha = -19.5°$ or even $\alpha = -25.5°$ for the fluctuating

drag and lift coefficient, respectively. Interestingly, both plateaus possess a similar behaviour with increasing Reynolds number: a continuous decrease in length towards a single point at $\alpha = 0°$ (1st plateau) and $\alpha = -3.25°$ (2nd plateau), the latter being obtained at $Re_D \geqslant 8.5\times10^5$–$9.0\times10^5$. Hence, the Reynolds number thus has a significant effect on the shape of the curves within their first parts. The decrease of both plateaus thereby induces a gradual convergence of the second part of the $\sqrt{(\overline{C_D'^2})}(\alpha)$ and $\sqrt{(\overline{C_L'^2})}(\alpha)$ curves to a single one for $Re_D \geqslant 4.0\times10^5$. Their shapes therefore resemble those of the mean global drag coefficient in Figure 4.11b to a high extend for Reynolds numbers above $Re_D \geqslant 8.5\times10^5$–$9.0\times10^5$.

Based on their overall shapes, the curves of the Strouhal number as a function of the incidence angle in the Figures 4.12e and 4.12f can be split up into two parts. The first one is characterised by clear changes in the behaviour of St_L with varying Reynolds number at negative incidence angles close to $0°$; here, the most interesting phenomena occur. At higher negative values for α, a near-perfect agreement in both the course of the curves and the actual values of the Strouhal number between the various Reynolds numbers is observed. This part of each curve shows a gradual, continuous decrease of St_L with decreasing α that ends in a levelling-off towards an asymptotic value of $St_L = 0.12$ to 0.14 at $\alpha = -45°$. This trend of St_L, i.e. being weakly dependent on α and highly independent on Re_D, becomes also clear by inspection of the underlying power spectra of the lift force at the various incidence angles for six Reynolds numbers in the range of $Re_D = 2.0\times10^5$ to 6.0×10^6 presented in Figure B.1 in Appendix B.

In contrast, for $-6.5° \leqslant \alpha$ the inverse situation is found: the value of the Strouhal number now depends to a high degree on the Reynolds number. Based on the values of St_L in both graphs, three distinct sub-branches can be distinguished. The first one is present up to a medium to high *critical* Reynolds number of 4.0×10^5. The $St_L(\alpha)$ curve is characterised by a sharp increase from $St_L = 0.14$ at $\alpha = 0°$ up to its absolute maximum of $St_L = 0.18$ at $\alpha_{cr} = -6.5°$. Around $\alpha = \alpha_{cr}$, a discontinuity exists in the Strouhal-number curve as the slope $dSt_L/d\alpha$ changes sign, whereupon the curve starts its previously described second trend line down to $\alpha = -45°$. The curve at $Re_D = 4.0\times10^5$ shows small fluctuations in the range of $\alpha = 0°$ to $-13°$, being an indication for an imminent transition from the first sub-branch to the second one. This latter sub-branch ranges from $Re_D = 4.5\times10^5$ to 8.0×10^5–8.5×10^5 and is defined by high, relatively constant Strouhal numbers of $St_L = 0.26$ to 0.28. It stretches down to $\alpha = -3.25°$ for high *critical* and all *upper transitional* Reynolds numbers and to $-6.5°$ in the *supercritical* flow regime. The curves suffer a subsequent significant drop in St_L at higher negative incidence angles down to the second overall trend line. Interestingly, each drop is preceded by a limited range of incidence angles in which no clear vortex-shedding frequency can be deduced from the underlying power spectra of the lift force, as exemplary shown for $\alpha = -9.75°$ at $Re_D = 6.0\times10^5$ in Figure B.1g. The length of this range initially increases for larger Reynolds numbers, reaches its maximum span of $\Delta\alpha = 13.5°$ around $Re_D = 5.5\times10^5$ in the *supercritical* flow regime, gradually decreases with further increasing Reynolds number, and finally disappears completely at $Re_D = 9.0\times10^5$, i.e. around the cross-over from the *upper transition* to the *transcritical* flow regime. This latter Reynolds number additionally marks the beginning of the third and final sub-branch that covers all Reynolds number up to at least 8×10^6. It is characterised by a steady decrease of the Strouhal number from $St_L = 0.26$ at $\alpha = 0°$ with decreasing incidence angle and a seamless transition into the second part of the overall trend line down to $\alpha = -45°$.

4.3.3 Cross-sectional mean pressure distributions

The development of the mean pressure distribution on the prism's surface with incidence angle is presented in Figure 4.13 for six Reynolds numbers between 2×10^5 and 6×10^6. By means of a scaled vectorial representation, Figure 4.14 gives an additional qualitative impression of these distributions. The values of the mean global drag and lift coefficients, as well as the cross-sectional pitch moment coefficient are added to the individual graphs to facilitate the correlation between the changes in the surface pressures and the resultant fluid-dynamic coefficients.

At the *subcritical* Reynolds number of 2×10^5, the mean pressure distribution at $\alpha = 0°$ is highly symmetric with respect to the virtual horizontal line through $s/D = 0.47$ and 2.33. Based on the classification by Igarashi [108], introduced in section 2.2.2, the flow belongs to the category of *symmetric flows*. The relatively constant negative mean pressures of $C_{p,cyl} = –1.08$ and $C_{pb} = –0.95$ on, respectively, the two side surfaces and the base of the prism demonstrate that after separation of the boundary layer no reattachment of the free shear layers takes place. The mean global drag coefficient thereupon reaches a high value of $C_D = 1.29$, whereas near-zero values for both the mean global lift and cross-sectional pitch moment coefficients are obtained. A rotation of the prism to $\alpha = –3.25°$ induces only slight changes in the cross-sectional surface pressure distribution (Figure 4.14). The turning of the rounded edge between the faces *I* and *II* into the wake induces a small relocation of the boundary layer separation point to, most probably, a position slightly further downstream that leads to a light overall reduction of the suction on face *II* compared to $\alpha = 0°$. The resultant light asymmetry in the pressure distribution leads nevertheless to a pronounced mean global lift coefficient of $C_L = 0.30$, the appearance of a small negative pitch moment coefficient $C_m = –0.01$, and a small reduction of the mean global drag coefficient. This proves that the flow field around the prism belongs at this angle of incidence to the *asymmetric flows*, i.e. the second sub-category of the *subcritical* or *perfect separated* flow regime. A doubling of this incidence angle to $\alpha = –6.5°$, i.e. near the critical angle, leads to a distinct asymmetry in the pressure values between both side surfaces *II* and *IV*. A reattachment of the lower free shear layer on the lateral face *II* is still prevented at this incidence angle. The migration of the separation point of the opposite boundary layer in upstream direction, in combination with the increased proximity of the free shear layer upon separation to its corresponding side surface *IV* allow a reattachment of this free shear layer to surface *IV* close to its trailing edge. The resultant one-sided reattachment-like flow field has switched to the *reattachment* or *separation* flow regime (Igarashi [108]). It is characterised by the formation of a recirculation bubble on the upstream portion of this prism's side face, which appears as a local increase in the suction pressure, and a secondary separation of the reattached boundary layer on or near the downstream upper rounded edge. As a result of the different positions of the boundary layer separation on the upper and lower faces of the prism, a much weaker communication of the two shear layers in the base region of the prism takes place, as is projected by the absolute minimum and absolute maximum of the fluctuating lift force and Strouhal number, respectively, at this incidence angle (Figure 4.12). The mean suction pressure at the base of the prism (face *III*) thereupon decreases and the mean global drag coefficient reaches its absolute minimum of $C_D = 1.08$ at $Re_D = 2\times10^5$ (Figure 4.11a). The clear imbalance between the mean pressure coefficients in cross-flow direction below and above the prism induces a large steady positive mean lift coefficient of $C_L = 0.63$ (Figure 4.11c) and a negative mean pitch moment of $C_m = –0.067$ (Figure 4.11e).

Induced by a wandering of the reattachment location in upstream direction along side face *IV* towards its leading edge, the separation bubble shrinks in size. The suction peak near the leading edge initially increases before reducing with every further rotation of the prism
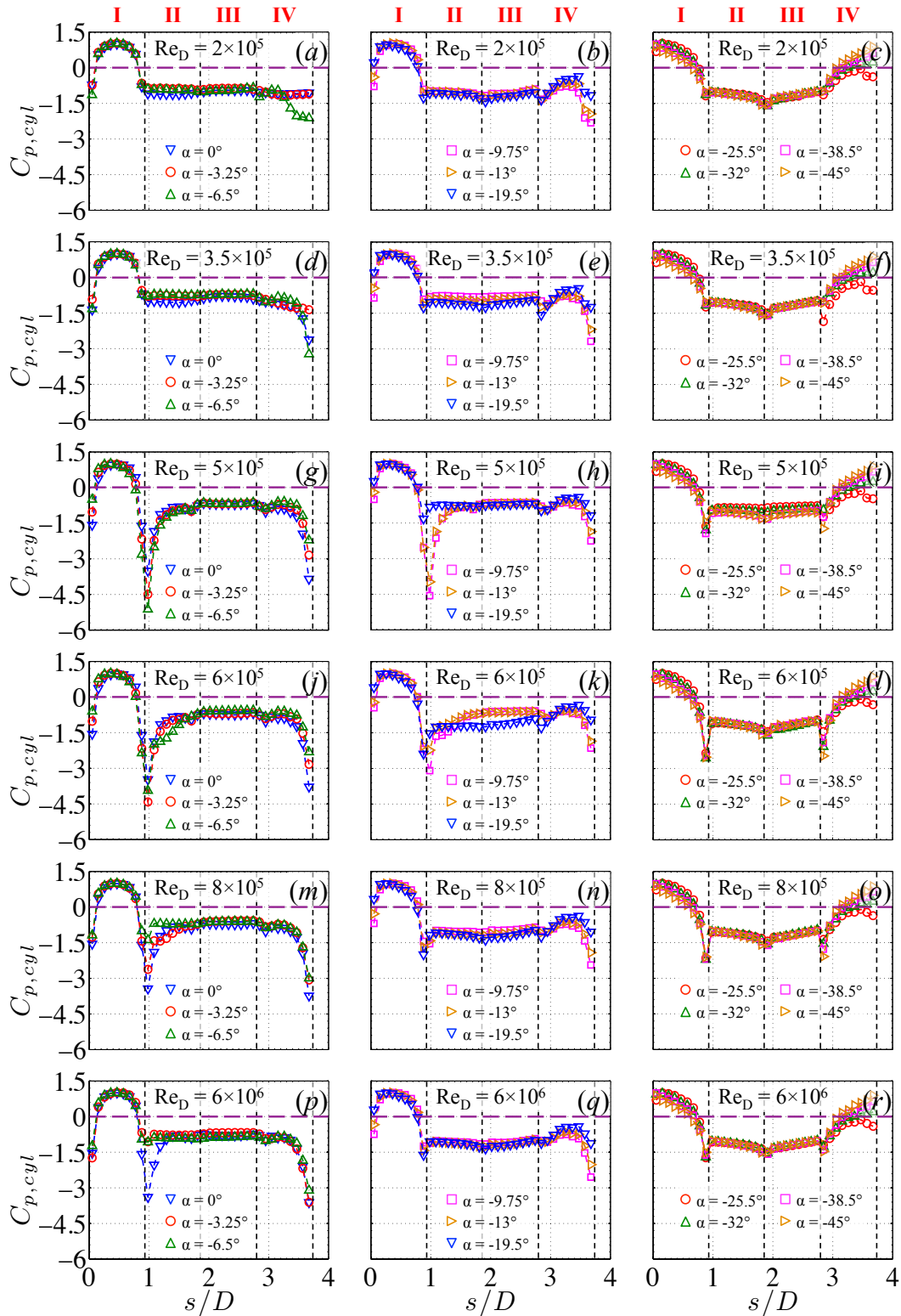
Figure 4.13: Development of the mean cross-sectional pressure distribution with incidence angle for a 2D slightly-rough (i.e. $k_s/D = 4.5 \times 10^{-4}$) square-section prism with edge roundness of $r/D = 0.16$ at selected Reynolds numbers that cover the *subcritical* to the *transcritical* flow regimes. (a)-(c): $Re_D = 2 \times 10^5$; (d)-(f): $Re_D = 3.5 \times 10^5$; (g)-(i): $Re_D = 5 \times 10^5$; (j)-(l): $Re_D = 6 \times 10^5$; (m)-(o): $Re_D = 8 \times 10^5$; (p)-(r): $Re_D = 6 \times 10^6$. Left column: $|\alpha| = 0°$ to $6.5°$; centre column: $|\alpha| = 9.75°$ to $19.5°$; right column: $|\alpha| = 25.5°$ to $45°$.

Figure 4.14: Qualitative scaled vectorial representation of the mean circumferential surface pressure distribution at the mid-span of a 2D slightly-rough (i.e. $k_s/D = 4.5 \times 10^{-4}$) square-section prism with edge roundness of $r/D = 0.16$ for incidence angles in the range of $\alpha = 0°$ to $-45°$. Top two rows: $Re_D = 2 \times 10^5$; centre rows: $Re_D = 3.5 \times 10^5$; bottom two rows: $Re_D = 5 \times 10^5$. The colours of the envelopes of the arrows match the colours of the respective curves in Figure 4.13.

Figure 4.14: Qualitative scaled vectorial representation of the mean circumferential surface pressure distribution at the mid-span of a 2D slightly-rough (i.e. $k_s/D = 4.5\times10^{-4}$) square-section prism with edge roundness of $r/D = 0.16$ for incidence angles in the range of $\alpha = 0°$ to $-45°$. Top two rows: $Re_D = 6\times10^5$; centre rows: $Re_D = 8\times10^5$; bottom two rows: $Re_D = 6\times10^6$. The colours of the envelopes of the arrows match the colours of the respective curves in Figure 4.13 (cont.).

towards $\alpha = -25.5°$, see figures 4.13b and 4.13c. The area on the upper lateral face IV with a reattachment-like flow thus grows steadily in upstream direction, whereas the flow on the lower lateral face II remains fully separated for all angles of incidence. At $\alpha = -32°$, the pressure on the upstream half of face IV has becomes negative. The resemblance of the overall pressure distribution on this face with that on face I suggests a complete absence of the separation bubble on face IV. This means that the boundary layer remains attached up to its separation over the downstream rounded edge. The flow field around the prism has thus switched to the *wedge* or *attached* flow regime. The continuous turning of the prism results furthermore in a migration of the stagnation point from $s/D = 0.47$ at $\alpha = 0°$ towards $s/D = 0$ at $\alpha = -45°$. During this transition, the increasing symmetry of the surface pressures between the upper and lower sides of the prism leads to a gradual decrease of both C_L and C_m to 0 at the second symmetric angle of $-45°$. Simultaneously, the suction at the base of the prism gets stronger. In combination with a wider lateral spreading of the free shear layers, a higher drag coefficient is obtained that slowly approaches the value of $C_D = 1.96$ at $\alpha = -45°$. The strong increase in the fluctuating drag with decreasing incidence angle in Figure 4.12a is most probably caused by the afterbody that is formed by the faces II and III while turning them into the wake. Interestingly, the values of the fluctuating lift coefficient and the Strouhal number gradually regain their initial values of $0°$ angle of incidence for $\alpha \to -45°$ and are not affected by this afterbody.

As Re_D increases, various Reynolds-number flow regimes are passed one after another for the prism at $0°$ angle of incidence, as has been described in detail in section 4.1. At the transitional Reynolds number of $Re_D = 3.5 \times 10^5$, we are in the middle of the *critical* flow regime with a fully-separated flow on the lower lateral face II and a reattachment-like flow on the upper lateral face IV. The secondary separation of the reattached boundary layer over the rear upper rounded edge introduces a smaller, asymmetric near wake (Figure 4.2c) and a lower mean suction on the base face III of $C_{pb} = -0.80$ (figure 4.11g), leading to a lower mean drag force of $C_D = 0.93$ in comparison to $C_D = 1.29$ at $Re_D = 2 \times 10^5$ in the *subcritical* flow regime. The light asymmetry of the surface pressures between both lateral faces and the somewhat higher suction pressures over the laminar separation bubble result in a steady, but still relatively small values of C_L and C_m. Surprisingly, an influence of the light asymmetry in $C_p(s/D)$ that is present at $\alpha = 0°$ is noticed in the mean surface pressure distributions for incidence angles as far down as about $\alpha = -25.5°$ at this specific Reynolds number. It mainly manifests itself in a somewhat shorter recirculation bubble on face IV, in particular at $\alpha = -6.5°$ and $-9.75°$. In addition, the higher suction peak at the upper front rounded edge compared to the previous *subcritical* Reynolds number and the somewhat higher negative pressure in the vicinity of the secondary separation point at the trailing edge of face IV for incidence angles of $-19.5°$ and $-25.5°$ are also directly related to it. As Figure 4.11 shows, these changes in $C_p(s/D)$ lead in particular to lower values of C_D, C_m, C_{pb}, $\sqrt{(\overline{C_L'^2})}$, and $\sqrt{(\overline{C_D'^2})}$ at those incidence angles, whereas the mean global lift coefficient and the Strouhal number remain practically unaffected. At angles of incidence between $-32°$ and $-45°$, the differences in the surface pressures between $Re_D = 2.0 \times 10^5$ and 3.5×10^5 are marginal. That explains the common values for all mean fluid-dynamic coefficients at these incidence angles, as well as the fluctuating drag and the Strouhal number. Hence, at $Re_D = 3.5 \times 10^5$ the flow around the prism slowly migrates from a clear *critical state* at low absolute incidence angles back to a *subcritical* flow state at large negative angles. The only exception are the somewhat higher values for the fluctuating lift at $Re_D = 3.5 \times 10^5$, which indicates a small increase in the communication between both shear layers in the base region, as well as their interaction with the prism surface.

For $Re_D \geqslant 5\times10^5$, the prism at $\alpha = 0°$ experiences a *supercritical* flow, marked by the presence of a large suction peak of about $C_{p,cyl} = -3.4$ to -3.8 – depending on the exact Reynolds number – at the leading edge of both lateral faces. Along these two side faces, it follows a distinct adverse pressure recovery region, a laminar separation bubble, and a secondary separation of the reattached turbulent boundary layer at the trailing edges of the faces *II* and *IV*. The suction at the base of the prism and the mean global drag are both low, while the symmetric surface pressure distribution induces both a zero mean global lift and cross-sectional pitch moment coefficient (Figure 4.11). With the exception of $Re_D = 6$ million, both suction peaks (and most probably also both recirculation bubbles) keep to exist down to an angle of incidence of about $\alpha = -13°$. At the former Reynolds number, a flat pressure distribution appears on the complete side face *II* as soon as the first non-zero incidence angle has been reached, see Figure 4.14.

Interesting to mention is the dynamic behaviour of the height of the suction peak(s) and the length of following adverse pressure recovery region with changing Reynolds number. For low Reynolds numbers up to about $Re_D = 4\times10^5$–4.5×10^5, an adverse pressure recovery region in combination with a preceding suction peak appears on the upper lateral face only, see, for example, the pressure distributions at $Re_D = 3.5\times10^5$ in Figure 4.14a. This explains the occurrence of a positive mean lift and negative mean pitch moment coefficient for all incidence angles down to $\alpha = -25.5°$ in the Figures 4.11c to 4.11f. In the range of 4.5×10^5–$5\times10^5 \leqslant Re_D \leqslant 6\times10^5$–$6.5\times10^5$, the lower lateral face experiences a stronger suction peak and a longer adverse pressure recovery region than the upper one (Figures 4.13g to 4.13l). This results in a sign inversion of C_L and C_m for incidence angles as low as $\alpha = -25.5°$ and $\alpha = -9.75°$ to $-13°$, respectively. The Figures 4.13m and 4.13n, as well as Figure 4.14 show that at $Re_D = 8\times10^5$ the situation has changed once more as the stronger suction peak and the longer adverse pressure recovery region have now both switched back to the upper lateral face. From this Reynolds number onwards, the prism experiences once again a positive mean lift and a negative mean pitch moment coefficient at low to moderate negative incidence angles.

4.3.4 Susceptibility to *galloping* and flutter

The results for C_L and C_m in the Figures 4.11c to 4.11f show that, depending on the actual Reynolds number, both the slope of the $C_L(\alpha)$ curves and of the $C_m(\alpha)$ curves at $\alpha = 0°$, i.e. $dC_L/d\alpha|_{\alpha = 0}$ and $dC_m/d\alpha|_{\alpha = 0}$, respectively, change more than once in absolute value and in sign. The values of both slopes, obtained by a least square fit through the values of C_L and C_m at $\pm3.25°$ and $0°$, are presented in Figure 4.15.

The values of $dC_L/d\alpha|_{\alpha = 0}$ can be used to derive a possible susceptibility of this specific square-section prism to 1-DoF transverse (plunge) *galloping*. In section 1.2.2 the classical *galloping* model that is based upon the quasi-steady theory by Glauert [88] and Den Hartog [61] was therefore introduced. It states that a bluff body becomes unstable in transverse *galloping* when the Glauert-Den Hartog stability criterion, given by equation (1.2), is fulfilled. Since the mean global drag coefficient at $\alpha = 0°$ is positive throughout each of the various Reynolds-number flow regimes, the lift slope $dC_L/d\alpha$ at this incidence angle has to be both negative and in absolute value larger than C_D at equal Reynolds number. Figure 4.15 reveals that this is the case within a limited Reynolds-number range of approximately 4.6×10^5–8.0×10^5 and thus spans the first part of the *supercritical* flow regime only. Hence, according to the classical *galloping* model, this specific slightly rough, rounded square-section prism is at these Reynolds numbers thus potentially unstable in 1-DoF transverse *galloping*.
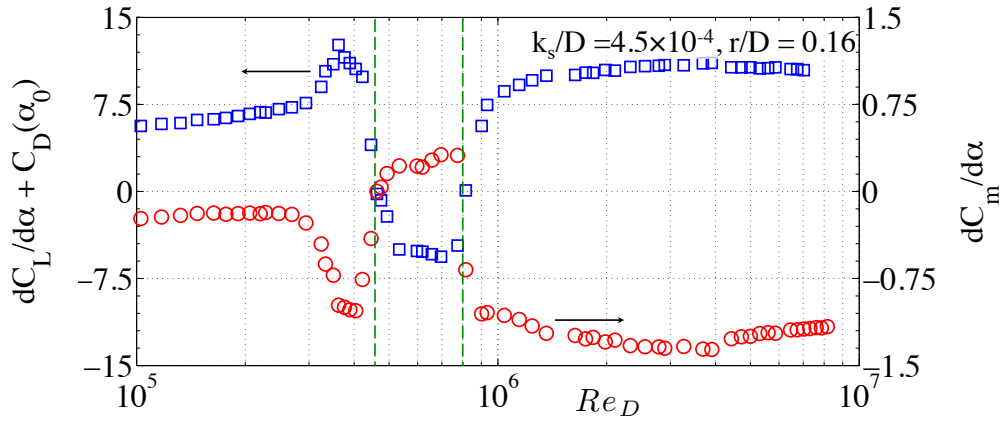
Figure 4.15: Development of the stability criteria for transverse *galloping*, $dC_L/d\alpha + C_D(\alpha_0)$ (blue squares), according to the quasi-steady theory by Den Hartog [61], and for torsional *galloping*, $dC_m/d\alpha$ (red circles), with Reynolds number for a 2D square-section prism with edge roundness of $r/D = 0.16$ and covered with a non-dimensional equivalent sand-grain surface roughness of $k_s/D = 4.5 \times 10^{-4}$.

In the case of torsional *galloping* or 1-DoF flutter, the bluff body starts to vibrate with a limit cycle oscillation in its first torsional mode along its elastic axis (Simiu and Scanlan [222], Blevins [32]). In section 1.2.2 it was outlined, that just like 1-DoF transverse *galloping*, torsional *galloping* occurs when both the free stream velocity exceeds a certain critical value and perturbations in the oncoming flow induce a small initial vibration of the structure. In contrast to transverse *galloping*, the resultant motion of the structure is a rotation about its axis in pure yaw, provided that the elastic axis of the prism coincides with the axis that goes through the centre of mass. Based once again on a linear quasi-steady analysis, torsional *galloping* may occur when equation 1.3 is satisfied. According to the results in Figure 4.15, the slope of the pitch moment of the prism can be positive or negative for different Reynolds numbers. Surprisingly, the negative values of $dC_m/d\alpha$ at $\alpha = 0°$ appear exactly at those Reynolds numbers where the Den Hartog criterion, i.e. equation (1.2), is not fulfilled and the prism is thus stable for 1-DoF transverse *galloping*, i.e. at $Re_D \leqslant 4.6 \times 10^5$ and $Re_D \geqslant 8.0 \times 10^5$. Although between these boundaries the necessary condition for torsional *galloping* is not met, torsional *divergence* could theoretically take place instead. For this latter static aeroelastic problem to occur, the sum of the structural stiffness and the aerodynamic torsional stiffness has to approach zero or become negative, which implies that $dC_L/d\alpha|_{\alpha = 0} > 0$. Since either 1-DoF transverse *galloping* or torsional *divergence* could take place at Reynolds numbers in the range of $Re_D = 4.6 \times 10^5$–8.0×10^5, the onset velocity of either one of these two instabilities that is exceeded first will determine which one of the two aeroelastic phenomena will appear at a certain Reynolds number within this range. Since the values of the slope of the mean pitch moment coefficient are only slightly positive, hence, $dC_m/d\alpha|_{\alpha = 0} \leqslant 0.32$, while the negative values of $dC_L/d\alpha|_{\alpha = 0}$ are approximately one order of magnitude larger at equal Reynolds number, the aerodynamic damping that counteracts the structural damping is larger in the latter case. It is therefore to be expected that the critical velocity of the 1-DoF transverse *galloping* instability is exceeded first, although other structural properties like the mass moment of inertia, the weight, and the eigenfrequency of the current prism also play an important role (Blevins [32], Païdoussis *et al.* [179]).

4.4 Résumé Chapter 4

The change in the fluid dynamics resulting from changes in the average height and texture of surface roughness, i.e. its shape and distribution, has so far been derived in the majority of applications from experiments and numerical simulations on two-dimensional and finite circular cylinders. Nowadays, a large amount of information is available on the effects of either a fully or partially roughened surface on the surface pressure distributions, the cross-sectional (i.e. local) and global forces, the local and global heat-transfer coefficients, the skin friction distributions, the angular transition and separation points of the boundary layer, and the eddy shedding frequency. Qualitative flow visualisation studies or quantitative data from experiments in wind or water tunnels or numerical simulations focussing on rough square-section prisms – whether "infinite" or finite, with sharp, rounded, or chamfered edges, isolated, paired, or clustered – are unfortunately still sought in vain in the literature. The aim of this chapter was to start filling this huge gap by presenting and quantitatively analysing the first results ever on the influence of surface roughness on the mean and fluctuating fluid dynamics of two-dimensional sharp-edged and rounded square-section prisms at incidence in a high-Reynolds-number cross-flow. The data presented were obtained in several wind tunnel experiments on square-section prisms with dimensionless edge radii of $r/D = 0$, 0.16, and 0.29, and on a circular cylinder. Many different combinations of edge roundness, non-dimensional equivalent sand-grain surface roughness height (i.e. $4.5 \times 10^{-6} \leqslant k_s/D \leqslant 1.4 \times 10^{-3}$), and incidence angle (i.e. $\alpha = -45°$ to $+3.25°$, and $45°$) were tested at high to very high Reynolds numbers covering the range from 10^5 to 10^7.

Of all flow regimes, the *subcritical* is the only one that is not affected by surface roughness at $\alpha = 0°$ and $45°$, regardless of the value of the edge rounding. This is true for all global and cross-sectional mean (i.e. C_D, C_L, C_m, C_{pb}, $(\Delta p/q)_{max}$, Z_w/D, and St_L) and global fluctuating (i.e. $\sqrt{(\overline{C_L'^2})}$ and $\sqrt{(\overline{C_D'^2})}$) fluid-dynamic quantities. Thus, the additional turbulence generated by the surface roughness, at least up to the highest tested value of $k_s/D = 0.14\%$, is ineffective in triggering the laminar-turbulent transition at those Reynolds numbers. This demonstrates that the laminar boundary is stable in this flow regime and its thickness is such that the tops of the roughness elements do not yet extend into regions of higher velocity within the boundary layer or even pierce the boundary layer. These observations are in very good agreement with the results for roughened circular cylinders. Fage and Warsap [74] found that even for a average relative roughness of $k/D = 2\%$ the mean drag coefficient of the circular cylinder was hardy altered at *subcritical* Reynolds numbers. The same results were obtained by Achenbach and Heinecke [5] for both C_D and St for mean relative roughness values as high as $k/D = 3\%$. In the experiments described in this chapter, the largest relative roughness of $k_s/D = 0.14\%$ was applied to the surface of the square-section prism with $r/D = 0.16$, i.e. with a relatively strong edge curvature. However, with each further increase in edge roundness, the cross-section of the prism approaches a perfect circle. It can thus be assumed, that also the flow around such a prism starts to increasingly resemble the circular cylinder flow when both are covered with the same roughness elements. It can therefore be argued that for the prism with $r/D = 0.29$ a higher surface roughness than the maximum investigated of $k_s/D = 0.1\%$ will neither have a noticeable effect on the fluid-dynamic quantities in the *subcritical* flow regime.

A second similarity with circular cylinders is the narrowing of the *subcritical* up to *upper transition* flow regime that is coupled with a shift in their bounding Reynolds numbers to lower values with increasing roughness height at the same two incidence angles. At $\alpha = 45°$, this trend is accompanied with a distinct rise of the absolute minimum values of the coefficients for the mean and fluctuating global drag, fluctuating lift, and mean cross-sectional base pressure,

as well as a descend of the maximum Strouhal number for both square-section prisms with non-zero edge rounding. This proves that the analogy to circular cylinders is given here as well. However, the amount by which these quantities change with increasing roughness height differs from those for a circular cylinder. That is not surprising, as a high edge curvature (i.e. low r/D value) implies a short arc length and the presence of a stronger adverse pressure gradient over the rounded edge. Consequently, the deceleration of the boundary-layer flow close to the prism's surface is higher and leads to an earlier separation. The near wake is thus wider and the interaction of the shear layers in the base region is higher, i.e. higher fluctuating forces and a lower Strouhal number. This leads to a higher suction at the base, which in turn results in a larger mean drag on the prism. Exactly the opposite was observed for $\alpha = 0°$. For rounded square-section prisms, not only the absolute minimum or maximum values of the previously listed quantities at the cross-over from the *critical* to the *supercritical* flow regime were found to be independent of the surface roughness height, but also their respective values in the latter flow regime. Combining these results with the aforementioned shift and narrowing of the various flow regimes with increasing roughness height, we can deduce the following. Although higher surface roughness induces an earlier and faster wandering of the primary separation, reattachment, and secondary separation points along the prism surface, their final positions at the cross-over to the *supercritical* flow regime are practically independent of the surface roughness height, as can be seen from the cross-sectional pressure distributions at the mid-section of the prism in Figure 4.5. This independence then persists at all *supercritical* Reynolds numbers, but ceases to exist once the *upper transition* is reached. Thus, at very high Reynolds numbers close to 10^7, the presence of a surface roughness is clearly noticeable in the values of the various fluid-dynamic coefficients.

Based on the quasi-steady theory, it was shown that the slightly rough (i.e. $k_s/D = 4.5 \times 10^{-4}$) square-section prism with rounded edges of $r/D = 0.16$ may tend to 1-DoF transverse *galloping* in a limited Reynolds-number range of $Re_D = 4.6 \times 10^5$–8×10^5 and to torsional *galloping* outside this range in the case it would have been mounted elastically in a cross-flow. However, following the discussion by Parkinson [180], the maximum amplitude of both *galloping* motions would be limited. For a smooth sharp-edged square-section prism in cross-flow, he found that the reattachment of the free shear layer to the trailing edge of the lateral face and the resultant sign reversal of $dC_y/d\alpha$ at the critical angle of about $\alpha = \pm 13°$ leads to a self-limitation of the *galloping* amplitude. By adding a continuous curvature at the upstream edges of the square-section prism, a migration of the separation point along this edge is favoured. The resulting deflection of the free shear layer that has separated from this edge is smaller, which causes it to reattach to the surface of the prism in the vicinity of the downstream rounded edge at a lower critical angle of about $|\alpha| = 6.5°$. In this sense, the *galloping* self-limitation of square-section prisms with rounded egdes will most probably occur at smaller incidence angles and thus at smaller amplitudes of oscillation. The circular cylinder is insensitive to motion-induced vibrations owing to its continuously curved cross-sectional shape. It is therefore to be expected that an increase of the edge roundness of the prism from $r/D = 0$ towards 0.5 leads to a steady decrease of the critical angle towards $\alpha = 0°$ and thus a gradual reduction of the maximum vibration amplitude of the limit cycle oscillation at a certain reduced velocity.

A challenging question that remains unanswered is whether this prism could theoretically behave like a *hard oscillator* at Reynolds numbers below 4.6×10^5 and above 8×10^5. This would mean that transverse *galloping* could still occur under certain conditions, even though the classical *galloping* model predicts a stable situation. Therefore not only the critical flow velocity has to be exceeded, but, in contrast to a *soft oscillator*, the prism would also have to be given

a certain minimum, unfortunately a priori unknown, initial transverse amplitude in order to potentially become unstable in plunge *galloping*. If the prism would from that moment on perform a limit cycle oscillation with a certain constant amplitude, which would increase with growing reduced velocity, the *hard oscillator*-theory would be proven correct at this Reynolds number. If, on the other hand, a gradual reduction in its transverse amplitude would occur for any chosen initial amplitude at all reduced velocities above the critical velocity, one would have to conclude that the prism is in fact stable in plunge *galloping* at certain or all Reynolds numbers outside the *supercritical* flow regime (Van Hinsberg [259]).

Chapter 5

Two smooth or slightly rough square-section prisms with rounded edges at incidence in a tandem configuration

Two or more parallel prismatic structures with either circular or square cross-sectional shapes placed close together are widely encountered in many practical situations such as chimney stacks, overhead power-line bundles, tube bundles in heat exchangers, skyscrapers in modern cities, struts of landing gears, interplane struts for holding apart the wings of biplanes and multiplanes, cables of suspension and stayed bridges, pipelines, risers, wind-assisted ship propulsion devices like Flettner rotors, foundation elements of fixed and floating offshore wind turbines and oil or gas rigs, etc.

The parallel placement of an identical second bluff body in the close vicinity of the first one results in most cases in a fluid-dynamic interference between the two bodies. This mutual flow field interaction induces changes in the instantaneous surface pressures that act on each one of them. Consequently, both bluff bodies experience not only altered resultant mean and fluctuating fluid-dynamic forces and moments, but the eddy shedding process and the flow structures in their separate or common wake are also modified. When mounted elastically in a uniform flow, this may lead to the occurrence of wake-induced instabilities, such as shear-layer impingement and reattachment, quasi-periodic vortices, wake galloping, or resonance. Besides these interference-induced vibrations, the same flow-induced instabilities as for isolated bluff bodies, described in Chapter 1, may occur. The interference effects and their strengths are largely dependent on both the relative arrangement to one another (i.e. in-line, side-by-side, or staggered), the spacing between them, the cross-sectional dimensions (equal or dissimilar), and the total angle of the incoming flow velocity vector with respect to the longitudinal axis of each of the two bluff bodies (i.e. perpendicular, yawed, pitched, or a combination of the latter two). This shows, that there exists an infinite number of possibilities to combine these parameters. Besides these governing interference parameters, the governing and influencing parameters listed in Chapter 2 (e.g. Reynolds number, turbulence intensity of the oncoming flow, geometric blockage, aspect ratio, surface roughness, edge roundness) for isolated bluff bodies also have an impact on the flow around a pair of circular or non-circular prismatic elements. As it is frankly impossible to investigate and discuss all possible combinations of those governing and influencing (interference) parameters, the emphasis of this chapter is on pairs of parallel 2D square-section prisms with rounded edges that have been placed in-line, i.e. in a tandem configuration, perpendicularly to the incoming flow. Selected governing and influencing parameters are the spacing between the two, the Reynolds number based on the undisturbed

incoming flow, the surface roughness height, and the incidence angle, the last one being equal for both prisms.

5.1 Classification of the flow regimes for two in-line circular cylinders and sharp-edged square-section prisms

In the previous chapters, it has been shown that the fluid-dynamic characteristics of single 2D rounded square-section prisms – with and without surface roughness – in a cross flow are a mixture of those belonging to circular cylinders and to sharp-edged square-section prisms, whereby the amount of edge roundness determines which one of the two extremes is more dominant. Hence, the smaller (or larger) the value of r/D, the more the flow around the square-section prism with edge roundness resembles that of a square-section prism with sharp edges (or of a circular cylinder). Based on these results, it can be argued that the same must hold for the flow around two parallel square-section prisms with rounded edges in a tandem configuration and positioned perpendicular to the incoming flow. This section therefore gives an overview of the flow categories that can be distinguished for a pair of circular cylinders on the one hand and for two square-section prisms with sharp edges on the other. The categorisation is mainly based on the kind of interference effects that take place with changing non-dimensional centre-to-centre spacing between the two bodies, S/L_{ref}, where L_{ref} equals the diameter or the side width for circular cylinders and square-section prisms, respectively. The two main types are a combination of *wake interference* and *proximity interference* for small values of S/D, and the sole occurrence of *wake interference* for larger S/D values. In the former case, the downstream bluff body is fully submerged in the turbulent wake of the upstream one and the two bluff bodies are that close together that the flow around the upstream body is (significantly) altered by the presence of the downstream one. In the latter case, the main difference is that now the gap between the two is sufficiently large that the fluid dynamics of the upstream cylinder or prism is barely influenced by the downstream one and thus nearly equals that of the respective isolated one. Although at first glance the main characteristics of the various classes seem to be very similar for both bluff-body pairs, various differences can nonetheless be marked that result from the possible migration or absolute fixation of the boundary layer separation and reattachment points along the surface, respectively at the sharp edges.

5.1.1 Pairs of circular cylinders in tandem

5.1.1.1 Categories of flow regimes

The *extended-body* regime or *Mode I* occurs at a very small centre-to-centre spacing of $1 \leqslant S/D \leqslant 1.2$ to 1.8 (Zdravkovich [292]) or $1 \leqslant S/D \leqslant 2$ (Zhou and Yiu [299]) between the two tandem cylinders, whereby the exact gap value of the upper boundary depends on the Reynolds number. This category is characterised by the absence of a reattachment of the free shear from the upstream circular cylinder on the surface of the downstream one. They instead overshoot and thus wrap around the second cylinder, which leads to a complete suppression of the eddy shedding in the base region of the upstream cylinder and a stagnant flow in the gap between the two cylinders. Hori [102] demonstrated the absence of a gap-flow by measuring the mean circumferential pressure distribution over two in-line circular cylinders. He found that the mean surface pressures close to the stagnation point of the downstream cylinder equalled the mean base pressure of the upstream cylinder. Since the resultant mean suction at the base of the second cylinder was furthermore lower than at its front surface, the former experienced

a negative drag, hence, a thrust force. Because of the relatively small spacing between the two tandem cylinders in this flow regime, the presence of the downstream cylinder and the induced flow modification around it are fed back to the upstream cylinder. The drag force that is experienced by the latter cylinder is therefore lower than that of a single isolated cylinder. This proves, that in this category *proximity* effects clearly dominate over *wake interference* effects. The unsteady flow and the periodic eddy shedding both occur in the wake of the downstream cylinder only, whereby these eddies are actually formed by the free shear layers that have separated from the upstream cylinder. The two cylinders therefore act effectively as a single streamlined elliptical structure with a periodic eddy shedding in its wake. The common wake behind the cylinder pair is narrow, which results in a shorter eddy-formation length and higher Strouhal numbers than for a single isolated cylinder. So obtained Hiwada *et al* [100] in their experiments on the flow around two tandem cylinders at $Re_D = 5 \times 10^4$ Strouhal numbers behind the downstream cylinder of $St_{L_2} = 0.24$–0.28 (Fig 5.1). Similar values were later measured by Igarashi [109] for Reynolds numbers of $Re_D = 1.5 \times 10^4$–4×10^4.
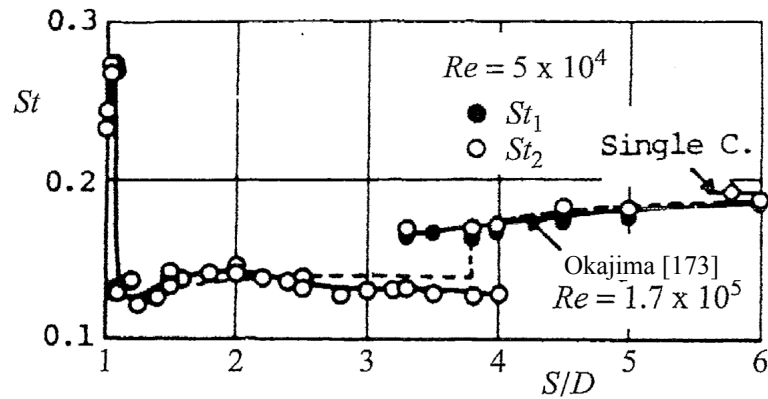
Figure 5.1: Effect of centre-to-centre spacing value S/D on the Strouhal number of two smooth circular cylinders in tandem at $Re_D = 5 \times 10^4$ (Adapted from Hiwada *et al.* [100]).

The *extended-body* regime is followed by the *reattachment* regime, the latter taking place at an increased cylinder-to-cylinder centre spacing of 1.2–$1.8 \leqslant S/D \leqslant 3.4$–$3.8$ (Zdravkovich [292]) or $2 \leqslant S/D \leqslant 5$ (Zhou and Yiu [299]). On the one hand, the gap between both cylinders is now sufficiently large to allow the free shear layers that have separated from the upstream cylinder to start rolling up behind the cylinder's base. The values of S/D are, on the other hand, still smaller than the eddy formation length of the upstream cylinder. Hence, during the process of roll-up, the free shear layers reattach on the downstream prism. Depending on the exact length of the gap, this reattachment is either alternately, permanently, or intermittently (Ishigai *et al.* [112], Hori [102], Igarashi [107, 109]). The eddy shedding from the upstream cylinder is thus still suppressed and only one common Kármán vortex street is formed in the wake of the downstream cylinder. This implies, that this category is still dominated by *proximity* effects, although at these spacing values wake-interference effects also slowly start to become visible and noticeable. The flow regime can therefore still be marked as *Mode I*.

In contrast to the former *extended-body* regime, the eddies behind the downstream cylinder are now shed with a lower frequency than that of a single isolated cylinder. Zhou and Yiu [299], for example, observed in their experiments that for $S/D = 2$ to 3 the reattachment of the free shear layers from the upstream cylinder occurred more often on the leeward side of the downstream cylinder, whereas for $S/D = 3$ to 5 the reattachment mostly took place on the windward

side. In the former case, this led to a strong influence on the development and separation of the downstream cylinder's boundary layer that resulted in weaker and smaller eddies being shed behind the downstream cylinder, whereas in the latter case the Kármán vortices were stronger. Hiwada *et al.* [100] found that the cross-over from the *extended-body* regime to the *reattachment* regime was accompanied with a discontinuous drop in the Strouhal number of the downstream cylinder to $St_{L_2} = 0.12$ to 0.15 (Figure 5.1). The graph shows, that this low value remains up to $S/D = 4$.

Similar to the *extended-body* regime, the proximity of both cylinders leads also in *reattachment* flow regime to a lower drag on the upstream cylinder than that of an isolated cylinder, although the difference between the two values gradually decreases with increasing gap length. As furthermore shown by Zdravokich [296], the value of C_{d_1} is nearly independent of the Reynolds number for $Re_D = 3.4 \times 10^3$–2.3×10^5, but experiences a light decrease with increasing S/D. In contrast, the mean drag of the downstream cylinder is – depending on the combination of S/D and Re_D – either negative or close to zero.

In the final *co-shedding* regime ($S/D \geqslant 3.4$–3.8 or $S/D \geqslant 5$, according to Zdravkovich [292] and Zhou and Yiu [299], respectively), which is also denoted as *Mode II*, the downstream cylinder is positioned sufficiently far downstream from the upstream one for the free shear layers from the latter cylinder to roll up into distinct eddies in the gap between both cylinders. As a result, the flow around the downstream cylinder is not only affected by the upstream non-uniform wake turbulence, as is the case in the previous *extended-body* regime, but it now also experiences a periodic vortex impingement.

While for $S/D > 5$–6 a fully developed and uncoupled vortex street is formed behind each cylinder, a *coupled eddy-shedding regime* appears for spacing values in the range of $3.4 < S/D < 5$–6. In the latter regime, the eddy-shedding mechanism in the near wake of the downstream cylinder is triggered by the arrival of the distinct vortices that have been shed by the upstream cylinder. This leads to a synchronisation of the two vortex streets both in phase and frequency, as a result of which a "*binary vortex street*" is formed (Igarashi [107, 109], Zdravkovich [295], Alam *et al.* [16], Alam [12], Wang *et al.* [266]). For spacing values larger than approximately 3.3, Hiwada *et al.* [100] obtained nearly equal values of St_{L_1} and St_{L_2}, see Figure 5.1. A slow rise with increasing S/D is observed from $St_{L_{1,2}} = 0.17$ around $S/D = 3.3$ towards $St_{L_{1,2}} = 0.19$ at $S/D = 6$, hence, gradually approaching that of a single isolated cylinder. In their wind tunnel experiments on two circular cylinders in tandem, Okajima and Sugitani [176] observed a similar behaviour for St_{L_2} with increasing spacing value. They measured the eddy shedding frequencies behind both cylinders simultaneously for $5 < S/D < 66$ at Reynolds numbers ranging from $Re_D = 1.6 \times 10^4$ to 2.36×10^5. Their data, presented in Figure 5.2, clearly show a gradual, but steady rise of St_{L_2} from 0.12 to 0.18 for Reynolds numbers up to about $Re_D = 9.4 \times 10^4$. In the same range, the Strouhal number of the upstream cylinder remains fixed at $St_{L_1} = 0.2$. Following the argumentation by Zdravkovich [295], the difference in the two trends results from the different flow conditions experienced by both cylinders. The upstream cylinder experiences a uniform oncoming free-stream. The vigorous interaction of both free shear layers in its base region produces a velocity defect in the near wake. This velocity defect is large in the vicinity of the cylinder, but decreases and therefore slowly dissolves downstream. For relatively small spacing values, the velocity of the oncoming flow experienced by the downstream cylinder equals the wake velocity of the upstream cylinder with $u_{wake} < U_\infty$. The calculation of the Strouhal number of each cylinder is based on the free-stream velocity, though. For the downstream cylinder, this leads to a lower Strouhal number than for the upstream one at small S/D values, but gradually approaches the latter one with increasing gap length. Wu *et al.* [278] indicated that
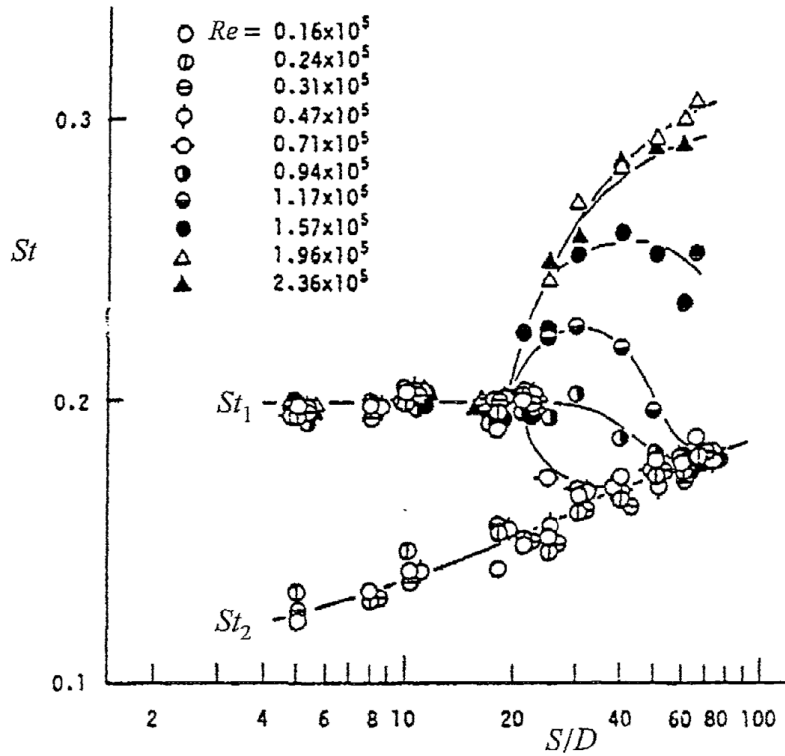
Figure 5.2: Combined influence of centre-to-centre spacing value S/D and Reynolds number on
the Strouhal number of two smooth circular cylinders in tandem (Okajima and Sugitani [176]).

the effect of a combination of vortex impingement on the downstream cylinder and an elevated
turbulence intensity of and streamwise structures in the approaching flow leads in addition to
a lower spanwise coherence of the wake behind the downstream cylinder. Zhou and Yiu [299]
furthermore showed that the eddies shed by the downstream cylinder are larger, but at the
same time weaker in *Mode II* than in *Mode I*, since in the *co-shedding* regime they are formed
closer to the base of the downstream cylinder.

Depending on the Reynolds number of the undisturbed oncoming flow, the boundary be-
tween the *reattachment* regime and the *co-shedding* regime varies between $S/D = 3.5$ and 5
(Zdravkovich [292], Xu and Zhou [280], Zhou and Yiu [299]). It is characterised by the *critical*
or *bistable flow* spacing S/D_{cr}, at which both flow regimes appear intermittently on either side
of S/D_{cr} (Igarashi [107], Xu and Zhou [280]). At the critical spacing, a drag inversion takes
place: for increasing S/D-values a discontinuous jump in the drag force on the downstream
cylinder from a small negative to a large positive value occurs at S/D_{cr} due to the transition
from *Mode I* to *Mode II*. This jump in C_{D_2} is coupled with a simultaneous jump in the Strouhal
number St_{L_2} to a higher value. The intermittent character of this transition was measured by
Hiwada *et al.* [100], as shown in Figure 5.1. For spacing values between 3.3 and 4.0, two clearly
separated Strouhal numbers are obtained for the downstream cylinder at each spacing value.
The lower one is associated with the *reattachment* regime, while the higher value belongs to
the *co-shedding* regime.

5.1.1.2 Influence of Reynolds number and surface roughness

The influence of the second governing parameter, i.e. the Reynolds number, on the flow be-
haviour around two smooth 2D circular cylinders in a tandem configuration has been investi-

gated experimentally by Pearcey *et al.* [184], Schewe and Jacobs [211], and Schewe *et al.* [212] over a wide range of Reynolds numbers up to *transcritical* values close to $\mathcal{O}(10^7)$. The measurement data by Pearcey *et al.* [184] include, among others, mean drag coefficients and Strouhal numbers for both cylinders, that were obtained at $S/D = 3.0$ (i.e. in the *reattachment* regime) and 5.0 (hence, belonging to the *co-shedding* regime) for $Re_D \leqslant 7{\times}10^5$ and $Re_D \leqslant 7{\times}10^6$, respectively. At both spacing values, the trend of the $C_{d_1}(Re_D)$ curve is similar to that of an isolated circular cylinder. Slightly lower values have been measured for $S/D = 3.0$ in the *subcritical* and *supercritical* flow regimes, that result from the mutual interference between both cylinders at this spacing. The downstream cylinder experiences a clear thrust force up to the start of the *critical* flow regime, at which point a sign inversion occurs and a positive drag is obtained. In contrast, C_{d_2} remains relatively constant for $S/D = 5.0$ within the complete range of studied Reynolds numbers. At *supercritical* Reynolds numbers, the drag on the upstream prism is at both spacing values lower than on the downstream one. This is attributed to the formation of separation bubbles on the surface of the upstream cylinder in the *supercritical* flow regime and the accompanied secondary turbulent boundary layer separation on the downstream half of the cylinder. The resultant sharp reduction in the width of the wake behind the upstream cylinder leads to a smaller shielding of the downstream cylinder by the upstream one. The surface pressures on the front portion of the downstream cylinder that is not shielded anymore thereupon increase and consequently raise the drag.

A similar behaviour of the mean drag force experienced by the upstream circular cylinder was recently confirmed by Schewe and Jacobs [211], and Schewe *et al.* [212] for spacing values of $S/D = 1.56$, 2.8, and 4.0 at Reynolds numbers between 10^5 and 10^7. They found that the mean drag coefficient of the downstream cylinder shows, on the contrary, an inverse development with Reynolds number compared to the upstream one, as presented in Figure 5.3. This inversed behaviour of C_D between both cylinders becomes even more distinct with decreasing gap length and results from the increased dominance of the *proximity* effects. At $S/D = 1.56$, the downstream cylinder experiences two drag inversions with zero-crossing. The first one occurs at the cross-over from the *reattachment* regime ($C_{D_2} < 0$) to the *co-shedding* regime ($C_{D_2} > 0$) in the *critical* flow regime and is coupled with the appearance of an asymmetric flow with steady lift force on the downstream cylinder of $C_{L_2} \approx 1$. The second one is found at the beginning of the *transcritical* flow regime, this time at the passage from the *co-shedding* regime back to the *reattachment* regime with $C_{D_2} < 0$ and coupled with a change in the topological flow structure. Only one jump in C_{D_2}, from the *reattachment* regime to the *co-shedding* regime, takes place in the *critical* flow regime at the larger spacing $S/D = 2.8$, whereas at $S/D = 4.0$ only small variations in C_{D_2} with changing Reynolds number have been obtained. At this largest spacing no zero-crossing was observed though, which means that the *co-shedding* regime is present in the complete investigated Reynolds-number range. As can be seen in the upmost graph of Figure 5.4, the trends of the fluctuating lift on the downstream circular cylinder at $S/D = 2.8$ and 4.0 agree well with that of an isolated circular cylinder. The higher values throughout the *subcritical* to *transcritical* flow regimes result from the impingement of the free shear layers ($S/D = 2.8$) or shed eddies ($S/D = 4.0$) onto the downstream cylinder. The curve of the Strouhal number $St_{L_2}(Re_D)$ for the downstream cylinder for the larger of these two spacing values is very close to that of an isolated circular cylinder (Figure 5.4). Within the *supercritical* flow regime, two clearly separated Strouhal numbers have been measured. Through wavelet analysis it has been demonstrated that the lower one of the two results from interference effects between both cylinders. For the tandem configuration with $S/D = 2.8$, a discontinuous jump from $St_L = 0.13$ to 0.34 appears at the cross-over from the *critical* to the *supercritical* flow regime. This value then gradually decreases with increasing Reynolds number while traversing
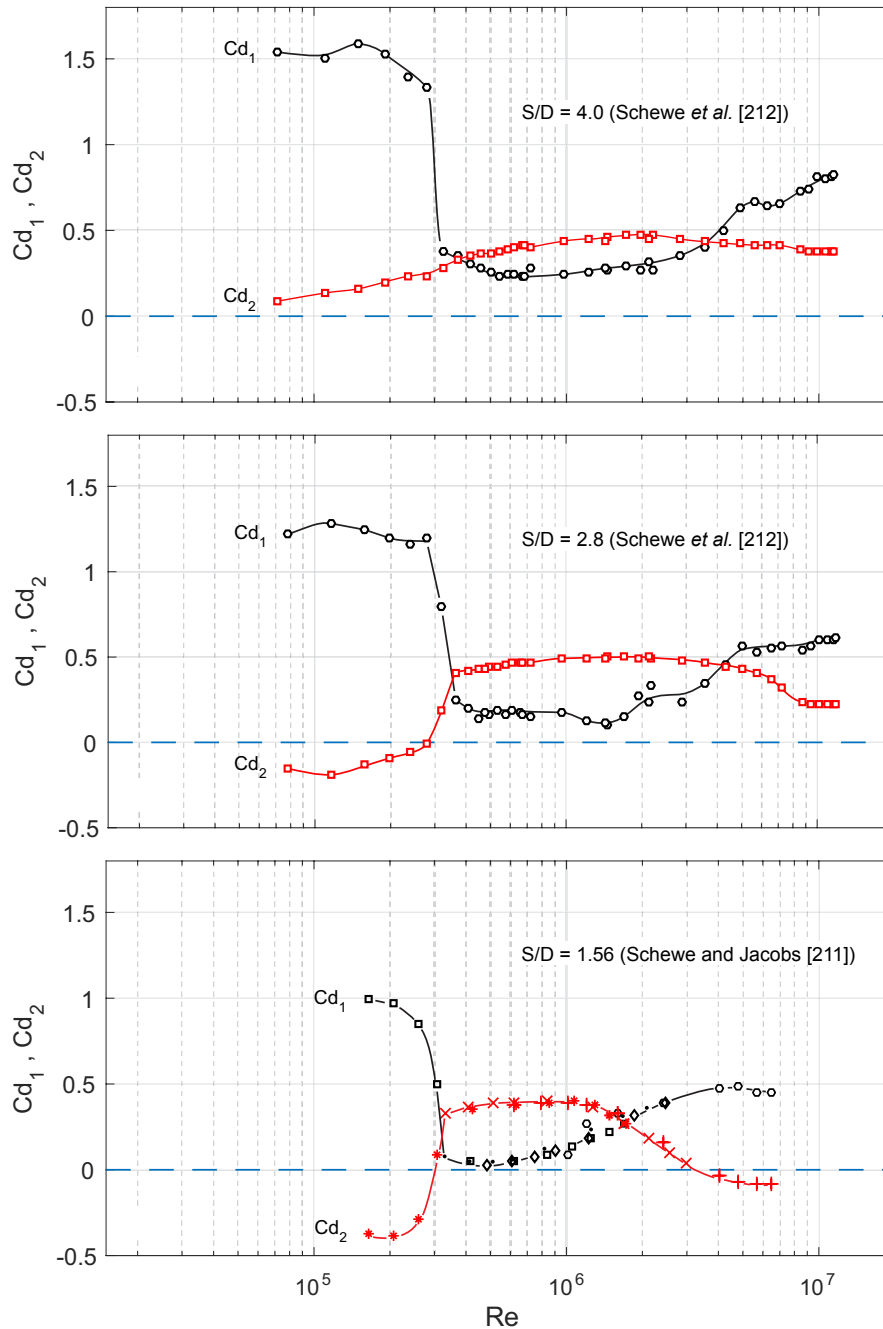
Figure 5.3: Mean drag coefficients of two in-line smooth circular cylinders for Reynolds numbers between 10^5 and 10^7 (Adapted from Schewe *et al.* [212]). Top: $S/D = 4.0$; centre: $S/D = 2.8$; bottom: $S/D = 1.56$.

the *supercritical* flow regime and *upper transition* before reaching a *transcritical* plateau with $St_L = 0.17$ around $Re_D = 10^7$.

In contrast to the many studies, both numerically and experimentally, on the influence of the height and texture of surface roughness on the fluid dynamics of isolated circular cylinders, hardly any investigations have been performed on in-line roughened circular cylinders up to today, despite their significant relevance to many engineering applications. Okajima [173] used polystyrene beads to simulate a surface roughness of $k/D = 0.9\%$. Two centre-to-centre spacing
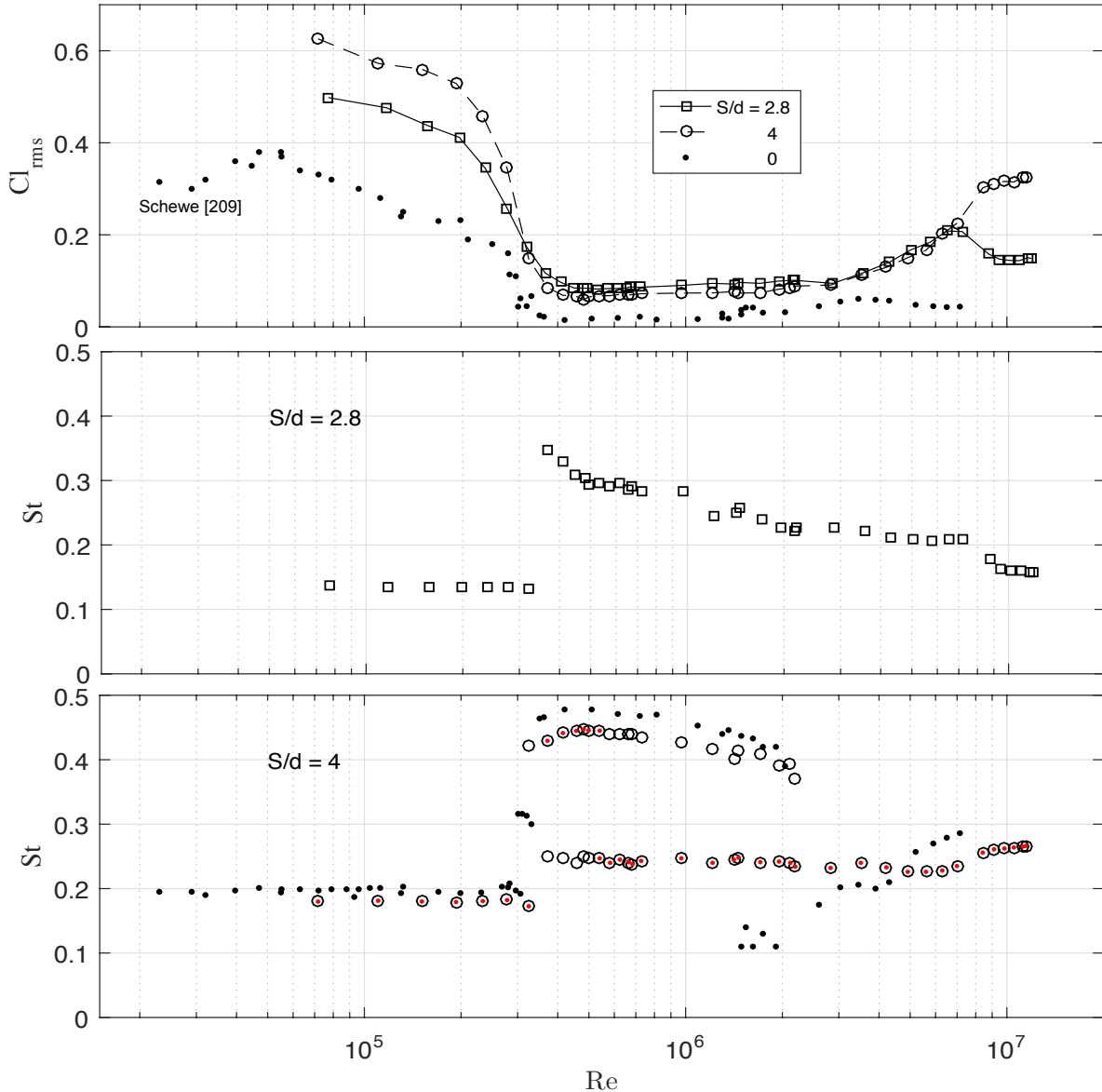
Figure 5.4: Fluctuating lift coefficient and Strouhal number of the downstream smooth cylinder for two in-line circular smooth cylinders ($S/D = 2.8$ and 4.0) at Reynolds numbers between 10^5 and 10^7 (Adapted from Schewe *et al.* [212]). Top: fluctuating lift; centre: Strouhal number for $S/D = 2.8$; bottom: Strouhal number $S/D = 4.0$. Reference: •, single smooth circular cylinder by Schewe [209].

values were selected, i.e. $S/D = 3.0$ and 5.0, for Reynolds number between $Re_D = 4 \times 10^4$ and 4×10^5. The downstream cylinder was either smooth or roughened, while the upstream cylinder was in both cases rough. Figure 5.5 gives an overview of the mean drag and Strouhal number of both roughened cylinders at the two spacing values, as well as those obtained for both in-line rough and smooth cylinder combinations, as function of the Reynolds number. For the upstream cylinder, the changes of both fluid-dynamic parameters with increasing S/D and Reynolds number are as expected. A comparison of the various curves for the downstream
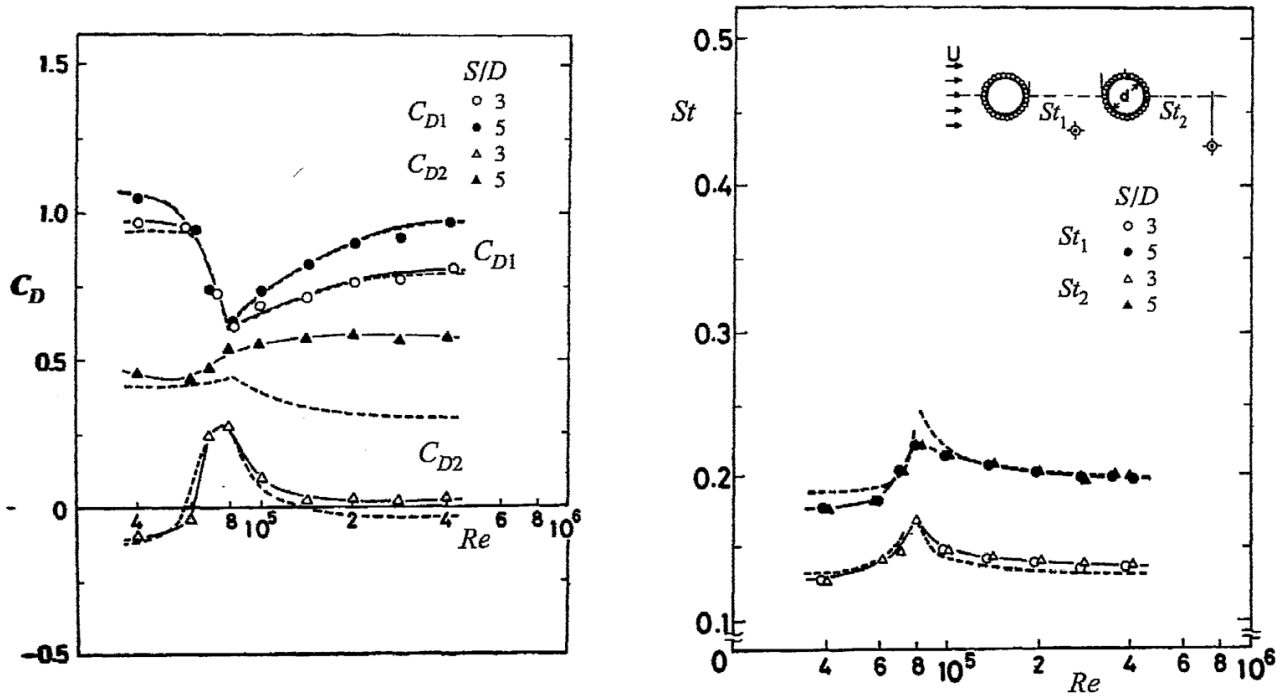
Figure 5.5: Impact of increased surface roughness height ($K/D = 0.9\%$) on the mean drag coefficient (left) and Strouhal number (right) of two circular cylinders in tandem ($S/D = 3.0$ and 5.0) for Reynolds numbers between 4×10^4 and 4×10^5 (Okajima [173]). The dashed lines show the reference data that were obtained for a combination of a rough upstream and smooth downstream circular cylinder in tandem at equal centre-to-centre spacings.

cylinder shows that the drag curve for $S/D = 5.0$ is the only one that is clearly altered by the surface roughness for all Reynolds numbers with the exception of the *subcritical* ones. Interestingly, the increased surface roughness has barely any effect on the curves of the Strouhal numbers for both cylinders. It is furthermore noticed, that both cylinders have equal Strouhal numbers at each spacing value.

5.1.2 Pairs of sharp-edged square-section prisms in tandem

Despite the various distinct differences between the flow characteristics of sharp-edged square-section prisms and circular cylinders, presented in Chapter 2, a variety of flow patterns, similar to those described above for two in-line circular cylinders, also appear one after the other with increasing centre-to-centre spacing between two tandem square-section prisms in cross-flow (Shiraishi *et al.* [220], Kareem [121], Sakamoto *et al.* [204], Sakamoto and Haniu [203], Luo [137], Ohya *et al.* [172], Luo and Teng [140], Takeuchi and Matsumoto [240], Tatsutani *et al.* [244], Hangan and Vickery [94], Luo *et al.* [139], Alam *et al.* [14, 15], Liu and Chen [134], Kim *et al.* [125], Sohankar and Etminan [232], Etminan *et al.* [72], Choi *et al.* [50], Sohankar [229, 230], Duchaine *et al.* [67], Shang *et al.* [216]). Besides S/D (and Re_D in case its value is smaller than 10^4, as was discussed in section 2.2.1) the angle of incidence of each of the two square prisms now has a tremendous influence on the flow structures and ensuing fluid-dynamic loading as well. This latter effect has for example been presented in experimental investigations of two-inline square-section prisms at various incidences between $0°$ and $45°$ by Reinhold *et al.* [188] and Du *et al.* [64–66].

In their experimental study on the flow over two sharp-edged square-section prisms in a tandem arrangement at Reynolds numbers of $Re_D = 2.76 \times 10^4$–5.52×10^4, Sakamoto *et al.* [204] found a significant effect of S/D on both the mean and fluctuating fluid-dynamic loads experienced by both prisms, as well as on the Strouhal number. They observed a jump in the mean and fluctuating drag, fluctuating lift, and Strouhal number at a spacing of $S/D = 4.0$. At this critical spacing between the *reattachment* regime ($S/D \leqslant 4.0$) and the *co-shedding* regime ($4.0 \leqslant S/D \leqslant 28$) the mean drag and fluctuating forces reach their maximum values, whereas the Strouhal number drops to its minimum of $St_L \approx 0.1$. In contrast to the *reattachment* regime, in which eddies are shed from the downstream prism only, the *co-shedding* regime is characterised by a synchronisation in frequency and phase of the eddy shedding behind both prisms. They noticed that this synchronisation remains present up to a spacing value of $S/D = 28$, above which both prisms shed eddies independently and at different frequencies with $St_{L_2} < St_{L_1}$. They furthermore reported that in the *co-shedding* regime the periodic vortex impingement onto the downstream prism leads to significantly larger fluctuating lift and drag forces acting on this prism than those measured on the upstream one or on an isolated prism. Similar flow observations were obtained in a later experimental study by Luo and Teng [140], in which the value of the critical spacing as $S/D_{cr} = 4.0$ was confirmed at $Re_D = 5.67 \times 10^4$. Sakamoto and Haniu [203] discovered that the value of the critical spacing decreases with increasing free-stream turbulence intensity for two tandem square-section prisms at $Re_D = 3.32 \times 10^4$, while Sohankar [229] observed a decrease of S/D_{cr} with increasing Reynolds number at $\alpha = 0°$. The effect of a variation in the prism-to-prism spacing in the range of $S/D = 1.5$ to 9 was studied in a wind tunnel experiment by Liu and Chen [134] at Reynolds numbers between 2×10^3 and 1.6×10^4. Their results show not only that the flow structures around both prisms are highly dependent on S/D, but also that a hysteresis phenomenon with two jumps between the *reattachment* regime and *co-shedding* regime is present for $S/D = 2.5$ to 3.25 as the spacing value is either progressively increased or decreased at $Re_D = 5.3 \times 10^3$. Using PIV, Kim *et al.* [125] investigated the flow structures around two square-section prisms in a tandem arrangement with $S/D = 1.5$ to 11 at Reynolds numbers between 5.3×10^3 and 1.6×10^4. It was demonstrated that, depending on the Reynolds number, the value of the critical spacing is positioned in the range of $S/D = 3.0$ to 4.0.

The previous overview has shown, that a large amount of studies, both numerically and experimentally, are available on the flow around and fluid-dynamic quantities of two sharp-edged square-section prisms in a tandem configuration at 0° angle of incidence. Du *et al.* [64–66] are one of the few who actually performed wind tunnel experiments to study the impact of a variation of the incidence angle of both in-line prisms on their fluid-dynamic characteristics. Two incidence angles, $\alpha = 0°$ and $45°$, and eight spacing values between $P/B\ (= S/D) = 1.75$ and 5 (with P the dimensional centre-to-centre spacing between both prisms with side widths B) were selected. The Reynolds number was kept constant at $Re_D = 8 \times 10^4$. Figure 5.6 presents the cross-sectional mean drag coefficients on both prisms as function of the spacing value P/B for both incidence angles. Regarding the upstream prism, the drag values lie at both incidence angles in the vicinity of those of the single prism and coincide with the values obtained by Sakamoto *et al.* [204] and Sohankar [230]. The change of the drag force on the downstream prism from negative (i.e. a thrust force) to positive at $P/B = 3$ to 3.5 for $\alpha = 0°$ implies that the flow around the tandem configuration switches around that spacing from the *reattachment* regime to the *co-shedding* regime. The absence of an eddy formation behind the upstream prism, together with the combination of the reattachment of the free shear layers from the upstream prism on the downstream one and a weak eddy shedding in its wake for $P/B < 3$–3.5
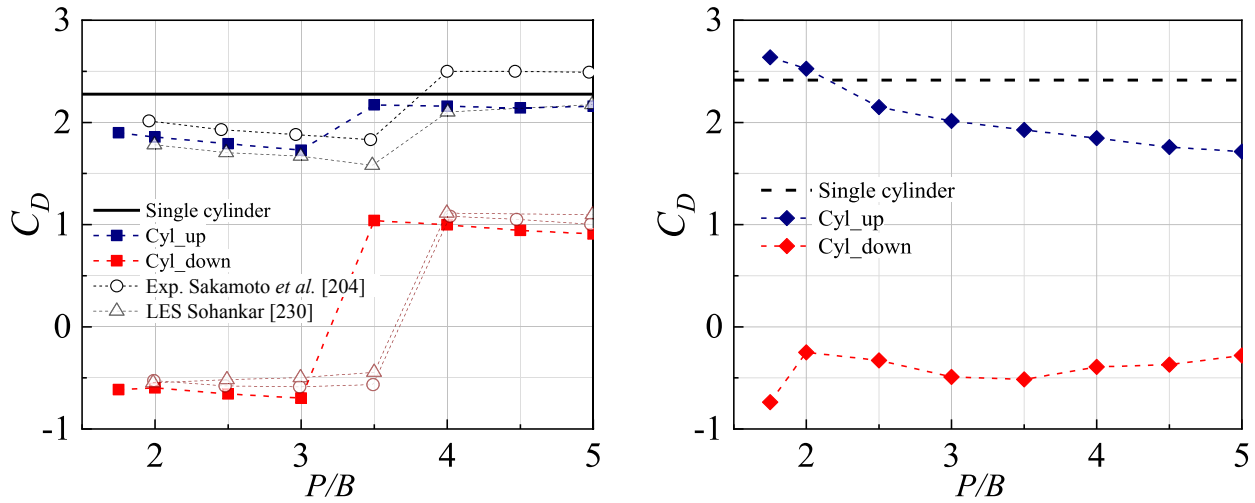
Figure 5.6: Effect of gap spacing on the mean drag coefficients of two in-line sharp-edged square-section prisms at incidence (Adapted from Du *et al.* [64]). Left: $\alpha = 0°$; right: $\alpha = 45°$.

induce only weak force fluctuations in both flow and cross-flow direction on both prisms (Figure 5.7). Above the critical spacing, the appearance of an vortex street in the gap between both prisms and its impingement on the downstream prism result in constant fluctuating lift and drag forces with high values that are close to those of an identical isolated sharp-edged square-section prism. Whereas in the former regime, the fluctuating lift forces on the downstream prism are larger than those of the upstream one, the latter regime is characterised by higher fluctuating lift forces on the upstream prism. Regarding the fluctuating drag forces, higher values are obtained on the downstream prism at all gap spacing values. The frequency with which the eddies are shed in the common near wake behind the downstream prism gradually decreases with increasing spacing value in the *reattachment* regime and reaches its minimum of $St_L = 0.1$ at the critical spacing, this value being consistent with the measurement by Sakamoto *et al.* [204] (Figure 5.8). In the subsequent *co-shedding* regime a recovery is observed; interestingly, at $P/B > 4$ the Strouhal number matches that one of a single prism at $\alpha = 45°$.

For the tandem configuration at 45° angle of incidence, the mean drag on the downstream prism remains negative at all spacing values between 1.75 and 5. This demonstrates that the *reattachment* regime is present at all investigated gap values and, at least up to $P/B = 5$, no cross-over to the *co-shedding* regime takes place. With the exception of the drag fluctuations of the downstream prism, the fluctuating forces change rapidly with growing gap size up to about $P/B = 3$. They thereupon level off and reach nearly constant values for $P/B \geqslant 4$. For the fluctuating lift on the downstream and fluctuating drag on the upstream prism, this plateau equals the level of a single prism, whereas the fluctuating lift experienced by the upstream prism nears values close to zero. The fluctuating drag on the downstream prism actually has a similar trend as the fluctuating lift on the upstream one, just with a much smaller amplitude variation. The trend of the Strouhal number for the tandem prisms at $\alpha = 45°$ with increasing P/B is the exact inverse of those for the fluctuating forces: an increase up to about $P/B = 3.5$, followed by nearly constant values for a larger gap spacing (Figure 5.8).
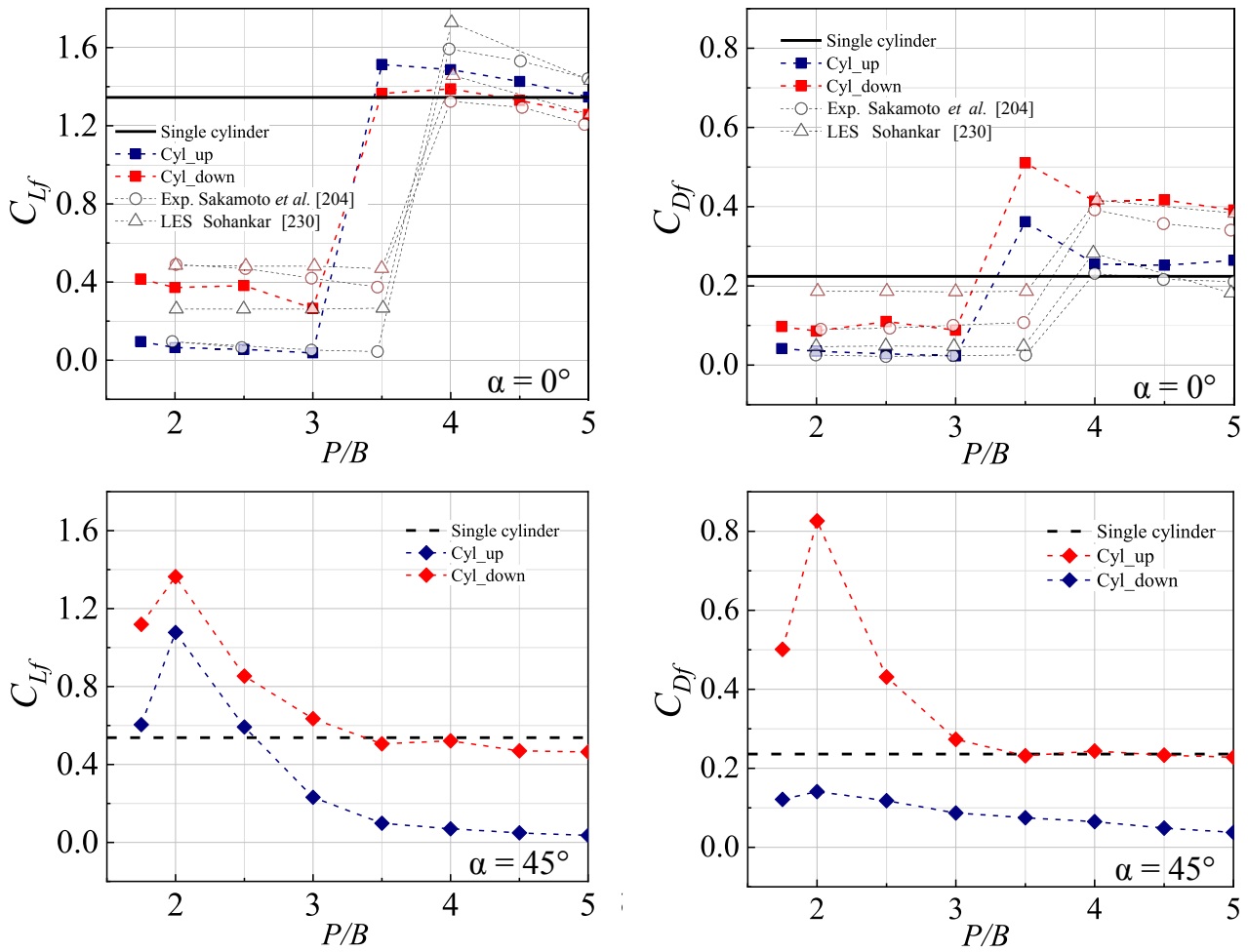
Figure 5.7: Effect of gap spacing on the fluctuating lift and drag coefficients of two in-line sharp-edged square-section prisms at incidence (Adapted from Du *et al.* [64]). Upper row: $\alpha = 0°$; lower row: $\alpha = 45°$.
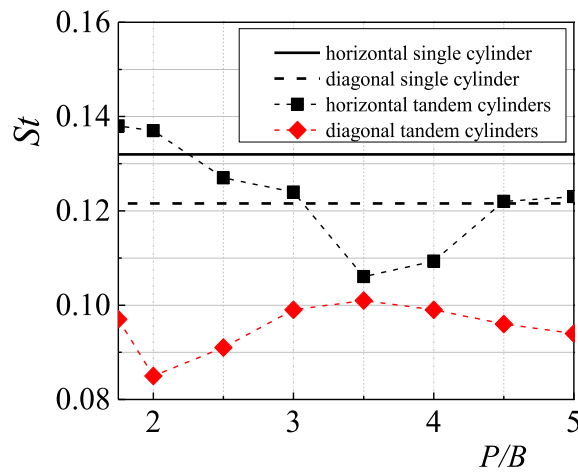
Figure 5.8: Effect of gap spacing on the Strouhal number of two in-line sharp-edged square-section prisms at $\alpha = 0°$ and $45°$ (Adapted from Du *et al.* [64]).

5.2 Separation effect on two smooth square-section prisms with $r/D = 0.16$ in tandem at the two "symmetric" incidence angles

In contrast to the huge amount of studies on the flow around two "infinite" smooth circular cylinders or sharp-edged square-section prisms, positioned one behind the other in a cross-flow, merely a handful of investigations are available on the fluid dynamics of a pair of inline square-section prisms with rounded edges. The few studies that do exist and focus on the combined effect of edge roundness and gap spacing have only been published recently and focus on low to very low Reynolds numbers of $Re_D = 100$ (Adeeb *et al.* [8], Datta *et al.* [55], Zhang *et al.* [297], Adeeb and Sohn [9]) or $Re_D = 3\times10^3$–4×10^3 (Virkam *et al.* [264]).

The results presented in this section on the various fluid-dynamic quantities of two parallel rounded square-section prisms have been obtained in a cross-flow with Reynolds numbers between 10^5 and 10^7. For that purpose, the same test section and measurement equipment were used as briefly described in section 3.1.1 for the single cylindrical and prismatic bluff body measurements. Small modifications were performed to the test section to be able to position a second square-section prism upstream of the first one, as shown in Figure 5.9. The test described in this section was conducted with two prisms having a fixed edge roundness of $r/D = 0.16$ and polished faces, i.e. $k_s/D = 4.5\times10^{-6}$. Two centre-to-centre spacing values, $S/D = 4.0$ and 5.6, were selected. The spacing variation was realised through a repositioning of the upstream prism, while the location of the downstream prism remained fixed at the position of the piezoelectric platform dynamometers. Two angles of incidence, $\alpha_{1,2} = 0°$ and
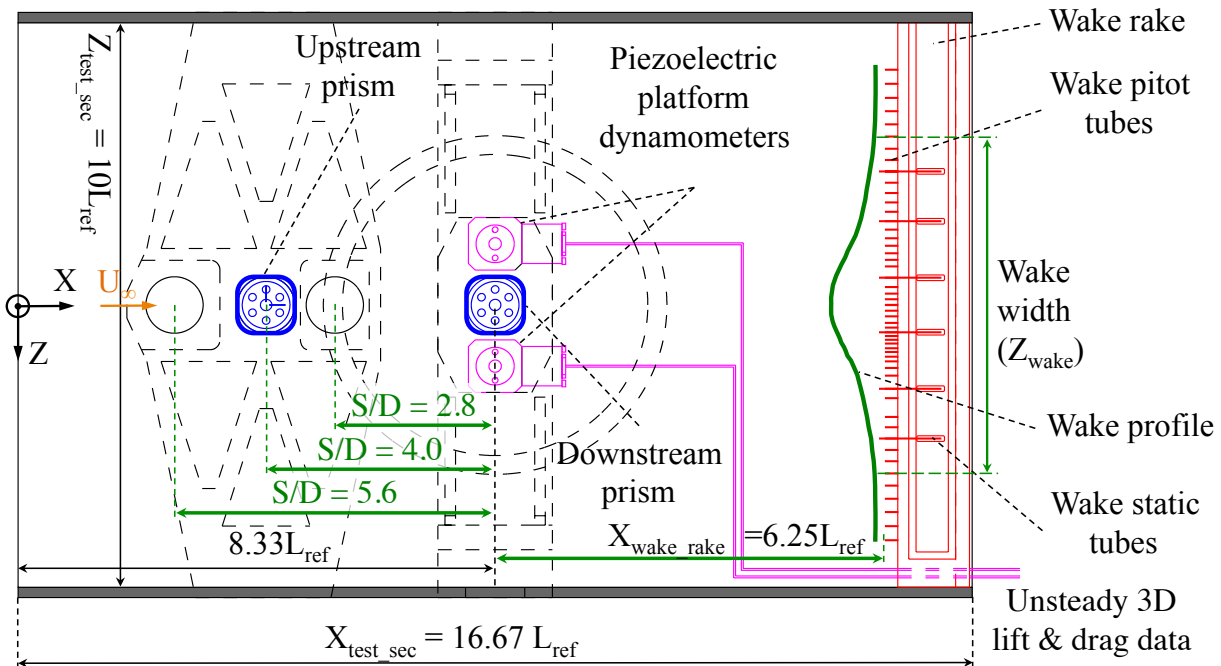
Figure 5.9: Experimental setup in the High-Pressure wind tunnel facility for fluid-dynamic tests on two 2D models in tandem: side view of test section with the two tandem models, piezoelectric platform dynamometers, and wake rake (Adapted from Van Hinsberg [259]).

45°, were investigated, whereby at each test run both prisms had the same incidence angle. The measurement procedure of scanning through the complete range of Reynolds numbers by a combined variation of the flow velocity and total air pressure in the HDG, see section 3.1.1, was maintained.

5.2.1 Mean global and cross-sectional fluid-dynamic coefficients

The Figures 5.10a and 5.10b present the development of the coefficient of the mean cross-sectional total wake drag coefficient of the tandem arrangement, obtained with the pressure rake in the wake behind both prisms, with increasing Reynolds number for $S/D = 4.0$ and 5.6 for both incidence angles. The shapes of the vertical wake profiles from which the total drag of both prisms was derived, are shown in Figure 5.11 for selected Reynolds numbers that cover the various occurring flow regimes. For comparison reasons, the data for the isolated smooth square-section prism with equal edge roundness have been included in both figures as well. The latter global drag coefficients were obtained with the piezoelectric platform dynamometers instead. Both $C_{D_{single}}(Re_D)$ curves in the Figures 5.10a and 5.10b have been multiplied by a factor two to facilitate the comparison with the results for each tandem configuration. At $\alpha = 0°$, an almost perfect match is found between both $Cd_{wake}(Re_D)$ curves for the two in-line prisms and the corresponding curve of the identical, single square-section prism at all Reynolds numbers. This even counts for the drag crisis and the Reynolds numbers at which the cross-overs from one flow regime to the next occurs. By inspection of the shapes of the wake profile, the widths of the wake, and the maximum total non-dimensional pressure losses $\left(\Delta p/q\right)_{max}$ in the Figures 5.11b and 5.11c, this equality of the total drag between both gap spacing values at equal *subcritical* to *supercritical* Reynolds numbers is evident. Surprisingly, even the asymmetry in the wake profiles in the *asymmetric* flow state is virtually identical.

At $\alpha = 45°$, the overall trend of the $Cd_{wake}(Re_D)$ curve for the larger of the two spacing values is still similar to that of the single prism configuration (Figure 5.10b). Deviations from the latter configuration do occur though, in particular at *subcritical* and *supercritical* Reynolds numbers at which, smaller, respectively higher mean total drag values are obtained. The changes in the wake profiles and in particular in the values of $\left(\Delta p/q\right)_{max}$ show a weaker dependence on the Reynolds number, though (Figure 5.11f). In contrast, the combination of $S/D = 4.0$ and $\alpha = 45°$ results in a mean total drag curve that highly differs from the others. With the exception of the short *supercritical* flow regime, both the value for Cd_{wake} and its variation with increasing Reynolds number are much smaller. In particular the discontinuous drop of the total drag curve in the *transcritical* flow regime down to the *subcritical* level is prominent. As seen in Figure 5.11e, it is caused by the sharp and sudden reduction of the maximum total non-dimensional pressure loss that indicates the presence of a much lower velocity defect and thus a shorter near wake, while the width of the wake remains unaffected.

The individual mean drag coefficients on each prism, C_{d_1} and C_{D_2}, are displayed in the Figures 5.10c to 5.10f for the two spacing values at both incidence angles, together with the mean global drag coefficient of the single prism. Because neither the global, nor the cross-sectional drag on the upstream prism was measured directly, C_{d_1} had to be derived in an indirect way as the difference between the mean cross-sectional total drag coefficient, Cd_{wake}, of each tandem configuration and the respective mean global drag coefficient experienced by the downstream prism, C_{D_2}.

For both $S/D = 4.0$ and 5.6, the mean global drag coefficient of the downstream prism is largely Reynolds-number independent. The only significant, but very gradual change of about
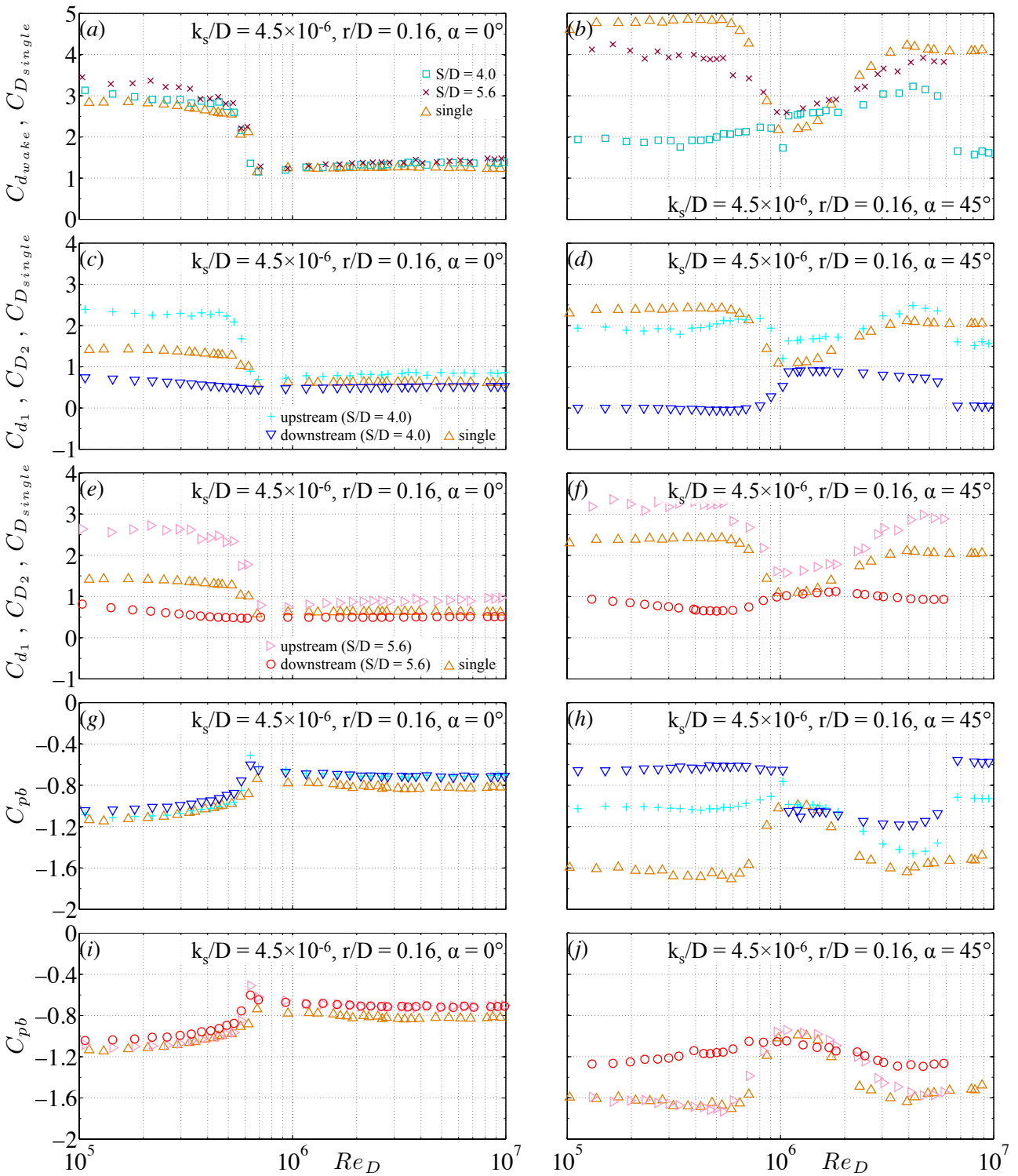
Figure 5.10: The Reynolds-number dependent mean global and cross-sectional drag and mean cross-sectional base pressure coefficients on two smooth square-section prisms ($r/D = 0.16$, $k_s/D = 4.5 \times 10^{-6}$, $\alpha = 0°$ and $45°$) in a tandem configuration with a prism centre-to-centre spacing of $S/D = 4.0$ and 5.6. Left column: $\alpha = 0°$; right column: $\alpha = 45°$. $\triangle$: single isolated prism ($r/D = 0.16$, $k_s/D = 4.5 \times 10^{-6}$), Van Hinsberg *et al.* [254].

33% in drag occurs in the *critical* flow regime. The cross-over to the *supercritical* flow regime is for both spacing values situated around $Re_D = 7 \times 10^5$. Similar to the single prism case, this
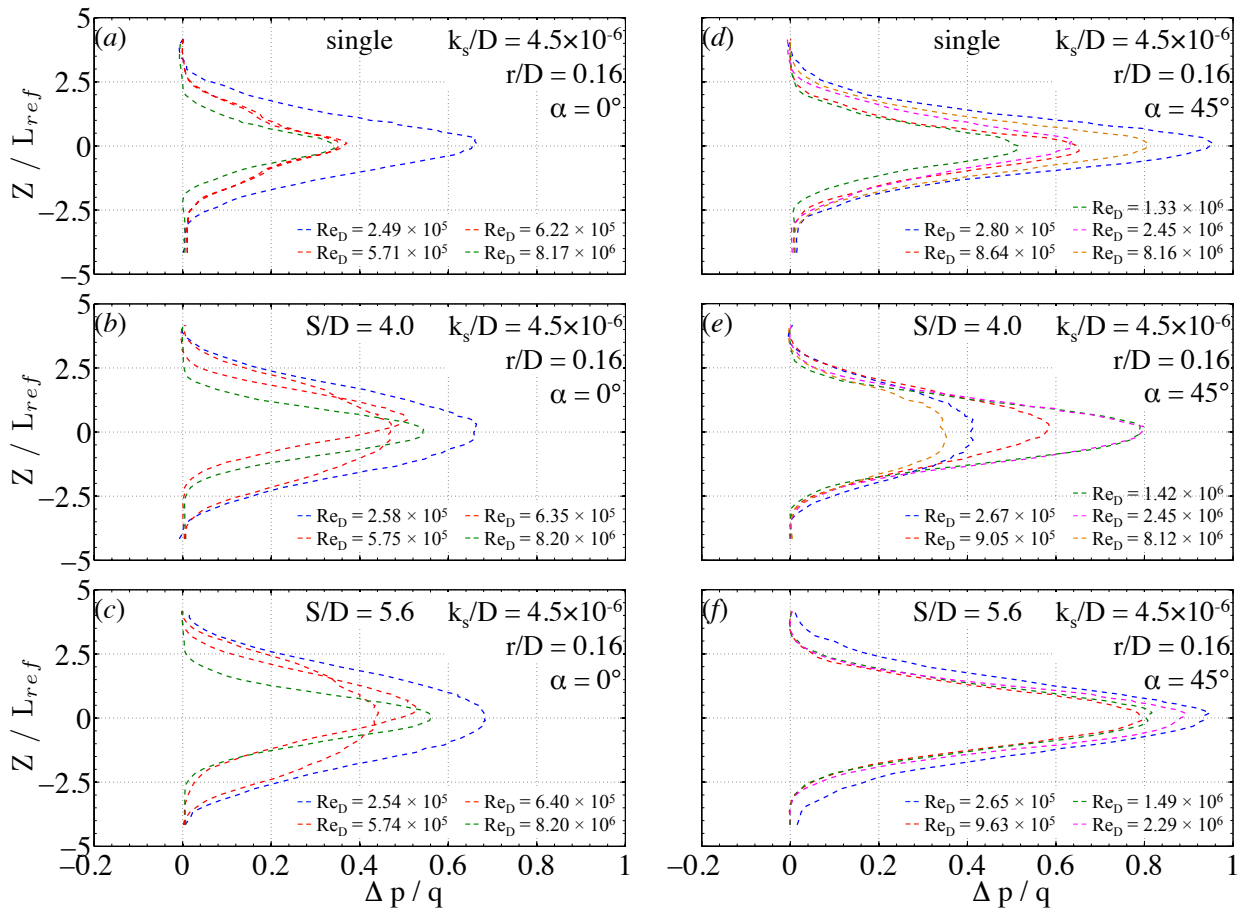
Figure 5.11: Influence of the prism centre-to-centre spacing on the mean vertical wake profile at $X/L_{ref} = 6.25$ behind the mid-span of the downstream one of two smooth tandem square-section prisms ($r/D = 0.16$, $k_s/D = 4.5{\times}10^{-6}$, $\alpha = 0°$ and $45°$) for selected Reynolds numbers in the various flow regimes. Left column: $\alpha = 0°$; right column: $\alpha = 45°$. Upper row: single, isolated prism configuration; centre row: $S/D = 4.0$; lower row: $S/D = 5.6$. $--$: *subcritical* flow regime; $--$: *critical* flow regime; $--$: *supercritical* flow regime; $--$: *upper transition*; $--$: *transcritical* flow regime.

flow regime lasts up to at least $Re_D = 10^7$. While the values of C_{D_2} are at all *subcritical* and *critical* Reynolds numbers significantly lower than for the single prism, the weaker descent in the latter flow regime leads to a convergence of both curves that results in mean global *super-critical* drag coefficients for the downstream prism that are at a similar level as for the single prism configuration. It can thus be argued, that, although the flow around the two tandem prisms can be classified as belonging to *co-shedding* regime, *proximity* effects are nonetheless present up to about $Re_D = 7{\times}10^5$. Both $C_{d_1}(Re_D)$ curves for the upstream prism have similar trends as both the total drag coefficient of the tandem configuration (obtained by the wake rake measurement) and the global drag coefficient of the single smooth prism. Because of the low *subcritical* and *critical* values of C_{D_2}, a significantly higher drag force than for the isolated prism is derived for the upstream prism in these two flow regimes at $S/D = 4.0$ and 5.6. The mean pressure at the base of both tandem prisms is for all Reynolds numbers nearly identical to those of the single prism, as shown in the Figures 5.10g and 5.10i. This would imply the presence of a lower mean pressure on the front face(s) of the downstream prism than on the same face(s) of the single prism, while on the front face(s) of the upstream prism much higher

mean pressures would have to be present. However, both the upstream tandem prism and the isolated prism experience the same undisturbed free stream. It can thus be argued, that the pressure distribution on the front face(s) of both latter configurations are similar or even equal. Hence, it must be concluded that the values of C_{d_1}, calculated by taking the difference between Cd_{wake} and C_{D_2}, are over-predicted at *subcritical* and *critical* Reynolds numbers.

At the incidence angle of $45°$, the mean cross-sectional drag coefficient for the upstream prism follows at both spacing values the $C_{D_{single}}(Re_D)$ curve of the single prism. The actual values of C_{d_1} fluctuate for $S/D = 4.0$ around those of $C_{D_{single}}$, while for $S/D = 5.6$ larger values are obtained at all Reynolds numbers. Because in the latter case a nearly perfect match between the base pressures of the upstream tandem prism and the single prism has been found, as displayed in Figure 5.10j, an over-prediction of C_{d_1} is present at all Reynolds numbers at $S/D = 5.6$. At the smaller spacing, a much lower mean suction at the base is obtained for the upstream prism than for the single prism at the majority of Reynolds numbers (Figure 5.10h). This means that for $S/D = 4.0$ C_{d_1} is also over-predicted. Compared to the upstream prism, the mean global drag coefficient of the downstream prism shows at both spacing values an inverse development with increasing Reynolds number. The stronger variation of C_{D_2} between the various flow regimes at $S/D = 4.0$ results from the sharp discontinuous steps in the mean base pressure coefficient at the cross-overs from the *critical* to the *supercritical* and from the *upper transition* to the *transcritical* flow regimes. At $S/D = 5.6$, a much weaker dependence of both C_{D_2} and C_{pb_2} on the Reynolds number has been measured. Interestingly, at all *subcritical* and *transcritical* Reynolds numbers, the downstream prism experiences at $S/D = 4.0$ no net drag force. This demonstrates, that in those two flow regimes the smaller centre-to-centre spacing equals the critical spacing.

5.2.2 Fluctuating loads due to eddy formation and shedding

The trend of the fluctuating lift on the downstream rounded square-section prism at $\alpha = 0°$ is not only equal for both spacing values, but also corresponds to that one of the single prism (Figure 5.12a). While the spacing itself has no pronounced influence on the values of $\sqrt{(\overline{C_L'^2})}_2$, the presence of the upstream prism generates for both spacing values slightly lower *subcritical* and *critical* lift fluctuations compared to the single prism case and considerably higher ones at all *supercritical* Reynolds numbers. Regarding the force fluctuations in flow-direction on the downstream prism, an inverted behaviour with increasing Reynolds number is observed in Figure 5.12c. The presence of the upstream prism induces significantly larger drag fluctuations on the downstream prism in the *subcritical* and *critical* flow regimes, that are at $S/D = 4.0$ in the former flow regime even more than twice as high as for an isolated prism. Then again, no variation in the values for $\sqrt{(\overline{C_D'^2})}_2$ by changes in the spacing and the Reynolds number or by the presence of a second prism is noted at *supercritical* Reynolds numbers.

Regarding the trend of the curve of the non-dimensional frequency of the shed eddies in the wake behind the downstream prism, a nearly perfect match with the curve for the single prism is obtained for both spacing values as well, as shown in Figure 5.12e. In particular the jump in the $St_L(Re_D)$ curves at the cross-over from the *critical* to the *supercritical* flow regime occurs in all three configurations at the exact same Reynolds number. The same even holds for the appearance of two Strouhal numbers, associated with the two main peaks in the power spectra of the global lift force presented in the Figures C.1a to C.1c, at equal Reynolds numbers in the *critical* flow regime. These results clearly show once more that the flow belongs at both
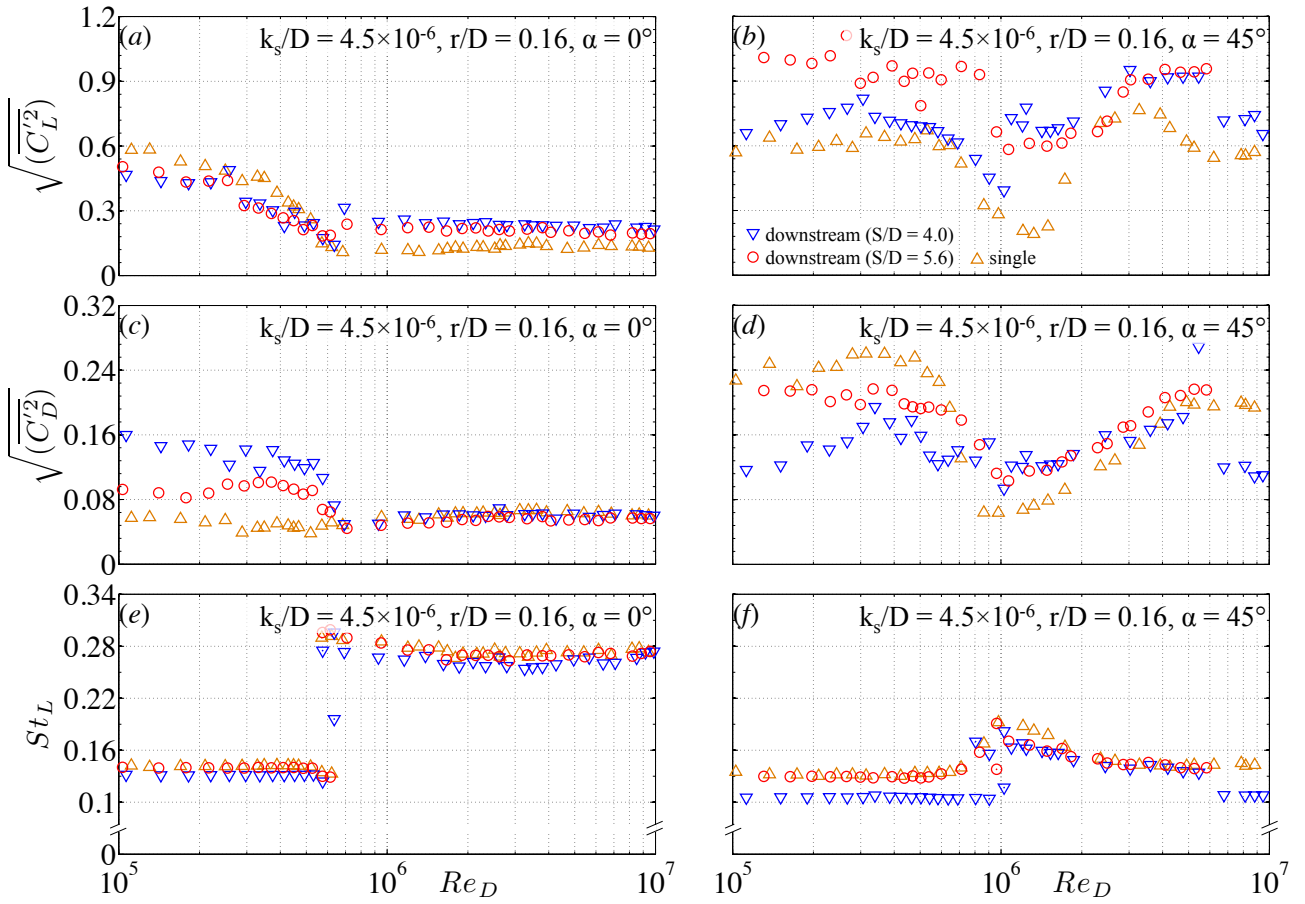
Figure 5.12: The Reynolds-number dependent fluctuating global lift and drag coefficients and the non-dimensional eddy-shedding frequency of the downstream prism of two smooth square-section prisms ($r/D = 0.16$ and $k_s/D = 4.5 \times 10^{-6}$) in a tandem configuration with $S/D = 4.0$ and 5.6 at $\alpha = 0°$ and 45°. $\triangle$: single isolated prism ($r/D = 0.16$ and $k_s/D = 4.5 \times 10^{-6}$), Van Hinsberg *et al.* [254]. In case of the occurrence of two peaks in the power spectra at a certain Reynolds number, the more dominant Strouhal number is indicated by an open symbol, while a dot within the symbol belongs to the secondary peak. Left column: $\alpha = 0°$; right column: $\alpha = 45°$. Upper row: single, isolated prism configuration; centre row: $S/D = 4.0$; lower row: $S/D = 5.6$.

spacing values to the *co-shedding* regime. The slightly lower Strouhal numbers for $S/D = 4.0$ signalise the presence of a very weak influence of the upstream prism on the eddy shedding process behind the downstream one. At $S/D = 5.6$, the congruence of the curves for the tandem configuration and the single prism demonstrate the absence of any of such interference effects.

Also at the second "symmetric" incidence angle, the trends of the curves of the fluctuating lift, fluctuating drag, and for Strouhal number as function of the Reynolds number coincide well with those for the single prism configuration. However, compared to $\alpha = 0°$, larger deviations at equal Reynolds and larger variations in the values with increasing Reynolds number take place. Whilst at the majority of Reynolds numbers higher lift fluctuations are experienced by the downstream prism at both spacing values than by the single prism, the values for the fluctuating drag are for all three cases at a similar level. The only exception is found in the outer two flow regimes for the smaller gap size, i.e. the *subcritical* and *transcritical* one, where

much lower fluctuations in flow direction have been obtained. The only deviations of the two $St_{L_2}(Re_D)$ curves from that one for the single prism are found for $S/D = 4.0$ at $Re_D \leqslant 8 \times 10^5$ and $Re_D > 6 \times 10^6$; hence, exactly at those Reynolds number at which $S/D = S/D_{cr}$. At both tandem configurations, the occurrence of two Strouhal numbers at equal Reynolds number is evident from the power spectra of the global lift force presented in the Figures C.1e and C.1f.

5.3 Surface-roughness effect on two square-section prisms with $r/D = 0.16$ in tandem at the two "symmetric" incidence angles

Chapter 4 was devoted to the impact of an increase in height of a uniformly-distributed surface roughness on the flow around isolated two-dimensional circular cylinders and square-section prisms with and without rounded edges at incidence. Placing the focus on the square-section prism with rounded edges of $r/D = 0.16$, the main effects of a higher surface roughness were found to be a narrowing of all flow regimes with the exception of the *transcritical* one, and their migration to lower Reynolds numbers. Additional changes in the main fluid-dynamic quantities, i.e. mean and fluctuating lift and drag, base pressure, and Strouhal number, were found to be dependent on the incidence angle. At $\alpha = 0°$, the left-bounded *supercritical* flow regime was open to the right and the *upper transition* and *transcritical* flow regimes only appeared for high non-dimensional surface roughness values of at least $k_s/D \geqslant 0.1\%$. The roughness itself had barely any effect on the absolute minimum or maximum values of all previously listed quantities at the cross-over from the *critical* to the *supercritical* flow regime, as well as on their respective values within the latter flow regime. For those surface roughness values where the *upper transition* and *transcritical* flow regimes appeared, the majority of the fluid-dynamic quantities showed a recovery of their values in the direction of their respective *subcritical* levels during the flow transition from the *supercritical* to the *transcritical* flow regime. At $\alpha = 45°$, the most striking differences with the aforementioned trends at $\alpha = 0°$ were the distinct rise of the absolute minimum values of the coefficients for the mean drag, fluctuating lift and drag, and base pressure, as well as a descend of the maximum Strouhal number with increasing roughness height at the *critical* Reynolds number. A higher k_s/D value resulted furthermore in an increased independence of the flow around the rounded square-section prism on the Reynolds number.

The results in the Figures 5.13 and 5.14 display that similar surface-roughness effects as described above for the isolated rounded square-section prism in a cross-flow also appear for two identical in-line square-section prisms with $r/D = 0.16$. By setting both smooth tandem prism configurations of section 5.2 as reference, the surface roughness height on both prisms was increased by a factor of 100 to $k_s/D = 4.5 \times 10^{-4}$ (i.e. "slightly rough"). A significant deviation occurs only for the upstream prism at $\alpha = 45°$, as is presented at a later stage.

Compared to the reference curves of the various fluid-dynamic coefficients, the curves for both slightly rough prisms clearly show a distinct shrinkage of the Reynolds-number ranges covered by the various flow regimes. This trend is accompanied with the common shifts of the two bounding Reynolds numbers of each flow regime towards lower Reynolds numbers with increasing surface roughness height. The combination of both trends results at $\alpha = 0°$ either in the appearance of both the *upper transition* and the *transcritical* flow regimes ($S/D = 4.0$) or the increase of the range of *supercritical* Reynolds numbers ($S/D = 5.6$). At $\alpha = 45°$, the *transcritical* flow regime is extended to lower Reynolds numbers for both spacing values.

149
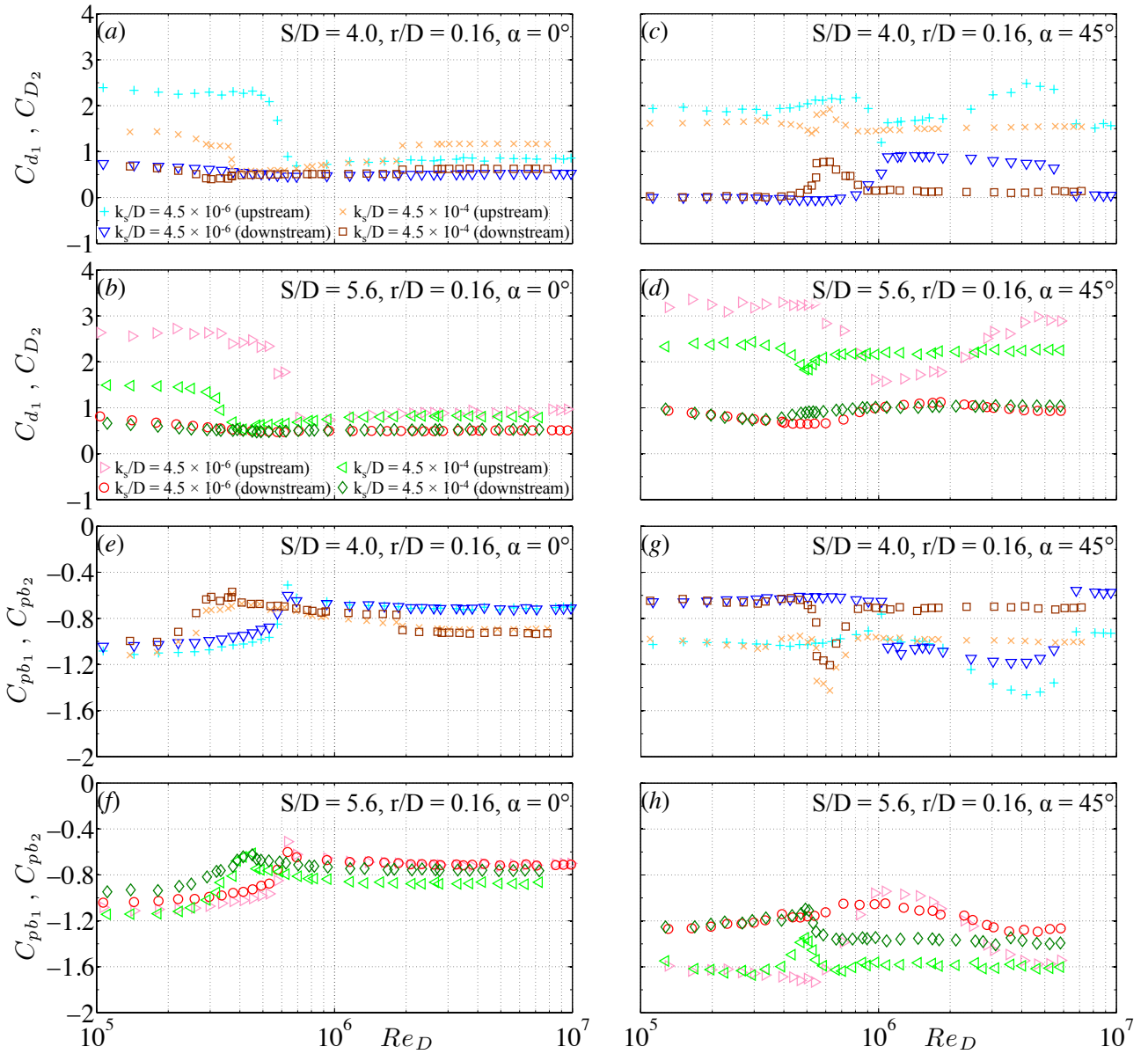
Figure 5.13: Impact of the non-dimensional equivalent sand-grain surface roughness height on the mean cross-sectional (upstream prism) and mean global (downstream prism) drag and mean cross-sectional base pressure coefficients on two square-section prisms ($r/D = 0.16$, $\alpha = 0°$ and $45°$) in a tandem configuration with a spacing of $S/D = 4.0$ and 5.6. Left column: $\alpha = 0°$; right column: $\alpha = 45°$.

In agreement with the results for the single rounded square-section prism, the *subcritical* values of each fluid-dynamic quantity remain for both prisms at all tandem configurations unaffected by a surface roughness increase. The only exception is formed by the values of C_{d_1} in the Figures 5.13a to 5.13d, for which a clear difference can be noticed between both curves. As discussed in section 5.2.1, the drag on the smooth upstream prism was not measured directly; its values were instead derived by taking the difference between $C_{d_{wake}}$ and C_{D_2}. This leads to an over-prediction of the values for C_{d_1} in this and the subsequent *critical* flow regime. The mid-sections of both slightly rough prisms were on the other hand equipped with 36 pressure taps, from which the mean pressure drag coefficients could be derived directly. Hence, based
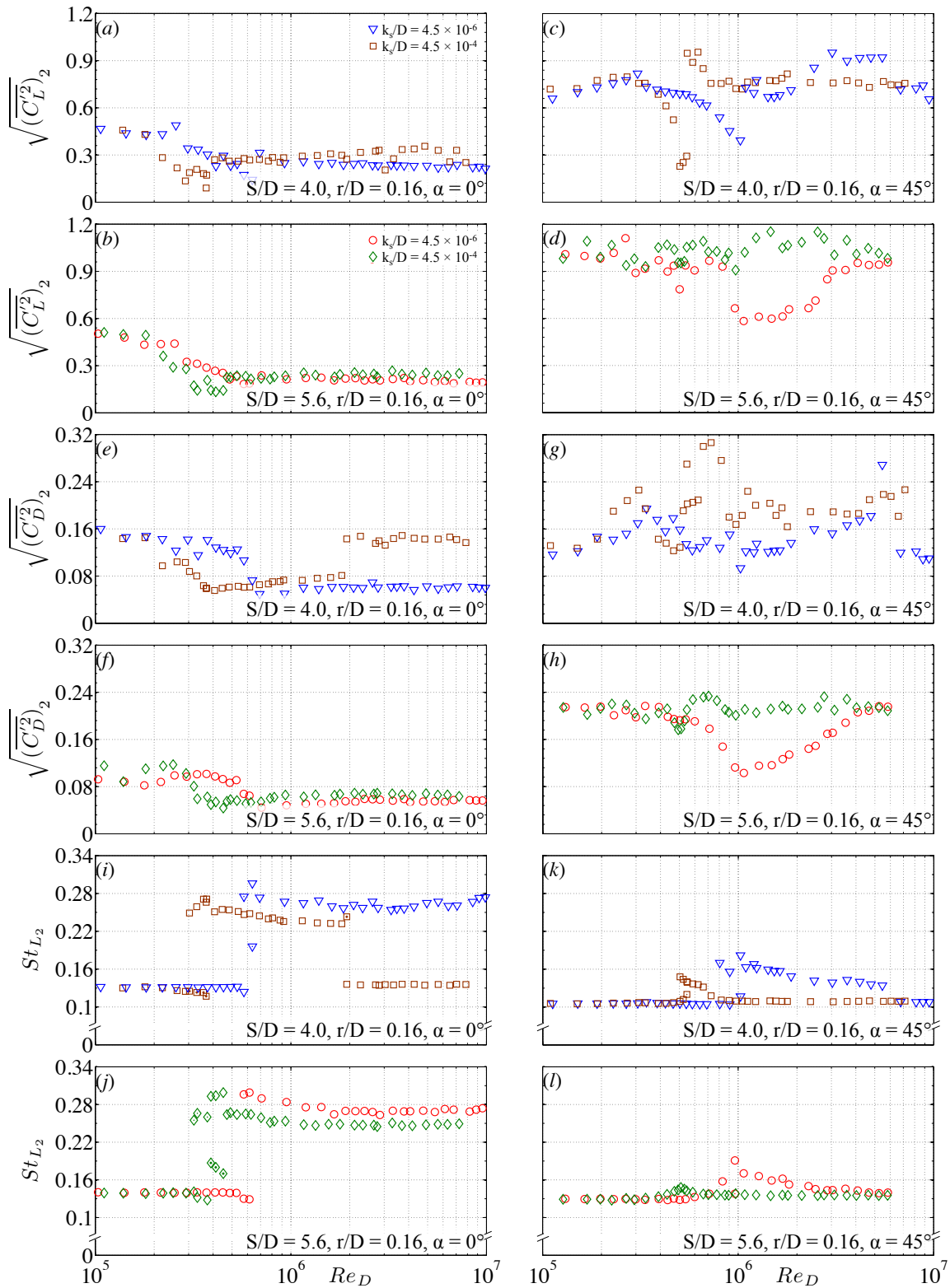
Figure 5.14: Impact of the non-dimensional equivalent sand-grain surface roughness height on the fluctuating global drag and lift coefficients and the Strouhal number of the downstream one of two square-section prisms ($r/D = 0.16$, $\alpha = 0°$ and $45°$) in a tandem configuration with a spacing of $S/D = 4.0$ and 5.6. In case of the occurrence of two peaks in the power spectra at a certain Reynolds number, the more dominant Strouhal number is indicated by an open symbol, while a dot within the symbol belongs to the secondary peak. Left column: $\alpha = 0°$; right column: $\alpha = 45°$.

on the behaviour of the drag on the single prism with increasing k_s/D value (section 4.1.1), the difference between both $C_{d_1}(Re_D)$ curves thus shows the amount of over-prediction of C_{d_1} for the smooth upstream prism in the *subcritical* and *critical* flow regimes at each tandem configuration. A second similarity with the single prism configuration is the independence on the roughness height of not only the absolute minimum values of C_{d_1}, C_{D_2}, and $C_{pb_{1,2}}$ of both prisms at the cross-over from the *critical* to the *supercritical* flow regime, but also of their nearly constant values at *supercritical* Reynolds numbers. The same holds for the fluctuating lift and drag forces on and the Strouhal numbers of the downstream prism at those Reynolds numbers.

At $\alpha = 45°$, the effect of an increased k_s/D value differs between the two slightly rough prisms. While for the upstream prism a weaker descend of C_{d_1} and C_{pb_1} in the *critical* flow regime is obtained that leads to higher *supercritical* values of both coefficients at both spacing values, the increased roughness does not alter the values of C_{D_2} and C_{pb_2} of the downstream prism obtained at *supercritical* Reynolds numbers. Hence, although both prisms form together a tandem constellation, each prism experiences its own development of the drag and base pressure with increased surface roughness at those Reynolds numbers. Based on the values of the mean global and cross-sectional drag coefficients, the higher surface roughness does not affect the classification of the flow around the tandem prism configurations. Like their smooth counterparts, the flow belongs in all four cases to the *co-shedding* regime. Noteworthy is furthermore the occurrence of a zero net drag on the downstream slightly rough prism at all *subcritical* and *transcritical* Reynolds numbers for the combination $S/D = 4.0$ and $\alpha = 45°$ (Figure 5.13c). Hence, in these two flow regimes the spacing of $S/D = 4.0$ equals once more the critical spacing between the *reattachment* and the *co-shedding* regimes.

The appearance of the *upper transition* and the *transcritical* flow regimes for $S/D = 4.0$ at $\alpha = 0°$ creates a stronger dependence of the flow around both slightly rough prisms on the Reynolds number. This leads to considerably higher drag fluctuations on the downstream prism, as well as much lower Strouhal numbers, both at a *subcritical* level, for $Re_D \rightarrow 10^7$. The opposite is found at $\alpha = 45°$ as a result of the weaker variation of the fluid-dynamic coefficients with Reynolds number in the *critical* flow regime and *upper transition* for both spacing values. In this case, high and relatively constant force fluctuations both in flow and in cross-flow direction together with low Strouhal numbers occur over a large range of Reynolds numbers.

5.4 Separation effect on slightly rough two square-section prisms with $r/D = 0.16$ in tandem at the two "symmetric" incidence angles

To obtain a more detailed trend of the impact of the centre-to-centre spacing between the two slightly rough (i.e. $k_s/D = 0.045\%$) square-section prisms with rounded edges of $r/D = 0.16$ on the flow behaviour around both tandem prisms a third spacing, i.e. $S/D = 2.8$, was additionally investigated at $\alpha = 0°$ and $45°$. For all three spacing values $S/D = 2.8$, 4.0, and 5.6, both prisms were equipped with 36 pressure that were equally spaced over each model's mid-span cross-section. By integration of their pressure values, the mean cross-sectional pressure drag, lift, and pitch moment coefficients ($C_{d_{1,2}}$, $C_{l_{1,2}}$, and $C_{m_{1,2}}$) of each prism could be derived separately. In addition, both ends of the downstream prism were connected to piezoelectric platform dynamometers. In that way, the time series of the spanwise-integrated lift and drag forces on that prism could be measured, from which – in a post-processing step – the respective

mean and fluctuating components, as well as the frequency of the eddy shedding in the wake of the downstream prism were extracted.

5.4.1 Mean cross-sectional fluid-dynamic coefficients

Figure 5.15 presents the development of the coefficients of the cross-sectional mean pressure drag on both tandem prisms $C_{d_{1,2}}$ with increasing Reynolds number for the three investigated prism-to-prism spacing values and for both incidence angles. The values of the single isolated prism with both equal edge roundness and surface roughness, presented and discussed in section 4.1, have been added to each graph to facilitate a direct comparison. For all three spacing val-

Figure 5.15: Variation of the mean cross-sectional drag coefficients on two slightly rough square-section prisms ($r/D = 0.16$, $k_s/D = 4.5\times10^{-4}$, $\alpha = 0°$ and $45°$) in a tandem configuration with $S/D = 2.8$, 4.0, and 5.6 for Reynolds numbers in the range of 10^5 to 10^7 (Van Hinsberg [259]). $\triangle$: single isolated prism with $r/D = 0.16$ and $k_s/D = 4.5\times10^{-6}$, Van Hinsberg *et al.* [254]. Left column: $\alpha = 0°$; right column: $\alpha = 45°$. Upper row: $S/D = 2.8$; centre row: $S/D = 4.0$; lower row: $S/D = 5.6$.

ues a good match between the *subcritical* values of C_{d_1} and those of the single prism at $\alpha = 0°$ is obtained. The *drag crisis* in the subsequent *critical* flow regime is for the smallest spacing not only steeper, but continues also up to slightly higher Reynolds numbers compared to the single prism case (Figure 5.15a). This results in *supercritical* values of the drag experienced by the upstream prism that are about twice as low as on the single prism. While the single prism possesses a right-unbounded *supercritical* flow regime with relatively constant drag coefficients

153

up to $Re_D = 10^7$, the presence of a second prism further downstream introduces an upper limit of the same flow regime at $Re_D = 7 \times 10^5$. This is followed by a significant recovery of C_{d_1} in the *upper transition* and the appearance of a second nearly constant *transcritical* plateau of approximately $C_{d_1} = 1.18$ for Reynolds numbers larger than 2.23×10^6. At the largest of the three spacing values, $S/D = 5.6$, both the shapes of the $C_{d_1}(Re_D)$ and $C_{d_{single}}(Re_D)$ curve and the mean drag values coincide very well at the majority of the Reynolds numbers (Figure 5.15c). The slightly steeper descent of C_{d_1} whilst traversing the drag crisis leads to small deviations between both curves in the *critical* flow regime. For the intermediate spacing of $S/D = 4.0$, the development of C_{d_1} with increasing Reynolds number is actually a mixture of the previous two trends. Up to about $Re_D = 1.85 \times 10^6$, the values of C_{d_1} coincide reasonable well with those of the single prism. The discontinuous jump at $Re_D = 1.85 \times 10^6$ from a nearly constant plateau of $C_{d_1} \approx 0.76$ to a second plateau with $C_{d_1} = 1.13$–1.17 marks the sudden transition from the *supercritical* to the *transcritical* flow regime. The gradual recovery of C_{d_1} in the *upper transition*, clearly present at $S/D = 2.8$, has thus disappeared at $S/D = 4.0$. At all *transcritical* Reynolds numbers, the mean cross-sectional drag coefficient corresponds at this intermediate spacing then again very well to the *transcritical* drag values obtained for the upstream prism at $S/D = 2.8$. The trends of the three $C_{d_1}(Re_D)$ curves thus clearly show that at $\alpha = 0°$ a larger prism spacing results in an increased range of Reynolds numbers for which the interference of the flow around the upstream prism by the direct presence of the downstream partner in its wake is either very weak or prevented completely. While for $S/D = 2.8$ the upper boundary of this range lies within the *critical* flow regime, it is shifted to the end of the *supercritical* flow regime for $S/D = 4.0$. At the largest spacing of $S/D = 5.6$, the flow around the upstream prism can even be treated as being equivalent to that one of an isolated prism in cross-flow at all investigated Reynolds numbers.

The curve of the mean cross-sectional drag coefficient of the downstream prism is for the smallest spacing of $S/D = 2.8$ characterised by multiple sudden jumps, several plateaus with relatively constant values, and large variations over relatively small ranges of Reynolds numbers. In the *subcritical* flow regime, the state of the flow around both tandem prisms changes successively over two sharp drops at $Re_D = 2 \times 10^5$ and 2.6×10^5 from the *co-shedding* regime (*Mode II* with $C_{d_2} > 0$) to the *reattachment* regime (*Mode I* with $C_{d_2} < 0$). At the *subcritical* Reynolds numbers between both sudden descents the net drag force on the downstream prism equals zero, meaning that the spacing $S/D = 2.8$ corresponds exactly to the critical spacing. At $Re_D \leqslant 2 \times 10^5$ the spacing $S/D = 2.8$ lies above the critical spacing S/D_{cr} and the free shear layers that have separated from the upstream prism can reattach on the downstream one. After having passed the second drop, the spacing value lies below the critical spacing, which implies that *proximity* interference effects are dominant, as a result of which the eddy shedding and formation of the Kármán vortex street take place behind the downstream prism only. The second zero-crossing of C_{d_2} around the *critical* Reynolds number of $Re_D = 3.6 \times 10^5$ terminates the *reattachment* regime and causes the flow state around the tandem configuration to return to the *co-shedding* regime, i.e. *Mode II*. The steep decline of the mean drag force on the upstream prism in the *critical* flow regime leads at all *supercritical* Reynolds numbers and in the first part of the *upper transition* to a paradox situation: the downstream prism experiences a higher positive mean drag force than the upstream one. As mentioned in paragraph 5.1.1.2, a similar observation was described by Schewe *et al.* [212] for two tandem smooth cylinders with centre-to-centre spacing values of $S/D = 1.56$, 2.8, and 4.0 within the *supercritical* flow regime. In the following *upper transition*, the mean cross-sectional drag on the downstream prism dips at $Re_D = 1.68 \times 10^6$ once more at exactly $C_{d_2} = 0$, meaning that the critical spacing is briefly touched upon in this flow regime,, however, without the occurrence of a change in the

flow state around the tandem configuration. In the final *transcritical* flow regime, the values for C_{d_2} are about half and one-third of those for the single prism and upstream tandem prism, respectively. Hence, by taking the arithmetic mean of the values of the drag coefficients of both tandem prisms at each *transcritical* Reynolds number, the results match those of the single prism at equal Reynolds number very well.

With larger spacing between both tandem prisms an increasing independence of C_{d_2} on the Reynolds number is achieved. At $S/D = 4.0$, the mean cross-sectional drag on the downstream prism varies between 0.18 and 0.72 over the displayed range of Reynolds numbers and is further characterised by three small to moderate discontinuous steps at approximately $Re_D = 2.8 \times 10^5$, 3.6×10^5, and 1.85×10^6, hence, at the end of the *subcritical*, *critical*, and *supercritical* flow regime, respectively. At the largest spacing value, the $C_{d_2}(Re_D)$ curve is relatively flat, implying a strong independence on Re_D. Whereas at $S/D = 2.8$ the mean drag on the upstream prism was at *transcritical* Reynolds numbers three times higher than that on the downstream one, this difference reduced to 2 and 1.5 at $S/D = 4.0$ and 5.6, respectively. As expected, this shows that with increasing gap spacing the interference of the flow around the downstream prism, induced by the presence of the upstream one that generates a highly turbulent oncoming flow that is experienced by the downstream prism, diminishes, but is nevertheless even at a centre-to-centre spacing of $S = 5.6D$ still clearly noticeable.

As displayed in Figure 5.16a to 5.16c, each curve of the mean cross-sectional base pressure coefficient shows a similar development with increasing Reynolds number as their respective curve of the cross-sectional drag coefficient $C_{d_{1,2}}$. Because a change in the (mean) base pressure is directly coupled with an alteration of the net (mean) pressure drag acting on the prism, it is not surprising that the discontinuous steps in C_{d_2} occurring in the *subcritical* and *critical* flow regimes at $S/D = 2.8$ and 4.0 and for both prisms at the cross-over from the *supercritical* to the *transcritical* flow regime at $S/D = 4.0$ appear in the corresponding curves of the mean base pressure as well. At those Reynolds numbers, at which the mean cross-sectional drag on the upstream prism equals that of the single prism, similar values of the base pressure coefficients are also obtained. Surprisingly, for $S/D = 2.8$ and 4.0 the base pressure coefficients of both tandem prisms are nearly equal and their values are close to those of the single prism. The strong divergence between the development of C_{pb_1} and C_{d_1} in this flow regime thus implies an accompanying distinct change of the surface pressure on the other three faces and in particular on the front surface of the upstream prism. In section 5.4.3 this behaviour is explored in more detail by analysing the changes that occur in the cross-sectional surface pressure distributions with varying Reynolds number.

At 45° angle of incidence, the appearance of the mean cross-sectional drag curve of the upstream prism in the Figures 5.15d to 5.15f resembles for each of the three spacing values the $C_d(Re_D)$ curve of the single prism, with the exception of the *upper transition* at the intermediate spacing of $S/D = 4.0$. For $S/D = 2.8$ and 5.6, C_{d_1} experiences in this flow regime a moderate recovery from the *drag crisis*. In contrast, a distinct bump – with high drag values that partly even overlap with $C_{d_{single}}$ at several Reynolds numbers and bounded at both sides by a discontinuous jump – occurs in the $C_{d_1}(Re_D)$ curve for $S/D = 4.0$. In addition, and similar to $\alpha = 0°$, the drag coefficients of the upstream prism are for the largest spacing nearly equal to those values of the single prism. Hence, based solely on the drag, the upstream prism can in that specific case be treated as being equivalent to an isolated prism in cross-flow.

For each tandem prism configuration, a unique development of the mean cross-sectional drag on the downstream prism with increasing Reynolds number can be observed. Roughly
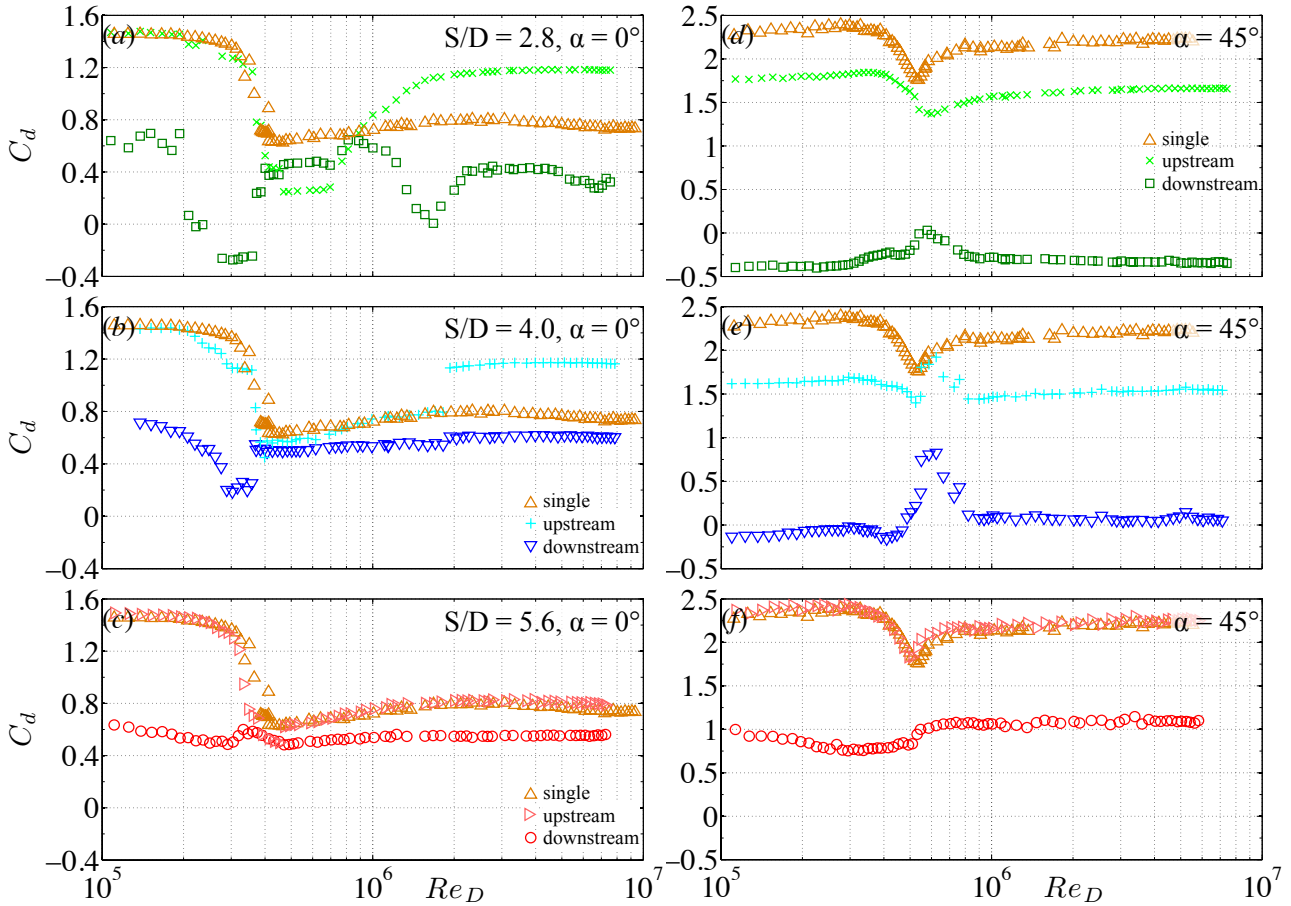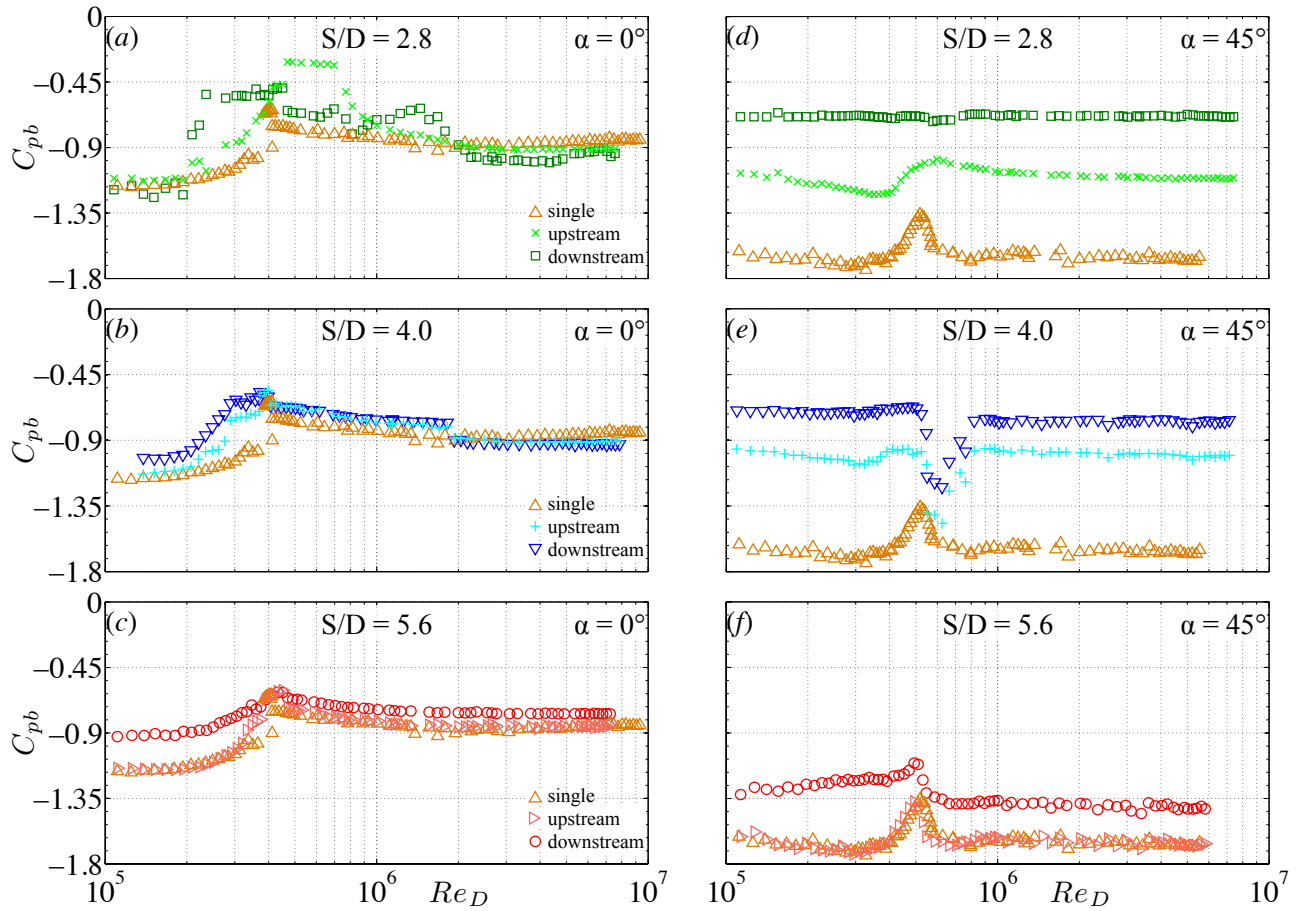
Figure 5.16: Variation of the mean cross-sectional base pressure coefficients on two slightly rough square-section prisms ($r/D = 0.16$, $k_s/D = 4.5 \times 10^{-4}$, $\alpha = 0°$ and $45°$) in a tandem configuration with $S/D = 2.8$, 4.0, and 5.6 for Reynolds numbers in the range of 10^5 to 10^7 (Van Hinsberg [259]). $\triangle$: single isolated prism with $r/D = 0.16$ and $k_s/D = 4.5 \times 10^{-6}$, Van Hinsberg *et al.* [254]. Left column: $\alpha = 0°$; right column: $\alpha = 45°$. Upper row: $S/D = 2.8$; centre row: $S/D = 4.0$; lower row: $S/D = 5.6$.

speaking, an increase of the spacing induces a shift of the $C_{d_2}(Re_D)$ curve from negative towards positive values. At $S/D = 2.8$, C_{d_2} shows a clear inverse trend with Reynolds number compared to C_{d_1}. Except at the *supercritical* and its direct neighbouring Reynolds numbers, the downstream prism experiences a thrust force. At Reynolds numbers of $5.4 \times 10^5 < Re_D < 6.0 \times 10^5$ the spacing $S/D = 2.8$ is equivalent to the critical spacing, since the net mean drag force on the downstream prism lies close to or equals zero. Regarding the associated mean pressure coefficients over the two base faces of both prisms, a relatively similar behaviour with the Reynolds number as for both mean drag coefficients is found, as displayed in Figure 5.16d. The flatness of the $C_{pb_2}(Re_D)$ curve implies a very weak dependence on the Reynolds number, though, even at those Reynolds numbers at which C_{d_2} possesses a distinct Reynolds-number-dependent variation. Identical trends for the mean cross-sectional drag on the upstream and downstream prism are obtained for the tandem configuration with the intermediate spacing $S/D = 4.0$. The same counts for both mean cross-sectional base pressure coefficients in Figure 5.16e. Similar to $S/D = 2.8$, the significantly lower suction at the base of both prisms compared to the single prism at equal Reynolds number reflects the strong interference effects between both tandem prisms at both spacing values. For Reynolds numbers up to approxi-
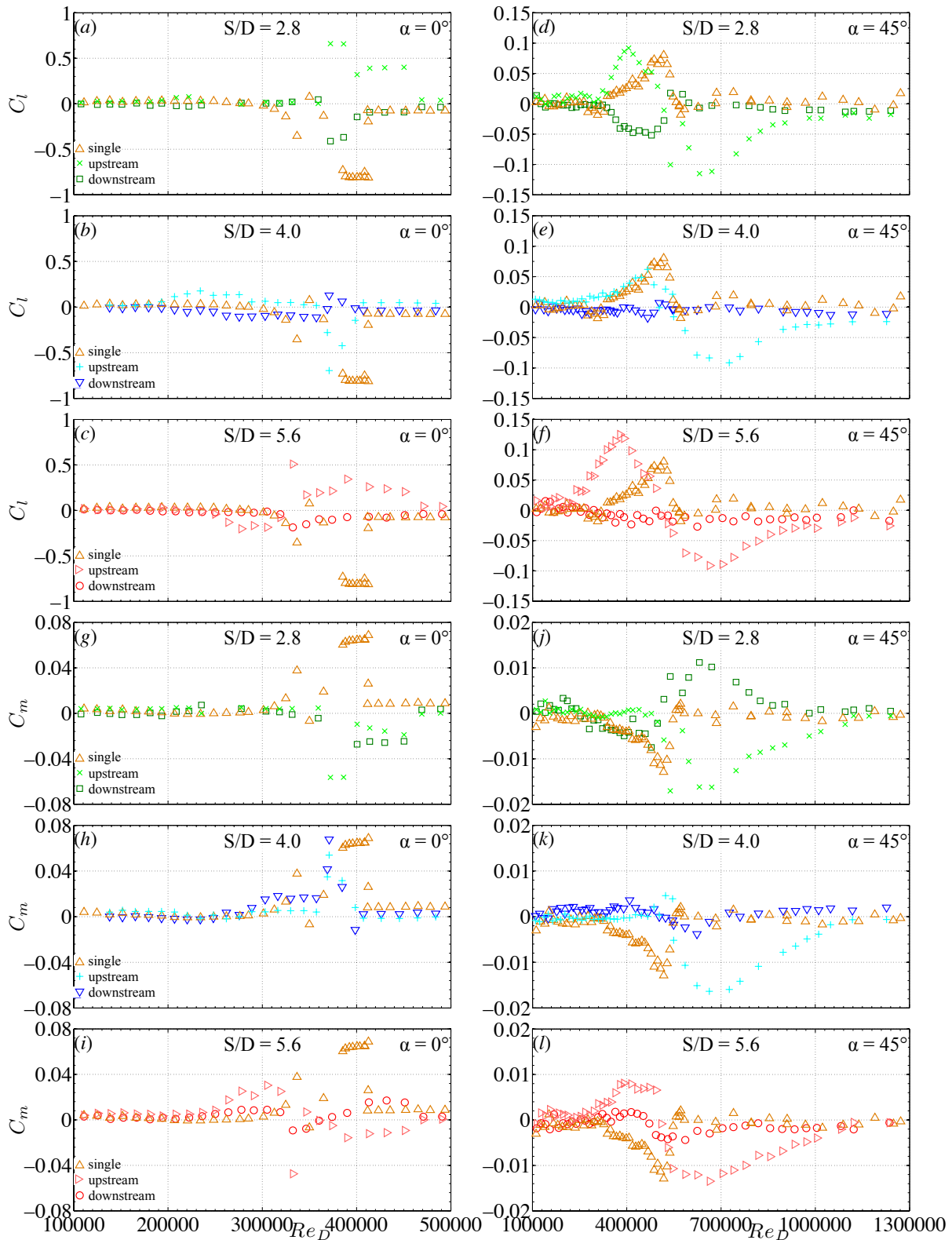
Figure 5.17: Variation of the mean cross-sectional lift and pitch moment coefficients on two slightly rough square-section prisms ($r/D = 0.16$, $k_s/D = 4.5 \times 10^{-4}$, $\alpha = 0°$ and $45°$) in a tandem configuration with $S/D = 2.8$, 4.0, and 5.6 for Reynolds numbers in the range of 10^5 to 10^7 (Van Hinsberg [259]). $\triangle$: single isolated prism with $r/D = 0.16$ and $k_s/D = 4.5 \times 10^{-6}$, Van Hinsberg *et al.* [254]. Left column: $\alpha = 0°$; right column: $\alpha = 45°$. Upper row: $S/D = 2.8$; centre row: $S/D = 4.0$; lower row: $S/D = 5.6$.

mately $Re_D = 4.7 \times 10^5$ within the *critical* flow regime, the mean cross-sectional drag on the downstream prism is slightly negative and the state of the flow around both prisms thus belongs to the *reattachment* regime (i.e. *Mode I*). The sign reversal of C_{d_2} at $Re_D \approx 4.7 \times 10^5$ induces a switch of the flow state to the *co-shedding* regime or *Mode II* with $4.0 > S/D_{cr}$, and remains in this flow state up to $Re_D = 7.13 \times 10^6$. A further gap increase to $S/D = 5.6$ leads to a strong flattening of the curve and in particular in the *critical* up to *upper transition* flow regimes an increased independence of C_{d_2} on the Reynolds number. The absence of a sign inversion in C_{d_2} proves that the state of the flow equals the *co-shedding* regime at all Reynolds numbers. The previously mentioned nearly perfect match between C_{pb_1} and $C_{pb_{single}}$ in combination with an approach of the C_{pb_2} towards both other curves for $S/D = 5.6$ reveals a strong reduction of the mutual interference between both tandem prisms at this gap length.

The variation of the mean cross-sectional lift and pitch moment coefficients with Reynolds number for all three spacing values are presented in Figure 5.17 for Reynolds numbers that cover the *subcritical* to low *supercritical* flow regimes at $\alpha = 0°$ (left column) and *subcritical* to low *transcritical* flow regimes at $\alpha = 45°$ (right column). Non-zero lift coefficients appear at the first incidence angle at *critical* Reynolds numbers only, while at the second this range extends up to the Reynolds number at which the cross-over from the *upper transition* to the *transcritical* flow regime takes place. For all three spacing values, the absolute maximum mean lift coefficient of the upstream prism reaches a similar value as that of the single prism; at the combination of $45°$ incidence angle and the largest spacing, it even exceeds $C_{l_{single,max}}$. At the majority of the presented configurations, a sign change in C_{l_1} furthermore takes place while traversing the *critical* flow regime. Interesting to mention is that at $\alpha = 45°$ the local maximum values of the lift coefficient of the upstream prism are at both sides of this sign reversal equally high. For the downstream prism, distinct changes in the lift coefficient are found for $S/D = 2.8$ at both incidence angles, whereas its dependence on the Reynolds number has decreased sharply for both other spacing values as C_{l_2} fluctuates around zero.

Similar trends are also found for both mean cross-sectional pitch moment coefficients. Although an increased Reynolds-number independence of C_{m_2} with larger S/D value can be noticed as well, it is not as pronounced as for C_{l_2}. In particular for the combination of $S/D = 4.0$ and $\alpha = 0°$ a strong variation of C_{m_2} is obtained with values that even exceed those of the upstream prism at most *critical* Reynolds numbers.

5.4.2 Fluctuating loads and Strouhal number

The value of the prisms' centre-to-centre spacing has not only a strong impact on the mean force coefficients, but also on their fluctuating parts. The direction of the trends with increasing gap size differ between both fluctuating force components at equal incidence angle, as well as between the two incidence angles for each of the two quantities separately. For $S/D = 2.8$, the downstream prism experiences at $\alpha = 0°$ in the *subcritical* and the first half of the *critical* flow regime a lower fluctuating lift than for the isolated prism, while in the majority of Reynolds numbers that belong to the *upper transition* and the following *transcritical* flow regime up to $Re_D = 7.7 \times 10^6$ higher RMS-values of the lift force are obtained. Only in a small range of Reynolds numbers from approximately $Re_D = 3 \times 10^5$ up to about 8×10^5, nearly equal values are obtained for both configurations (Figure 5.18a). The cross-over from the *supercritical* to the *upper transition* is marked by a discontinuous step of $\Delta \sqrt{\overline{(C_L'^2)}}_2 = 0.14$ and is followed by a relatively broad dip in the latter flow regime with a minimum of $\sqrt{\overline{(C_L'^2)}}_2 = 0.15$ at
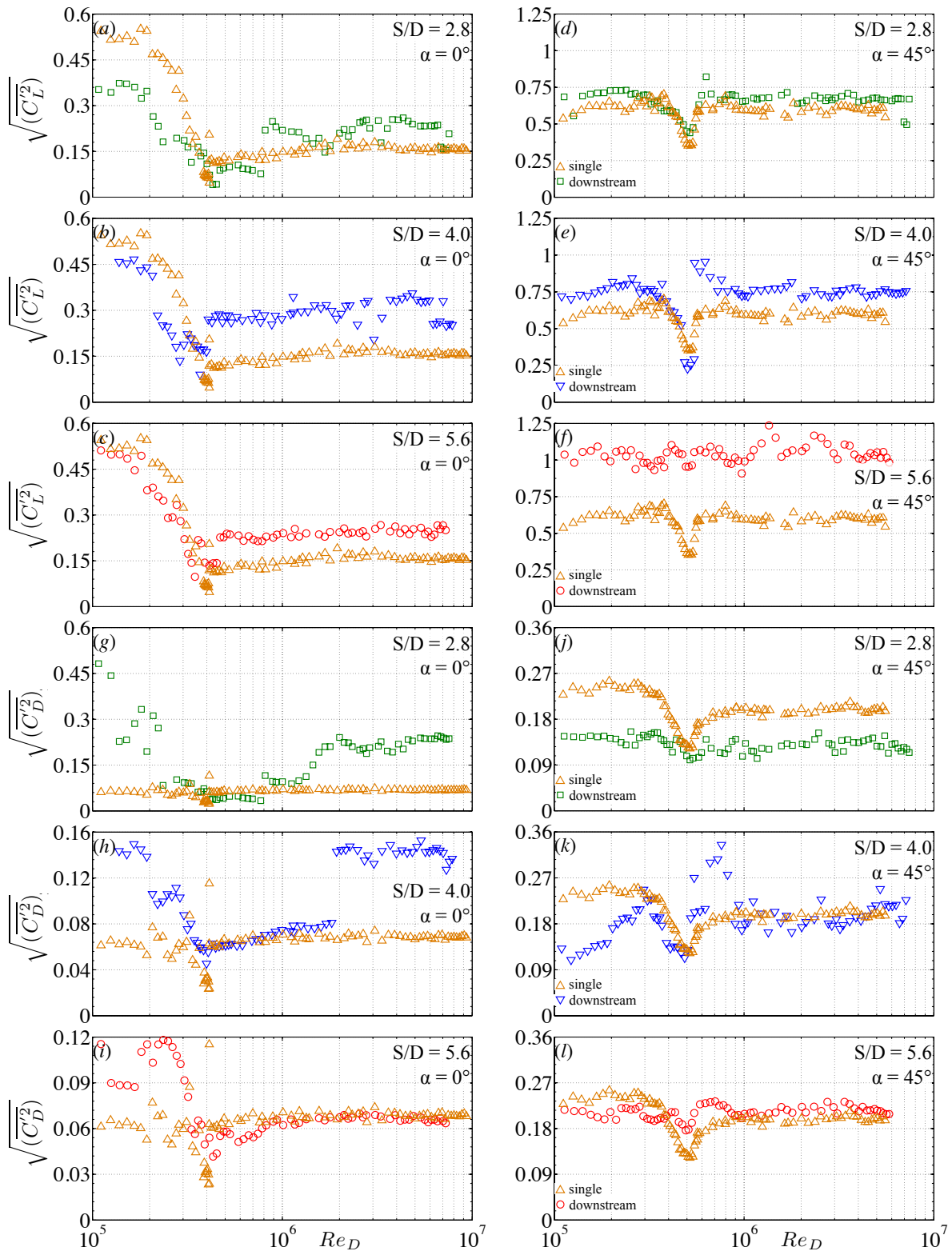
Figure 5.18: Development of the fluctuating global drag and lift coefficients of the downstream one of two slightly rough square-section prisms ($r/D = 0.16$, $k_s/D = 4.5 \times 10^{-4}$, $\alpha = 0°$ and $45°$) with Reynolds number for a tandem configuration with $S/D = 2.8$, 4.0, and 5.6 (Van Hinsberg [259]). $\triangle$: single isolated prism ($r/D = 0.16$, $k_s/D = 4.5 \times 10^{-6}$), Van Hinsberg *et al.* [254]. (*a*)-(*f*): fluctuating global lift coefficient; (*g*)-(*l*): fluctuating global drag coefficient. Left column: $\alpha = 0°$; right column: $\alpha = 45°$.

$Re_D = 1.68 \times 10^6$. it correlates with the dip in the $C_{d_2}(Re_D)$ curve and the Reynolds number at which a net drag force of zero is found on the downstream prism in Figure 5.15a. Figure 5.18d shows that, in contrast to $\alpha = 0°$, both the development of the $\sqrt{(\overline{C'^2_L})}_2(Re_D)$ curve and the individual fluctuating lift values coincide at $45°$ angle of incidence well with the results of the single prism. With larger gap size between both tandem prisms, the appearance of the curve of the fluctuating lift on the downstream prism at $\alpha = 0°$ increasingly resembles that one of the single prism. Noteworthy is in particular the clear approach of both curves at *subcritical* and *critical* Reynolds numbers and the flattening of the curve as a result of the extension of the *supercritical* flow regime to higher Reynolds numbers, in combination with the absence of the *upper transition* at both $S/D = 4.0$ and 5.6, as well as of the *transcritical* flow regime at $S/D = 5.6$. At $\alpha = 45°$, an increasing divergence of the trend of the $\sqrt{(\overline{C'^2_L})}_2(Re_D)$ curve with increasing gap spacing becomes visible. While for $S/D = 4.0$, the curve of the fluctuating lift on the downstream prism resembles still to a large extend that one of the single prism, an nearly flat curve is obtained for $S/D = 5.6$. This means, that besides this growing Reynolds-number independence of $\sqrt{(\overline{C'^2_L})}_2$ for larger gaps sizes over all flow regimes, an increasing shift away from the single prism data to distinctly higher values is thus also obtained.

The distribution of the fluctuating drag on the downstream prism as function of the Reynolds number at $\alpha = 0°$, presented in the Figures 5.18g to 5.18i, possesses at all three spacing values a qualitatively similar trend over all flow regimes as the respective $C_{d_1}(Re_D)$ curves presented in Figure 5.15. The steep jumps of C_{d_1} at $Re_D = 7 \times 10^5$ (i.e. at the transition from the *supercritical* flow regime to the *upper transition*) and at $Re_D = 1.85 \times 10^6$ (hence, at the abrupt cross-over from the *supercritical* to the *transcritical* flow regime) for $S/D = 2.8$ and 4.0, respectively, are clearly recognisable in the associated $\sqrt{(\overline{C'^2_L})}_2(Re_D)$ curves as well. Apart from the end of the *critical* and in the complete following *supercritical* flow regime in which equal values for the downstream and the single prism are found, significantly higher drag fluctuations are experienced by the downstream prism at all other Reynolds numbers. For the smallest spacing at $\alpha = 45°$, a similar (inverted) behaviour can be observed: a relatively good agreement between the values of the fluctuating drag on the downstream prism and those on the single prism over a small part within the *critical* flow regime and at the *supercritical* Reynolds number (i.e. $Re_D = 5.78 \times 10^5$) and considerably lower values at all other flow regimes. An increased gap size between both tandem prisms leads to a gradual approach of the fluctuating drag values of those latter flow regimes towards the curve of the single prism. For $S/D = 4.0$, this is only the case for the *transcritical* flow regime, while for $S/D = 5.6$ the other flow regimes have followed as well.

Figure 5.19 presents the dependence of the non-dimensional frequency with which the eddies are shed in the wake of the downstream prism, St_{L_2}, on the Reynolds number for all three spacing values at both incidence angles. The trend of the Strouhal number with increasing gap spacing is clearly visible: at both incidence angles it induces a (gradual) shift of St_{L_2} in one or several flow regimes towards the curve belonging to the single prism.

At $\alpha = 0°$, the *critical* flow regime is at all three spacing values characterised by the appearance of two Strouhal numbers at equal Reynolds number, associated with the two main and clearly separated peaks in the PSDs of the time series of the global lift force on the downstream prism, as shown in Figure E.1. A similar occurrence of a double Strouhal number is found as well in the second half of the *upper transition* (i.e. at $1.0 \times 10^6 \leqslant Re_D \leqslant 1.68 \times 10^6$) for $S/D = 2.8$ and at $Re_D = 1.85 \times 10^6$ at which the sudden transition from the *supercritical* to the
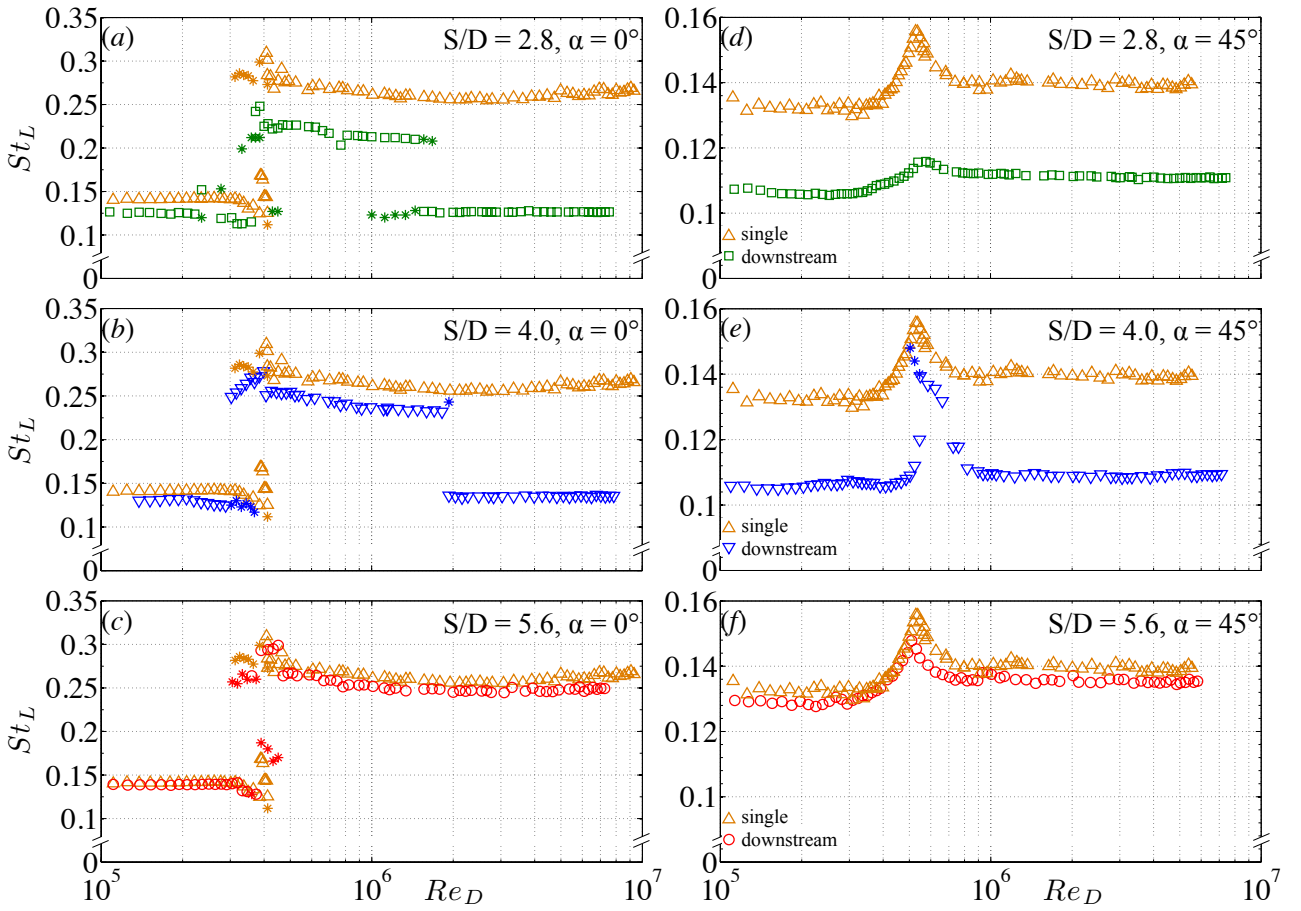
Figure 5.19: Development of the Strouhal number of the downstream one of two slightly rough square-section prisms ($r/D = 0.16$, $k_s/D = 4.5 \times 10^{-4}$, $\alpha = 0°$ and $45°$) with Reynolds number for a tandem configuration with a prism-to-prism spacing of $S/D = 2.8$, 4.0, and 5.6 (Van Hinsberg [259]). $\triangle$: single isolated prism ($r/D = 0.16$, $k_s/D = 4.5 \times 10^{-6}$), Van Hinsberg *et al.* [254]. In the case of the occurrence of two peaks in the power spectra at a certain Reynolds number, the more dominant Strouhal number is indicated by an open symbol, while the star belongs to the secondary peak. Left column: $\alpha = 0°$; right column: $\alpha = 45°$. Top row: $S/D = 2.8$; centre row: $S/D = 4.0$; bottom row: $S/D = 5.6$

transcritical flow regime takes place for the intermediate spacing. Whereas an increase in the gap size leads to a clear rise of the *supercritical* values of the Strouhal number towards $St_{L_{single}}$, the values in the *transcritical* flow regime are practically not influenced by a larger S/D value and remain at an equal level with the Strouhal numbers in the *subcritical* flow regime.

The shape of the $St_{L_2}(Re_D)$ curve at $\alpha = 45°$ clearly resembles that one of the single prism at each of the three spacing values. Despite equal trends, large deviations in the values of the Strouhal numbers between both curves at equal Reynolds number can nonetheless be observed for $S/D = 2.8$ and 4.0. They appear in exactly those Reynolds-number regimes, in which the mean cross-sectional drag coefficient on the downstream prism is negative or near-zero, as was presented in the Figures 5.15d and 5.15e. In contrast, for Reynolds numbers that lie inside the range spanned from the upper *critical* flow regime up to the end of the *upper transition* and at which, in addition, the mean cross-sectional drag coefficient is positive, a fairly good match between St_{L_2} and $St_{L_{single}}$ is obtained (Figure 5.19e).

At both incidence angles, the Strouhal numbers obtained for $S/D = 5.6$ match at all flow

161

regimes well with those for the single prism. A possible interpretation that this spacing is thus large enough to prevent an interference by the upstream prism of the eddy shedding frequency of the downstream prism, is misleading though. The previous comparison of the mean cross-sectional and fluctuating global lift and drag coefficients on the downstream tandem prism for $S/D = 5.6$ with those on the single prism, as well as their mean cross-sectional base pressure coefficients has proven that wake interference effects are still unmistakably present at this spacing. At the same time, the mean cross-sectional drag and base pressure coefficients of the upstream and the single prism are nearly equal at all Reynolds numbers. It can thus be argued, that with high probability this also counts for the Strouhal number of the upstream prism. Most probably, the arrival of the vortices shed by the upstream prism triggers and controls the eddy shedding process in the wake of the downstream prism. This results in a synchronisation of the eddy shedding frequency of the downstream prism with that of the upstream one, whereby the latter is then again most probably equal to the eddy shedding frequency of the isolated single prism.

5.4.3 Sectional mean pressure distributions

An overview of the quantitative distributions of the mean pressure coefficient $C_{p,cyl}$ along the mid-span cross-section of both tandem prisms at $0°$ and $45°$ angle of incidence is shown in the Figures 5.20 and 5.23 for selected Reynolds numbers that cover the various flow regimes. For the complete picture of the mutual flow influence between the upstream (left column) and downstream (centre column) tandem prism as a result of *proximity* and/or *wake interference* effects, the mean coefficients of the surface pressures on the equivalent single prism are shown at approximately the same Reynolds numbers in the right column of both figures. An additional qualitative impression of the mean cross-sectional surface pressure distributions on both tandem prisms is presented in the Figures 5.21 ($\alpha = 0°$) and 5.24 ($\alpha = 45°$) for each spacing value by means of a scaled vectorial representation. In these two latter figures, both prisms are foreseen with their values for the mean cross-sectional drag, lift, and pitch moment coefficients at specific Reynolds numbers.

5.4.3.1 Incidence angle of $0°$

Starting with the smallest prism-to-prism distance of $S/D = 2.8$ at $\alpha_{1,2} = 0°$ in Figure 5.20a the attached boundary layer on the upstream prism separates at the forward-directed rounded edges between the surfaces *I* and *II* and the surfaces *I* and *IV* of the prism. The constant and nearly equal negative pressures on both side surfaces *II* and *IV* and the base *III* imply that absence of a reattachment of the two free shear layers on the side faces at this *subcritical* Reynolds number. The comparable values for the average cross-sectional surface pressure coefficient on the front face C_{pf_1} of the upstream and the single prism and the equal mean base pressure coefficients in Figure 5.22a explain the similar high mean drag coefficients on both prisms. The large difference in the surface pressure distributions between both tandem prisms at $Re_D \leqslant 1.51 \times 10^5$ in Figure 5.20, in combination with the negative values of the average cross-sectional surface pressure coefficient on the front face of the downstream prism of $C_{pf_2} =$ –0.51 to –0.57 for $Re_D \leqslant 2.0 \times 10^5$ (Figure 5.22a) suggest a clear interaction between the downstream prism and the free shear layers coming from the upstream prism. Since the average suction is at the base of the downstream prism about twice as high as on its front face, the resultant mean drag coefficient of $C_{d_2} \approx 0.7$ is still positive, but clearly lower than for the upstream prism at equal *subcritical* Reynolds number.

The constant values of C_{pf_1} in combination with the gradual decrease of the base pressure on
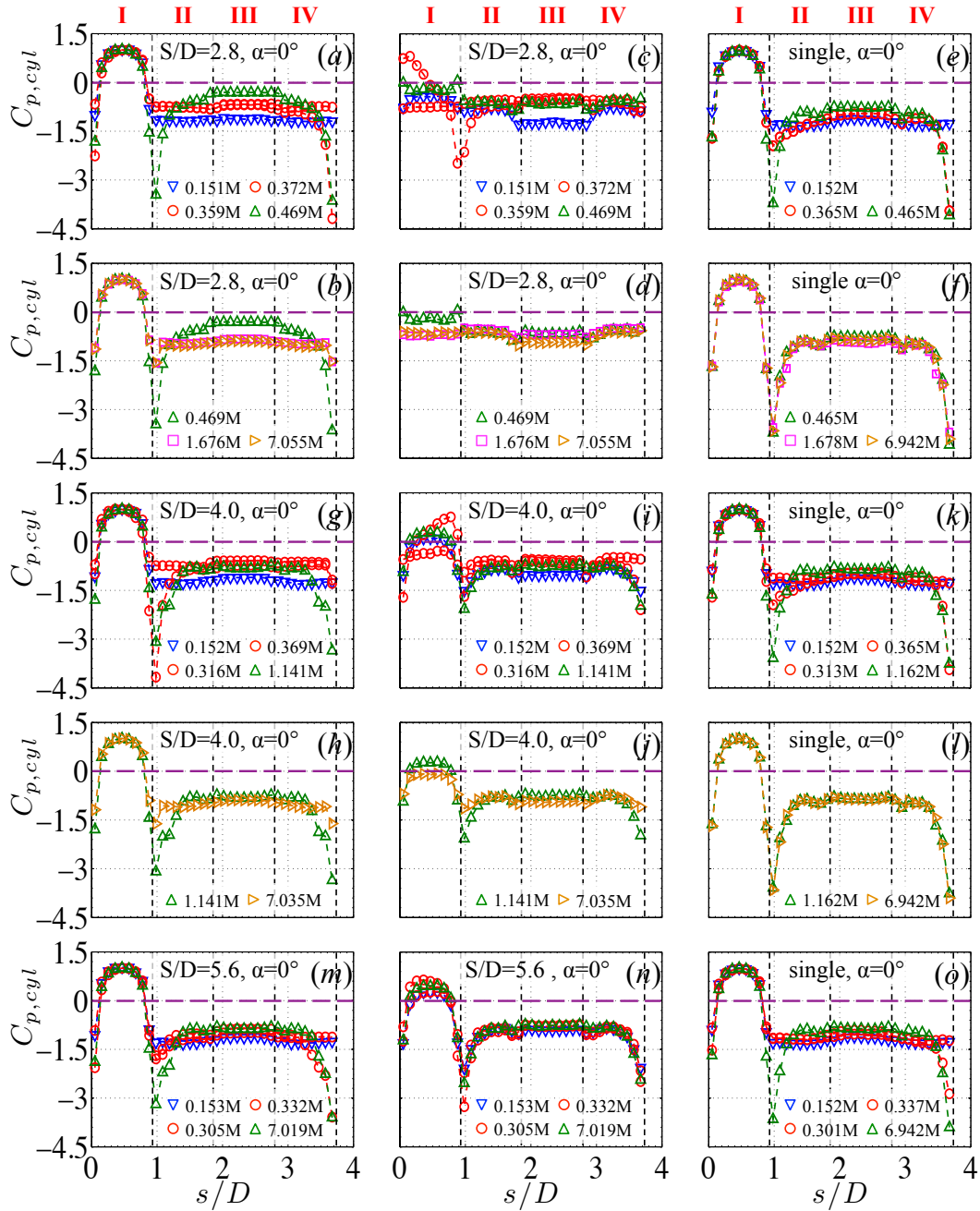
Figure 5.20: Mean circumferential cross-sectional pressure distribution with prism centre-to-centre spacing on two slightly rough square-section prisms ($r/D = 0.16$, $k_s/D = 4.5 \times 10^{-4}$, and $\alpha = 0°$) in a tandem configuration of $S/D = 2.8$, 4.0, and 5.6 at selected Reynolds numbers that cover the *subcritical* to the *transcritical* flow regimes (Adapted from Van Hinsberg [259]). The non-dimensional circumferential distance s/D equals 0 at the centre of the upper windward-directed rounded edge and increases in counter clockwise direction. Left column: upstream prism; centre column: downstream prism; right column: isolated prism. Top two rows: $S/D = 2.8$; centre rows: $S/D = 4.0$; bottom two rows: $S/D = 5.6$. M in the Reynolds number equals "million".

Figure 5.21: Qualitative scaled vectorial representation of the mean circumferential cross-sectional pressure distribution on two slightly rough square-section prisms ($r/D = 0.16$, $k_s/D = 4.5 \times 10^{-4}$, and $\alpha = 0°$) in a tandem configuration with $S/D = 2.8$, 4.0, and 5.6 for the same selected Reynolds numbers as presented in Figure 5.20 (Adapted from Van Hinsberg [259]). Left column: $S/D = 2.8$; centre column: $S/D = 4.0$; right column: $S/D = 5.6$.

the upstream prism within the first half of the *critical* flow regime up to $Re_D = 3.59 \times 10^5$ leads to a steady decrease of C_{d_1}. The mean cross-sectional lift and pitch moment coefficient both
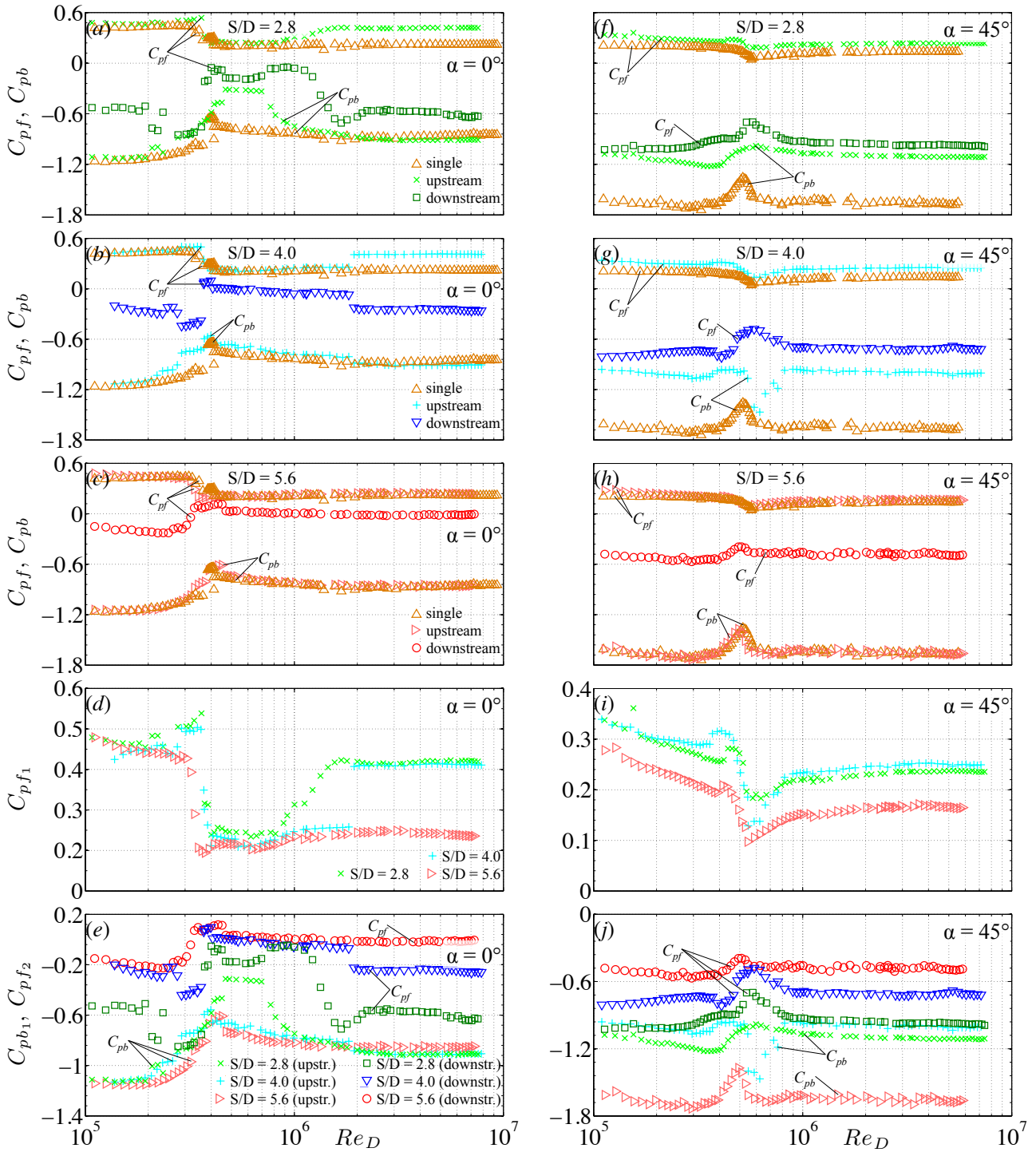
Figure 5.22: Average cross-sectional surface pressure coefficient on the front face I for $\alpha = 0°$ and the faces I and II for $\alpha = 45°$ on two slightly rough square-section prisms ($r/D = 0.16$, $k_s/D = 4.5 \times 10^{-4}$, $\alpha = 0°$ and $45°$) in a tandem configuration, together with the mean cross-sectional base pressure coefficient as function of the Reynolds number and spacing (Adapted from Van Hinsberg [259]). C_{pf_1} and C_{pb_1}: upstream prism; C_{pf_2}: downstream prism. Left column: $\alpha = 0°$; right column: $\alpha = 45°$.

remain practically zero as a result of the nearly perfect symmetry of $C_{p,cyl}$ between the upper and lower face of the upstream prism (Figures 5.20a and 5.21b). In the range of $Re_D = 2.78$–

3.59×10^5 an overlap of the values for C_{pf_2} and C_{pb_1} is found. This indicates, that the free shear layers coming from the upstream prism reattach on the side faces of the downstream prism. They thereby enclose the fluid in the gap between both prisms and prevent an exchange of fluid with the surrounding outer flow. The stagnant fluid induces an overall suction effect on the downstream prism that leads to a negative value for C_{d_2}; i.e. the flow around the tandem prism constellation has switched from *Mode II* to *Mode I*. The similar height of the two peaks at $f_L D / U_\infty = 0.115$ and 0.212 in the PSD of the lift fluctuations on the downstream prism at $Re_D = 3.59 \times 10^5$ proves that the flow over this prism not only alternates between the *subcritical* and *supercritical* state, but also resides in each of the two states over an overall equal mean time period. The second half of the *critical* flow regime is characterised by a highly asymmetric flow around both tandem prisms. The qualitative surface pressure distribution on the upstream prism in Figure 5.21c indicates the presence of a shallow laminar separation bubble in the vicinity of the upper upstream-directed rounded edge, in combination with a re-separation of the turbulent reattached boundary layer at the downstream upper edge of the prism. The equal negative pressures on face *II* at $Re_D = 3.59 \times 10^5$ and 3.72×10^5 in Figure 5.20a imply that the lower free shear layer remains separated up to the base region. The asymmetric flow leads to a positive mean cross-sectional lift and negative mean cross-sectional pitch moment coefficient. In addition, a smaller near wake is induced directly behind the upstream prism that results in a further reduction of the mean cross-sectional drag coefficient. The strong asymmetric pressure distribution on the downstream prism demonstrates the presence of *proximity* interference effects between both prisms. Since the side face on which a laminar separation bubble and a secondary re-separation of the turbulent boundary layer occur has been inverted in comparison to the upstream prism, the downstream prism experiences a downward-directed lift force. The presence of a positive pressure on the upper half of the front surface *I* leads to a lower value for C_{pf_2} than at $Re_D = 3.59 \times 10^5$. Coupled with a relatively small change of the value for C_{pb_2}, the mean drag coefficient C_{d_2} becomes positive again, indicating a return of the flow state around both prisms to *Mode II*.

In the following *supercritical* flow regime, the symmetry in the mean pressure distribution on both prisms has been restored. The Figures 5.21a (and 5.21b) and 5.21d indicate the existence of a separation bubble on the leading section of each side face of the upstream prism together with a continuous decline of the suction on the two faces in the direction of the rounded trailing edge. The re-separation of the boundary layer at the two trailing edges generates a smaller downstream lateral spreading of the free shear layers in the gap between both prisms than in the previous *subcritical* and *critical* flow regimes. The combination of a low mean negative base pressure and the large upstream-directed components of the suction peaks at both upstream edges leads to a lower mean drag force than on the single prism at equal Reynolds number. The close approximation of the values of C_{pf_2} and C_{pb_1} at all *supercritical* Reynolds numbers in Figure 5.22a proves that also in this flow regime the fluid in the gap between the two prisms is still to a large extend enclosed by the free shear layers from the upstream prism. However, the lower negative values of C_{pf_2} indicate that shielding of the downstream prism by the upstream one has reduced compared to the previous two flow regimes. Along with $|C_{pb_2}| > |C_{pb_1}|$ this leads to an increased drag force on the downstream prism that is even higher than that one on the upstream prism.

In contrast to the single prism for which the *supercritical* flow regime extends up to at least $Re_D = 10^7$, the presence of a second prism at $S = 2.8D$ in the near wake terminates this flow regime already at $Re_D = 7 \times 10^5$. The steady rise of the drag on the upstream prism with increasing Reynolds number results from an interplay of a significant increase of both C_{pf_1} and the mean suction on the base surface (Figures 5.22d and 5.22e) and of a progressive

reduction of both the height and width of the suction peaks on the two upstream rounded edges in Figure 5.20b. The values of C_{pf_2} and C_{pb_2} slowly converge with increasing Reynolds number towards the same negative value (Figures 5.22a and 5.16a). Simultaneously, an overall flattening of the surface pressures on the downstream prism takes place, as shown in Figure 5.20d. Both phenomena lead to a gradual decrease of the mean drag coefficient C_{d_2} towards zero at $Re_D = 1.68 \times 10^6$. Because the value of C_{pf_2} lies at this Reynolds number in close proximity to C_{pb_1}, the shielding of the downstream has increased significantly in the range of $Re_D = 1.12$–1.68×10^6 as a result of the increased lateral spreading of the free shear layers from the upstream prism.

In the final *transcritical* flow regime, both tandem prisms experience a mean surface pressure distribution that seems to be independent of the Reynolds number. Whereas only minor changes in $C_{p,cyl}$ between $Re_D = 1.68 \times 10^6$ and 7.06×10^6 can be observed in Figure 5.20b, small variations in both C_{pf_2} and C_{pb_2} in opposite directions, but with different magnitudes induce somewhat larger changes in the mean drag coefficient on the downstream prism with increasing *transcritical* Reynolds number. From the qualitative representation in Figure 5.21f it can be clearly deduced that the increase in C_{d_2} mainly results from the higher suction at the base of the downstream prism.

For the two larger centre-to-centre spacing values, the results for the average cross-sectional surface pressure coefficient on the front face and at the base of the upstream prism gradually approach the values for the single prism. Distinct deviations in C_{pf_1} compared to $C_{pf_{single}}$ only occur for the intermediate prism at $Re_D \geqslant 1.85 \times 10^6$ and are, similar to $S/D = 2.8$, the result of the appearance of the *transcritical* flow regime, as shown in Figure 5.22b. Interestingly, a direct comparison of the three $C_{pf_1}(Re_D)$ curves in Figure 5.22d visualises the occurrence of similar to nearly equal values of C_{pf_1} for all three spacing values in each of the flow regimes. Hence, although the presence of the downstream prism alters the surface pressures in several flow regimes for $S/D = 2.8$ and 4.0, these *proximity* or *wake interference* effects have barely any impact on the value of C_{pf_1} within each flow regime. Regarding the mean cross-sectional base pressure on the upstream prism, it was discussed already in section 5.4.1 that an increase in the gap size from $S/D = 2.8$ to 4.0 leads to a shift of the *supercritical* values of C_{pb_1} towards the curve for the single prism, whereas the *critical* flow regime follows the same trend with a further increase to $S/D = 5.6$. This behaviour of C_{pb_1} is also clearly recognisable in the surface pressure distributions in Figure 5.20 and explains the steady or increasing value for the resultant mean cross-sectional drag coefficient at the two *critical* and the *supercritical* Reynolds numbers with increased S/D value.

Compared to the smallest spacing, the larger gap sizes of $S/D = 4.0$ and 5.6 induce at the majority of Reynolds numbers a reduction in the shielding of the downstream prism, expressed by a diminished mean suction on the front face of the downstream prism, as presented in Figure 5.22e. Simultaneously, local regions with high negative pressure values appear at both forward-directed rounded edges of the downstream prism in the *subcritical*, *supercritical*, and *transcritical* flow regimes for the intermediate spacing and in all flow regimes for the largest spacing value. For each flow regime, the heights of the suction peaks furthermore increase with growing S/D value. The influence of the proximity to the upstream prism can nevertheless still be noticed even at $S/D = 5.6$, despite the relative large spacing between both tandem prisms. Owing to the presence of those two suction peaks and the small dip in the $C_{p,cyl}(s/D)$ curve at the trailing edge of the side faces *II* and *IV* just upstream of both curved rear edges at the *subcritical* to *supercritical* flow regimes (Figures 5.20n, and 5.21l to 5.21n), a clear resemblance with the surface pressure distribution on a single prism at *supercritical* Reynolds numbers

in Figure 5.20o is given. This shows that, although the Reynolds number that is based on the undisturbed free-stream velocity is for the tandem configuration classified as within the *subcritical* or *critical* flow regime, the downstream prism experiences a highly altered and more turbulent oncoming flow field that induces a shift of the local flow around that prism to *supercritical* Reynolds numbers. This is confirmed by the values for C_{pf_2} in Figure 5.22c that lie in the (near) vicinity of the *supercritical* values of $C_{pf_{single}}$ at all investigated Reynolds numbers and thus strongly deviate from those for C_{pb_1}. The cause is found in the impingement of the vortical structures, being produced by the process of rolling up of the free shear layers in the gap between both prisms, onto the downstream prism. As a result, the boundary layer on that prism is already turbulent at the location of separation from the surface over the two front rounded edges. This leads to the formation of a shallow separation bubble over each of its side faces, in combination with a strong suction peak at both leading edges. The secondary separation of the reattached turbulent boundary layer at each trailing edge therefore induces a decrease of the mean suction pressure at the base of the downstream prism towards values being equal to the single prism configuration, as has been discussed earlier. It is the combination of these two phenomena that leads to an increase of the mean drag force on the downstream prism.

Within the *critical* flow regime, a similar distinct asymmetry in the pressure distribution appears for both prisms that results from the occurrence of a one-sided separation bubble and the associated strong suction peak at that side of the prism. The presence of two main peaks in the associated PSDs of the lift fluctuations, presented in Figure E.1, demonstrate that also at $S/D = 4.0$ and 5.6 the frequency with which the eddies are shed in the wake of the downstream prism alternates between *subcritical* and *supercritical* values. The surface pressure distributions show that, despite the strong temporal changes in the eddy shedding process, inversed trends are found between both prisms in the *asymmetric bistable* flow state. The side face of the downstream prism at which one of the two shear layer reattaches first is thereby most probably triggered by the behaviour of the flow around and in the (near) wake of the upstream prism.

5.4.3.2 Incidence angle of 45°

Regarding the pressure distributions on the upstream one of the two tandem prisms at $\alpha = 45°$, a good match of the values on the two upstream-directed faces *I* and *II* with those of the single prism is visible in the Figures 5.23 and 5.24. The trend of the average cross-sectional surface pressure coefficient over these two faces, i.e. C_{pf1}, in the Figures 5.22f to 5.22g follows for all three spacing values the curve of the single prism. At $S/D = 2.8$ and 4.0, slightly higher values for C_{pf1} are obtained at all Reynolds numbers, though, and result from the faintly lower negative peak pressure coefficients at both shoulder edges in comparison to the single prism at equal Reynolds number. In addition and in contrast to the single prism, a small imbalance of the negative peak pressure between the upper and lower shoulder of the upstream prism is not only found in the *critical* flow regime for all three spacing values, but also at all Reynolds numbers that belong to the *supercritical*, *upper transition*, and the first part of the *transcritical* flow regime. It is mainly this deviation from a perfectly symmetric pressure distribution between the two upper and the two lower prism faces that is responsible for the extended occurrence of both non-zero lift and pitch moment coefficients up to *transcritical* Reynolds numbers of approximately $Re_D = 1.1–1.2 \times 10^6$, as displayed in Figure 5.17 and discussed in section 5.4.1.

The flatness of the $C_{p,cyl}(s/D)$ curve on the two base faces *III* and *IV* of the upstream prism for $S/D = 2.8$ and 4.0 is the obvious proof for a mutual interference between both tandem prisms in the sense of a modification of the flow in the near wake behind the upstream prism, induced by the presence of the downstream prism, and being fed back to the upstream
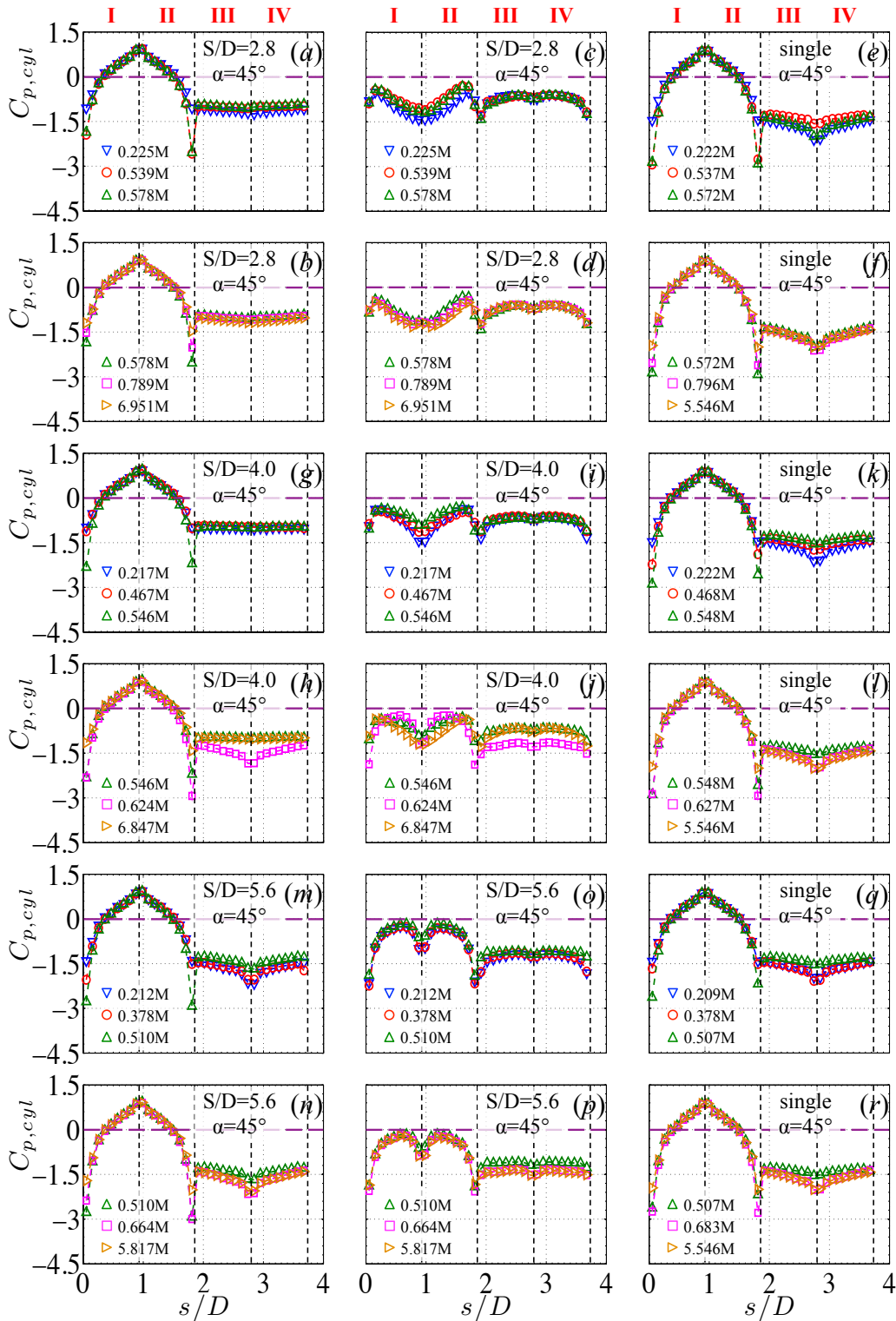
Figure 5.23: Mean circumferential cross-sectional pressure distribution with prism-to-prism spacing on two slightly rough square-section prisms ($r/D = 0.16$, $k_s/D = 4.5 \times 10^{-4}$, and $\alpha = 45°$) in a tandem configuration of $S/D = 2.8$, 4.0, and 5.6 at selected Reynolds numbers that cover the *subcritical* to the *transcritical* flow regimes (Adapted from Van Hinsberg [259]). The non-dimensional circumferential distance s/D equals 0 at the centre of the upper windward-directed rounded edge and increases in counter clockwise direction. Left column: upstream prism; centre column: downstream prism; right column: isolated prism. Top two rows: $S/D = 2.8$; centre rows: $S/D = 4.0$; bottom two rows: $S/D = 5.6$. M in the Reynolds number equals "million".

one. The combination of a much lower mean cross-sectional suction at the base and a slightly higher value for C_{pf1} leads to a significantly lower mean cross-sectional drag coefficient on this prism compared to an isolated prism, as was presented in Figure 5.15. Interestingly, an exception forms the pressure distribution at several Reynolds numbers in the *upper transition* for $S/D = 4.0$. In this case, a clear V-shaped pressure distribution, being characteristic for the single prism, also appears on both base faces of the upstream prism (Figure 5.23h). Because at these few Reynolds numbers the values for C_{pf1} are also equal to $C_{pfsingle}$, a nearly perfect match of the resultant mean cross-sectional drag coefficients is obtained at both configurations (Figure 5.15e). The same observation can be made for the pressure distributions and resultant C_{d_1} values at all investigated Reynolds numbers for the largest spacing $S/D = 5.6$. Hence, in these two latter cases the flow around the upstream prism seems to be practically unaffected by the presence of the downstream prism (with the exception of small differences in height of the negative peak pressures over both shoulder edges).

The impact of a change of the incidence angle of both tandem prisms from $0°$ to $45°$ and the associated alteration of the shielding of the downstream prism both become obvious from the surface pressure distributions on the downstream prism. Independent of the Reynolds number and spacing between both prisms, the downstream prism experiences on all four faces a pure mean suction (Figure 5.24). For all three spacing values, a similar general trend of the pressure distribution is found on both upstream-directed faces *I* and *II*. However, the actual shape of the pressure distribution on these two faces differs significantly among the three spacing values, and is for $S/D = 4.0$ in addition clearly Reynolds-number dependent. At the lowest spacing, it has a clear concave shape. With increasing spacing, this U-shape gradually transforms into a "double bump"-shape. Interestingly, the position of the local maximum of the negative pressure remains fixed on the upstream-directed rounded edge between both faces, whereas the pressure value itself increases for larger S/D value.

In Figure 5.15d it was shown that the downstream prism experiences at a spacing of $S/D = 2.8$ a negative mean drag force in each Reynolds-number flow regime, which implies a strong shielding at this small spacing value. At low *subcritical* Reynolds numbers and throughout the complete *transcritical* flow regime, the values for C_{pf_2} are just slightly lower than those for C_{pb_1}, from which it can be derived that the enclosed flow in the gap between both prisms is practically stagnant. The latter results from the reattachment of the free shear layers from the upstream prism on both front faces of the downstream prism, most probably around $s/d = 0.15$ on the upper face and $s/d = 1.71$ on the lower face, as at these positions $C_{p,cyl}$ reaches its largest negative values. The decrease of C_{pf_2} at higher *subcritical* Reynolds numbers and in the *critical* flow regime shows the reduction of the amount of shielding of the downstream prism. It is caused by the decreased lateral spreading of the free shear layers in the gap between both prisms as can be derived from the decrease of the suction pressure at the base of the upstream prism. Because C_{pb_2} is practically independent of the Reynolds number throughout all flow regimes (Figures 5.23c and 5.23d), the increase in C_{d_2} at those Reynolds numbers is a direct result of its decreased shielding. At the *supercritical* Reynolds number of $Re_D = 5.78 \times 10^5$, the width of the near wake behind this prism reaches its smallest value, and so does the shielding of the downstream prism, both being obvious from the minimum values for C_{pf_2} and C_{d_2} at this Reynolds number. In the following *upper transition*, the opening of the near wake behind the upstream prism (i.e. an increase of both C_{pb_1} and C_{d_1}) results in a gradual recovery of the shielding of the downstream prism. Hence, a larger interference of the flow around the downstream prism by the close presence of the upstream one occurs: the decrease of the mean base pressure of the upstream prism leads to a larger suction on the faces *I* and *II* of the
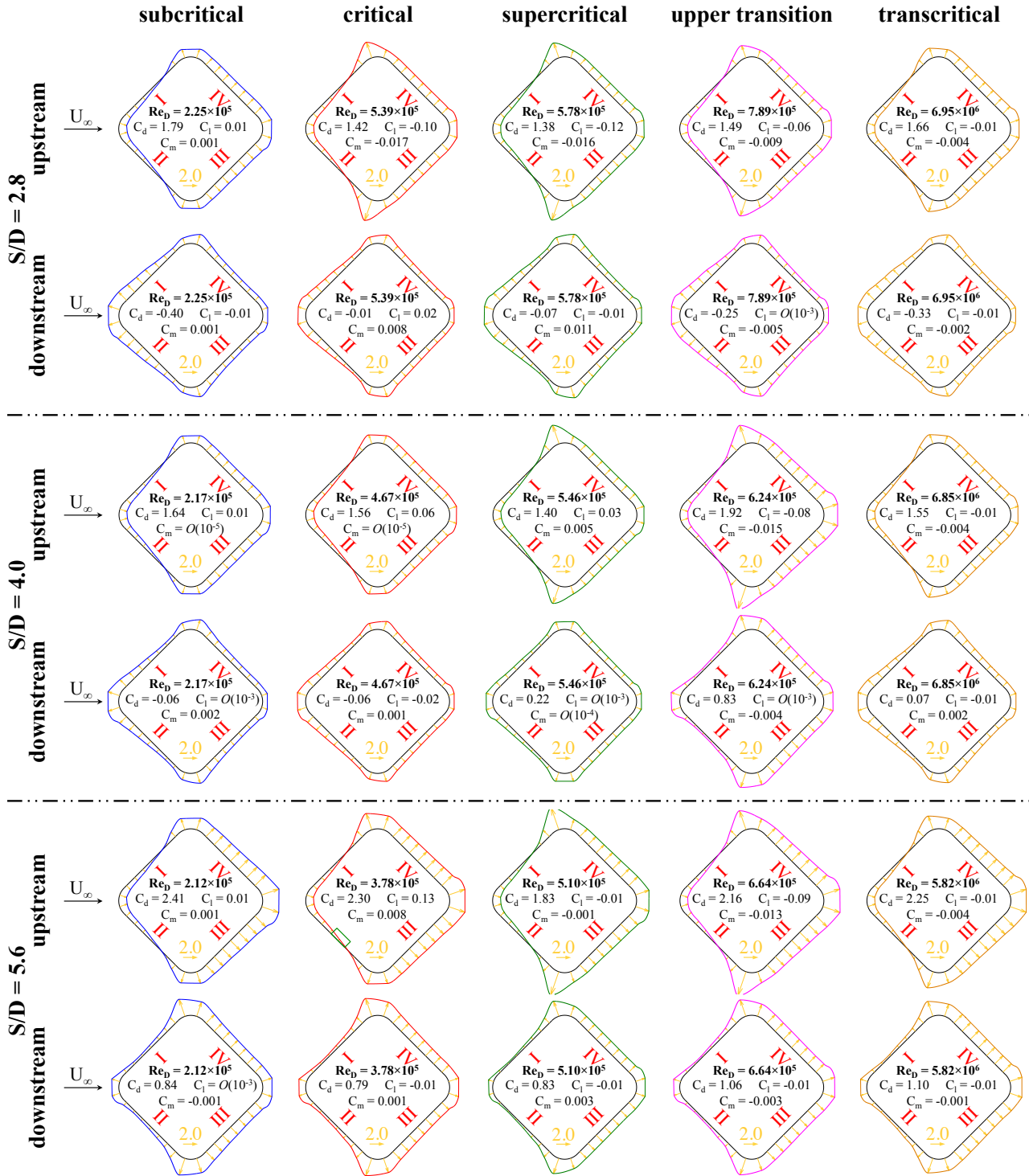
Figure 5.24: Qualitative scaled vectorial representation of the mean circumferential cross-sectional pressure distribution on two slightly rough square-section prisms ($r/D = 0.16$, $k_s/D = 4.5 \times 10^{-4}$, and $\alpha = 45°$) in a tandem configuration with $S/D = 2.8$, 4.0, and 5.6 for the same selected Reynolds numbers as presented in Figure 5.23 (Van Hinsberg [259]). Left column: $S/D = 2.8$; centre column: $S/D = 4.0$; right column: $S/D = 5.6$.

downstream prism and the value for C_{pf_2} slowly approaches C_{pb_1} once more. The foregoing provokes a gradual increase of the thrust force on the downstream prism towards the *subcritical* level in the *transcritical* flow regime.

The main effect of an increase in S/D is a reduction of the interference between both tandem prisms and thus also of the shielding of the downstream prism. As previously mentioned, the fluid dynamics of the upstream prism approaches that one of a single, isolated prism with increasing gap size. The larger spacing allows the free shear layers that have separated from the upstream prism to curl inward towards the main centreline of the gap between both prisms. For $S/D = 5.6$, the appearance of a steady "double bump"-shape of the pressure distribution on both front faces of the downstream prism is evidence for a distinct change of the flow behaviour in the gap. Based on the distribution of the surface pressure on those two faces, the impingement of the eddies occurs most probably in the vicinity of $s/d = 0.57$ to 0.67 (faces *I*) and $s/d = 1.19$ to 1.29 (face *II*). Compared to $S/D = 2.8$, the large difference between C_{pb_1} and C_{pf_2} at all Reynolds numbers in Figure 5.22j indicates that the shielding of the downstream prism has reduced significantly. In combination with the higher mean suction at its base, which slowly nears that of the upstream prism (Figure 5.16f), a clear positive, but relatively Reynolds-number-independent mean drag force acts on the downstream prism. Its value is nonetheless still about twice as small as that of both the upstream and of the single prism, owing to the lower velocity of the oncoming flow experienced by the downstream prism than the free-stream velocity U_∞.

For the intermediate spacing, the distribution of the mean pressure on the faces *I* and *II* differs significantly between the various flow regimes. At *subcritical* and low *critical* Reynolds numbers, the partial shielding of the downstream prism induces a clear V-shaped pressure distribution in between both reattachment locations at $s/D = 0.15$ to 0.26 and $s/D = 1.61$ to 1.71 of the free shear layers from the upstream prism. Although these reattachment points are similar to those found for $S/D = 2.8$ in the same flow regimes, the larger gap size and the consequent alteration of the shape of the pressure distribution from U to V are responsible for the larger difference between C_{pb_1} and C_{pf_2} compared to the smallest spacing. The rough balance between the negative values of C_{pf_2} and C_{pb_2} explains the only slightly negative values for C_{d_2} in Figure 5.15e. The following decrease of C_{pf_2} reveals a reduction in the amount of shielding that results from the decreasing width of the near wake behind the upstream prism and the accompanying migration of both mean reattachment locations on the downstream prism in the direction of the upstream-directed rounded edge between the faces *I* and *II*. The imbalance between C_{pf_2} and C_{pb_2} grows with increasing Reynolds number and the small thrust force (*Mode I*) on the downstream prism becomes a positive drag force (*Mode II*) around $Re_D = 4.7 \times 10^5$, i.e. at the cross-over from the *critical* to the *supercritical* flow regime. The switch from the *reattachment* to the *co-shedding* regime induces a gradual transformation of the mean pressure distribution from a V-shape into a clear "double bump'"-shape at Reynolds numbers that belong to the first part of the *upper transition* (Figure 5.23j). In this latter flow regime, an almost perfect match is found between the surface pressure distributions for $S/D = 4.0$ and $S/D = 5.6$ at equal Reynolds numbers in the beginning of the *transcritical* flow regime (Figure 5.24). The same thus also counts for the values of the derived coefficients C_{pf_2}, C_{pb_2}, and C_{d_2}. This demonstrates, that instead of a shear-layer reattachment, an eddy impingement onto faces *I* and *II* of the downstream prism takes place in this small range of Reynolds numbers, which then again results in the lowest shielding of the downstream prism (and thus the highest value for C_{d_2}) for this tandem configuration. With a further increase in Re_D, the lateral spreading of both free shear layers in the gap increases, as a consequence of which their reattachment on the downstream prism re-appears. The increased shielding leads to a gradual re-migration of

the "double bump'"-shape into a concave V-shape, as displayed in Figure 5.23j. The associated large decrease in C_{pb_2} is mainly responsible for the sharp decrease of C_{d_2} towards nearly zero, but still positive *transcritical* values.

5.5 Résumé Chapter 5

The emphasis of this chapter was placed on the analysis of the fluid dynamic behaviour of a pair of identical "infinite" square-section prisms with rounded edges, positioned in a tandem configuration perpendicular to a uniform flow. The impact of various governing and influencing parameters, i.e. the Reynolds number based on the undisturbed oncoming flow, the edge roundness, incidence angle, and surface roughness height of the two prisms, and the spacing between them were presented and discussed. The data were obtained in several wind tunnel experiments in the High-Pressure wind tunnel facility by using the same measurement techniques as in the single prism tests discussed in the previous two chapters. The test section was only slightly modified to allow for the placement and incidence angle variation of a second prism at various upstream locations of the single prism position, i.e. at prism centre-to-centre positions of $S/D = 2.8$, 4.0, and 5.6. In this way, an absolute minimum of boundary conditions was altered to ensure a profound comparison between the results of the single prism and the tandem configurations at equal Reynolds numbers between 10^5 and 10^7. As reference, the single prism with a square cross-section and non-dimensional rounded edges of $r/D = 0.16$, either with smooth ($k_s/D = 4.5 \times 10^{-6}$) or slightly roughened ($k_s/D = 4.5 \times 10^{-4}$) faces, was selected.

An increase of the surface roughness on the two tandem prisms with $S/D = 4.0$ and 5.6 at $\alpha = 0°$ and $45°$ induces similar roughness-related changes in the various coefficients (i.e. the mean drag and base pressure coefficients of both prisms, and in the fluctuating force coefficients and the Strouhal number of the downstream prism) as found for an identical single prism at the same incidence angles. This includes, among other things, a common shift of the various flow regimes towards lower Reynolds numbers together with a convergence of their respective bounding Reynolds numbers. In particular at $\alpha = 45°$ a significantly increased Reynolds-number independent behaviour of the fluid-dynamic coefficients of both prisms is in that way obtained. This is even more evident for the larger of the two spacing values owing to the weaker drag crisis that occurs in the *critical* flow regime. Regardless of the combination of gap spacing and angle of incidence, the values of the various fluid-dynamic quantities listed above are not affected by the larger roughness height at *subcritical* Reynolds numbers. The same applies to the minimum or maximum values at the cross-over from the *critical* to the *supercritical* flow regime and the plateau of the latter at $\alpha = 0°$.

At a constant angle of incidence, a variation of the gap size between the two slightly rough tandem prisms has a particular effect on the flow around and the resulting pressures and forces on the downstream prism. For the two "symmetric" incidence angles, the effect of a variation in S/D is most pronounced at $\alpha = 45°$ and results from a larger lateral distance between both free shear layers in the (near) wake behind the upstream prism and the resulting stronger shielding of the downstream prism by the upstream one. For the low gap value of $S/D = 2.8$, the downstream prism experiences a thrust force either only in certain flow regimes for $\alpha = 0°$ or in all flow regimes at $\alpha = 45°$. In the first case, the state of the flow around the tandem prism configuration switches multiple times between *Mode I*, with $C_{d_2} < 0$, a stagnant fluid in the gap between both prisms resulting from a reattachment of the shear layers from the upstream on the downstream prism and $S/D < S/D_{cr}$, and *Mode II*, with $C_{d_2} > 0$ and $S/D > S/D_{cr}$. The

mutual interference resulting from the proximity to the downstream prism also alters the flow over the upstream prism. This leads in particular to a decrease in the mean pressure on the base face(s) of the upstream prism and thus to a reduction of its mean overall pressure drag. The decrease of both the *proximity* and *wake interference* effects with increasing gap spacing causes the fluid-dynamic quantities to gradually approach the values for the isolated single prism. At the largest spacing of $S/D = 5.6$, the flow state around both tandem prisms equals *Mode II* at all Reynolds numbers and at both incidence angles. While the flow around the downstream prism is still altered by shielding effects, the mean pressure drag on the upstream prism equals that of a single prism. Weak *proximity* effects are nonetheless still noticeable in the mean surface pressure distribution of the upstream prism at Reynolds numbers that belong to the *critical* ($\alpha = 0°$) and the *critical* to *upper transition* ($\alpha = 45°$) flow regimes and lead to a different behaviour of the mean lift and pitch moment compared to the single prism.

The trends and values of the fluid-dynamic parameters related to the eddy shedding process, i.e. the fluctuating lift, fluctuating drag, and the Strouhal number of the downstream prism depend strongly on the combination of the investigated governing and influencing parameters and which one of them is taken as the main variable. Starting from the reference configuration, hence, two prisms with square cross-sections, non-dimensional rounded edges of $r/D = 0.16$, and smooth surfaces of $k_s/D = 4.5 \times 10^{-6}$, positioned in-line at $\alpha = 0°$ or $\alpha = 45°$, the following main results can be summarised:

(a.) *increase of roughness on the faces of both tandem square-section prisms.*
The common shift of the various flow regimes towards lower Reynolds numbers together with a convergence of their respective bounding Reynolds numbers, resulting from an increased surface roughness height by e.g. marine fouling or snow and ice accumulation, leads to a lengthening of the uppermost flow regime, i.e. the *supercritical* and the *transcritical* one for $\alpha = 0°$ and $45°$, respectively. While at the lower of the two incidence angles the values of both fluctuating forces and the Strouhal number are hardly altered by the increased surface roughness of $\Delta k_s/D = 1 \times 10^2$ within each flow regime, their independence on the Reynolds number increases significantly at $\alpha = 45°$. The latter results in high fluctuating lift and drag forces at most Reynolds numbers, with the only exception of a small dip in the limited range of Reynolds numbers that covers the *critical* to *upper transition* flow regimes. The Strouhal number, on the other hand, behaves inversely with increasing Reynolds number. Hence, while at $\alpha = 0°$ the high-frequency eddy shedding induces only weak pressure fluctuations on the downstream prism at high to very high Reynolds numbers, the exact opposite occurs at $\alpha = 45°$, i.e. the downstream prism experiences high force fluctuations, but at relatively low frequencies.

(b.) *variation of gap size between both slightly rough square-section prisms in tandem.*
Also in this case, a distinction must be made between both "symmetric" incidence angles, based on the behaviour of the free shear layers in the gap between the two tandem prisms and the resultant amount of shielding of the downstream prism. Placing a second identical square-section prism closely upstream hardly affects the values of the pressure fluctuations in cross-flow direction on the surface of the original single prism. The frequency with which those surface pressures fluctuate in transverse direction can be lowered, though. In contrast, the presence of the second tandem prism increases the values of the pressure fluctuations on the initial prism in flow direction at $\alpha = 0°$, while decreasing them at $45°$. The former results from the occurrence of the *upper transition* and *transcritical* flow regimes at Reynolds number beyond 1×10^6.

Increasing the gap between both in-line prisms at $\alpha = 45°$ causes a switch of the flow state around both prisms from *Mode I* to *Mode II*, which results in a significant rise of the fluctuating lift well beyond the values for the single prism, while they remain at a similar level at $\alpha = 0°$. The influence of the second (hence, upstream) prism on the fluctuating drag and Strouhal number of the downstream prism decreases sharply with increasing S/D, leading to an approximation and even a nearly perfect overlap of their values with those of the single prism in the various flow regimes. Since the state of the flow belongs at both incidence angles to the *co-shedding* regime, the lift and drag fluctuations experienced by the originally single prism now result from a combination of the impinging vortices coming from the upstream prism and the eddy shedding in its own near wake. The increase in Strouhal number with increasing centre-to-centre spacing is most likely caused by the stronger synchronisation of the eddy shedding frequency with that of the upstream one, the latter being equal to the eddy shedding frequency of the isolated single prism, in combination with a reduction of the velocity defect in the near wake behind the upstream prism.

Chapter 6

Summary

The studies summarised and discussed in this monograph represent the state-of-the-art of flows over stationary two-dimensional prismatic bluff bodies with square cross-sections and rounded lateral edges at high to very high Reynolds numbers. The focus was placed on configurations of isolated, single prisms and pairs of two identical prisms arranged in-line in a steady and uniform cross-flow. Cross-sectional surface pressure distributions at mid-span of the prisms provided mean sectional lift, pressure drag, pitch moment, and base pressure coefficients, as well as information on the locations of boundary layer separation, the occurrence and positions of a reattachment of the free shear layer(s), and the subsequent re-separation of the turbulent boundary layer. The time-resolved global, hence, spanwise-integrated lift and drag forces, obtained with piezoelectric platform dynamometers, were used to identify the extent of unsteadiness in the flow around the isolated or tandem prisms along with jumps of the flow from one Reynolds-number flow regime or flow state to another. The resultant power spectral density of the time series of the lift force provided the main frequency (or the two main frequencies at Reynolds numbers in the *asymmetric critical* flow state) of the eddy shedding, while the RMS values of the lift and drag forces were measures of the vigorousness of the shedding process in the near wake. Furthermore, the vertical wake rake give insight in the mean cross-sectional total drag coefficient of the tandem arrangement and the non-dimensional mean pressure loss in the near wake, from which the (a)symmetry and the width of the (common) near wake could be derived. Several governing and influencing model parameters (i.e. the roundness of the prism's lateral edges, the height of the surface roughness elements, and the centre-to-centre spacing between both tandem prisms) and flow parameters (hence, the Reynolds number and the angle of incidence) were selected and the impact of a change in their values – either individually, in pairs, or in combinations of three or more simultaneously – on the mean and time-resolved fluid-dynamic behaviour of the isolated and tandem prisms was analysed.

The results presented have demonstrated the capability of the various investigated model parameters in altering the process of eddy shedding in the near wake of single, isolated prismatic bluff bodies. Most prominent are the three facts that (*1*) rounding the sharp lateral edges of smooth square-section prisms can significantly lower the fluctuating lift and drag values, thereby simultaneously increasing the shedding frequency, (*2*) increasing the surface roughness height has exactly the opposite effect, and (*3*) a combination of both can even result in a complete suppression of the eddy shedding. While edge roundness can thus be considered a valuable passive countermeasure for *galloping* in high Reynolds-number flows with $Re_D = 1{\times}10^5$ to $1{\times}10^7$, with the greatest gain in the *supercritical* flow regime, surface roughness can be used to counteract vortex-induced vibrations (VIV). The increased height of the roughness elements

not only has the potential of reducing the oscillation amplitudes in both flow and cross-flow direction, but also of preventing the occurrence of resonance (hence, a "locking-in" of the eddy shedding frequency with the natural frequency of the prism) by shifting the shedding frequency to lower values and thus away from the natural frequency. Adding a roundness to the sharp edges of square-section prisms also introduces a dependence of its fluid dynamics on the Reynolds number, which increases the more its cross-sectional shape approaches a circle. By subsequently placing roughness elements on the faces of the rounded square-section prism, this dependence on the Reynolds number can then again be (partially) counteracted. In Chapter 4 it has even been demonstrated that a specific combination of the two parameters leads to a complete suppression of the periodic eddy shedding in a limited range of Reynolds numbers belonging to the *upper transition* for incidence angles in the range of $3.25°$ to $19.5°$. This latter behaviour at Reynolds numbers in the *upper transition* is actually already known from experiments on two-dimensional smooth circular cylinders, but has never been demonstrated for rounded square-section prisms.

However, it should be kept in mind that a variation of either of these two influencing model parameters will also lead to an alteration of other important fluid-dynamic quantities of the prismatic bluff body, such as its experienced mean drag, mean lift, and mean pitch moment. In addition, the two main governing flow parameters, i.e. the Reynolds number and the angle of incidence of the oncoming flow, must also be taken into account. Especially when highly dynamic flow conditions (e.g. atmospheric turbulence or wind gusts) exist or are expected to occur frequently, a distinct variation of the free-stream velocity or direction may result in temporal and intermittent transitions of the flow over the prism to neighbouring Reynolds-number flow regimes or flow states, respectively. The resulting temporal fluctuations of the fluid dynamics of the prism may even make the applied or intended passive countermeasure(s) against the undesired flow-induced vibration counterproductive. Owing to this complex interplay of the various governing and influencing parameters, the degree of edge roundness or the exact height of the surface roughness elements should therefore be well-considered beforehand. The results presented in this work now allow first resilient comparisons with other passive and active flow control methods.

Apart from having gained a better and detailed understanding of the flow around two identical square-section prisms with rounded lateral edges in a tandem constellation, the results are also useful in various applications. For example, the ocean currents around steel foundations of in particular semi-submersible floating platforms for marine renewables and offshore drilling rigs are characterised by very high Reynolds numbers, even though the ocean surface current velocity is generally below 1 m/s. The flexible mooring lines allow combinations of large amplitudes and low frequencies of the possible translational (surge, sway, and heave) and rotational (roll, pitch, and yaw) platform motions, as well as a dynamic coupling between them, which may cause strong vibrations and harmonic motions of the upper structure, resulting in severe (periodic) loads and moments on the blades and the hub of floating renewables, while being uncomfortable for rig operators and drillers as they experience those (harmonic) motions over long periods of time.

The reduction or suppression of these flow- and motion-induced vibrations is to date still a serious hot issue in the offshore and wind-engineering industry, mainly owing to the missing robust procedures to predict the motions precisely. The current high-fidelity Computational Fluid Dynamics codes and reduced-order models commonly used in the design process of floating offshore structures are mainly based on validation data from experiments performed at incorrect, hence, relatively "low" Reynolds numbers in wind tunnels, water tunnels, and water

towing tanks. Robust and accurate statistical data at full-scale Reynolds numbers are still very rare, as there are only a handful of test facilities in which systematic experiments can be performed at high to very high Reynolds-number flows with low freestream velocities. The unique experimental data, findings, and thorough analyses in Chapter 5 of this work now allow a first improvement of the commonly applied numerical and reduced-order models.

Another frequently discussed issue with respect to floating offshore structures is the natural increase of soft and hard marine fouling over time upon their placement in the ocean. The current data have shown that, depending on the direction of the ocean current, the gradual increase in natural hard marine fouling on submersed foundation elements may significantly enhance the amplitudes of the platform's motions over an increasing range of operating Reynolds numbers, while simultaneously lowering their frequencies. The numerical capture of the flow over the surface of foundation elements covered with roughness elements requires an enormous computational effort. Indeed, an extremely fine numerical grid directly adjacent to the surface is required to correctly reproduce the behaviour of the flow over the roughness elements, which at those high Reynolds numbers are either situated entirely inside the very thin boundary layer or pierce through the surface boundary layer at very high roughness values. Furthermore, a minimum number of vibration cycles per studied roughness value is required to obtain good statistical average and fluctuating force and moment values. A reduced order modelling, derived from phenomenological schemes based on the presented unique results, can therefore be regarded as a solid initial step towards updating and optimising numerical schemes that take into account the high-Reynolds-number fluid-dynamic effects of marine growth on prismatic foundation elements.

Worth mentioning are several open points that have not yet been addressed in this monograph, but which demonstrate the necessity and meaningfulness of further research efforts.

The conclusions drawn in this monograph are based on wind tunnel experiments on stationary single and tandem square-section prisms. As a next logical step, experimental wind tunnel measurements on the flow over elastically-mounted single and tandem prisms, which are either forced to oscillate or free to vibrate in flow and/or cross-flow direction at very high Reynolds numbers, are highly encouraged and recommended. Their realisation in the High-Pressure wind tunnel facility Göttingen (HDG) is, however, much more complex than in conventional, easily accessible wind or water tunnels. Due to the limited space inside the facility, the required components of the test setup and their sizes must both be reduced to a minimum, while still serving their purpose even at total air pressures of $p_{0_{max}} = 10$ MPa. Safety aspects play a key role here, since the test section cannot be accessed immediately once the total air pressure in the facility has exceeded a certain lower threshold. In particular when *galloping* sets in, or, in the case of VIV, the reduced velocity approaches the values at which the eddy shedding frequency "locks" into the natural frequency of the prismatic bluff body, there must be the possibility to activate a damping system. Despite these challenges, the feasibility of such measurements in the HDG is currently being explored.

In the parametric studies of the flow around the two identical tandem square-section prisms, both were treated as separate bluff bodies with a mutual influence between the flow around each one of them. However, in relation to floating offshore structures, a more realistic scenario is their treatment as a single body. For furure investigations on the variation of the angle of incidence of the oncoming flow around both prisms, this implies a staggered configuration, thereby combining a variation of their relative positions with a simultaneous change of their incidence angles. Since only one pair of piezoelectric platform dynamometer is currently available to measure the time-dependent global lift and drag forces from which the eddy shedding

frequency can be derived, the second prism must in this case be placed both upstream and downstream of the first one to obtain the time series of the lift and drag forces on and the shedding frequencies of the eddies in the wake behind both prisms separately. This could be facilitated and even automated by mounting the ends of both prisms at both sides on a turntable with the dynamometers in-between. To avoid large geometric blockage ratios that lead to wall interference effects and to stay below the maximum allowable total aerodynamic force that can be absorbed by the test section, investigations on offshore structures with three or more pillars in the HDG are not possible without a significant downscaling and thus a large reduction in the maximum possible Reynolds number. To overcome this problem, one could think of additional tests on clusters of three or more foundation elements in other facilities, such as water tunnels. The experiments would have to be carried out at lower Reynolds numbers to avoid cavitation, but at the same time there would be a much easier accessibility for optical measurements techniques. An identical experiment with two prisms at an equal Reynolds number that can be achieved in both facilities, would then serve as a reference case for comparing the fluid-dynamic results. The measurements in the HDG on two prisms would then cover the high to very high Reynolds-number range.

The analysis of the flow around the single and tandem square-section prisms, as well as the behaviour of the surface boundary layer and the free shear layers on each of the prisms is based on mean pressure and time-dependent force measurements. To gain a better understanding of the highly unsteady flow field, especially in the gap between the two tandem prisms, it is of great value to advance the implementation of optical measurement techniques – first and foremost Particle Image Velocimetry – in the HDG. However, the limited space inside the HDG for the cameras, the few available windows for the laser beam, and a remote-controlled system for adjusting the alignment of both laser sheets after a pressure change are just some of the numerous challenges that have to be overcome. One of the most important and currently also most challenging issues is the selection of tracer particles that do not agglomerate at high pressures, do not react with the internal seals of the wind tunnel, can follow the unsteady flow at 10 MPa as well as at atmospheric pressures, and do not deposit on the model (thereby increasing the surface roughness) or on the internal parts of the HDG, e.g. by dissolving into thin air after having remained over a certain time inside the HDG. Moreover, their introduction into the flow from outside the HDG is still an unsolved issue, as a certain minimum overpressure to the internal pressure of the HDG is required, which could destroy their sphericity. However, confidence can be placed in the expectation that these issues will be solved in the next couple of years.

Bibliography

[1] Achenbach, E. (1968) *Distribution of local pressure and skin friction in cross flow around a circular cylinder up to Re = 5×10⁶*. J. Fluid Mech., **34(4)**, pp. 625–639. doi: 10.1017/S0022112068002120

[2] Achenbach, E. (1971) *Influence of surface roughness on the cross-flow around a circular cylinder.* J. Fluid Mech., **46(2)**, 321–335. doi: 10.1017/S0022112071000569

[3] Achenbach, E. (1977) *The effect of surface roughness on the heat transfer from a circular cylinder to the cross flow of air.* J. Heat Mass Transf., **20(4)**, 359–369. doi: 10.1016/0017-9310(77)90157-0

[4] Achenbach, E. (1979) *Strömung und konvektiver Wärmeübergang beim Kreiszylinder und bei der Kugel.* Habilitation Thesis, RWTH Aachen, Aachen, Germany, 1979

[5] Achenbach, E., Heinecke, E. (1981) *On vortex shedding from smooth and rough cylinders in the range of Reynolds numbers 6×10³ to 5×10⁶*. J. Fluid Mech., **109**, pp. 239–251. doi: 10.1017/S002211208100102X

[6] Adachi, T. (1997) *Effects of surface roughness on the universal Strouhal number over the wide Reynolds number range.* J. Wind Eng. Ind. Aerod., **69-71**, pp. 399–412. doi: 10.1016/S0167-6105(97)00172-4

[7] Adams, T., Grant, C., Watson, H. (2012) *A simple algorithm to relate measured surface roughness to equivalent sand-grain roughness.* Int. J. Mech. Eng. and Mechatron., **1(2)**, pp. 66–71. doi: 10.11159/ijmem.2012.008

[8] Adeeb, E., Haider, B.A., Sohn, C.H. (2018) *Influence of rounded corners on flow interference between two tandem cylinders using FVM and IB-LBM.* Int. J. Heat Fluid Flow, **28(7)**, pp. 1648–1663. doi: 10.1108/HFF-08-2017-0319

[9] Adeeb, E., Sohn, C.H. (2021) *Flow and heat transfer characteristics of cylindrical structures with corner radius variation: Tandem, SIDE-BY-SIDE, and Flow-induced vibration.* Heat Transf. Eng., **42(3-4)**, pp. 251–269. doi: 10.1080/01457632.2019.1699293

[10] Ain, Q.U., Mahmood, R., Awrejcewicz, J., Siddique, I., Majeed, A.H., Pawłowski, W. (2022) *Effectiveness of splitter plate to control fluid forces on a circular obstacle in a transient flow: FEM computations.* Sci Rep., **12(1)**, pp. 13602-1–12. doi: 10.1038/s41598-022-17947-w

[11] Ajith Kumar, R., Sohn, C.H., Gowda, B.H.L. (2009) *Influence of corner radius on the near wake structure of a transversely oscillating square cylinder*. J. Mech. Sci. Technol., **23**, pp. 2390–2416. doi: 10.1007/s12206-009-0630-y

[12] Alam, M.M. (2016a) *Lift forces induced by the phase lag between the vortex shed-dings from two tandem bluff bodies*. J. Fluids Struct., **65**, pp. 217–237. doi: 10.1016/j.jfluidstructs.2016.05.008

[13] Alam, Md.M., Abdelhamid, T., Sohankar, A. (2020) *Effect of cylinder corner radius and incidence angle on heat transfer and flow topology*. Int. J. Mech. Sci., **175**, pp. 105566-1–14. doi: 10.1016/j.ijmecsci.2020.105566

[14] Alam, M.M., Bai, H., Zhou, Y. (2016b) *The wake of two staggered square cylinders*. J. Fluid Mech., **801(2)**, pp. 475–507. doi: 10.1017/jfm.2016.303

[15] Alam, M.M., Moriya, M., Takai, K., Sakamoto, H. (2002) *Suppression of fluid forces acting on two square prisms in a tandem arrangement by passive control of flow*. J. Fluids Struct., **16(8)**, pp. 1073–1092. doi: 10.1006/jfls.2002.0458

[16] Alam, M.M., Moriya, M., Takai, K., Sakamoto, H. (2003) *Fluctuating fluid forces acting on two circular cylinders in a tandem arrangement at a subcritical Reynolds number*. J. Wind Eng. Ind. Aerod., **91(1-2)**, pp. 139–154. doi: 10.1016/S0167-6105(02)00341-0

[17] Almosnino, D., McAlistar, K.W. (1984) *Water tunnel study of transition flow around circular cylinders*. In: *NASA Tech. Mem., No. 85879* (pp. 1–32)

[18] Amandolèse, X., Hémon, P. (2010) *Vortex-induced vibration of a square cylinder in wind tunnel*. C. R. - Mec., **338(1)**, pp. 12–17. doi: 10.1016/j.crme.2009.12.001

[19] Bahrami, A., Hacişevki, H. (2019) *Comparison of flow structures in the wake region of a square cylinder or a U shape cylinder*. Ocean Eng., **187**, pp. 106211-1–11. doi: 10.1016/j.oceaneng.2019.106211

[20] Bai, H., Alam, Md.M. (2018) *Dependence of square cylinder wake on Reynolds number*. Phys. Fluids, **30**, pp. 015102-1–19. doi: 10.1063/1.4996945

[21] Barrero-Gil, A., Alonso, G., Sanz-Andreas, A. (2010) *Energy harvesting from transverse galloping*. J. Sound Vib., **329(14)**, pp. 2873–2883. doi: 10.1016/j.jsv.2010.01.028

[22] Basu, R.I. (1985) *Aerodynamic forces on structures of circular cross-section. Part 1. Model-scale data obtained under two-dimensional conditions in low-turbulence streams*. J. Wind Eng. Ind. Aerod., **21(3)**, pp. 273–294. doi: 10.1016/0167-6105(85)90040-6

[23] Batham, J.P. (1973) *Pressure distributions on circular cylinders at critical Reynolds numbers*. J. Fluid Mech., **57(2)**, pp. 209–228. doi: 10.1017/S0022112073001114

[24] Bearman, P.W. (1969) *On vortex shedding from a circular cylinder in the critical Reynolds number region*. J. Fluid Mech., **37(3)**, pp. 577–585. doi: 10.1017/S0022112069000735

[25] Bearman, P.W., Trueman, D.M. (1972) *An investigation of the flow around rectangular cylinders*. The Aeronaut. Quart., **23(3)**, pp. 229–237. doi: 10.1017/S0001925900006119

[26] Bearman, P.W., Gartshore, I.S., Maull, D.J., Parkinson, G.V. (1987) *Experiments on flow-induced vibration of a square-section cylinder*. J. Fluids Struct., **1(1)**, pp. 19–34. doi: 10.1016/S0889-9746(87)90158-7

[27] Bearman, P.W., Harvey, J.K. (1993) *Control of circular cylinder flow by the use of dimples*. AIAA J., **31(10)**, pp. 1753–1756. doi: 10.2514/3.11844

[28] Behara, S., Mittal, S. (2011) *Transition of the boundary layer on a circular cylinder in the presence of a trip.* J. Fluids Struct., **27(5)**, pp. 702–715. doi: 10.1016/j.jfluidstructs.2011.03.017

[29] Bishop, R.E.D., Hassan, A.Y. (1964) *The lift and drag forces on a circular cylinder in a flowing fluid.* Proc. R. Soc. A: Math. Phys. Eng. Sci., **277(1368)**, pp. 51–75. doi: 10.1098/rspa.1964.0005

[30] Blenk, H., Fuchs, D., Liebers, F. (1935) *Über die Messung von Wirbelfrequenzen.* Luftfahrtforsch., **12**, pp. 38–41

[31] Blevins, R.D. (1977) *Flow-induced vibration.* Van Nostrand Reinhold, New York, USA, 1977. ISBN: 978-0442206512

[32] Blevins, R.D. (2006) *Flow-induced vibration.* Second Edition Reprint. Krieger Publishing Company, Malabar, USA, 2006. ISBN: 978-1575241838

[33] Blevins R.D., Iwan, W.D. (1974) *The galloping response of a two-degree-of-freedom system.* J. Appl. Mech., **41(4)**, pp. 1113–1118. doi: 10.1115/1.3423443

[34] Bokaian, A.R., Geoola, F. (1984) *Hydroelastic instabilities of square cylinders.* J. Sound Vib., **92(1)**, pp. 117–141. doi: 10.1016/0022-460X(84)90378-X

[35] Borgoltz, A., Intaratep, N., Devenport, W.J. (2020) *Experiment 3 - Flow past a circular cylinder.* AOE-3054 Course Manual. Department of Aerospace and Ocean Engineering, Virginia Polytechnic Institute and State University, USA

[36] Brooks, N.P.H. (1960) *Experimental investigation of the aeroelastic instability of bluff cylinders.* M.Sc. Thesis, University of British Columbia, Vancouver, Canada, 1960. doi: 10.14288/1.0105916

[37] Brun, C., Aubrun, S., Goossens, T., Ravier, Ph. (2008a) *Coherent structures and their frequency signature in the separated shear layer on the sides of a square cylinder.* Flow Turbul. Combust., **81**, pp. 97–114. doi: 10.1007/s10494-008-9152-4

[38] Brun, S., Goossens, T. (2008b) *3D coherent vortices in the turbulent near wake of a square cylinder.* Comptes Rendus Mécanique, **336(4)**, pp. 363–369. doi: 10.1016/j.crme.2008.01.002

[39] Buresti, G. (1981) *The effect of surface roughness on the flow regime around circular cylinders.* J. Wind Eng. Ind. Aerod., **8(1-2)**, pp. 105–114. doi: 10.1016/0167-6105(81)90011-8

[40] Camichel, C., Dupin, C., Teissié-Solier, M. (1927) *Sur l'application de la loi de similitude aux période de formation des tourbillons alternés de Bénard-Kàrmàn.* Comptes Rendus Mécanique, **185(19)**, pp. 1536–1539

[41] Cantwell, B.J. (1976) *A flying hot wire study of the turbulent near wake of a circular cylinder at a Reynolds number of 140,000.* Ph.D. Thesis, Calif. Inst. Tech., Pasadena, USA, 1976

[42] Cao, Y., Tamura, T. (2016) *Large-eddy simulations of flow past a square cylinder using structured and unstructured grids.* Comput. Fluids, **137**, pp. 36–54. doi: 10.1016/j.compfluid.2016.07.013

[43] Cao, Y., Tamura, T., Kawai, H. (2020) *Spanwise resolution requirements for the simulation of high-Reynolds-number flows past a square cylinder*. Comput. Fluids, **196**, pp. 104320-1–16. doi: 10.1016/j.compfluid.2019.104320

[44] Carassale, L., Freda, A., Marré-Brunenghi, M. (2013) *Effects of free-stream turbulence and corner shape on the galloping instability of square cylinders*. J. Wind Eng. Ind. Aerod., **123(Part B)**, pp. 274–280. doi: 10.1016/j.jweia.2013.09.002

[45] Carassale, L., Freda, A., Marré-Brunenghi, M. (2014) *Experimental investigation on the aerodynamic behavior of square cylinders with rounded corners*. J. Fluids Struct., **44**, pp. 195–204. doi: 10.1016/j.jfluidstructs.2013.10.010

[46] Catalano, P., Wang, M., Iaccarino, G., Moin, P. (2003) *Numerical simulation of the flow around a circular cylinder at high Reynolds numbers*. Int. J. Heat Fluid Flow, **24**, pp. 463–469. doi: 10.1016/S0142-727X(03)00061-4

[47] Chen, J.M., Liu, C.-H. (1999) *Vortex shedding and surface pressures on a square cylinder at incidence to a uniform air stream*. Int. J. Heat Fluid Flow, **20(6)**, pp. 592–597. doi: 10.1016/S0142-727X(99)00047-8

[48] Chen, W.-L., Huang, Y., Chen, C., Yu, H., Gao, D. (2022) *Review of active control of circular cylinder flow*. Ocean Eng., **258**, pp. 111840-1–37. doi: 10.1016/j.oceaneng.2022.111840

[49] Cheng, W., Pullin, D., Samtaney, R., Zhang, W., Gao, W. (2017). *Large-eddy simulation of flow over a cylinder with Re_D from $3.9{\times}10^3$ to $8.5{\times}10^5$: A skin-friction perspective*. J. Fluid Mech., **820**, pp. 121–158. doi: 10.1017/jfm.2017.172

[50] Choi, C.-B., Jang, Y.-J., Yang, K.-S. (2012) *Secondary instability in the near-wake past two tandem square cylinders*. Phys. Fluids, **24**, pp. 024102. doi: 10.1063/1.3682373

[51] Choi, H., Jeon, W.-P., Kim, J. (2008) *Control of flow over a bluff body*. Annu. Rev. Fluid Mech., **40(1)**, pp. 113–139. doi: 10.1146/annurev.fluid.39.050905.110149

[52] Cincotta, T.T., Jones, G.W. Jr., Walker, W.W. (1966) *Experimental investigation of wind induced oscillation effects on cylinders in two dimensional flow at high Reynolds numbers*. In: *NASA Tech. Mem., No. X-57779* (pp. 20.1–35)

[53] Coutanceau, M., Defaye, J.R. (1991) *Circular cylinder wake configurations: a flow visualisation survey*. Appl. Mech. Rev., **44(6)**, pp. 255–305. doi: 10.1115/1.3119504

[54] Dalton, C., Zheng, W. (2003) *Numerical solutions of a viscous uniform approach flow past square and diamond cylinders*. J. Fluids Struct., **18(3-4)**, pp. 455–465. doi: 10.1016/j.jfluidstructs.2003.07.010

[55] Datta, B., Dey, P., Das, A.K., Debbarma, D. (2019) *Numerical analysis of fluid forces and heat transfer characteristics around tandem rounded corners square cylinders*. J. Eng. Res. Appl., **9(6)**, pp. 40–51. doi: 10.9790/9622-0906014051

[56] Davies, M.E. (1976). *A comparison of the wake structure of a stationary and oscillating bluff body, using a conditional averaging technique*. J. Fluid Mech., **75(2)**, pp. 209–231. doi: 10.1017/S0022112076000189

[57] De, A.K., Dalal, A. (2006). *Numerical simulation of unconfined flow past a triangular cylinder*. Int. J. Numer. Methods Fluids, **52(7)**, pp. 801–821. doi: 10.1002/fld.1210

[58] Delany, N.K., Sorensen, N.E. (1953) *Low speed drag of cylinders of various shapes*. In: *NACA Tech. Rep., No. TR-3038* (pp. 1–22)

[59] Demartino, C., Koss, H.H., Georgakis, C.T., Ricciardelli, F. (2015a) *Effects of ice accretion on the aerodynamics of bridge cables*. J. Wind Eng. Ind. Aerod., **138**, pp. 98–119. doi: 10.1016/j.jweia.2014.12.010

[60] Demartino, C., Ricciardelli, F. (2015b) *Aerodynamic stability of ice-accreted bridge cables*. J. Fluids Struct., **52**, pp. 81–100. doi: 10.1016/j.jfluidstructs.2014.10.003

[61] Den Hartog, J.P. (1932) *Transmission line vibration due to sleet*. IEEJ Trans. Electr. Electron. Eng., **51(4)**, pp. 1074–1076. doi: 10.1109/T-AIEE.1932.5056223

[62] Deniz, S., Staubli, Th. (1997) *Oscillating rectangular and octagonal profiles: Interaction of leading- and trailing-edge vortex formation*. J. Fluids Struct., **11(1)**, pp. 3–31. doi: 10.1006/jfls.1996.0065

[63] Drescher, H. (1956) *Messung der auf querangeströmte Zylinder ausgeübten zeitlich veränderten Drücke*. Z. Flugwiss., **4(1-2)**, pp. 17–21

[64] Du, X., Chen, R., Xu, H., Ma, W. (2019a) *Experimental study on aerodynamic characteristics of two tandem square cylinders*. Fluid Dynam. Res., **51(5)**, pp. 055508. doi: 10.1088/1873-7005/ab37b3

[65] Du, X., Xu, H., Ma, W., Dai, C., Liu, Q. (2019b) *Experimental study on aerodynamic characteristics of two square cylinders at various incidence angles*. J. Wind Eng. Ind. Aerod., **191(3)**, pp. 154–169. doi: 10.1016/j.jweia.2019.05.019

[66] Du, X., Chen, R., Dong, H., Ma, W., Xu, H., Zhao, Y. (2021) *Aerodynamic characteristics of two closely spaced square cylinders in different arrangements*. J. Wind Eng. Ind. Aerod., **208**, pp. 104462-1–9. doi: 10.1016/j.jweia.2020.104462

[67] Duchaine, F., Boileau, M., Sommerer, Y., Poinsot, T. (2014) *Large eddy simulation of flow and heat transfer around two square cylinders in a tandem arrangement*. J. Heat Transf., **136(10)**, pp. 101702-1–10. doi: 10.1115/1.4027908

[68] Durão, D.F.G., Heitor, M.V., Pereira, J.C.F. (1988) *Measurements of turbulent and periodic flows around a square cross-section cylinder*. Exp. Fluids, **6**, pp. 298–304. doi: 10.1007/BF00538820

[69] Dutta, S., Muralidhar, K., Panigrahi, P.K. (2003) *Influence of the orientation of a square cylinder on the wake properties*. Exp. Fluids, **34**, pp. 16–23. doi: 10.1007/s00348-002-0484-x

[70] Eisner, F. (1925) *Druckmessung an umströmten Zylindern*. Z. Angew. Math. Mech., **5**, pp. 486–489

[71] Erturk, E., Gökçöl, O. (2018) *ISteady flow over a square cylinder at high Reynolds numbers*. Int. J. Mech. Eng. Techn., **9(13)**, pp. 638–649

[72] Etminan, A., Moosavi, M., Ghaedsharafi, N. (2011) *Determination of flow configurations and fluid forces acting on two tandem square cylinders in cross-flow and its wake patterns.* Int. J. Mech., **5(2)**, pp. 63–74

[73] Fage, A. (1929a) *The air flow around circular cylinder in the region where boundary layer separates from the surface.* Lond. Edinb. Dublin philos. mag. j. sci., **7(42)**, pp. 253–273. doi: 10.1080/14786440208564737

[74] Fage, A., Warsap, J.H. (1929b) *The effect of turbulence and surface roughness on the drag of a circular cylinder.* In: *Tech. Rep., Reports & Memoranda 1283* (pp. 1–15), Aeron. Res. Comm., London, UK, 1929

[75] Fage, A., Falkner, V.M. (1931) *Further experiments on the flow around a circular cylinder.* In: *Tech. Rep., Reports & Memoranda 1369* (pp. 1–13), Aeron. Res. Comm., London, UK, 1931

[76] Farell, C., Blessmann, J. (1983) *On critical flow around smooth circular cylinders.* J. Fluid Mech., **136**, pp. 375–391. doi: 10.1017/S0022112083002190

[77] Feng, C.C. (1968) *The measurement of vortex-induced effects in flow past stationary and oscillating circular and D-section cylinders.* M.Sc. Thesis, University of British Columbia, Vancouver, Canada, 1968. doi: 10.14288/1.0104049

[78] Fitridge, I., Dempster, T., Guenther, J., de Nys, R. (2012) *The impact and control of biofouling in marine aquaculture: a review.* Biofouling, **28(7)**, pp. 649–669. doi: 10.1080/08927014.2012.700478

[79] Flamand, O. (1995) *Rain-wind induced vibration of cables.* J. Wind Eng. Ind. Aerod., **57(2-3)**, pp. 353–362. doi: 10.1016/0167-6105(94)00113-R

[80] Försching, H. (1976) *Hochdruck-Windkanal fÃ¼r aerodynamische und aeroelastische Untersuchungen - insbesondere von Hochbaukonstruktionen - bei Reynoldszahlen bis 1,5×10^7 in inkompressibler Strömung* In: *DLR internal Rep., No. 253*

[81] Försching, H., Melzer, E., Schewe, G. (1981) *Ein neuer Windkanal für gebäudeaerodynamische und aeroelastische Untersuchungen bei Reynoldszahlen bis 10^7.* Konstr. Ingenieurbau Berichte, **35-36**, pp. 127–133

[82] Forteath, G.N.R., Picken, G.B., Ralph, R., Williams, J. (1982) *Marine growth studies on the North Sea oil platform Montrose Alpha.* Mar. Ecol. Prog. Ser., **8(1)**, pp. 61–68. doi: 10.3354/meps008061

[83] Fransson, J.H.M., Konieczny, P., Alfredsson, P.H. (2004) *Flow around a porous cylinder subject to continuous suction or blowing.* J. Fluids Struct., **19(8)**, pp. 1031–1048. doi: 10.1016/j.jfluidstructs.2004.06.005

[84] Fujita, H., Suzuki, H., Sawaga, A., Takaishi, T. (1999) *The aeolian tone characteristics of a circular cylinder in high Reynolds number flow.* In: *Proc. 5th AIAA/CEAS Aeroacoustics Conference and Exhibit*, Bellevue, USA, 1999. doi: 10.2514/6.1999-1849

[85] Fung, Y.C. (2008) *An introduction to the theory of aeroelasticity.* Dover Publications, Inc., Mineola, New York, USA, 2008. ISBN: 978-0486469362

[86] Gaster, M. (1971). *Vortex shedding from circular cylinders at low Reynolds numbers.* J. Fluid Mech., **46(4)**, pp. 749–756. doi: 10.1017/S002211207100082X

[87] Gerrard, J.H. (1978) *The wakes of cylindrical bluff bodies at low Reynolds number.* Philos. Trans. A Math. Phys. Eng. Sci., **288(A1354)**, pp. 351–382. doi: 10.1098/rsta.1978.0020

[88] Glauert, H. (1919) *The rotation of an aerofoil about a fixed axis.* (British) Advisory Committee for Aeronautics, R & M No.959. In: *Technical Report of ARC for 1918-1919.* (pp. 443–447), H.M. Stationery Office, London, UK, 1919

[89] Groh, R. (2016, Octobre 15) *Boundary layer separation and pressure drag* [Blog post]. Retrieved from https://aerospaceengineeringblog.com/boundary-layer-separation-and-pressure-drag/ at January 7, 2022

[90] Gupta, S., Wipf, T.J., Fanous, F., Baenziger, M., Hahm, Y.H. (1994) *Structural failure analysis of 345 kV transmission line.* IEEE Trans. Power Deliv., **9(2)**, pp. 894–903. doi: 10.1109/61.296272

[91] Güven, O., Farell, C., Patel, V.C. (1980) *Surface-roughness effects on the mean flow past circular cylinders.* J. Fluid Mech., **98(4)**, pp. 673–701. doi: 10.1017/S0022112080000341

[92] Hacişevki, H., Teimourian, A. (2015) *Comparison of flow structures in the wake region of two similar normal flat plates in tandem and a square cylinder.* Exp. Therm. Fluid Sci., **69**, pp. 169–177. doi: 10.1016/j.expthermflusci.2015.08.007

[93] Hallam, M.G., Heaf, N.F., Wootton L.R. (1977) *Dynamics of marine structures: Methods of calculating the dynamic response of fixed structures subject to wave and current action.* Construction Industry Research and Information Association, London, UK, 1977. ISBN: 978-0860170235

[94] Hangan, H., Vickery, B. J. (1999) *Buffeting of two-dimensional bluff bodies.* J. Wind Eng. Ind. Aerod., **82(1-3)**, pp. 173–187. doi: 10.1016/S0167-6105(99)00003-3

[95] Head, M.R. (1982) *Flow visualisation II.* In: Merzkirch, W. (Ed.) *Proc. 2nd Int. Symp.* (pp. 399–403), Hemisphere Publishing Corp, Washington, 1982

[96] Hearn, C.J. (2011) *Hydrodynamics of coral reef systems.* In: Hopley, D. (Ed.) *Encyclopedia of Modern Coral Reefs: Structure, Form and Process.* (pp. 563–573), Encyclopedia of Earth Sciences Series, Springer Netherlands, Dordrecht, 2011. doi: 10.1007/978-90-481-2639-2_277

[97] Henry, P.-Y., Nedrebø, E.L., Myhaug, D. (2016) *Visualisation of the effect of different types of marine growth on cylinders' wake structure in low* Re *steady flow.* Ocean Eng., **115(4)**, pp. 182–188. doi: 10.1016/j.oceaneng.2016.02.023

[98] Higuchi, H., Kim, H.J., Farell, C. (1989) *On flow separation and reattachment around a circular cylinder at critical Reynolds numbers.* J. Fluid Mech., **200**, pp. 149–171. doi: 10.1017/S0022112089000601

[99] Hikami, Y., Shiraishi, N. (1988) *Rain-wind induced vibrations of cables stayed bridges.* J. Wind Eng. Ind. Aerod., **29(1-3)**, pp. 409–418. doi: 10.1016/0167-6105(88)90179-1

[100] Hiwada, M., Mabuchi, L., Yanagihara, H. (1982) *Fluid flow and heat transfer around two circular cylinders.* Bull. JSME, **25(209)**, pp. 1737–1745. doi: 10.1299/jsme1958.25.1737

[101] Homann, F. (1936) *Einfluss großer Zähigkeit bei Strömung um Zylinder.* Forsch. Ing-Wes. A, **7**, pp. 1–10. doi: 10.1007/BF02578758

[102] Hori, E. (1959) *Experiments on flow around a pair of parallel circular cylinders.* In: *Proc. 9th Japan Nat. Congress Appl. Mech.*, Tokyo, Japan, 1959.

[103] Horton, H.P. (1968) *Laminar separation bubbles in two and three dimensional incompressible flow.* Ph.D. Thesis, University of London, London, UK, 1968

[104] Hu, J.C., Zhou, Y., Dalton, C. (2006) *Effects of corner radius on the near wake of a square prism.* Exp. Fluids, **40**, pp. 106–118. doi: 10.1007/s00348-005-0052-2

[105] Huang, R.F., Lin, B.H. (2011) *Effects of flow patterns on aerodynamic forces of a square cylinder at incidence.* J. Mech., **27(3)**, pp. 347–355. doi: 10.1017/jmech.2011.37

[106] Huang, R.F., Lin, B.H., Yen, S.C. (2010) *Time-averaged topological flow patterns and their influence on vortex shedding of a square cylinder in crossflow at incidence.* J. Fluids Struct., **26(3)**, pp. 406–429. doi: 10.1016/j.jfluidstructs.2010.01.003

[107] Igarashi, T. (1981) *Characteristics of the flow around two circular cylinders arranged in tandem: 1st Report.* Bull. JSME, **24(188)**, pp. 323–331. doi: 10.1299/jsme1958.24.323

[108] Igarashi, T. (1984a) *Characteristics of the flow around a square prism.* Bull. JSME, **27(231)**, pp. 1858–1865. doi: 10.1299/jsme1958.27.1858

[109] Igarashi, T. (1984b) *Characteristics of the flow around two circular cylinders arranged in tandem: 2nd Report, Unique Phenomenon at Small Spacing.* Bull. JSME, **27(233)**, pp. 2380–2387 . doi: 10.1299/jsme1958.27.2380

[110] Igarashi, T. (1997) *Drag reduction of a square prism by flow control using a small rod.* J. Wind. Eng. Ind. Aerodyn., **69-71**, pp. 141–153. doi: 10.1016/S0167-6105(97)00150-5

[111] Inoue, Y., Kushibe, A., Umemura, K., Mizushima, Y., Sawaguchi, T., Nakamura, T., Otsuka, H., Chiba, Y. (2020) *Fatigure-resistant Fe-Mn-Si-based alloy seismic dampers to counteract long-period ground motion.* Jpn Archit. Rev., **4(1)**, pp. 76–87. doi: 10.1002/2475-8876.12193

[112] Ishigai, S., Nishikawa, E., Nishimura, K., Cho, K. (1972) *Experimental study on structure of gas flow in tube banks with tube axis normal to flow: Part 1, Karman Vortex Flow from Two Tubes at Various Spacings.* Bull. JSME, **15(86)**, pp. 949–959 . doi: 10.1299/jsme1958.15.949

[113] Jahjouh, M. (2021) *The effect of marine growth and damage severity on the modal parameters of offshore wind turbine supporting structures: an experimental study.* J. Vibroeng., **23(2)**, pp. 407–418. doi: 10.21595/jve.2020.21429

[114] James, W.D., Paris, S.W., Malcolm, G.V. (1980) *Study of viscous cross flow effects on circular cylinders at high Reynolds numbers.* AIAA J., **18(9)**, pp. 1066–1072. doi: 10.2514/3.50855

[115] James, W.D., Vogel, J.M. (1996) *Variation of section drag coefficient with variation of Reynolds number for square cylinders with various corner radii.* In: *Report for Valmont Industries.*, 1996

[116] Jones, G.W. Jr. (1968) *Unsteady lift forces generated by vortex shedding about large, stationary, and oscillating cylinders at high Reynolds numbers.* In: *Proc. 26th ASME Symp. unsteady flow*, Philadelphia, USA, 1968

[117] Jones, G.W. Jr., Cincotta, J.J., Walker, R.W. (1969) *Aerodynamic forces on a stationary and oscillating circular cylinder at high Reynolds numbers.* In: *NASA Tech. Rep., No. R-3000* (pp. 1–62)

[118] Jusoh, I., Wolfram, J. (1996) *Effects of marine growth and hydrodynamic loading on offshore structures.* J. Mek., **1(1)**, pp. 77–98

[119] Kamiya, N., Suzuki, S., Nishi, T. (1979) *On the aerodynamic force acting on a circular cylinder in the critical range of the Reynolds number.* In: *Proc. 12th Fluid and Plasma Dynamics Conf.*, Williamsburg, USA, 1979. doi: 10.2514/6.1979-1475

[120] Kaneko, S., Nakamura, T., Inada, F., Kato, M., Ishihara, K., Nishihara, T. (2014) *Flow-induced vibrations. Classifications and lessons from practical experiences.* Second Edition, Elsevier Ltd., Amsterdam, The Netherlands, 2014. ISBN: 978-0081013182

[121] Kareem, A. (1987) *The effect of aerodynamic interference on the dynamic response of prismatic structures.* J. Wind. Eng. Ind. Aerodyn., **25(3)**, pp. 365–372. doi: 10.1016/0167-6105(87)90028-6

[122] Ke, J. (2019) *RANS and hybrid LES/RANS simulations of flow over a square cylinder.* Adv. Aerodyn., **1**, pp. 1–24. doi: 10.1186/s42774-019-0012-9

[123] Kerckhof, F.,Rumes, B., Jacques, T., Degraer, S., Norro, A. (2010) *Early development of the subtidal marine biofouling on a concrete offshore windmill foundation on the Thornton Bank (southern North Sea): first monitoring results.* Int. J. Soc. for Underw. Technol., **29(3)**, pp. 137–149. doi: 10.3723/ut.29.137

[124] Kim, S., Karrila, S.J. (1991) *Microhydrodynamics: Principles and selected applications.* Butterworth-Heinemann, Boston, USA, 1991. ISBN: 978-0750691734

[125] Kim, M.K., Kim, D.K., Yoon, S.H., Lee, D.H. (2008) *Measurements of the flow fields around two square cylinders in a tandem arrangement.* J. Mech. Sci. Tech., **22**, pp. 397–407. doi: 10.1007/s12206-007-1041-6

[126] Knisely, C.W. (1990) *Strouhal numbers of rectangular cylinders at incidence, A review and new data.* J. Fluids Struct., **4(4)**, pp. 371–393. doi: 10.1016/0889-9746(90)90137-T

[127] Kovasznay, L.S.G (1949) *Hot-wire investigations of the wake behind cylinders at low Reynolds numbers.* Proc. R. Soc. A: Math. Phys. Eng. Sci., **198(1053)**, pp. 174–190. doi: 10.1098/rspa.1949.0093

[128] Laneville, A., Parkinson, G.V. (1971) *Effects of turbulence on galloping of bluff cylinders.* In: *Proc. 3rd Int. Conf. on Wind Effects on Buildings and Structures.* (pp. 787–797), Tokyo, Japan, 1971. doi: 10.13140/2.1.3509.2800

[129] Langhamer, O., Wilhelmsson, D., Engström, J. (2009) *Artificial reef effect and fouling impacts on offshore wave power foundations and buoys - a pilot study.* Estuar., Coast. and Shelf Sci., **82(3)**, pp. 426–432. doi: 10.1016/j.ecss.2009.02.009

[130] Lee, B.E. (1975) *The effect of turbulence on the surface pressure field of a square prism.* J. Fluid Mech., **69(2)**, pp. 263–282. doi: 10.1017/S0022112075001437

[131] Lehmkuhl, O., Rodríguez, I., Borrell, R., Chiva, J., Oliva, A. (2014) *Unsteady forces on a circular cylinder at critical Reynolds numbers.* Phys. Fluids, **26(12)**, pp. 125110. doi: 10.1063/1.4904415

[132] Letchford, C., Mason, M. (2011) *Drag of square section tubes.* In: Geurts, C. (Ed.) *Proc. 13th Int. Conf. Wind Eng.* (pp. 1–9), Amsterdam, the Netherlands, 2011

[133] Li, Y., Chan, C.K., Mei, B., Zhu, Z. (2015) *LES of incompressible heat and fluid flow past a square cylinder at high Reynolds numbers.* Int. J. Comput. Fluid Dyn., **29(3-5)**, pp. 272–285. doi: 10.1080/10618562.2015.1058373

[134] Liu, C.H., Chen, J.M. (2002) *Observations of hysteresis in flow around two square cylinders in a tandem arrangement.* J. Wind. Eng. Ind. Aerodyn., **90(9)**, pp. 1019–1050. doi: 10.1016/S0167-6105(02)00234-9

[135] Loiseau, H., Szechenyi, E. (1972) *Analyse expérimentale des portances sur un cylindre immobile soumis à un écoulement perpendiculaire à son axe à des nombres de Reynolds élevés.* La Recherche Aérospatiale, **5**, pp. 279–291

[136] Loiseau, H., Szechenyi, E. (1974) *Dynamic lift on a cylinder in high Reynolds number flow.* In: Naudascher, E. (Ed.) *Flow-induced structural vibrations.* (pp. 755–761), Springer-Verlag, Berlin, Germany, 1974

[137] Luo, S.C. (1989) *Fluctuating aerodynamic forces acting on a square cylinder that is downstream of an identical one.* Eng. J. Singapore, **16**, pp. 14–25.

[138] Luo, S.C., Chew, Y.T., Ng, Y.T. (2003) *Characteristics of square cylinder wake transition flows.* Phys. Fluids, **15(9)**, pp. 2549–2559. doi: 10.1063/1.1596413

[139] Luo, S.C., Li, L.L., Shah, D.A. (1999) *Aerodynamic stability of the downstream of two tandem square section cylinders.* J. Wind. Eng. Ind. Aerodyn., **79(1-2)**, pp. 79–103. doi: 10.1016/S0167-6105(98)00111-1

[140] Luo, S.C., Teng, T.C. (1990) *Aerodynamic forces on a square section cylinder that is downstream to an identical cylinder.* J. Aeronaut., **94(936)**, pp. 203–212. doi: 10.1017/S0001924000022880

[141] Luo, S.C., Tong, X.H., Khoo, B.C. (2007) *Transition phenomena in the wake of a square cylinder.* J. Fluids Struct., **23(2)**, pp. 227–248. doi: 10.1016/j.jfluidstructs.2006.08.012

[142] Luo, S.C., Yazdani, Md.G., Chew, Y.T., Lee, T.S. (1994) *Effects of incidence and afterbody shape on flow past bluff cylinders.* J. Wind. Eng. Ind. Aerodyn., **53(3)**, pp. 375–399. doi: 10.1016/0167-6105(94)90092-2

[143] Lyn, D.A., Einav, S., Rodi, W., Park, J.-H. (1995) *A Laser-Doppler velocimetry study of ensemble-averaged characteristics of the turbulent near wake of a square cylinder.* J. Fluid Mech., **304**, pp. 285–319. doi: 10.1017/S0022112095004435

[144] Malizia, F., Blocken, B. (2020) *Bicycle aerodynamics: History, state-of-the-art and future perspectives.* J. Wind. Eng. Ind. Aerodyn., **200**, pp. 104134. doi: 10.1016/j.jweia.2020.104134

[145] Miau, J.J., Fang, C.H., Chen, M.C., Wang, C.T., Lai, Y.H. (2014) *Discrete transition of flow over a circular cylinder at precritical Reynolds numbers.* AIAA J., **52(11)**, pp. 2576–2586. doi: 10.2514/1.J052909

[146] Minelli, G., Dong, T., Noack, B., Krajnović, S. (2020). *Upstream actuation for bluff-body wake control driven by a genetically inspired optimization.* J. Fluid Mech., **893(A1)**, pp. A1-1–29. doi: 10.1017/jfm.2020.220

[147] Minguez, M., Brun, C., Pasquetti, R., Serre, E. (2011) *Experimental and high-order LES analysis of the flow in near-wall region of a square cylinder.* Int. J. Heat Fluid Flow, **32**, pp. 558–577. doi: 10.1016/j.ijheatfluidflow.2011.03.009

[148] Modi, V.J., Slater, J.E.. (1983) *Unsteady aerodynamics and vortex induced aeroelastic instability of a structural angle section.* J. Wind. Eng. Ind. Aerodyn., **11(1-3)**, pp. 321–334. doi: 10.1016/0167-6105(83)90110-1

[149] Mutlu Sumer, B., Fredsøe, J. (2006) *Hydrodynamics around cylindrical structures.* Revised Edition. World Scientific Publishing Co. Pte. Ltd., Singapore, 2006. ISBN: 978-9812700391

[150] Nakamura, Y. (1979) *On the aerodynamic mechanism of torsional flutter of bluff structures.* J. Sound Vib., **67(2)**, pp. 163–177. doi: 10.1016/0022-460X(79)90481-4

[151] Nakamura, Y., Mizota, T. (1975a) *Unsteady lifts and wakes of oscillating rectangular prisms.* ASCE J. Eng. Mech. Div., **101(6)**, pp. 855–871. doi: 10.1061/JMCEA3.0002077

[152] Nakamura, Y., Mizota, T. (1975b) *Torsional flutter of rectangular prisms.* ASCE J. Eng. Mech. Div., **101(2)**, pp. 125–142. doi: 10.1061/JMCEA3.0002001

[153] Nakamura, Y., Tomonari, Y. (1982). *The effects of surface roughness on the flow past circular cylinders at high Reynolds numbers.* J. Fluid Mech., **123**, pp. 363–378. doi: 10.1017/S0022112082003103

[154] Nakayama, Y. (2018) *Introduction to fluid mechanics.* Second edition Butterworth-Heinemann, Oxford, UK, 2018. ISBN: 978-0081024379

[155] Naudascher, E., Rockwell, D. (1994) *Flow-induced vibrations: an engineering guide.* Dover Publications, Inc., Mineola, USA, 1994. ISBN: 978-0486442822

[156] Niemann, H.-J., Hölscher, N. (1990) *A review of recent experiments on the flow past circular cylinders.* J. Wind Eng. Ind. Aerod., **33**, pp. 197–209. doi: 10.1016/0167-6105(90)90035-B

[157] Nikitas, N., Macdonald, J.H.G. (2014) *Aerodynamic forcing characteristics of dry cable galloping at critical Reynolds numbers.* Eur. J. Mech. B/Fluids, **49(A)**, pp. 243–249. doi: 10.1016/j.euromechflu.2014.09.005

[158] Nishioka, M., Sato, H. (1978). *Mechanism of determination of the shedding frequency of vortices behind a cylinder at low Reynolds numbers.* J. Fluid Mech., **89(1)**, pp. 49–60. doi: 10.1017/S0022112078002451

[159] Norberg, C. (1993) *Flow around rectangular cylinders: pressure forces and wake frequencies.* J. Wind Eng. Ind. Aerod., **49(1-3)**, pp. 187–196. doi: 10.1016/0167-6105(93)90014-F

[160] Norberg, C. (1998) *LDV-measurements in the near wake of a circular cylinder.* In: Bearman, P.W., Williamson, C.H.K. (Eds.) *Proc. 1998 ASME Fluid Eng. Div. - Summer meeting, Advances in understanding of bluff body wakes and flow-induced vibration.* (pp. 1–12), ASME, Washington D.C., USA, 1998

[161] Novak, M. (1969) *Aeroelastic galloping of prismatic bodies.* ASCE J. Eng. Mech. Div., **95(1)**, pp. 115–142. doi: 10.1061/JMCEA3.0001072

[162] Novak, M., Davenport, A.G. (1970) *Aeroelastic instability of prisms in turbulent flow.* ASCE J. Eng. Mech. Div., **96(1)**, pp. 17–39. doi: 10.1061/JMCEA3.0001210

[163] Novak, M. (1971) *Galloping and vortex induced oscillations of structures.* In: *Proc. 3rd Int. Conf. on Wind Effects on Buildings and Structures.* (pp. 799–809), Tokyo, Japan, 1971

[164] Novak, M. (1972) *Galloping oscillations of prismatic structures.* J. of the ASCE, **98(1)**, pp. 27–46. doi: 10.1061/JMCEA3.0001575

[165] Novak, M. (1974a) *Galloping oscillations of prisms in smooth and turbulent flows.* In: Naudascher, E. (Ed.) *Flow-induced structural vibrations.* (pp. 769–774), Springer-Verlag, Berlin, Germany, 1974

[166] Novak, M., Tanaka, H. (1974b) *Effect of turbulence on galloping instability.* ASCE J. Eng. Mech. Div., **100(1)**, pp. 27–47. doi: 10.1061/JMCEA3.0001861

[167] Novak, M., Tanaka, H. (1977) *Pressure correlations on a vibrating cylinder.* In: Eaton, K.J. (Ed.) *Proc. 4th Int. Conf. Wind Effects on Buildings and Structures.* (pp. 227–232), Cambridge University Press, London, UK, 1977

[168] Obasaju, E.D. (1983) *An investigation of the effects of incidence on the flow around a square section cylinder.* The Aeronaut. Quart., **34(4)**, pp. 243–259. doi: 10.1017/S0001925900009768

[169] Öngören, A., Rockwell, D. (1988). *Flow structure from an oscillating cylinder. Part 2. Mode competition in the near wake.* J. Fluid Mech., **191**, pp. 225–245. doi: 10.1017/S0022112088001570

[170] Oggiano, Sætran, L. (2010) *A low drag suit foir ski-cross competitions.* Procedia Eng., **2**, pp. 2387–2392. doi: 10.1016/j.proeng.2010.04.004

[171] Oggiano, L., Brownlie, L., Troynikov, O., Morten Bardal, L., Sæter, C., Sætran, L. (2013) *A review on skin suits and sport garment aerodynamics: guidelines and state of the art.* Procedia Eng., **60**, pp. 91–98. doi: 10.1016/j.proeng.2013.07.018

[172] Ohya, Y., Okajima, A., Hayashi, M. (1989) *Wake interference and vortex shedding.* In: Cheretnisinoff, N.P. (Ed.) *Encyclopedia Fluid Mech., Vol. 8* (pp. 323–389), Gulf Publishing Company, Houston, 1989

[173] Okajima, A. (1979) *Flow around two tandem circular cylinders at very high Reynolds numbers.* Bull. JSME, **22(166)**, pp. 504–511. doi: 10.1299/jsme1958.22.504

[174] Okajima, A. (1982) *Strouhal numbers of rectangular cylinders.* J. Fluid Mech., **123**, pp. 379–398. doi: 10.1017/S0022112082003115

[175] Okajima, A., Nakamura, T. (1973) *Flow around a circular cylinder with surface roughness in the high Reynolds number range.* In: *Tech. Rep., Kyushuu Univ., Kumamoto, Japan, No. 40*

[176] Okajima, A., Sugitani, K. (1984) *Flow around a circular cylinder immersed in a wake of an identical cylinder (In Japanese).* Trans. JSME, **50**, pp. 2531–2538.

[177] Ong, M.C., Utnes, T., Holmedal, L.E., Myrhaug, D., Pettersen, B. (2009) *Numerical simulation of flow around a smooth circular cylinder at very high Reynolds numbers.* Mar. Struct. **22**, pp. 142–153. doi: 10.1016/j.marstruc.2008.09.001

[178] Ozgoren, M. (2006) *Flow structure in the downstream of square and circular cylinders.* Flow Meas. Instrum., **17(4)**, pp. 225–235. doi: 10.1016/j.flowmeasinst.2005.11.005

[179] Païdoussis, M.P., Price, S.J., de Langre, E. (2011) *Fluid-structure interactions. Cross-flow-induced instabilities.* Cambridge University Press, Cambridge, UK, 2011. ISBN: 978-1107652958

[180] Parkinson, G.V. (1971) *Wind-induced instability of structures.* Philos. Trans. A Math. Phys. Eng. Sci., **269(1199)**, pp. 395–409. doi: 10.1098/rsta.1971.0040

[181] Parkinson, G.V. (1974) *Mathematical models of flow-induced vibrations of bluff bodies.* In: Naudascher, E. (Ed.) *Flow-induced structural vibrations.* (pp. 81–127), Springer-Verlag, Berlin, Germany, 1974

[182] Parkinson, G.V. (1989) *Phenomena and modelling of flow-induced vibrations of bluff cylinders.* Prog. Aerosp. Sci., **26(2)**, pp. 169–224. doi: 10.1016/0376-0421(89)90008-0

[183] Parkinson, G.V., Smith, J.D. (1964) *The square prism as an aeroelastic non-linear oscillator.* Q. J. Mech. Appl. Math., **17(2)**, pp. 225–239. doi: 10.1093/qjmam/17.2.225

[184] Pearcy, H.H., Cash, R.F., Salter, I.J., Boribond, A. (1982) *Interference effects on the drag loading for groups of cylinders in uni-directional flow.* In: *Nat. Maritime Inst. Rep., No. R130* (pp. 27147)

[185] Peltzer, R.D. (1982) *Vortex shedding from a vibrating cable with attached spherical bodies in a linear shear flow.* Ph.D. Thesis, Virginia Polytech. Inst. State Univ., Blacksburg, USA, 1982

[186] Polhamus, E.C. (1958) *Effect of flow incidence and Reynolds number on low-speed aerodynamic characteristics of several noncircular cylinders with applications to directional stability and spinning.* In: *NACA Tech. Rep., No. TR-4176* (pp. 1–25)

[187] Ran, Y., Deng, Z., Yu, H., Chen, W., Gao, D. (2023) *Review of passive control of flow past a circular cylinder.* J. Vis., **24**, pp. 1–44. doi: 10.1007/s12650-022-00858-3

[188] Reinhold, T.A., Tieleman, H.W., Maher, F.J. (1977) *Interaction of square prisms in two flow fields.* J. Wind. Eng. Ind. Aerodyn., **2(3)**, pp. 223–241. doi: 10.1016/0167-6105(77)90024-1

[189] Relf, E.F., Simmons, L.F.G. (1925) *On the frequency of eddies generated by the motion of circular cylinders through a fluid.* Lond. Edinb. Dublin Philos. Mag. J. Sci., **49(290)**, pp. 509–511. doi: 10.1080/14786442508634628

[190] Ribeiro, J.L.D. (1991) *Effects of surface roughness on the two-dimensional flow past circular cylinders I: mean forces and pressures.* J. Wind. Eng. Ind. Aerodyn., **37(3)**, pp. 299–309. doi: 10.1016/0167-6105(91)90015-O

[191] Richardson, S.A. Jr., Martucelli, J.R., Price, W.S. (1965) *Research study on galloping of electric power transmission lines. Part 1.* In: *Proc. 1st Int. Conf. Wind Effects on Buildings and Structures.* (pp. 612–686), Teddington, UK, 1965

[192] Robichaux, J., Balachandar, S., Vanka, S.P. (1999) *Three-dimensional Floquet instability of the wake of square cylinder.* Phys. Fluids, **11(3)**, pp. 560–578. doi: 10.1063/1.869930

[193] Rockwell, D.O. (1977) *Organized fluctuations due to flow past a square cross section cylinder.* J. of Fluids Eng., **99(3)**, pp. 511–516. doi: 10.1115/1.3448831

[194] Rodríguez, I., Lehmkuhl, O., Chiva, J., Borrell, R., Oliva, A. (2015) *On the flow past a circular cylinder from critical to super-critical Reynolds numbers: Wake topology and vortex shedding.* Int. J. Heat Fluid Flow, **55**, pp. 91–103. doi: 10.1016/j.ijheatfluidflow.2015.05.009

[195] Rodríguez, I., Lehmkuhl, O., Piomelli, U., Chiva, J., Borrell, R., Oliva, A. (2016) *Numerical simulation of roughness effects on the flow past a circular cylinder.* J. Phys: Conf. ser., **745(3)**, pp. 032043-1–8. doi: 10.1088/1742-6596/745/3/032043

[196] Roshko, A. (1953) *On the development of turbulent wakes from vortex streets.* Ph.D. Thesis, Calif. Inst. Tech., Pasadena, USA, 1953

[197] Roshko, A. (1961) *Experiments on the flow past a circular cylinder at very high Reynolds numbers.* J. Fluid Mech., **10(3)**, pp. 345–356. doi: 10.1017/S0022112061000950

[198] Roshko, A. (1993) *Perspectives on bluff body aerodynamics.* J. Wind. Eng. Ind. Aerodyn., **49(1-3)**, pp. 79–100. doi: 10.1016/0167-6105(93)90007-B

[199] Ruscheweyh, H. (1974) *Beitrag zur Windbelastung hoher kreiszylinderähnlicher schlanker Bauwerke im natürlichen Wind bei Reynoldszahlen bis Re = 1.4×10^7.* Ph.D. Thesis, RWTH Aachen, Aachen, Germany, 1974

[200] Saha, A.K., Muralidhar, K., Biswas, G. (2000) *Experimental study of flow past a square cylinder at high Reynolds numbers.* Exp. Fluids, **29**, pp. 553–563. doi: 10.1007/s003480000123

[201] Saha, A.K., Biswas, G., Muralidhar, K. (2001) *Two-dimensional study of the turbulent wake behind a square cylinder subject to uniform flow.* J. Fluids Eng., **123(3)**, pp. 595–603. doi: 10.1115/1.1383549

[202] Saha, A.K., Biswas, G., Muralidhar, K. (2003) *Three-dimensional study of flow past a square cylinder at low Reynolds numbers.* Int. J. Heat Fluid Flow, **24(1)**, pp. 54–66. doi: 10.1016/S0142-727X(02)00208-4

[203] Sakamoto, H., Haniu, H. (1988) *Effect of free-stream turbulence on characteristics of fluctuating forces acting on two square prisms in tandem arrangement.* J. Fluids Eng., **110(2)**, pp. 140–146. doi: 10.1115/1.3243526

[204] Sakamoto, H., Haniu, H., Obata, Y. (1987) *Fluctuating forces acting on two square prisms in a tandem arrangement.* J. Wind. Eng. Ind. Aerodyn., **26(1)**, pp. 85–103. doi: 10.1016/0167-6105(87)90037-7

[205] Samson, J.E., Battista, N.A., Khatri, S., Miller, L.A. (2017) *Pulsing corals: A story of scale and mixing.* Biomath, **6**, pp. 1712169-1–14. doi: 10.11145/j.biomath.2017.12.169

[206] Samson, J.E., Miller, L.A. (2020) *Collective pulsing in Xeniid corals: Part II - Using computational fluid dynamics to determine if there are benefits to coordinated pulsing.* Bull. Math. Biol., **82(67)**, pp. 1–21. doi: 10.1007/s11538-020-00741-y

[207] Sarpkaya, T. (1978) *Fluid forcs on oscillating cylinders.* J. Waterw. Port, Coast. Ocean Eng., **104**, pp. 275–290. doi: 10.1061/JWPCDX.0000101

[208] Schewe, G. (1983a) *Über asymmetrische Strömungszustände im kritischen Reynolds-Zahl-Bereich eines querangeströmten Kreiszylinders.* In: *Proc. GAMM-Wiisenschaftliche Jahrestagung*, Hamburg, Germany, 1983

[209] Schewe, G. (1983b) *On the force fluctuations acting on a circular cylinder in crossflow from subcritical up to transcritical Reynolds numbers.* J. Fluid Mech., **133**, pp. 265–285. doi: 10.1017/S0022112083001913

[210] Schewe, G. (1986) *Sensitivity of transition phenomena to small perturbations in flow around a circular cylinder.* J. Fluid Mech., **172**, pp. 33–46. doi: 10.1017/S0022112086001635

[211] Schewe, G., Jacobs, M. (2019) *Experiments on the flow around two tandem circular cylinders from sub- up to transcritical Reynolds numbers.* J. Fluids Struct., **88**, pp. 148–166. doi: 10.1016/j.jfluidstructs.2019.05.001

[212] Schewe, G., van Hinsberg, N.P., Jacobs, M. (2021) *Investigation of the steady and unsteady forces acting on a pair of circular cylinders in crossflow up to ultra-high Reynolds numbers.* Exp Fluids, **62**, pp. 176–194. doi: 10.1007/s00348-021-03268-7

[213] Schlichting, H., Gersten, K. (2017) *Boundary layer theory.* Ninth edition Springer-Verlag, Berlin, Germany, 2017. ISBN: 978-3662529171

[214] Schmidt, L.V. (1966) *Fluctuating force measurements upon a circular cylinder at Reynolds number up to 5×10^6.* In: *NASA Tech. Mem., No. X-57779* (pp. 15.1)

[215] Schoefs, F., Boukinda, M. (2004) *Modelling of marine growth effects on offshore structures loading using kinematics field of water particle.* In: *Proc. 14th Int. Offshore and Polar Eng. Conf. and Exhib.*, Toulon, France, 2004

[216] Shang, J., Zhou, Q., Alam, M.M., Liao, H., Cao, S. (2019) *Numerical studies of the flow structure and aerodynamic forces on two tandem square cylinders with different chamfered-corner ratios.* Phys. Fluids, **31**, pp. 075102-1–15. doi: 10.1063/1.5100266

[217] Sharma, A., Eswaran, V. (2004) *Heat and fluid flow across a square cylinder in the two-dimensional laminar flow regime*. Numer. Heat Transf., Part A: Applications, **45(3)**, pp. 247–269. doi: 10.1080/10407780490278562

[218] Shih, W.C.L., Wang, C., Coles, D., Roshko, A. (1993) *Experiments on flow past rough circular cylinders at large Reynolds numbers*. J. Wind. Eng. Ind. Aerodyn., **49(1-3)**, pp. 351–368. doi: 10.1016/0167-6105(93)90030-R

[219] Shi, W., Park, H.-C., Baek, J.-H., Kim, C.-W., Kim, Y.-C., Shin, H.-K. (2012) *Study on the marine growth effect on the dynamic response of offshore wind turbines*. Int. J. Precis. Eng. Manuf., **13(7)**, pp. 1167–1176. doi: 10.1007/s12541-012-0155-7

[220] Shiraishi, N., Matsumoto, M., Shirato, H. (1986) *On aerodynamic instabilities of tandem structures*. J. Wind. Eng. Ind. Aerodyn., **23(1-3)**, pp. 437–447. doi: 10.1016/0167-6105(86)90061-9

[221] Shirayama, S., Ohta, T. (2001) *A visualization of a vector-field by a homogenized nascent-particles tracking*. J. Vis., **4(2)**, pp. 185–196. doi: 10.1007/BF03182572

[222] Simiu, E. Scanlan, R.H. (1996) *Wind Effects on Structures: Fundamentals and applications to design*. John Wiley, New York, USA, 1996. ISBN: 978-0471121572

[223] Singh, S.P., Mittal, S. (2004) *Flow past a cylinder: shear layer instability and drag crisis*. Int. J. Numer. Methods Fluids, **47(1)**, pp. 75–98. doi: 10.1002/fld.807

[224] Singh, A.P., De, A.K., Carpenter, V.K., Eswaran, V., Muralidhar, K. (2009) *Flow past a transversely oscillating square cylinder in free stream at low Reynolds numbers*. Int. J. Numer. Methods Fluids, **61(6)**, pp. 658–682. doi: 10.1002/fld.1979

[225] Slater,J.E. (1969) *Aeroelastic instability of a structural angle section*. Ph.D. Thesis, University of British Columbia, Vancouver, Canada, 1969

[226] Smith, J.D. (1962) *An experimental study of the aeroelastic instability of rectangular cylinders*. M.Sc. Thesis, University of British Columbia, Vancouver, Canada, 1962

[227] So, R.M.C. So, Wang, X.Q., Xie, W.-C.. Zhu, J. (2008) *Free-stream turbulence effects on vortex-induced vibration and flow-induced force of an elastic cylinder* J. Fluids Struct., **24(4)**, pp. 481–495. doi: 10.1016/j.jfluidstructs.2007.10.013

[228] Sohankar, A. (2006) *Flow over a bluff body from moderate to high Reynolds numbers using large eddy simulation*. Comput. Fluids, **35(10)**, pp. 1154–1168. doi: 10.1016/j.compfluid.2005.05.007

[229] Sohankar, A. (2012) *A numerical investigation of the flow over a pair of identical square cylinders in a tandem arrangement*. Int. J. Numer. Methods Fluids, **70(10)**, pp. 1244–1257. doi: 10.1002/fld.2739

[230] Sohankar, A. (2014) *A LES study of the flow interference between tandem square cylinder pairs*. Theor. Comput. Fluid Dyn., **28**, pp. 531–548. doi: 10.1007/s00162-014-0329-2

[231] Sohankar, A., Davidson, L., A., Norberg, C. (2000) *Large eddy simulation of flow past a square cylinder: comparison of different subgrid scale models*. J. Fluids Eng., **122(1)**, pp. 39–47. doi: 10.1115/1.483224

[232] Sohankar, A., Etminan, A. (2009). *Forced-convection heat transfer from tandem square cylinders in cross flow at low Reynolds numbers*. Int. J. Numer. Methods Fluids, **60(7)**, pp. 733–751. doi: 10.1002/fld.1909

[233] Sohankar, A., Mohagheghian, S., Dehghan, A.A., Dehghan Manshadi, M. (2015) *A smoke visualization study of the flow over a square cylinder at incidence and tandem square cylinders*. J. Vis., **18**, pp. 687–703. doi: 10.1007/s12650-015-0275-0

[234] Sohankar, A., Norberg, C., Davidson, L. (1995) *Numerical simulation of unsteady flow around a square two-dimensional cylinder*. In: *Proc. 12th Austral. Fluid Mech. Conf.*, Sidney, Australia, 1995 (pp. 517–520)

[235] Sohankar, A., Norberg, C., Davidson, L. (1998) *Low-Reynolds-number flow around a square cylinder at incidence: Study of blockage, onset of vortex shedding and outlet boundary condition*. Int. J. Numer. Methods Fluids, **26(1)**, pp. 39–56. doi: 10.1063/1.4989745

[236] Sohankar, A., Norberg, C., Davidson, L. (1999) *Simulation of three-dimensional flow around a square cylinder at moderate Reynolds numbers*. Phys. Fluids, **11(2)**, pp. 288–306. doi: 10.1063/1.869879

[237] Spraul, C., Pham, H.-D., Arnal, V., Reynaud, M. (2017) *Effect of marine growth on floating wind turbines mooring lines responses*. In: *Proc. 23ème Congrès Français de Mécanique.* (pp. 1–17), Lille, France, 2017

[238] Stadler, H., Bauknecht, A., Siegrist, S., Flesch, R., Wolf, C.C., van Hinsberg, N.P., Jacobs, M. (2017) *Background-oriented Schlieren imaging of flow around a circular cylinder at low Mach numbers*. Exp Fluids, **58**, pp. 114-125. doi: 10.1007/s00348-017-2398-7

[239] Szechenyi, E. (1975). *Supercritical Reynolds number simulation for two-dimensional flow over circular cylinders*. J. Fluid Mech., **70(3)**, pp. 529–542. doi: 10.1017/S002211207500217

[240] Takeuchi, T., Matsumoto, M. (1992) *Aerodynamic response characteristics of rectangular cylinders in tandem arrangement*. J. Wind. Eng. Ind. Aerodyn., **41(1-3)**, pp. 565–576. doi: 10.1016/0167-6105(92)90466-N

[241] Tamura, T., Miyagi, T., Kitagishi, T. (1998) *Numerical prediction of unsteady pressures on a square cylinder with various corner shapes*. J. Wind. Eng. Ind. Aerodyn., **74-76**, pp. 531–542. doi: 10.1016/S0167-6105(98)00048-8

[242] Tamura, T., Miyagi, T. (1999) *The effect of turbulence on aerodynamic forces on a square cylinder with various corner shapes*. J. Wind. Eng. Ind. Aerodyn., **83(1-3)**, pp. 135–145. doi: 10.1016/S0167-6105(99)00067-7

[243] Tanida, Y., Okajima, A., Watanabe, Y. (1973). *Stability of a circular cylinder oscillating in uniform flow or wake*. J. Fluid Mech., **61(4)**, pp. 769–784. doi: 10.1017/S0022112073000935

[244] Tatsutani, K., Devarakonda, R., Humphrey, J.A.C. (1993) *Unsteady flow and heat transfer for cylinder pairs in a channel*. Int. J. Heat Mass Transf., **36(13)**, 3311–3328. doi: 10.1016/0017-9310(93)90013-V

[245] Theophanatos, A. (1988) *Marine growth and the hydrodynamic loading of offshore structures*. Ph.D. Thesis, Strathclyde University, Glasgow, UK, 1988. doi: 10.48730/qx63-8r70

[246] Timmer, N., Veldhuis, L. (2021) *The impact of skinsuit zigzag tape turbulators on speed skating performance*. Appl. Sci., **11(3)**, pp. 988-1–18. doi: 10.3390/app11030988

[247] Toebes, G.H. (1969) *The unsteady flow and wake near an oscillating cylinder*. J. Fluids Eng. Trans. ASME., **91**, pp. 493–502. doi: 10.1115/1.3571165

[248] Torum, A., Anand, N.M. (1985) *Free span vibrations of submarine pipelines in steady flows–Effect of free-stream turbulence on mean drag coefficients*. J. Energy Resour. Technol., **107(4)**, pp. 415–420. doi: 10.1115/1.3231212

[249] Trias, F.X., Gorobets, A., Oliva, A. (2015) *Turbulent flow around a square cylinder at Reynolds number 22,000: A DNS study*. Comput. Fluids, **123**, pp. 87–98. doi: 10.1016/j.compfluid.2015.09.013

[250] Tritton, D.J. (1988) *Physical Fluid Dynamics*. Second Edition Reprint. Oxford University Press, Oxford, UK, 1988. ISBN: 978-0198544937

[251] Valentín, D., Valero, C., Egusquiza, M., Presas, A. (2022) *Failure investigation of a solar tracker due to wind-induced torsional galloping*. Eng. Fail. Anal., **135**, pp. 106137-1–11. doi: 10.1016/j.engfailanal.2022.106137

[252] Van Dyke, M. (1982) *An album of fluid motion*. The Parabolic Press, USA, 1982. ISBN: 978-0915760022

[253] van Hinsberg, N.P. (2015) *The Reynolds number dependency of the steady and unsteady loading on a slightly rough circular cylinder: From subcritical up to high transcritical flow state*. J. Fluids Struct., **55**, pp. 526–539. doi: 10.1016/j.jfluidstructs.2015.04.002

[254] van Hinsberg, N.P., Schewe, G., Jacobs, M. (2017) *Experiments on the aerodynamic behavior of square cylinders with rounded corners at Reynolds numbers up to 12 million*. J. Fluids Struct., **74**, pp. 214–233. doi: 10.1016/j.jfluidstructs.2017.08.002

[255] van Hinsberg, N.P., Schewe, G., Jacobs, M. (2018) *Experimental investigation on the surface roughness effect of square cylinders with rounded corners at high Reynolds numbers up to 10^7*. J. Wind Eng. Ind. Aerod., **173**, pp. 14–27. doi: 10.1016/j.jweia.2017.12.003

[256] van Hinsberg, N.P. (2020) *The Reynolds-number effect on the steady and unsteady aerodynamic loading on smooth and slightly-rough square-section cylinders with rounded corners*. In: Dillmann, A., Heller, G., Krämer, E., Wagner, C., Tropea, C, Jakirlić (Eds.) *New Results in Numerical and Experimental Fluid Mechanics XII. DGLR 2018. Notes on Numerical Fluid Mechanics and Multidisciplinary Design. Vol. 142* (pp. 399–403), Springer, Cham, 2020. doi: 10.1007/978-3-030-25253-3_66

[257] van Hinsberg, N.P. (2021a) *Mean and unsteady loading on square prisms with rounded edges: hard marine growth, incidence, and Reynolds number effects*. Mar. Struct., **75**, pp. 1–20. doi: 10.1016/j.marstruc.2020.102886

[258] van Hinsberg, N.P. (2021b) *Aerodynamics of smooth and rough square-section prisms at incidence in very high Reynolds-number cross-flows*. Exp Fluids, **62**, pp. 50–66. doi: 10.1007/s00348-021-03143-5

[259] van Hinsberg, N.P. (2022) *Two identical tandem square prisms with rounded edges and hard marine fouling at incidence in crossflow: Effect of spacing and Reynolds number on unsteady fluid dynamics.* Ocean Eng., **262**, pp. 112302-1–32. doi: 10.1016/j.oceaneng.2022.112302

[260] van Oudheusden, B.W., Scarano, F., van Hinsberg, N.P., Watt, D.W. (2005) *Phase-resolved characterization of vortex shedding in the near wake of a square-section cylinder at incidence.* Exp Fluids, **39**, pp. 86–98. doi: 10.1007/s00348-005-0985-5

[261] van Oudheusden, B.W., Scarano, F., van Hinsberg, N.P., Roosenboom, E.W.M. (2007) *Quantitative visualization of the flow around a square-section cylinder at incidence.* J. Wind. Eng. Ind. Aerodyn., **96(6-7)**, pp. 913–922. doi: 10.1016/j.jweia.2007.06.030

[262] Vaz, G., Mabilat, R., van der Wal, R., Gallagher, P. (2007) *Viscous flow computations on smooth cylinders: A detailed numerical study with validation.* In: *Proc. 26th ASME Int. Conf. Offshore Mech. Arctic Eng.*, San Diego, USA, 2007. doi: 10.1115/OMAE2007-29275

[263] Vickery, B.J. (1966) *Fluctuating lift and drag on a long cylinder of square cross-section in a smooth and in a turbulent stream.* J. Fluid Mech., **25(3)**, pp. 481–494. doi: 10.1017/S002211206600020X

[264] Virkam, C.K., Ravindra, H.V., Krishne Gowda, Y.T. (2020) *Visualisation of flow past square cylinders with corner modification.* J. Mech. Energy Eng., **4(3)**, pp. 285–294. doi: 10.30464/jmee.2020.4.3.285

[265] Virlogeux, M. (2005) *State-of-the-art in cable vibrations of cable-stayed bridges.* Bridge Struct., **1(3)**, pp. 133–168. doi: 10.1080/15732480500301004

[266] Wang, L.J., Alam, M.M., Zhou, Y. (2017) *Two tandem cylinders of different diameters in crossflow: effect of an upstream cylinder on wake dynamics.* J. Fluid Mech., **836**, pp. 5–42. doi: 10.1017/jfm.2017.735

[267] Warschauer, K.A., Leene, J.A. (1971) *Experiments on mean and fluctuating pressures of circular cylinders at cross flow at very high Reynolds numbers.* In: *Proc. 3rd Int. Conf. Wind Eff. Build. Struct.*, Tokyo, Japan, 1971 (pp. 305–315)

[268] Weier, T., Gerbeth, G., Mutschke, G., Platacis, E., Lielausis, O.. (1998). *Experiments on cylinder wake stabilization in an electrolyte solution by means of electromagnetic forces localized on the cylinder surface.* Exp. Therm. Fluid Sci., **16(1-2)**, pp. 84–91. doi: 10.1016/S0894-1777(97)10008-5

[269] Werlé, H. (1974) *Hydrodynamic tunnel at the service of aerospace research.* ONERA Techn. Rep., Publ. 156 (Rev. FV)

[270] Wieselsberger, C. (1921) *Neuere Feststellungen über die Gesetze des Flüssigkeits- und Luftwiderstandes.* Phys. Z., **22**, pp. 321–328

[271] Williamson, C.H.K. (1988) *The existence of two stages in the transition to three-dimensionality of a cylinder wake.* Phys. Fluids, **31(11)**, pp. 3165–3168. doi: 10.1063/1.866925

[272] Williamson, C.H.K. (1996) *Vortex dynamics in the cylinder wake.* Annu. Rev. Fluid Mech., **28**, pp. 477–539. doi: 10.1146/annurev.fl.28.010196.002401

[273] Williamson, C.H.K., Roshko, A. (1988) *Vortex formation in the wake of an oscillating cylinder.* J. Fluids Struct., **2**, pp. 355–381. doi: 10.1016/S0889-9746(88)90058-8

[274] Williamson, C.H.K., Govardhan, R. (2004) *Vortex-induced vibrations.* Annu. Rev. Fluid Mech., **36**, pp. 413–455. doi: 10.1146/annurev.fluid.36.050802.122128

[275] Wolfram, J., Theophanatos, A. (1985) *The effects of marine fouling on the fluid loading of cylinders: some experimental results.* In: Proc. 17th Offshore Techn. Conf., Houston, USA, 1985. doi: 10.4043/4954-MS

[276] Wolfram, J. (1991) *Effect of marine growth on vortex shedding and fatigue life of tubular members: results from a case study.* In: Proc. 1st Int. Offshore and Polar Eng. Conf. (pp. 362–369), Edinburgh, UK, 1991. doi: 10.1201/9781315229256-84

[277] Wright, C.S., Murphy, J., Pakrashi, V. (2016) *The dynamic effects of marine growth on a tension moored floating wind turbine.* In: Soares, C.G. (Ed.) Proc. 2nd Int. Conf. on Renew. Energies Offshore. (pp. 723–732), Lisbon, Portugal, 2016. doi: 10.1201/9781315229256-85

[278] Wu, J., Welch, L.W., Welsh, M.C., Sheridan, J., Walker, G.J. (1994) *Spanwise wake structures of a circular cylinder and two circular cylinders in tandem.* Exp. Therm. Fluid Sci., **9(3)**, pp. 299–308. doi: 10.1016/0894-1777(94)90032-9

[279] Xu, W. (2020) *Vortex shedding and VIV suppression.* In: Cui, W., Fu, S., Hu, Z. (Eds.) Ency Ocean Eng. (pp. 1–9), Springer, Singapore. doi: 10.1007/978-981-10-6963-5_279-1

[280] Xu, G., Zhou, Y. (2004) *Strouhal numbers in the wake of two inline cylinders.* Exp Fluids, **37**, pp. 248–256. doi: 10.1007/s00348-004-0808-0

[281] Yamagishi, Y., Oki, M. (2004) *Effect of groove shape on flow characteristics around a circular cylinder with grooves.* J. Vis., **7**, pp. 209–216. doi: 10.1007/BF03181635

[282] Yamagishi, Y., Oki, M. (2005) *Effect of the number of grooves on flow characteristics around a circular cylinder with triangular grooves.* J. Vis., **8(1)**, pp. 57–64. doi: 10.1007/BF03181603

[283] Yamagishi, Y., Oki, M. (2007) *Numerical simulation of flow around a circular cylinder with curved sectional grooves.* J. Vis., **10**, pp. 179–186. doi: 10.1007/BF03181829

[284] Yan, Y., Zhao, T., He, Z., Yang, Z., Zhang, L. (2021) *Numerical investigation on the characteristics of flow and heat transfer enhancement by micro pin-fin array heat sink with fin-shaped strips.* Chem. Eng. Process., **160**, pp. 108273. doi: 10.1016/j.cep.2020.108273

[285] Yang, S.-H., Ringsberg, J.W., Johnson, E. (2016) *The influence of biofouling on power capture and the fatigue life of mooring lines and power cables used in wave energy converters.* In: Soares, C.G. (Ed.) Proc. 2nd Int. Conf. on Renew. Energies Offshore. (pp. 711–722), Lisbon, Portugal, 2016. doi: 10.1201/9781315229256-84

[286] Yen, S.C., Yang, C.W. (2011) *Flow patterns and vortex shedding behavior behind a square cylinder.* J. Wind. Eng. Ind. Aerodyn., **99(8)**, pp. 868–878. doi: 10.1016/j.jweia.2011.06.006

[287] Yoon, D., Yang, K., Choi, C. (2010) *Flow past a square cylinder with an angle of incidence.* Phys. Fluids, **22(4)**, pp. 043603-1–12. doi: 10.1063/1.3388857

[288] Yucel, M., Bekdaş, G., Nigdeli, S.M., Sevgen, S. (2019) *Estimation of optimum tuned mass damper parameters via machine learning.* J. Build. Eng., **26**, pp. 100847. doi: 10.1016/j.jobe.2019.100847

[289] Zan, S.J., Matsuda, K. (2002) *Steady and unsteady loading on a roughened circular cylinder at Reynolds numbers up to 900,000.* J. Wind. Eng. Ind. Aerodyn., **90(4-5)**, pp. 567–581. doi: 10.1016/S0167-6105(01)00213-6

[290] Zdravkovich, M.M. (1981) *Review and classification of various aerodynamic and hydrodynamic means for suppressing vortex shedding.* J. Wind. Eng. Ind. Aerodyn., **7(2)**, pp. 145–189. doi: 10.1016/0167-6105(81)90036-2

[291] Zdravkovich, M.M. (1982) *Modification of vortex shedding in the synchronisation range.* J. Fluids Eng., **104**, pp. 513–517. doi: 10.1115/1.3241895

[292] Zdravkovich, M.M. (1987) *The effects of interference between circular cylinders in cross flow.* J. Fluids Struct., **1(2)**, pp. 239–261. doi: 10.1016/S0889-9746(87)90355-0

[293] Zdravkovich, M.M. (1990) *Conceptual overview of laminar and turbulent flows past smooth and rough circular cylinders.* J. Wind. Eng. Ind. Aerodyn., **33(1-2)**, pp. 53–62. doi: 10.1016/0167-6105(90)90020-D

[294] Zdravkovich, M.M. (1997) *Flow around circular cylinders. Vol 1: Fundamentals.* Oxford University Press, Oxford, UK, 1997. ISBN: 978-0198563969

[295] Zdravkovich, M.M. (2003) *Flow around circular cylinders. Vol 2: Applications.* Oxford University Press, Oxford, UK, 2003. ISBN: 978-0198565611

[296] Zdravkovich, M.M., Pridden, D.L. (1977) *Interference between two circular cylinders; series of unexpected discontinuities.* J. Ind. Aero., **2(3)**, pp. 255–270. doi: 10.1016/0167-6105(77)90026-5

[297] Zhang, W., Chen, X., Yang, H., Liang, H., Wei, Y. (2019) *Forced convection for flow across two tandem cylinders with rounded corners in a channel.* Int. J. Heat Mass Transf., **130**, 1053–1069. doi: 10.1016/j.ijheatmasstransfer.2018.10.125

[298] Zhang, B., Song, B., Mao, Z., Tian, W., Li, B. (2017) *Numerical investigation on VIV energy harvesting of bluff bodies with different cross sections in tandem arrangement.* Energy, **133**, pp. 723–736. doi: 10.1016/j.energy.2017.05.051

[299] Zhou, Y., Yiu, M.W. (2006) *Flow structure, momentum and heat transport in a two-tandem-cylinder wake.* J. Fluid Mech., **548**, pp. 17–48. doi: 10.1017/S002211200500738X

Appendix A

Combined effect of the surface roughness height and prism's edge roundness value on the PSD of the global lift force of square-section prisms at $\alpha = 0°$ and $45°$ and circular cylinders

The following figures display the effect of a change in surface roughness height from $k_s/D = 4.5 \times 10^{-6}$ to 1×10^{-3} on the power spectra of the time series of the global lift force that acts on a 2D square-section prism with various possible edge-roundness values and on a 2D circular cylinder. The selected edge roundness values are: $r/D = 0$, 0.16, and 0.29. The incidence angle is either $0°$ or $45°$. The presented Reynolds numbers are chosen in such a way that they cover all flow regimes.

Appendix A: Combined effect of the surface roughness height and prism's edge roundness value on the PSD of the global lift force of square-section prisms at $\alpha = 0°$ and $45°$ and circular cylinders

A.1 Incidence angle of 0°
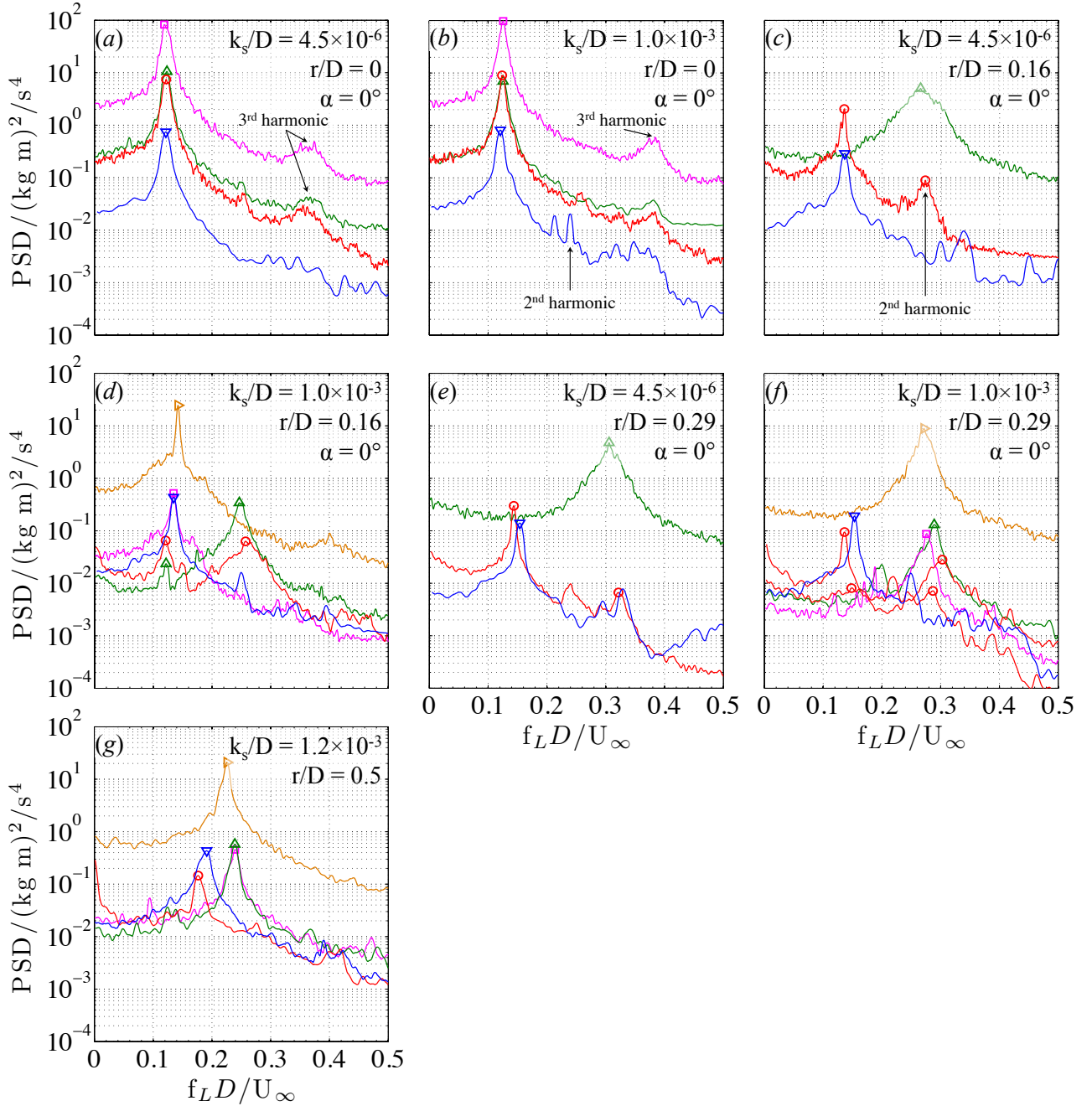
Figure A.1: Combined influence of k_s/D and r/D on the PSD of the time series of the global lift force of a two-dimensional square-section prism at $\alpha = 0°$ for selected Reynolds numbers. (a)-(b): $r/D = 0$; (c)-(d): $r/D = 0.16$; (e)-(f): $r/D = 0.29$; (g): $r/D = 0.5$;. ──: *subcritical flow regime*; ──: *critical flow regime*; ──: *supercritical flow regime*; ──: *upper transition*; ──: *transcritical flow regime.* The corresponding Strouhal numbers are indicated by the symbols on the curves and listed in Table A.1. In the case of the occurrence of two Strouhal numbers at equal Reynolds number, both have been highlighted in the graphs.

Appendix A: Combined effect of the surface roughness height and prism's edge roundness value on the PSD of the global lift force of square-section prisms at $\alpha = 0°$ and $45°$ and circular cylinders

Table A.1: Values of the Strouhal numbers – based on the main and, when applicable, also the secondary frequency peak in the PSDs of the time series of the lift $L(t)$ in Figure A.1 – for selected Reynolds numbers in the various flow regimes of perfectly smooth and rough square-section prisms with edge roundness values of $r/D = 0$, 0.16, or 0.29 at $\alpha = 0°$ and of a circular cylinder.

Incidence angle / °	Edge roundness	Surface roughness height	Flow regime	Reynolds number	Strouhal number(s)[†]	
					$St_{L,1}$	$St_{L,2}$
0	0	4.5×10^{-6}	–	1.269×10^{5}	0.122	–
			–	5.474×10^{5}	0.122	–
			–	9.439×10^{5}	0.123	–
			–	6.159×10^{6}	0.119	–
		1.0×10^{-3}	–	1.189×10^{5}	0.121	–
			–	5.382×10^{5}	0.124	–
			–	9.548×10^{5}	0.125	–
			–	6.011×10^{6}	0.126	–
	0.16	4.5×10^{-6}	subcritical	1.163×10^{5}	0.136	–
			critical	5.481×10^{5}	0.136	0.274
			supercritical	5.913×10^{6}	0.266	–
		1.0×10^{-3}	subcritical	1.127×10^{5}	0.135	–
			critical	1.873×10^{5}	0.121	0.257
			supercritical	2.327×10^{5}	0.246	0.122
			upper transition	2.622×10^{5}	0.134	–
			transcritical	5.912×10^{6}	0.142	–
	0.29	4.5×10^{-6}	subcritical	1.184×10^{5}	0.154	–
			critical	2.428×10^{5}	0.144	0.322
			supercritical	6.130×10^{6}	0.306	–
		1.0×10^{-3}	subcritical	1.115×10^{5}	0.153	–
			critical	1.624×10^{5}	0.136	0.287
			critical	1.821×10^{5}	0.303	0.148
			supercritical	1.984×10^{5}	0.289	–
			upper transition	3.338×10^{5}	0.276	–
			transcritical	6.021×10^{6}	0.272	–
–	0.5	1.2×10^{-3}	subcritical	1.058×10^{5}	0.191	–
			critical	1.702×10^{5}	0.177	–
			supercritical	1.950×10^{5}	0.239	–
			upper transition	2.553×10^{5}	0.243	——
			transcritical	6.163×10^{6}	0.226	–

[†] $St_{L,1}$ and $St_{L,2}$ correspond to the dimensionless eddy shedding frequencies at the main and secondary peak, respectively.

A.2 Incidence angle of 45°
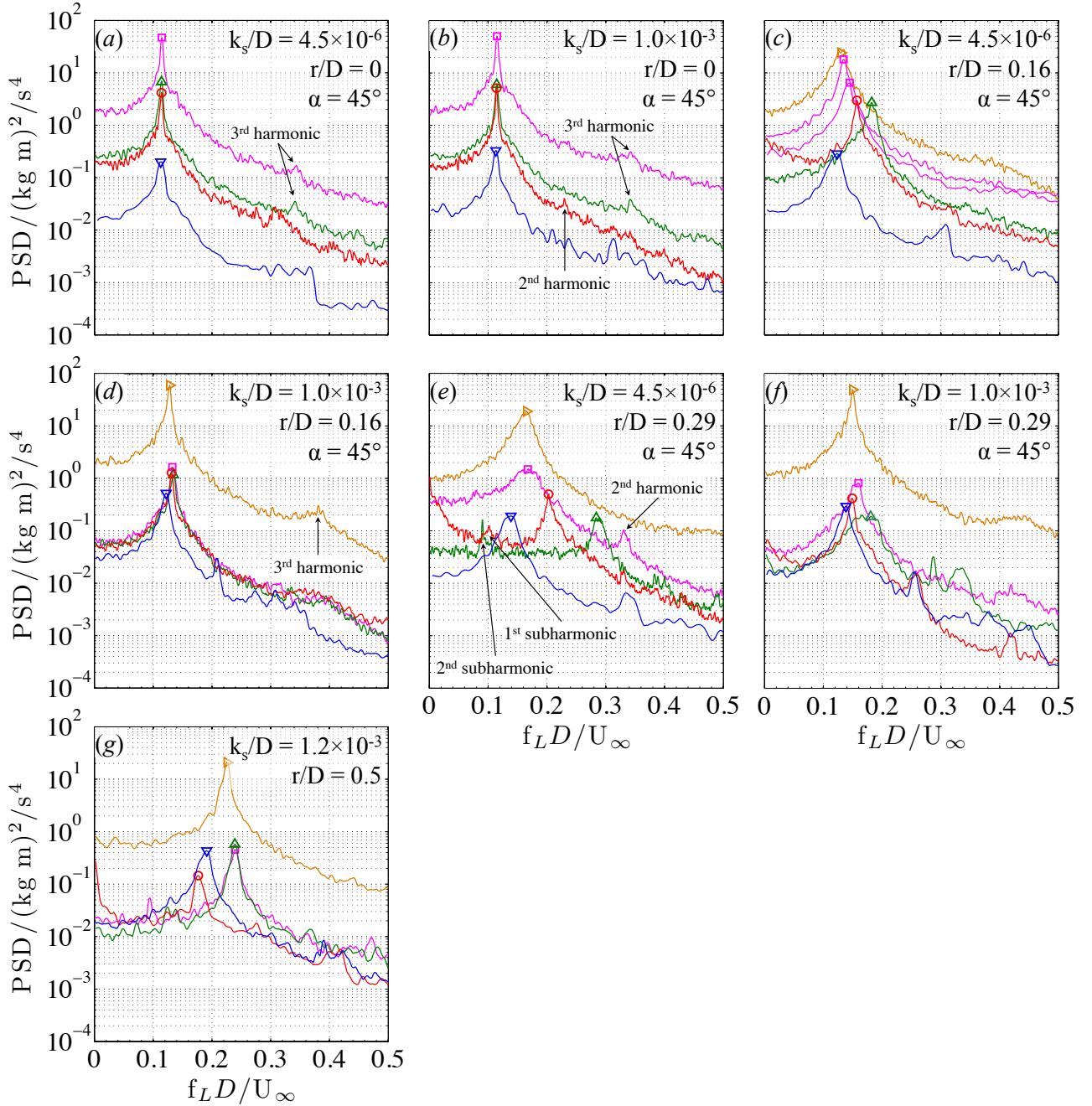
Figure A.2: Combined influence of k_s/D and r/D on the PSD of the time series of the global lift force of a two-dimensional square-section prism at $\alpha = 45°$ for selected Reynolds numbers. (a)-(b): $r/D = 0$; (c)-(d): $r/D = 0.16$; (e)-(f): $r/D = 0.29$; (g): $r/D = 0.5$;. —: *subcritical flow regime*; —: *critical flow regime*; —: *supercritical flow regime*; —: *upper transition*; —: *transcritical flow regime*. The corresponding Strouhal numbers are indicated by the symbols on the curves and listed in Table A.2. In the case of the occurrence of two Strouhal numbers at equal Reynolds number, both have been highlighted in the graphs.

Appendix A: Combined effect of the surface roughness height and prism's edge roundness value on the PSD of the global lift force of square-section prisms at $\alpha = 0°$ and $45°$ and circular cylinders

Table A.2: Values of the Strouhal numbers – based on the main and, when applicable, also the secondary frequency peak in the PSDs of the time series of the lift $L(t)$ in Figure A.2 – for selected Reynolds numbers in the various flow regimes of perfectly smooth and rough square-section prisms with edge roundness values of $r/D = 0$, 0.16, or 0.29 at $\alpha = 45°$ and of a circular cylinder.

Incidence angle / $°$	Edge roundness	Surface roughness height	Flow regime	Reynolds number	Strouhal number(s)[†] $St_{L,1}$	$St_{L,2}$
45	0	4.5×10^{-6}	–	1.114×10^5	0.113	–
			–	5.437×10^5	0.114	–
			–	9.492×10^5	0.114	–
			–	6.125×10^6	0.115	–
		1.0×10^{-3}	–	1.205×10^5	0.113	–
			–	5.242×10^5	0.114	–
			–	9.667×10^5	0.115	–
			–	6.202×10^6	0.115	–
	0.16	4.5×10^{-6}	subcritical	1.317×10^5	0.123	–
			critical	9.219×10^5	0.157	–
			supercritical	1.032×10^6	0.182	–
			upper transition	2.190×10^6	0.145	–
				3.232×10^6	0.135	–
			transcritical	6.048×10^6	0.130	–
		1.0×10^{-3}	subcritical	1.319×10^5	0.122	–
			critical	2.322×10^5	0.131	–
			supercritical	2.418×10^5	0.135	–
			upper transition	2.590×10^5	0.133	–
			transcritical	6.173×10^6	0.128	–
	0.29	4.5×10^{-6}	subcritical	1.198×10^5	0.139	–
			critical	5.652×10^5	0.203	–
			supercritical	6.315×10^5	0.284	–
			upper transition	2.534×10^6	0.168	–
			transcritical	5.864×10^6	0.165	–
		1.0×10^{-3}	subcritical	1.091×10^5	0.139	–
			critical	1.845×10^5	0.149	–
			supercritical	2.064×10^5	0.186	–
			upper transition	2.260×10^5	0.160	–
			transcritical	6.300×10^6	0.150	–
–	0.5	1.2×10^{-3}	subcritical	1.058×10^5	0.191	–
			critical	1.702×10^5	0.177	–
			supercritical	1.950×10^5	0.239	–
			upper transition	2.553×10^5	0.243	–
			transcritical	6.163×10^6	0.226	–

[†] $St_{L,1}$ and $St_{L,2}$ correspond to the dimensionless eddy shedding frequencies at the main and secondary peak, respectively.

Appendix B

Power spectra of the global lift force for a slightly rough square-section prism with rounded egdes of $r/D = 0.16$ at incidence angles between $0°$ and $45°$

Appendix B: Power spectra of the global lift force for a slightly rough square-section prism with rounded egdes of $r/D = 0.16$ at incidence angles between $0°$ and $45°$

Figure B.1: Influence of incidence angle on the PSDs of the time series of the global lift force on a 2D square-section prism ($r/D = 0.16$ and $k_s/D = 4.5 \times 10^{-4}$) at selected Reynolds numbers that cover the *subcritical* to the *transcritical* flow regimes. First and third row: $0° \leqslant |\alpha| \leqslant 13°$; second and fourth row: $19.5° \leqslant |\alpha| \leqslant 45°$. The corresponding Strouhal numbers are indicated by the symbols on the curves and listed in each graph.

Appendix B: Power spectra of the global lift force for a slightly rough square-section prism with rounded egdes of $r/D = 0.16$ at incidence angles between $0°$ and $45°$
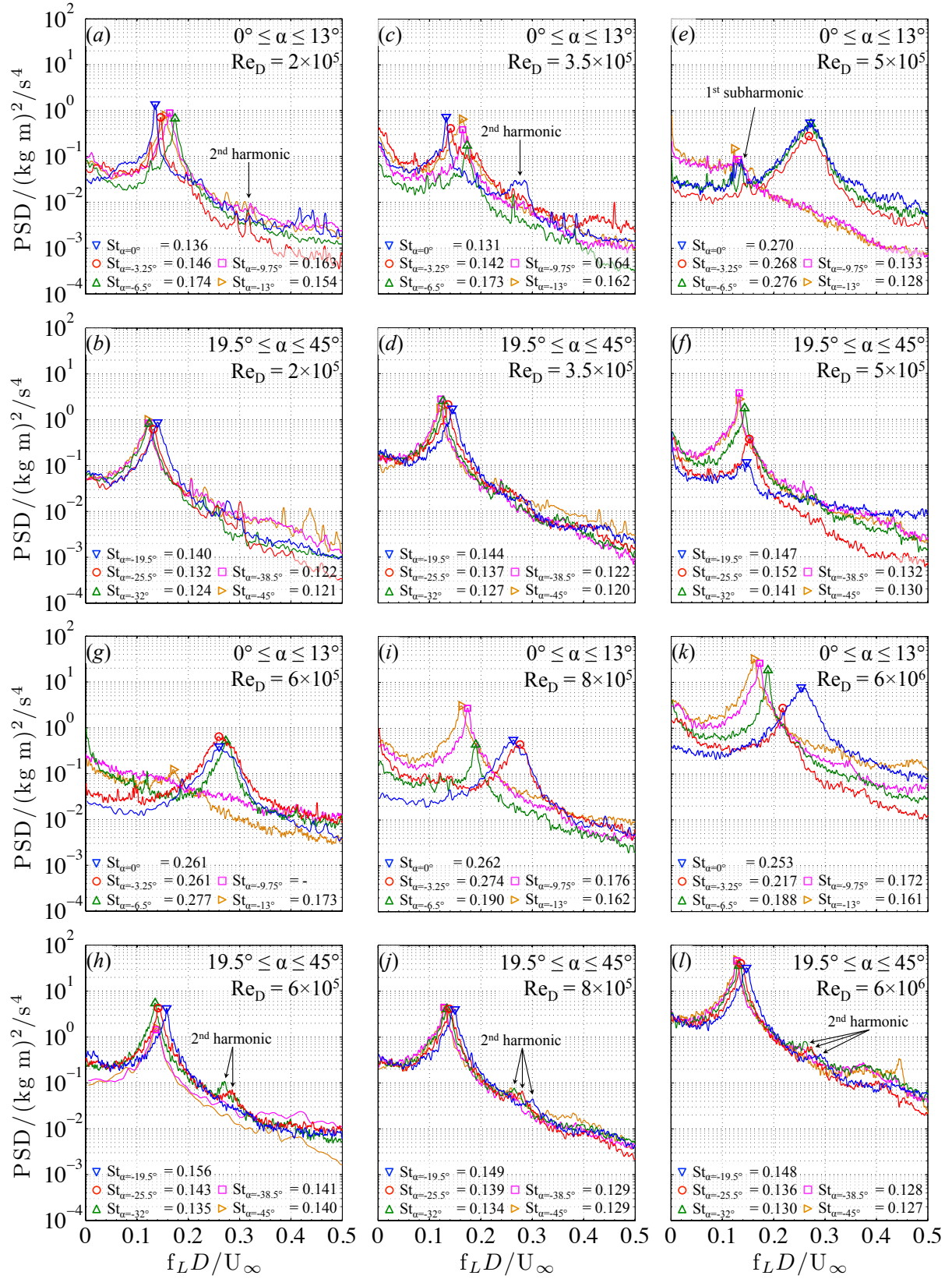
Appendix C

Power spectra of the global lift force on the downstream prism of two smooth square-section prisms with edge roundness of $r/D = 0.16$ in a tandem configuration with prism centre-to-centre spacing of $S/D = 4.0$ or 5.6 and at incidence angles of either $0°$ or $45°$

Appendix C: Power spectra of the global lift force on the downstream prism of two smooth square-section prisms with edge roundness of $r/D = 0.16$ in a tandem configuration with prism centre-to-centre spacing of $S/D = 4.0$ or 5.6 and at incidence angles of either $0°$ or $45°$
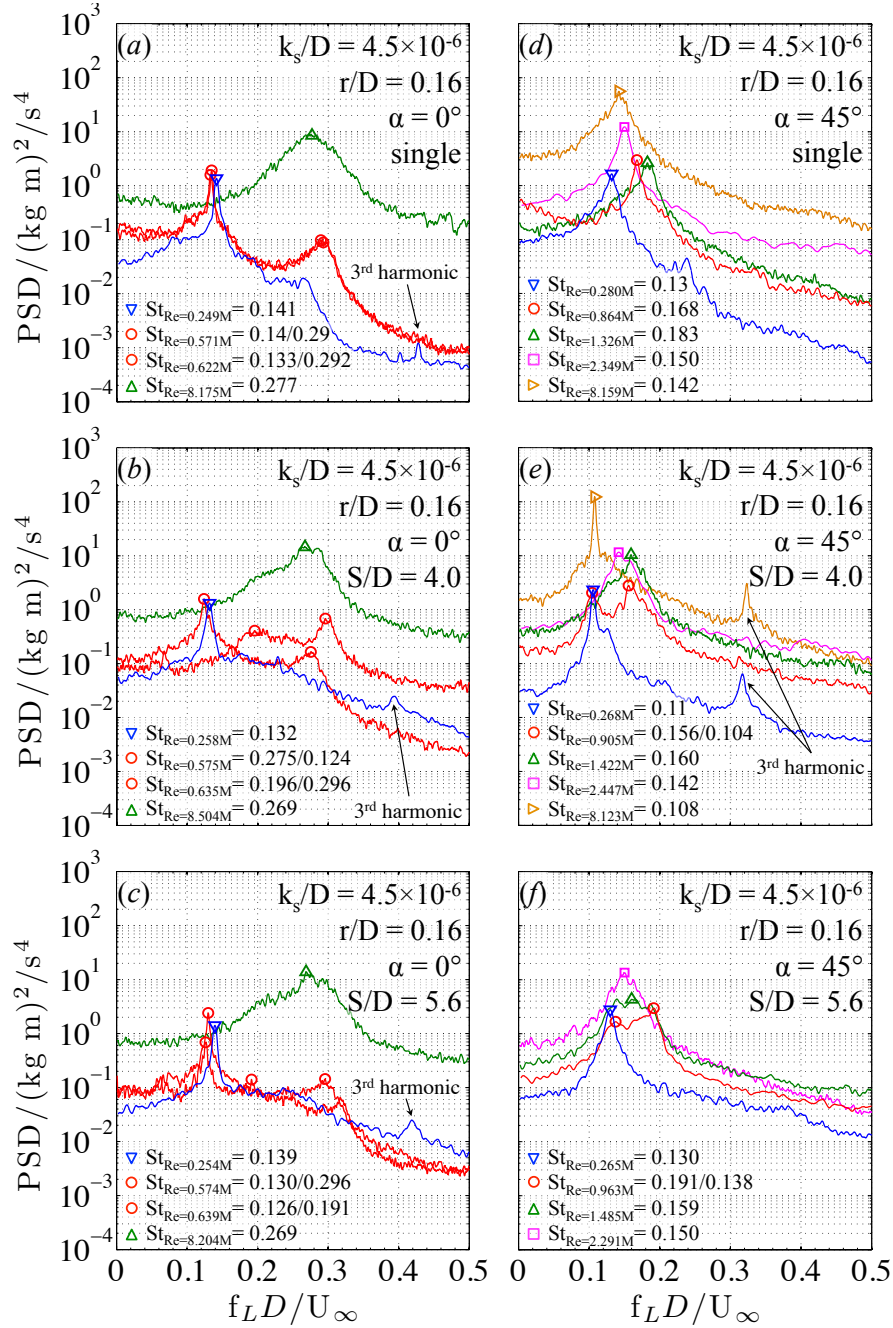
Figure C.1: Influence of the prisms' centre-to-centre spacing on the PSDs of the time series of the global lift force that acts on the downstream one of two 2D smooth tandem square-section prisms ($r/D = 0.16$, $\alpha = 0°$ and $45°$) at selected Reynolds numbers that cover the *subcritical* to the *transcritical* flow regimes. Left column: $\alpha = 0°$; right column: $\alpha = 45°$. Upper row: single, isolated prism configuration; center row: $S/D = 4.0$; lower row: $S/D = 5.6$. —: *subcritical flow regime*; —: *critical flow regime*; —: *supercritical flow regime*; —: *upper transition*; —: *transcritical flow regime*. The corresponding Strouhal numbers are indicated by the symbols on the curves and listed in each graph. M in the Reynolds number equals "million".

Appendix C: Power spectra of the global lift force on the downstream prism of two smooth square-section prisms with edge roundness of $r/D = 0.16$ in a tandem configuration with prism centre-to-centre spacing of $S/D = 4.0$ or 5.6 and at incidence angles of either $0°$ or $45°$

Appendix D

Effect of surface roughness height on the power spectra of the global lift force on the downstream prism of two square-section prisms with edge roundness of $r/D = 0.16$ in a tandem configuration with prism centre-to-centre spacing of $S/D = 4.0$ or 5.6 and at incidence angles of either $0°$ or $45°$

Appendix D: Effect of surface roughness height on the power spectra of the global lift force on the downstream prism of two square-section prisms with edge roundness of $r/D = 0.16$ in a tandem configuration with prism centre-to-centre spacing of $S/D = 4.0$ or 5.6 and at incidence angles of either $0°$ or $45°$
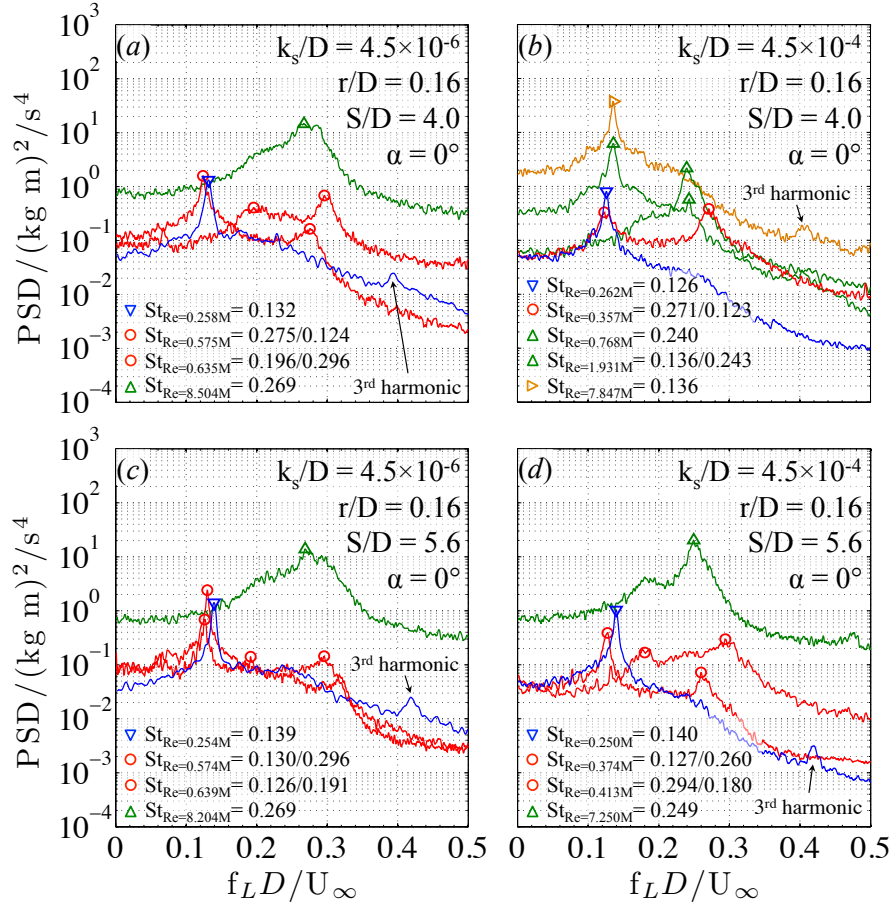
Figure D.1: Combined impact of increased surface roughness and gap spacing on the power spectral density of the time series of the global lift force that acts on the downstream one of two tandem square-section prisms ($r/D = 0.16$, $\alpha = 0°$) at selected Reynolds numbers in the *subcritical* to *transcritical* flow regimes. Left column: $k_s/D = 4.5{\times}10^{-6}$; right column: $k_s/D = 4.5{\times}10^{-4}$. Upper row: centre-to-centre spacing of $S/D = 4.0$; lower row: centre-to-centre spacing of $S/D = 5.6$. —: *subcritical flow regime*; —: *critical flow regime*; —: *supercritical flow regime*; —: *upper transition*; —: *transcritical flow regime*. The corresponding Strouhal numbers are indicated by the symbols on the curves and listed in each graph. M in the Reynolds number equals "million".

Appendix D: Effect of surface roughness height on the power spectra of the global lift force on the downstream prism of two square-section prisms with edge roundness of $r/D = 0.16$ in a tandem configuration with prism centre-to-centre spacing of $S/D = 4.0$ or 5.6 and at incidence angles of either $0°$ or $45°$
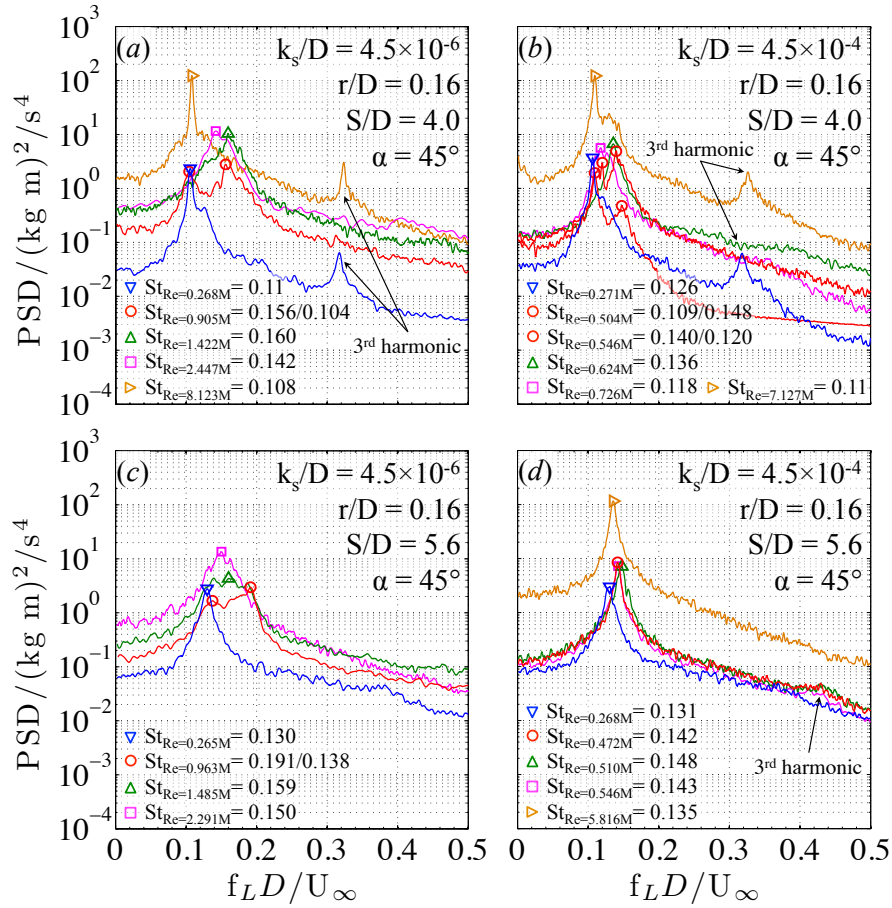

Figure D.2: Combined impact of increased surface roughness and gap spacing on the power spectral density of the time series of the global lift force that acts on the downstream one of two tandem square-section prisms ($r/D = 0.16$, $\alpha = 45°$) at selected Reynolds numbers in the *subcritical* to *transcritical* flow regimes. Left column: $k_s/D = 4.5\times10^{-6}$; right column: $k_s/D = 4.5\times10^{-4}$. Upper row: centre-to-centre spacing of $S/D = 4.0$; lower row: centre-to-centre spacing of $S/D = 5.6$. —: *subcritical flow regime*; —: *critical flow regime*; —: *supercritical flow regime*; —: *upper transition*; —: *transcritical flow regime*. The corresponding Strouhal numbers are indicated by the symbols on the curves and listed in each graph. M in the Reynolds number equals "million".

Appendix E

Effect of gap spacing on the power spectra of the global lift force on the downstream prism of two slightly rough square-section prisms with edge roundness of $r/D = 0.16$ in a tandem configuration at incidence angles of either $0°$ or $45°$

Appendix E: Effect of gap spacing on the power spectra of the global lift force on the downstream prism of two slightly rough square-section prisms with edge roundness of $r/D = 0.16$ in a tandem configuration at incidence angles of either $0°$ or $45°$
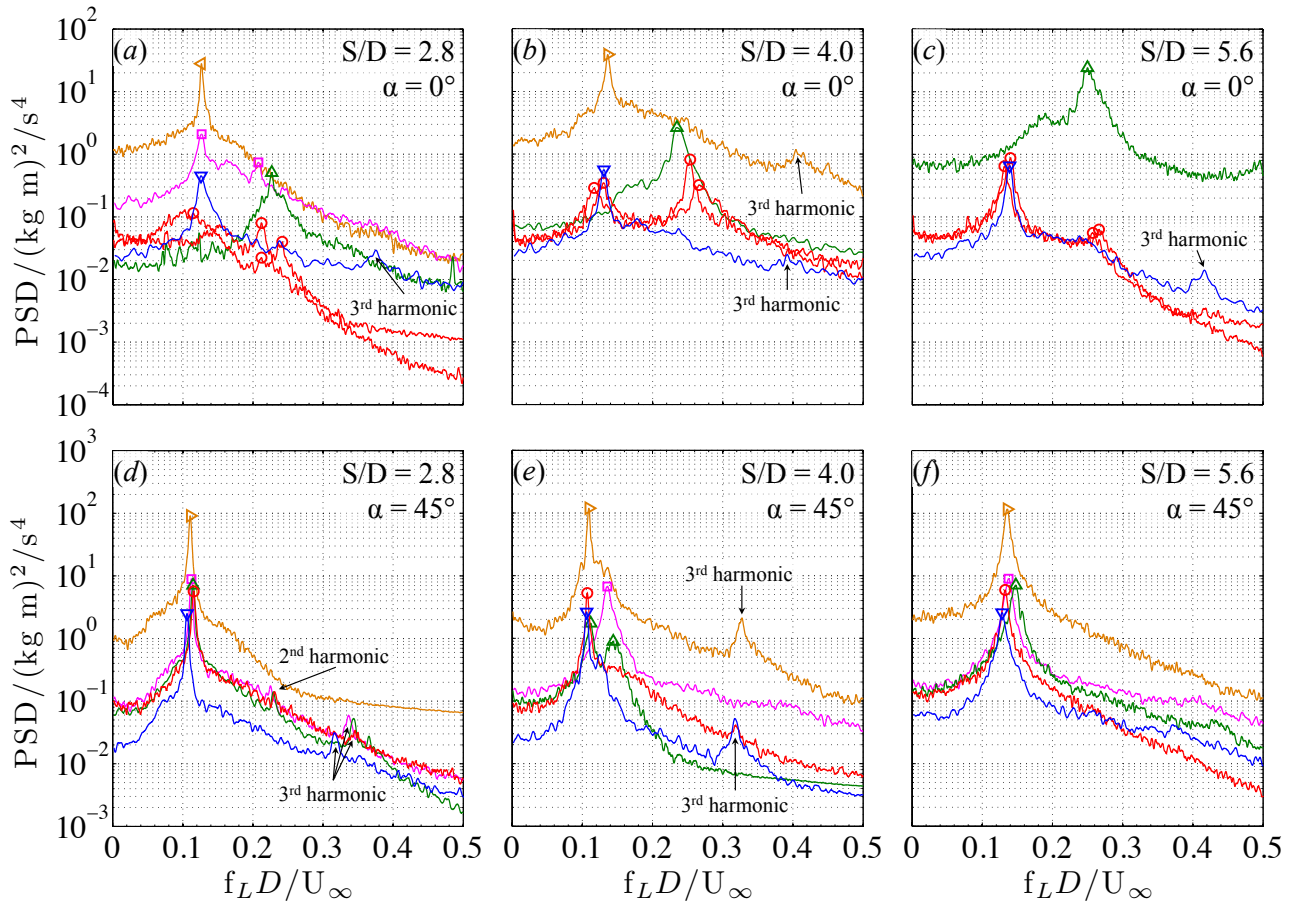
Figure E.1: Influence of the gap spacing on the power spectral density of the time series of the global lift force that acts on the downstream one of two slightly rough square-section prisms in tandem ($r/D = 0.16$, $k_s/D = 4.5{\times}10^{-4}$) at $\alpha = 0°$ and $45°$) for the same selected Reynolds numbers as presented in the Figures 5.20 to 5.24 (Adapted from Van Hinsberg [259]). Left column: $S/D = 2.8$; center column: $S/D = 4.0$; right column: $S/D = 5.6$. Upper row: $\alpha = 0°$; lower row: $\alpha = 45°$. ——: *subcritical flow regime*; ——: *critical flow regime*; ——: *supercritical flow regime*; ——: *upper transition*; ——: *transcritical flow regime*. The corresponding Strouhal numbers are indicated by the symbols on the curves.

Curriculum vitae

Personal data

Name:	Nils Paul van Hinsberg
Date of birth:	January 03, 1980, 's-Hertogenbosch, The Netherlands
Citizenship:	Dutch
Family status:	married

Academic qualifications

Since Aug. 2018:	Habilitation (Qualification as a University lecturer)
	Gottfried Wilhelm Leibniz University Hannover, Germany
Apr. 2019 – Feb. 2020:	Certification for teaching and learning at University level
	Georg-August-Universität Göttingen, Germany
Dec. 2005 – Dec. 2009:	Ph.D. (*magna cum laude*) in Fluid Mechanics
	Technical University of Darmstadt, Germany
Sep. 2002 – Aug. 2004:	M.Sc. in Aerospace Engineering, major in Experimental Aerodynamics
	Delft University of Technology, The Netherlands
Sep. 2001 – Aug. 2002:	Major in aerodynamics, Erasmus Munuds exchange programme
	École Nationale Supérieure de l'Aéronautique et de l'Espace (SUPAERO)
	Toulouse, France
Aug. 1999 – Oct. 2001:	B.Sc. in Aerospace Engineering
	Delft University of Technology, The Netherlands
Aug. 1998 – Aug. 1999:	Propaedeutic exam (*cum laude*) in Aerospace Engineering
	Delft University of Technology, The Netherlands
Aug. 1992 – Jun. 1998:	Humanistic Gymnasium
	Dr. Mollercollege, Waalwijk, The Netherlands
Sept. 1984 – Jul. 1992:	Primary School
	Pastoor van Haarenschool, Waalwijk, The Netherlands

Scientific career

Since Nov. 2022:	*German Aerospace Center (DLR e.V.), Göttingen, Germany*
	Research scientist at the Institute of Aerodynamics and Flow Technology
Jan. 2022 – Oct. 2022:	*Hamburg Ship Model Basin, Germany*
	Project manager
Jan. 2013 – Dec. 2021:	*German Aerospace Center (DLR e.V.), Göttingen, Germany*
	Research scientist and group leader at the Institute of Aeroelasticity
Apr. 2012 – Dec. 2012:	*TNO, Rijswijk, The Netherlands*
	Project manager and research scientist at Dept. of Technical Sciences
Mar. 2010 – Mar. 2012:	*Eidgenössische Technische Hochschule Zürich, Switzerland*
	Postdoctoral scientist at Institute of Fluid Dynamics (Prof. em. Dr. T. Rösgen)
Dec. 2005 – Dec. 2009:	*Technical University of Darmstadt, Germany*
	Scientific assistant at Institute of Fluid Mechanics and Aerodynamics
	(Prof. i. R. Dr.-Ing. C. Tropea)
Jun. 2005 – Nov. 2005:	*German Aerospace Center (DLR), Köln, Germany*
	Young researcher at Institute of Propulsion Technology
Dec. 2004 – May 2005:	*Technische Universität Braunschweig, Germany*
	Young researcher at Institute of Fluid Mechanics (Prof. a.D. Dr.-Ing. R. Radespiel)

Lecturing

Since 2024:	"Flow-induced vibrations of bluff-body structures" (Graduate course)
	Technische Universität Braunschweig, Germany
Since 2019:	"Flow-induced vibrations" (Graduate course)
	Gottfried Wilhelm Leibniz University Hannover, Germany
2010 – 2012:	"Experimental methods for engineers" (Graduate course)
	Eidgenössische Technische Hochschule Zürich, Switzerland
2006 – 2009:	"Fundamental fluid mechanics" (Undergraduate course)
	Technical University of Darmstadt, Germany